Wet-chemical synthesis of thin film materials for 3D all-solid-state Li-ion batteries

PhD candidate: ir. E.J. van den Ham
Promotor: Prof. Dr. A. Hardy
Co-promotor: Prof. Dr. M.K. Van Bael

Hasselt University – Diepenbeek, Belgium

Want wij kennen ten dele
(1 Korinthe 13:9)

Table of contents

Part IV: **Current colletor materials**

List of acronyms

(a)	Amorphous
2x5 Si	Micro-cylinders of Si (p. 34)
2x5 TiN	Micro-cylinders of Si coated with TiN (p. 34)
ALD	Atomic layer deposition
ATN	Acetonitrile
AZO	ZnO:Al
BSE	Back scattered electrons
CA	Citric acid
CSD	Chemical solution deposition
CV	Cyclic voltammetry / cyclic voltammogram
CVD	Chemical vapour deposition
DEE	1,1-diethoxyethane
DFT	Density functional theory
e-B.	E-Beam evaporation
ED	Electron Diffraction
ESD	Electrostatic spray deposition
FTIR	Fourier transform infrared spectroscopy
GATR	Grazing angle attenuated total reflectance
GCMS	Gas chromatography-mass spectrometry
GGG	$Gd_3Ga_5O_{12}$
HT-XRD	High-temperature XRD (page 40)
ICP-AES	Inductively coupled plasma atomic emission spectroscopy
isXRD	in-situ heating XRD (page 40)
ITO	In_2O_3:Sn
JCPDS	Joint Committee on Powder Diffraction Standards
LATP	$Li_{1.3}Al_{0.3}Ti_{1.7}(PO_4)_3$
Li-ion	Lithium-ion
LIB	Li-ion battery
LiPON	Nitrogen dopen lithium phosphate
LLT	$Li_{0.35}La_{0.55}TiO_3$ / $Li_{3x}La_{(2/3)-x}TiO_3$
LLTO	$Li_5La_3Ta_2O_{12}$
LLZO	$Li_7La_3Zr2O_{12}$
LMO	$LiMn_2O_4$
LTO	$Li_4Ti_5O_{12}$
LTP	Titanium containing lithium phosphates
LWO	Li_2W2O_7
MS	Mass spectroscopy
NASICONs	Sodium(Na) Super(S) Ionic(I) Conductors(CON)
NGO	$NdGaO_3$
PC	Polycarbonate
PLD	Pulsed laser deposition
PLS	Pulsed laser sintering
Sap.	Sapphire
SEI	Solid electrolyte-interface
SEM	Scanning Electron Microscopy
SEM	Secondary electrons
SPM/APM	Sulphuric acid-peroxide / ammonia-peroxide treatment
Sput.	Sputtering
STO	$SrTiO_3$
TCO	Transparent conductive oxide
TEM	Transmission electron microscopy
TGA	Thermal gravimetric analysis
TGA-DSC	thermogravimetric analysis with coupled differential scanning calorimetry
UPD	Underpotential deposition
USD	Ultrasonic spray deposition
UV-VIS	Ultraviolet-visible light spectroscopy
XPS	X-ray photoelectron spectroscopy
XRD	X-ray Diffraction

Part I - Chapter 1

Introduction

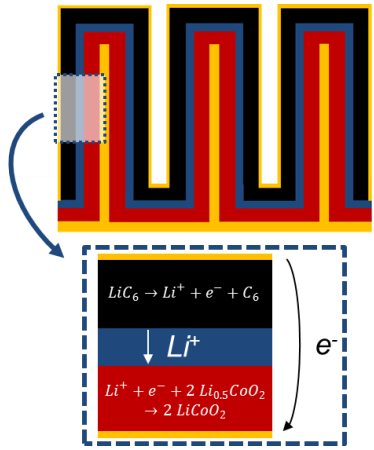

1. Introduction

Energy; something that drives us all. Broadly defined, energy is the capability of a system to perform work. For ease of usage, it is crucial that a system can provide work on demand, such as switching on a light bulb or driving a car. Hence, energy should be available (in other words: stored) for a system to provide work, which brings us to energy storage. The energy can be stored in different forms, such as chemical or kinetic energy. Over the last decades, one particular form of energy storage is of great interest in view of the transition to renewable energy sources: electric potential energy. In practice the term 'electrical energy' is often used. The interest in this form of energy mainly lies in the fact that a large number of sustainable energy sources such as windmills and photovoltaics yield electrical energy, which needs to be consumed directly, or stored for later use. Among several options, rechargeable batteries receive great attention because of their beneficial combination of high operating efficiency, ease of operation and storage capacity.[1,2] Within a battery system, electrical energy is converted to chemical energy with high efficiencies. Combined with the ease of usage, the commercial breakthrough of rechargeable lithium-ion (Li-ion) batteries in the 1990s revolutionized how people live, work and travel today.[2,3]

1.1 Li-ion batteries

Although Li-ion batteries are relatively expensive and suffer from more safety risks than other battery systems, the main advantage of Li-ion batteries lies in the high energy and power density.[2,4] In other words, less volume and mass are required to store the energy for a system to provide an equal amount of work.

Like other rechargeable battery systems, Li-ion batteries consist of four types of functional materials:

(i) Electrode materials, providing Li-ion and electron (e^-) storage. Electrode materials are subdivided in positive electrodes ('cathodes') and negative electrodes ('an-

odes'). Common electrodes are graphite (negative) and lithium cobalt oxide (positive).[3]

(ii) Electrolyte materials, facilitating Li-ion transport between the positive and negative electrode. Usually, this is a non-aqueous solvent with dissolved lithium salts. In many battery systems, the electrolyte is combined with a (porous) separator to prevent positive and negative electrodes from touching each other.

(iii) Current collector materials, allowing e^- transport between the electrodes and the external load of the system. In most systems, current collectors consist of metals such as copper or aluminium.

(iv) Packaging and scaffolding materials, responsible for the mechanical strength and protection against the surroundings.

For a typical battery, consisting of graphite as negative electrode and lithium cobalt oxide ($LiCoO_2$) as positive electrode, the half reactions during discharge are shown in Equations 1 and 2.[2,3]

$$LiC_6 \rightarrow Li^+ + e^- + C_6 \quad \textbf{(1)}$$

$$Li^+ + e^- + 2\ Li_{0.5}CoO_2 \rightarrow 2\ LiCoO_2 \quad \textbf{(2)}$$

During discharging, an electrochemical reaction occurs between lithiated graphite (LiC_6) and delithiated lithium cobalt oxide ($Li_{0.5}CoO_2$), yielding a cell voltage of about 3.7 V. As a result of the delithiation of graphite (Equation 1), the Li^+ ions travel to the lithium cobalt oxide through the electrolyte. Because of the electronic insulation function of the electrolyte, the electrons move via the current collector of the negative electrode, through the external load utilizing the current (e.g. a light bulb), towards the current collector of the positive electrode into the lithium cobalt oxide (Figure 1).

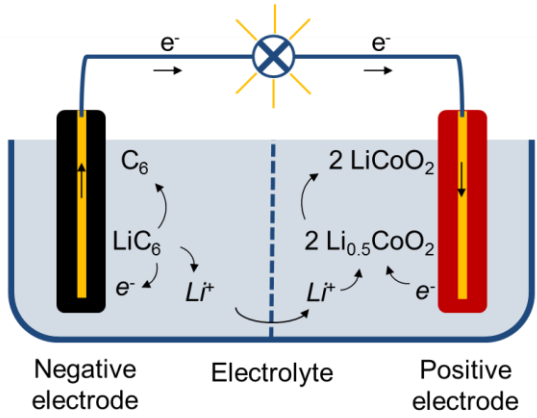

Figure 1: Schematic representation of a discharging graphite-lithium cobalt oxide battery.

During charging of the battery, the opposite reactions occurs, where the external load provides work to reverse the reactions, delithiating the lithium cobalt oxide and lithiating the graphite back to the initial state.

1.2 Improving Li-ion batteries: all-solid-state

Although rechargeable Li-ion batteries have been developed into a mature technology, some important issues remain to be solved. First of all, the lifetime of the batteries is limited. This issue is related to side reactions occurring with the liquid electrolyte, forming a SEI, which acts as a passivating layer. In addition, due to the use of non-aqueous solvents for the electrolyte, contemporary Li-ion batteries pose an inherent safety risk.[5] Strong temperature variations or a short circuit can cause combustion of the flammable liquid electrolyte.

Successful implementation of a solid electrolyte into a Li-ion battery, yielding an all-solid-state Li-ion battery, would greatly improve the issues contemporary Li-ion batteries suffer from. The lifetime of Li-ion batteries could be improved significantly, as SEI formation does not occur for an electrochemically stable, inorganic

electrolyte.[6,7] In addition, the safety of the system is strongly increased because flammable solvents are not required.[5,7] Solid electrolytes also yield advantages for device integration. Scalability is an advantage, since much thinner electrode separation can be used with a solid-state approach. Also the thermal stability of the solid electrolyte is an advantage, which makes Li-ion batteries suitable for integration in photovoltaic applications.[8,9]

1.3 Towards 3D all-solid-state Li-ion batteries

Though the advantages of all-solid-state Li-ion batteries are clear, scientific and technical hurdles have to be cleared before an all-solid-state Li-ion battery is realized. This is mainly due to the lower Li-ion conductivity in most solids as compared to liquid electrolytes. Simply replacing a liquid electrolyte by a solid-state counterpart would be undesirable. The 10 µm electrolyte thickness currently used for high capacity Li-ion batteries would lead to a huge resistance, deteriorating the battery's performance.[10]

To solve this problem, either the Li-ion conductivity of the solid electrolyte needs to improved, or the thickness of the electrolyte layer needs to be reduced significantly.[11]

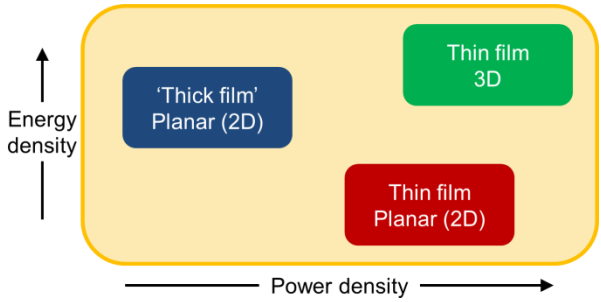

Figure 2: Relation between energy density, power density and battery architecture for all-solid-state Li-ion batteries with thin film solid electrolytes and thin film electrodes.

Ideally, both reduced thickness and improved conductivity are realized in a thin film configuration of the solid electrolyte, yielding little resistance over the electrolyte layer.[8]

Downscaling the electrolyte layer to submicron thicknesses while maintaining thick electrode layers (in the order of microns) yields additional issues however. Since Li-ions are inserted at the electrolyte-electrode interface and electrons at the current collector-electrode interface, the high thickness of the electrode poses transport issues for both the Li-ions and electrons. Hence, a thick film electrode yields high energy density, but little power density. Reducing electrode thickness is therefore desired to improve the power density. However, this leads to a significant energy density loss because thin films only have little energy capacity per footprint area (Figure 2).[11]

To achieve both high energy density and high power density, 3D architectures are required (Figure 2). Since a thin-film architecture is established all over the battery, the power density remains unaltered, but much more electrode material is available per footprint area, increasing the energy density (Figure 3).[11,12]

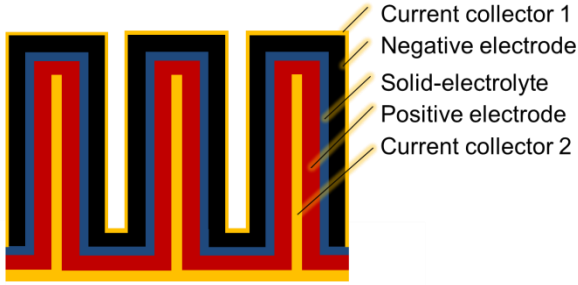

Figure 3: Schematic representation of a 3D thin film all-solid-state battery.

1.4 Deposition of 3D thin film battery materials

Although the concept is simple, realization of the thin film 3D all-solid-state Li-ion batteries poses a major challenge. Deposition of

materials on 3D dimensional scaffolds requires development of deposition processes. Thus far, progress was mostly established with vacuum based deposition methods. Current collector materials such as TiN, which poses superior Li-ion blocking and high electronic conductivity, have been established as 3D thin films by ALD.[6,13] In addition, high temperature stable Pt is available as a current collector material via ALD as well.[14,15] For positive and negative electrode materials several high quality coatings have been established, showing good electrochemical activity. This includes ALD deposited $LiCoO_2$,[16] which was named before (Equation 1), but also other electrode materials such as MnO_x,[17] $LiFePO_4$,[18] $Ti_3(PO_4)_3$ and TiO_2 [15,19,20] have been demonstrated by ALD. For CVD, reports were made on 3D deposited poly-Si,[21] $Li_4Ti_5O_{12}$ and TiO_2.[22,23] The solid electrolyte, as core of the thin film 3D all-solid-state battery, was deposited successfully in the form of LiPON and lithium silicates by ALD as well as lithium phosphate by CVD.[24,25] However, integration of current collectors, electrodes and electrolytes to yield a fully functioning 3D thin film all-solid-state battery has not yet been shown.

1.5 Wet-chemical synthesis for 3D thin film batteries

Though these results are a major step forward, the vacuum based character of these deposition methods leads to high cost for practical applications. In addition, not all materials can be prepared with these methods because multi-metal based materials pose a challenge (e.g. Li insertion during synthesis)[16,19,22,23] and metal-ion precursor specific diffusion limitations.[22,25] Hence, new routes are sought to use methods that are more cost effective, more up-scalable and a higher degree of deposition freedom with respect to complex multi-metal-ion materials.

Especially in the field of ceramics, wet-chemical synthesis routes are shown to be able to yield high quality materials, showing a higher degree of stoichiometric control and lower crystallization temperatures compared to other methods.[26] In addition, most of these methods are very cost-effective and up-scalable, which is an intrinsic advantage.[27] Wet-chemical synthesis routes proved ver-

satile for a broad range of battery materials, [28] including thin film electrolytes and various electrode materials.[29–35]

Efforts have been made to use these wet-chemical routes to prepare 3D all-solid-state batteries. First, porous solid electrolyte structures were applied. Various reports were made for 3D ordered macro porous all-solid-state Li-ion batteries.[36–41] However, the final performance of the full devices established with this approach was slightly disappointing, mostly ascribed to low electronic conductivity and degradation of the 3D networks.[40] Recently, reports were made of 3D patterned solid electrolyte, enabling preparation of electrolyte-separated electrode compartments with sizes down to the micron scale. Although this method has a big advantage in terms of thermal budgets because the electrolyte deposition can be done prior to deposition of the electrodes, only limited 3D enhancement is possible because of the length-scales used.[42]

In view of a superior gain in energy and power density, a wet-chemical approach attempting to prepare components for a 3D *thin film* all-solid-state Li-ion battery have been done as well. Deposition of active $LiCoO_2$ electrodes was shown on rods with submicron diameters with wet-chemical synthesis in combination with spray-coating. Though this was an excellent first result, the energy density per footprint area only doubled, where much higher capacity gains were to be expected.[43] Recently, Gielis et al. reported the conformal deposition of TiO_2 on high aspect micro-cylinders using spray-coating as well, although only limited functional properties could be shown.[44]

Both these highly promising examples give rise to the question how wet-chemical synthesis methods can be applied for 3D thin film all-solid-state Li-ion battery materials in a competitive way. Further development of this field would yield more freedom in terms of material choice regarding multi-metal based materials, as well as a huge gain in cost reduction and scalability to realize 3D thin film all-solid-state Li-ion battery materials.

1.6 The scope of this thesis

This thesis is focussed on the deposition and characterization of functional thin film battery materials by means of wet-chemical routes. Especially the feasibility for 3D depositions is investigated.

Part I (Chapter 1 and 2) holds the introduction and experimental methods used. They include details on wet-chemical synthesis routes and spray-coating in Chapter 2.

Part II is oriented towards solid electrolyte films (Chapters 3-6), both planar and 3D. In chapter 3 an overview of inorganic solid electrolyte materials is given. Chapter 4 is dedicated to the synthesis and characterization of planar lithium lanthanum titanate (LLT) by means of aqueous CSD. In chapter 5, the 3D deposition of LLT is discussed. In chapter 6, the synthesis of the garnet solid electrolyte films is discussed, especially $Li_7La_3Zr_2O_{12}$.

In Part III, a high voltage negative electrode material in the form of tungsten oxide is discussed (Chapters 7-10). The hallmark of this material is the high volumetric capacity and the fact that it can be combined with less electrochemically stable solid electrolytes, such as LLT. In chapter 7 the deposition of tungsten oxide via a colloidal suspension is discussed, including the electrochemical properties. Chapter 8 continues with investigation of addition of lithium to the precursor system discussed in Chapter 7; aimed at the synthesis of Li_xWO_3 films. In chapter 9, the 3D deposition of tungsten oxide is discussed, including electrochemical comparisons between planar and 3D depositions. At the end of Part III, the 3D stacked combination of LLT and tungsten oxide is studied in Chapter 10.

Part IV (Chapter 11) discusses the last category of functional battery materials: current collectors. The 3D deposition of indium tin oxide (ITO) is discussed, including its use as a current collector for 3D thin-film Li-ion batteries.

Finally, conclusions are drawn in chapter 12.

2. References

[1] M. S. Whittingham, *MRS Bull.* **2008**, *33*, 411.
[2] B. Scrosati, J. Garche, *J. Power Sources* **2010**, *195*, 2419.
[3] K. Ozawa, *Solid State Ionics* **1994**, *69*, 212.
[4] J.M. Tarascon, M. Armand, *Nature* **2001**, *414*, 359.
[5] P. Knauth, *Solid State Ionics* **2009**, *180*, 911.
[6] L. Baggetto, J. F. M. Oudenhoven, T. Van Dongen, J. H. Klootwijk, M. Mulder, R. A. H. Niessen, M. De Croon, P. H. L. Notten, *J. Power Sources* **2009**, *189*, 402.
[7] K. Takada, *Acta Mater.* **2013**, *61*, 759.
[8] J. F. M. Oudenhoven, L. Baggetto, P. H. L. Notten, *Adv. Energy Mater.* **2011**, *1*, 10.
[9] N. Kamaya, K. Homma, Y. Yamakawa, M. Hirayama, R. Kanno, M. Yonemura, T. Kamiyama, Y. Kato, S. Hama, K. Kawamoto, A. Mitsui, *Nat. Mater.* **2011**, *10*, 682.
[10] P. Arora, Z. Zhang, *Chem. Rev.* **2004**, *104*, 4419.
[11] J. W. Long, B. Dunn, D. R. Rolison, H. S. White, *Chem. Rev.* **2004**, *104*, 4463.
[12] P. H. L. Notten, F. Roozeboom, R. A. H. Niessen, L. Baggetto, *Adv. Mater.* **2007**, *19*, 4564.
[13] H. C. M. Knoops, L. Baggetto, E. Langereis, M. C. M. van de Sanden, J. H. Klootwijk, F. Roozeboom, R. a. H. Niessen, P. H. L. Notten, W. M. M. Kessels, *J. Electrochem. Soc.* **2008**, *155*, G287.
[14] J. Dendooven, R. K. Ramachandran, K. Devloo-Casier, G. Rampelberg, M. Filez, H. Poelman, G. B. Marin, E. Fonda, C. Detavernier, *J. Phys. Chem. C* **2013**, *117*, 20557.
[15] M. E. Donders, J. F. M. Oudenhoven, L. Baggetto, H. C. M. Knoops, M. C. M. van de Sanden, W. M. M. Kessels, P. H. L. Notten, *ECS Trans.* **2010**, *33*, 213.
[16] M. E. Donders, W. M. Arnoldbik, H. C. M. Knoops, W. M. M. Kessels, P. H. L. Notten, *J. Electrochem. Soc.* **2013**, *160*, A3066.
[17] F. Mattelaer, P. M. Vereecken, J. Dendooven, C. Detavernier, *Chem. Mater.* **2015**, *27*, 3628.
[18] T. Dobbelaere, F. Mattelaer, J. Dendooven, P. Vereecken, C. Detavernier, *Chem. Mater.* **2016**, *28*, 3435.
[19] T. Dobbelaere, F. Mattelaer, J. Dendooven, P. M. Vereecken, C. Detavernier, *ECS Trans.* **2016**, *75*, 35.
[20] E. Eustache, P. Tilmant, L. Morgenroth, P. Roussel, N. Rolland, T. Brousse, C. Lethien, *ECS Trans.* **2013**, *58*, 119.

[21] L. Baggetto, H. C. M. Knoops, R. a. H. Niessen, W. M. M. Kessels, P. H. L. Notten, *J. Mater. Chem.* **2010**, *20*, 3703.
[22] J. Xie, P.-P. R. M. L. Harks, D. Li, L. H. J. Raijmakers, P. H. L. Notten, *Solid State Ionics* **2016**, *287*, 83.
[23] J. Xie, J. F. M. Oudenhoven, D. Li, C. Chen, R.-A. Eichel, P. H. L. Notten, *J. Electrochem. Soc.* **2016**, *163*, A2385.
[24] Y.-C. Perng, J. Cho, S. Y. Sun, D. Membreno, N. Cirigliano, B. Dunn, J. P. Chang, *J. Mater. Chem. A* **2014**, *2*, 9566.
[25] J. Xie, J. F. M. Oudenhoven, P.-P. R. M. L. Harks, D. Li, P. H. L. Notten, *J. Electrochem. Soc.* **2014**, *162*, A249.
[26] D. Segal, T. Aea, F. Culham, U. K. Ox, **1997**, *7*, 1297.
[27] R. Schwartz, T. Schneller, R. Waser, *Comptes Rendus Chim.* **2004**, *7*, 433.
[28] L. Fu, H. Liu, C. Li, Y. Wu, E. Rahm, R. Holze, H. Wu, *Prog. Mater. Sci.* **2005**, *50*, 881.
[29] K. Takada, K. Fujimoto, T. Inada, A. Kajiyama, M. Kouguchi, S. Kondo, M. Watanabe, *Appl. Surf. Sci.* **2002**, *189*, 300.
[30] Y. H. Rho, K. Kanamura, *J. Solid State Chem.* **2004**, *177*, 2094.
[31] Y. H. Rho, K. Dokko, K. Kanamura, *J. Power Sources* **2006**, *157*, 471.
[32] Y. H. Rho, K. Kanamura, M. Fujisaki, J. Hamagami, S. Suda, T. Umegaki, **2002**, *151*, 151.
[33] M. Vinod, D. Bahnemann, *J. Solid State Electrochem.* **2001**, *6*, 498.
[34] S. Takase, C. Kubo, R. Aono, Y. Shimizu, *J. Sol-Gel Sci. Technol.* **2016**, *79*, 564.
[35] H. Liu, Y. P. Wu, E. Rahm, R. Holze, H. Q. Wu, *J. Solid State Electrochem.* **2004**, *8*, 450.
[36] K. Kanamura, N. Akutagawa, K. Dokko, *J. Power Sources* **2005**, *146*, 86.
[37] K. Dokko, N. Akutagawa, Y. Isshiki, K. Hoshina, K. Kanamura, *Solid State Ionics* **2005**, *176*, 2345.
[38] E. J. Van Den Ham, I. Kokal, H. T. Hintzen, **2012**, *146*, 2012.
[39] K. Kanamura, N. Akutagawa, K. Dokko, *J. Power Sources* **2005**, *146*, 86.
[40] M. Hara, H. Nakano, K. Dokko, S. Okuda, A. Kaeriyama, K. Kanamura, *J. Power Sources* **2009**, *189*, 485.
[41] I. Kokal, E. J. van den Ham, a. C. a. Delsing, P. H. L. Notten, H. T. Hintzen, *Ceram. Int.* **2015**, *41*, 737.
[42] I. Kokal, O. F. Göbel, E. J. Van Den Ham, J. E. Elshof, P. H. L. Notten, H. T. Hintzen, *Ceram. Int.* **2015**, 1.

[43] M. M. Shaijumon, E. Perre, B. Daffos, P.-L. Taberna, J. M. Tarascon, P. Simon, *Adv. Mater.* **2010**, *22*, 4978.
[44] S. Gielis, Chemical Solution Deposition of Oxides for Energy Storage Applications: A Breaktrough in Coating High Aspect Ratio 3D Structures, Hasselt University, **2015**.

Part I - Chapter 2

Experimental methods

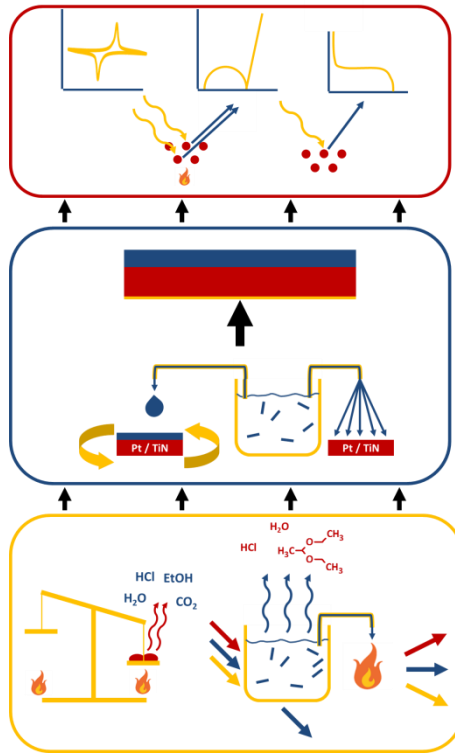

Abstract

The experimental methods used during the research presented in this thesis are explained in this chapter in general terms. First, a short introduction is given for the wet-chemical synthesis routes used. Next, several deposition methods are discussed. This includes ultrasonic spray deposition, which was frequently used during the studies presented in this thesis. Finally, the characterization methods used are discussed. A general overview of the spectroscopic, gravimetrical, diffraction, microscopy and electrochemical methods is given.

1. Wet-chemical synthesis routes

1.1 Chemical solution deposition (CSD)

The synthesis method to obtain oxide films most often applied in this thesis is chemical solution deposition (CSD). Essentially, this wet-chemical method is based on the synthesis and stabilization of metal-complexes in a suitable solvent, followed by deposition on a substrate and a final anneal to form the oxide material. However, this involves a lot of separate steps that need to be optimized in order to obtain smooth films. For instance, stabilization of the (several different) metal complex(es) in the solvent is crucial, as precipitation would lead to inhomogeneous deposition and / or local stoichiometric differences in the material.

There is a broad spectrum of CSD approaches, involving different starting products, solvents and stabilizing ligands.[1,2] The main approach used within this thesis is based on citrate ligand coordination to a metal ion in water under appropriate pH conditions. This is based on the electron donating citrate ligand, which coordinate to the metal ion via carboxylate groups. A simple example is lithium citrate. Since Li^+ is such a small ion with a low oxidation state, one citrate ligand can host several lithium ions, with a maximum of three; one Li^+ on every carboxylate group. For other metals this complexation occurs differently, depending on pH conditions. For instance, W^{6+} complexation with citrates leads to a complex consisting of one citrate ligand per W^{6+} ion, combined with non-bridging oxygen (oxo ligand) and water (aqua ligand) coordination.[3]

Once a mono/multi metal ion precursor is obtained, it is deposited on a substrate via a specific deposition technique, such as spin-or spray-coating (c.f. Section 1.1 to 1.3). Upon heating the liquid film, gelation occurs together with evaporation of the solvent (water). At higher temperature decomposition of the citrate ligand occurs, via intermediate products M-O-C bonds are decomposed to form M-O-M bonds. This leads to amorphous or crystalline oxide formation. The latter step is strongly influenced by the final synthesis temper-

ature applied, similar to other deposition methods such as ALD, CVD or sputtering.

In the specific case of multi-metal oxides there is a small difference however; since molecular mixing of the metal complexes applies both in the liquid (before deposition) and solid phase (after deposition), the resulting film consist of metal-ions in the same stoichiometry all over the substrate or in- and out-of-plane directions. This is a large difference with for instance ALD, which is based on stacked (atomic) layers of different metal oxides (concentration difference for out-of-plane direction), followed by a solid-state reaction to form the multi-metal oxide. Although CSD requires a thermal budget for the removal of stabilizing ligands to form the final oxide, the molecular mixing is one of the main benefits of the CSD approach. However, perfect control over chemistry to ensure homogeneity is required to achieve molecular mixing. Once this is realized, difficult diffusion of (large) metal-ions is no longer required. Therefore, crystallization temperatures may be lowered and secondary phase formation can be prevented.

1.2 Other wet chemical methods

Besides CSD, a long list of wet-chemical synthesis routes is available for the synthesis of oxides.[4] Though all these methods have their pros and cons compared to (aqueous) CSD, one other approach was used during this research: deposition of stable suspensions. As the name suggests, deposition of stable suspensions does not (solely) involve molecular solutions. Instead, a suspension consisting of particles is deposited, which are sintered to form a film. This does not mean that the liquid phase only consists of solvent, as a mixture of particles and molecular precursors is also possible. In comparison with (aqueous) CSD, suspension-based precursors may be less stable over time. In addition, molecular mixing does not apply once the (oxide) particles are formed, implying that mixing has to take place during the formation of the colloidal suspension, and no segregation should occur afterwards. Despite these challenges, successful deposition of suspensions has one major advantage, since removal of organic ligands (i.e. coordinate bonding) can take place before the deposition. Hence, the

advantage of a suspension-based precursors lies in smaller thermal budget requirements, since removal of solvent(s) and organic additives (lacking coordinate bonds) generally require a low temperature to be removed from the film.

1.3 Spin-coating

Within the field of wet-chemical synthesis, spin-coating is a well-established deposition method. The basic principle is simple: a few drops of precursor solution are deposited on a substrate, followed by rotating the substrate. Typically, the speed of the rotation is chosen between 1000 and 6000 rpm. Since most of the material leaves the substrate upon rotation, the yield of deposited material per cycle is relative low. Therefore, a multi-step deposition is often applied, using intermediate anneals to make sure the previous deposition cycle is fixed to the substrate and no longer consists of a liquid film.[5] The method is highly popular because ease of use and low surface roughness. For instance, for In_2O_3:Sn (ITO) thin films, a sub-nm roughness was achieved.[6] The main drawback of spin-coating is that this method is laborious if thick films (500 – 1000 nm) are required, especially when the solute has a low solubility limit. Therefore, it is often considered only suitable for lab-scale applications.[7,8] In addition, it is a planarizing method and is therefore no candidate deposition method for 3D deposition.

1.4 Dip-coating

The next technique that is often applied is dip-coating. Here, a substrate is dipped in the precursor solution, with well controlled withdrawal rate.[8] Depending on the desired thickness, this procedure is repeated after an intermediate anneal. By controlling the precursor wetting, viscosity and solvent evaporation, good results can be achieved yielding smooth films. Just as with spin-coating, precursor concentration dictates the thickness of the obtained films. Nevertheless, dip-coating can easily be applied on industrial scale, because there are no intrinsic issues to up-scale the immersion process.[9] In essence 3D deposition should be possible with

dip-coating, although only few successful examples are found in literature.[10,11]

1.5 Spray-coating

The final deposition method considered was used extensively during this study. The main difference with the previous two deposition methods is that spray-coating does not rely on an excess of precursor solution for film formation. Instead, small droplets are generated which are supposed to form a film under optimized conditions. This different approach has a large practical advantage: a high yield of deposition. Besides initiation, cleaning and loss due to overspray, all the precursor solution or suspension is deposited on the substrate. Furthermore, the spray-based character makes roll-to-roll processing possible, giving spray-coating a huge upscaling potential.[7,12] More importantly for this study: spray-coating is capable of coating 3D structures down to the micron scale.[13 –15]

1.5.1 Various spray-coat systems

A wide variety of different spray-coating types can be found in literature (Figure 1).[16–27] The lack of consensus regarding definitions is probably due to the fact that many different physical processes are used as a driving force for spray transportation, yielding a solution or slurry / suspension borne coating. Essentially, spray-coating can be defined as a way to distribute particles, dissolved salts or molecules yielding a coating on a carrier with the help of a spray. The carrier can be a particle or a substrate.

While this definition of spray-coating is not very useful because of its broadness, some divisions can be made. From a coating application perspective, spray-coating can be divided into two classes, namely i) spraying a coating on particles and ii) spraying a coating on a substrate. Note that this involves 'coating' of particles or surfaces, meaning that for instance 'spray drying' essentially is a different synthesis method as it is primarily aimed at the synthesis of particles, not coatings.[28,29]

For films, one of the most used types of spray-coating is electro-spraying, also referred to as 'electrodynamic spraying' or 'electrostatic spray deposition' (ESD).[16,20,24,34] As the name suggests, ESD utilizes electrostatic interactions between the precursor droplets produced and the substrate. This is achieved by creating a potential difference in the order of 10 kV between the spray nozzle and the substrate. Hence, several precursor properties are crucial, including a low surface tension and (sufficient) electronic conductivity.[34] ESD is therefore rarely used in combination with aqueous precursor systems.[35] Upon optimization of an organic precursor with additives such as acetic acid, crack free metal oxide films can be realized.[34] In addition, the flow rate of the precursor, nozzle height, voltage difference and deposition temperature (T_d) were shown to be of major influence on the morphology of ESD deposited films.[17]

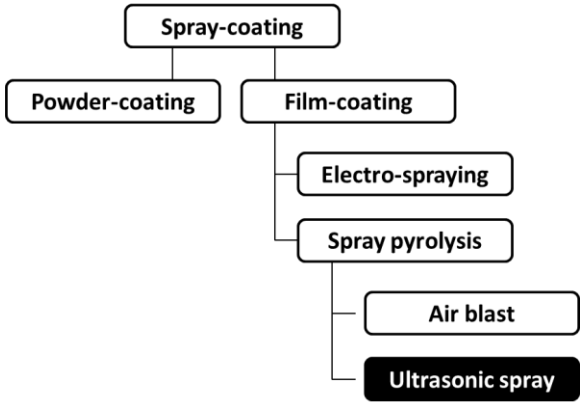

Figure 1: Division of different spray-coating methods

The second common class of spray-coating is often referred to as 'spray pyrolysis'.[22,23,25–27,32–40] By definition, pyrolysis (or thermolysis) suggests high temperature treatments and breakage of covalent bonds, possibly under inert conditions.[41] Therefore, the definition of 'spray pyrolysis' seems inappropriate in some cases. Especially so, since the term 'pyrolysis' is sometimes used without

knowing the details of the precursor system, meaning that pyrolysis may not be applicable.[27] Nevertheless, the atomization (i.e. droplet generation) of so-called 'spray pyrolysis' can occur in different ways. The most simple atomization occurs via air blasting. Precursor droplets are formed while exposing the precursor solution to high velocity airflow, creating a spray.[31,40] Although cost-effective, reproducibility of these systems is limited due to broad droplet size distributions.[31] Alternatively, atomization occurs via a transducer (i.e. a ceramic plate to transfer kinetic energy) which vibrates at high frequency, this issue is circumvented. This is often referred to as 'ultrasonic atomization' due to the fact that transducer frequencies surpass ultrasonic frequencies. Since this method of atomization was used during this study, more insights in ultrasonic spray deposition will be provided in this chapter.

1.5.2 Ultrasonic spray deposition

Although rarely used, this term clearly indicates how atomization of the precursor solution, suspension or slurry occurs. The process of ultrasonic spray deposition (USD) can be described in a four subsequent steps, namely (i) atomization, (ii) spray formation and shaping, (iii) droplet transport and evaporation and (iv) film formation.

1.5.2.1 Atomization

As mentioned before, USD depends on a transducer vibrating at or above ultrasonic frequencies to form the droplets. Simply said, this process consists of a number of subsequent steps, as described in the patent of Berger et al.[42]

(i) Automated precursor transport to the transducer, often done with a syringe connected to a syringe pump;
(ii) Precursor wetting of transducer, forming a precursor film;
(iii) Transducer vibration at high frequencies, leading to high speed movement of the liquid film on top;
(iv) Capillary wave formation within the precursor film;
(v) Collapse of capillary waves, creating a precursor droplet;

(vi) Movement of the droplet to the nozzle for spray formation and shaping by a carrier gas.

The physical phenomenon utilized during ultrasonic atomization via the transducer, is the occurrence of capillary waves. These capillary waves in the precursor film go through three different phases while changing the frequency and amplitude of the vibrations, namely (i) initiation, (ii) modulation and finally (iii) turbulence. Handling the physics behind these individual steps in great detail goes beyond the scope, but an intuitive example is shown in Figure 2.

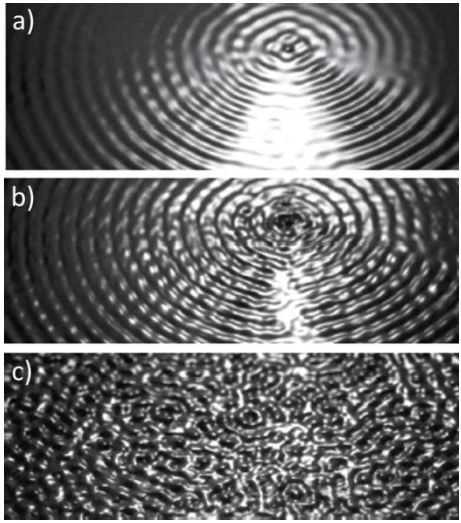

Figure 2: simulated image of capillary wave a) initiation, b) modulation and c) turbulence.[43]

For the droplet formation, creating stable capillary waves is crucial. From physics, these stable waves can be described in equation 1[43]

$$\nu^2 \propto \frac{\sigma}{\rho}\left|\frac{2\pi}{\lambda}\right|^{\frac{1}{3}} \quad \textbf{(1)}$$

where ν is the angular frequency (i.e. transducer vibration frequency), σ the liquid surface tension, ρ the liquid density, and λ

the wavelength of the capillary waves. Thus, beside precursor properties that can be tuned by changing the precursor chemistry, the main atomization parameter is the vibration frequency. This is related to the wavelength of the capillary waves; the square of the frequency scales with the wavelength to the power -1/3 ($\nu^2 \propto \lambda^{-\frac{1}{3}}$).

While the formation of stable capillary waves can be tuned with the frequency, the turbulence or collapse of these films can be caused by a change of amplitude. As the acceleration (a) of a confined precursor volume on the wave can be described as the second derivative of the amplitude (A) over time of the wave (Equation 2), acceleration of the confined volume soars at high frequency ($\nu = 1/t$) and a large amplitude.[42,43] Hence, it becomes clear why ultrasonic frequencies ($\nu > 20$ kHz) are much more suitable for atomization than for instance supersonic frequencies, because it leads to larger acceleration at comparable amplitude.

$$a = \frac{\partial^2 A}{\partial t^2} \qquad \textbf{(2)}$$

The acceleration cannot become infinite, since the capillary wave will collapse at high accelerations. Once again, further details go beyond the scope of this thesis, but a schematic representation can be found in Figure 3.

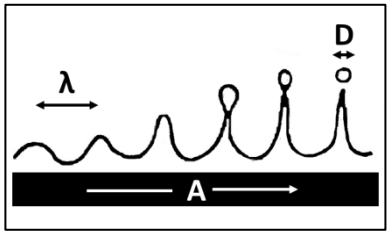

Figure 3: collapse of capillary waves as function of the applied amplitude (A) with droplet diameter D for a fixed wavelength (λ). The image was partly adopted from stated reference.[44]

For USD, these principles imply that three main factors are of influence for successful atomization with a fixed vibration frequency:

(i) the surface tension of the precursor, (ii) the density of the liquid and (iii) the amplitude of the transducer frequency. For example, a low surface tension combined with a high density (i.e. small wavelengths at a fixed frequency) requires small amplitudes to achieve atomization (e.g. diethyl-ether or isopropanol). Or the opposite: a low density, high surface tension precursor (e.g. water) will require larger amplitudes for atomization.

Using ultrasonic atomizers leads to intrinsic advantages. First of all, a well-defined droplet size distribution results from the collapsed capillary waves. According to Berger et al., the droplets generated via the ultrasonic atomization obey Equation 3.

$$D_{0.5} = 0.34\left(\frac{8\pi\sigma}{\rho\nu^2}\right)^{1/3} \quad \textbf{(3)}$$

Where $D_{0.5}$ is the median of the drop diameter, σ the surface tension of the liquid, ρ the density of the liquid and ν the frequency of the transducer. Since the droplet size is defined by the confined volume acceleration of the capillary wave, it is no surprise equations 1 and 3 are related. For a typical ethanol / water precursor (50/50 vol%), the mean droplet size at 20°C is 8.6 µm just after atomization.[45] This well-defined droplet size distribution, mainly consisting of small droplets, increases the reproducibility considerably, especially compared to air blast deposition.

A second advantage of ultrasonic atomization is that the droplet size distribution is virtually independent of the flow rate. This is due to the fact that droplet atomization only depends on the precursor properties and the transducer vibration (amplitude and frequency). Obviously, no unlimited precursor volumes (i.e. high flowrate per unit time) can be atomized due to the limited size of the transducer and the precursor film volume on top of it. Practically speaking, the droplet size distribution is the same while using a precursor flowrate of 0.4 or 4 ml·min^{-1}. This feature enables exclusion of at least one parameter in an already intertwined set of different variables during USD.

1.5.2.2 Spray formation and shaping

If atomization occurs, the droplets are transported to the nozzle with a carrier gas, which can mechanically be shaped in several ways. Different shapes can be generated by changing the nozzle type. For relative small deposition areas, the so called Accumist® nozzle (Sono-Tek) is used.

The main parameter for shaping the spray with a fixed nozzle type is the carrier gas pressure. In case no pressure is applied, a shroud leaves the nozzle; gravity and natural convection dictate the direction of the shroud. Therefore, the spray lacks shaping and is very vulnerable to external airflow (e.g. exhaust inlet), yielding inhomogeneous deposition. If the carrier gas pressure is increased, the spray shaping increases, quickly transporting the droplets to the substrate in a cone-shaped spray. At higher pressures, the droplets gain higher velocity which can have consequences for the droplet impact on the substrate (c.f. next section). In addition, the high pressure leads to a larger gas flow over the substrate which can lead to deposition temperature deviations.[31]

Since the precursor flowrate has virtually no influence on the droplet size distribution, the precursor flow (before atomization) only influences the mass flux of the spray (after atomization).

1.5.2.3 Droplet transport and evaporation

Once the droplet leaves the nozzle as part of a well-defined spray due to the carrier gas pressure, several forces are acting on the droplets. Especially for large droplets, gravity forces can influence the trajectory. However, for the small droplets used during this study ($D_{0.5}$ < 10 µm), gravity forces are of little significance.[15]

A second force encountered is drag due to resistance of surrounding air, which has a much lower velocity. This can be expressed with the Stokes force, which dictates that the drag is (almost) linearly related to the product of droplet size and speed. Since a carrier gas is applied for spray shaping, increasing the velocity of the droplets and surrounding gas simultaneously, this is the main parameter to minimize drag.[15] The drag encountered only affects

the outer limits (outer diameter) of the spray, slowing down only the outermost droplets of the spray.[46]

The final (significant) force acting on the droplets is the thermophoretic force, although it is only valid for deposition on a heated surface. This force arises from the large temperature gradient present up to 5 mm above the heated surface.[31] Thermophoretic forces act especially in case of a carrier gas, due to forced convection between the nozzle and the substrate, leading to an even larger temperature gradient.[15] The thermophoretic force retards droplets from the heated surfaces, due to the much higher kinetic energy of the gas molecules close to the surface compared to the droplet and surrounding gas.[32] Therefore, the thermophoretic forces slow down the droplet approaching the surface, while the (strong) temperature increase strongly reduces the droplet size due to evaporation.[15,31,46,47]

1.5.2.4 Film formation

The complex interplay of forces, changing droplet size, decomposition reactions and surface chemistry hinder a complete understanding of the film formation mechanism. Nevertheless, Perednis et al. tried to formulate a simple model for their metal halide / alkoxide salt / organic solvent precursor.[31,32] This was further elaborated upon by Filipovic et al.[15] In this model, the deposition temperature is the leading parameter dictating the film formation. It must be noted though, that the temperatures indicated in the following may vary strongly, depending on the choice of precursor.

If the deposition temperature is too low (<150°C), the solvent evaporates after droplet impact. Depending on the solvent mixture and decomposition / precipitation behavior, this can lead to non-uniform deposition due to diffusional differences (also known as the 'coffee stain effect').[48] In addition, a low deposition temperature can lead to droplet splashing. This depends on the velocity, surface tension and diameter of the droplet (which is defined by the dimensionless Weber (*We*) number). Large droplets with a high velocity and low surface tension readily lead to splashing. For ul-

trasonic deposition (i.e. small droplets), splashing can easily be avoided by increasing the deposition temperature, since this lowers both the velocity and droplet diameter.

If more intermediate deposition temperatures (200-400°C) are reached, additional effects can come into play: the Leidenfrost effect. Intuitively, this effect is recognized when a water droplet hits a hot surface, leading to the droplet hovering over the surface. This phenomenon is based on the formation of a stable vapor film between the droplet and the heated surface.[49] This results in 'CVD like' deposition behavior, since material is deposited via the vapor phase present between the droplet and the substrate. This temperature regime is reported to yield very smooth films.[15,32,49] The temperature at which the Leidenfrost effect starts occurring is influenced by many factors, including solvent, solute, surface roughness and wetting behavior.[40,50] For a typical aqueous or organic precursor on silicon substrates, the Leidenfrost point lies between 280 and 400°C.[40,49]

Within the intermediate temperature regime, (below the Leidenfrost point) droplets are evaporated upon hitting the substrate. Decomposition occurs on the surface before the coffee stain effect occurs. Larger droplets take longer to evaporate, and thus have the possibility to spread among immobilized smaller droplets, yielding relative smooth morphologies as well.[15,31]

If the deposition temperature is further increased (>400°C), too high temperatures can be reached for film formation. In this case, the (smallest) droplets completely evaporate before hitting the surface. This leads to powder / gel formation before the precursor wets the substrate, resulting in poor adhesion to the substrate. The occurrence of this mechanism depends on the solubility of the solute in the chosen solvent. It is speculated that this is the reason why lower precursor concentrations (in the order of 10 to 100 mM) are often used to obtain high quality coatings.[13,27,30,31] Especially so for ultrasonic atomizing systems, since the atomization hardly depends on concentration of (molecular) precursors (unless surface active species such as surfactants are used, altering the surface tension).

2. Substrates

Since a large number of different substrates is used during the study presented in this thesis, an overview is shown here.

2.1 Planar substrates

- **Si**: monocrystalline silicon substrates with native SiO_x. These substrates are suitable for morphology analysis of deposited films, but tend to react with lithium (ions) and other metals. In addition, these substrates exhibit a (very) low electronic conductivity. Supplier: imec, Belgium.
- **SiO_x**: thermally grown silicon oxide on monocrystalline Si substrates. The substrate characteristics are comparable to Si, but the SiO_x makes them even more electronically insulating than Si substrates. These substrates were used to study ITO deposition (Chapter 11). Supplier: imec, Belgium.
- **Si_3N_4**: Si_3N_4 (80 nm) on top of Si with SiO_x in between. These substrates yield high thermal stability (approx. up to 800°C), prevent lithium diffusion into Si, but are non-conductive. Supplier: imec, Belgium.
- **TiN**: TiN (80 nm) on top of monocrystalline Si with SiO_x in between. Known as a suitable lithium blocker and highly conductive material,[51] it is often used as a current collector during this study. However, TiN is susceptible to oxidation reactions above 450°C. Supplier: imec, Belgium.
- **Pt**: sputtered Pt (100 nm) on top of TiN substrates, as described above. Pt is the current collector most often used for this study because of the high electronic conductivity and high temperature stability. Supplier: Ghent University, Belgium.
- **GGG**: polished monocrystalline $Gd_3Ga_5O_{12}$ substrates. These substrates were used to study crystallization of garnet electrolytes (Chapter 6). The material is strongly insulating. Supplier: Alineason, Germany.
- **ITO**: In_2O_3:Sn films (200 nm) on glass substrates. A well-known transparent conductive oxide which was used as a

reference material during this study (Chapter 11) . Supplier: Sigma-Aldrich, Belgium.

2.2 Non-planar substrates

The non-planar substrates used during this study serve as scaffolds for the functional materials deposited on top. To study the morphology, functional properties and deposition mechanism of the deposited materials, various substrates were used.

- **3D Si (2x5)**: micro-cylinders of 50 micron, with a diameter of 2 micron at the top (3 at the bottom), placed 5 micron apart (Figure 4). Although the micro cylinders themselves have an aspect ratio of about 25 (50/2), 50 micron long cylinders with an inter-cylinder distance of 5 micron yields 3D structures of with an aspect ratio 10 (50/5). Supplier: imec, Belgium.
- **3D TiN (2x5)**: similar to 3D Si (2x5), but coated with 20 nm of TiN to ensure electronic conductivity. This feature is of importance to determine the functional properties of the deposited materials. Supplier: imec, Belgium.
- **3D TiN (2x10)**: similar to the previous 3D TiN substrate, but the inter-cylinder distance amounts 10 µm. The aspect ratio of the 3D structure is therefore 5 (50/10). Supplier: imec, Belgium.
- **Si trenches**: Si structures with varying aspect ratio (1 to 21), which were used to study the deposition and conformality of the deposited coatings (Figure 5). Supplier: Philips, the Netherlands (in cooperation with Eindhoven University of Technology).

In this study, conformality of a deposited coating is defined as the lowest thickness divided by the highest thickness of a 3D film, times 100%.

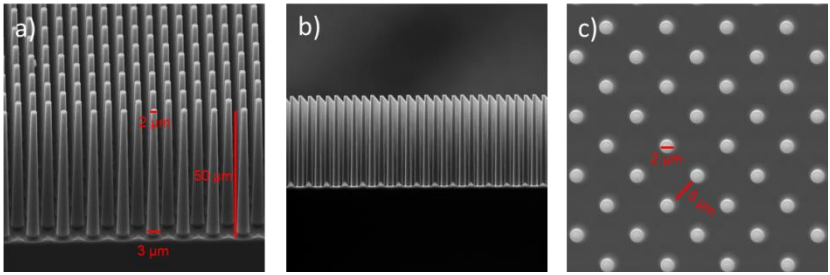

Figure 4: SEM micrograph of 3D Si (2x5), with side (a and b) and top (c) views.

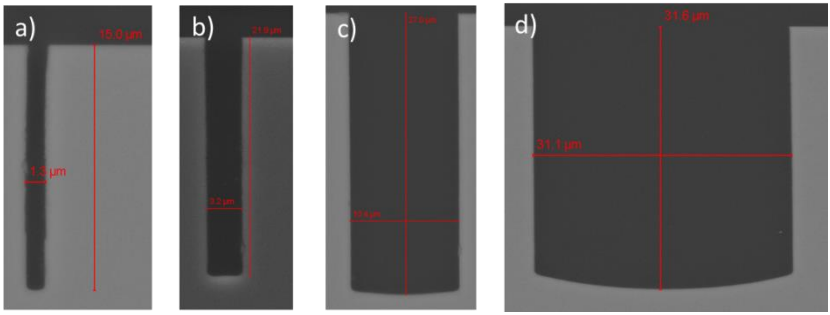

Figure 5: SEM micrograph (cross section) of Si trenches, with aspect ratios of (a) 15 , (b) 7, (c) 3 and (d) 1.

3. Characterization methods

3.1 Spectroscopic methods

3.1.1 Inductively coupled plasma atomic emission spectroscopy (ICP-AES)

For the stoichiometry of multi-metal oxides, as well as reproducible film deposition, the concentration of the starting precursor is of crucial importance. To be able to determine mono-metal solution precursor concentration, ICP-AES is applied for all the aqueous solutions prepared during the research presented in this thesis.

The physical phenomenon utilized during these experiments is based on element specific photon emission.

ICP-AES is also used for analysis of films deposited, by dissolving the films in a strong acid or base. This allows determination of the amount and composition of the material deposited.

3.1.2 Ultraviolet-visible light (UV-VIS) spectroscopy

In the specific case of a non-aqueous tungsten precursor discussed in chapter 6 and 7, UV-VIS spectroscopy is used. By analysing the light specific wavelengths absorbed by the precursor with a spectrometer, insights in the oxidation state and / or metal-complex formation can be established.

3.1.3 Fourier transform infrared (FTIR) spectroscopy

Especially in case of citrate based metal complexes (abundantly used during this study), FTIR spectroscopy allows determination of specific chemical bonds present. The absorption occurring at specific wavenumbers by, for instance, O-H stretching vibrations leads to determination of the chemical groups present in the gel.[52]

Due to infrared light coupling via a crystal, grazing angle attenuated total reflectance FTIR (GATR-FTIR) spectroscopy allows the analysis of films as well. This is utilized to understand how and if decomposition reactions proceed in view of oxide formation.

3.1.4 X-ray photoelectron spectroscopy (XPS)

With XPS, a sample is exposed to high energy X-rays, leading to emission of electrons from the sample. By measuring the energy difference between the incident X-rays and emitted electrons, the binding energy of the atoms present in the sample can be calculated. These binding energies are correlated with elements with specific oxidation states.[52] Therefore, XPS yields valuable information about the composition of the sample, including the oxidation state. Because the method only has a shallow penetration depth in the nanometer range, ion beam milling is often applied to ablate parts

of the sample, enabling composition analysis deeper into the sample.

3.2 Electron microscopy

Secondary electron microscopy is often used to analyse the morphology of deposited films, using top-view or cross sectional analysis of the films. The versatile magnification range allows analysis of structures down to 50 nm. In addition, back scattered electrons can also be used to compose micrographs. This yields information about the distribution of light and heavy elements present.

For larger magnifications, transmission electron microscopy is used. In contrast with SEM, analysis of films requires special specialized sample preparation. This is due to the fact that the sample needs to be semi-transparent for the electron beam, which in practice means only very small thicknesses (< 200 nm) are allowed.[52] Therefore, TEM is frequently used for powders, which are easily prepared on a metal (copper) grid. TEM allows characterization of particles down to 10 nm. In addition, TEM can also be used to determine if (small) particles are crystalline, by measuring electron diffraction patterns.[53]

3.3 Thermogravimetric and spectrometry

3.3.1 Thermal gravimetric analysis (TGA)

During TGA, a dried sample of the precursor is inserted into a crucible. By heating the sample in presence of a preferred gas (e.g. dry air), the sample weight changes due to (among others) drying or decomposition reactions. By closely measuring the weight loss, decomposition of the precursor gel can be tracked. The results can yield powerful insights in precursor synthesis, the occurrence of solid-state reactions or oxidation reactions combination with other analysis methods. For instance, TGA can be coupled with differential scanning calorimetry (TGA-DSC). In this case thermal events are monitored together with the weight change. In some cases these events coincide (e.g. combustion; leading weight loss and heat generation) but thermal events can also occur without signifi-

cant weight loss (e.g. melting or crystallization).[52] Another method used in this thesis is TGA analysis coupled with mass spectrometry (TGA-MS). Here, the products evolving from the decomposition reactions are analysed in a mass spectrometer, leading to a much better understanding about the cause of the decompositions reaction. A schematic representation is shown in Figure 6.

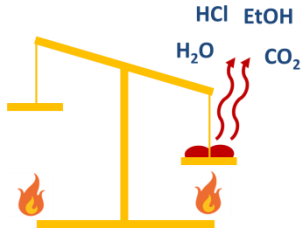

Figure 6: Schematic representation of TGA-MS.

3.3.2 Headspace gas chromatography coupled mass spectrometry (GCMS)

The reaction products produced during the synthesis of a specific precursor can yield information of the precursor composition in the liquid phase. Some of these products may be volatile, such as hydrocarbons or chlorine gas. After additions of reagents to a small vessel and immediate closure, the volatile products are contained. A small volume of the headspace (Figure 7) is inserted into a gas chromatograph (GC). After separation of the products in the column of the GC, a mass spectrometer (MS) analyses the weight of fragments that leave the column. Hence, the composition of the volatile products produced during the precursor synthesis are known.

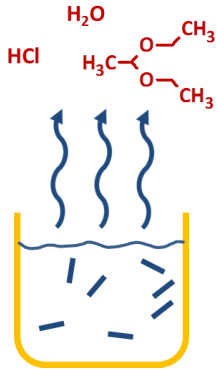

Figure 7: Schematic representation of headspace measurements.

3.4 Various types of X-ray diffraction (XRD)

Within materials science and inorganic chemistry, X-ray diffraction (XRD) is a very established method to check the crystallinity of samples. It is based on interference of reflected X-ray beams at specific angles. By turning the source and detector around the sample, a fingerprint pattern is obtained regarding the crystalline phase(s) present in the sample. This data is cross-referenced with calculations, a crystallographic database and / or literature. By doing so, various properties of the crystalline material can be tracked, including the occurrence of phase segregation, the lattice parameter of certain phases, and preferential growth of a certain material. In this thesis, the method is also used to track lithium intercalation into materials, since this is often accompanied with changes in the crystalline lattice.[53]

XRD can be applied for powders and films, although the latter usually requires longer measuring times because less material is available for diffract of X-rays. In addition, XRD of thin films often suffers from large background diffractions related to the substrate used.

Besides XRD at room temperature, two types of XRD in combination with sample heating are used. High-Temperature-XRD (HT-XRD) is used for powders, enabling to identify which crystallographic phase occurs at a certain temperature. It involves heating the sample, followed by an isothermal period in which the diffractogram is recorded. In addition to this, in-situ XRD (isXRD) is utilized to track phase changes in real-time. In other words, diffractograms are recorded continuously while maintaining a constant heating rate (or isotherm if desired).

3.5 Electrochemical methods

3.5.1 Electrochemical test cell with liquid electrolyte

The thin film electrode materials, synthesized with the methods described previously, are allowed to react with a metallic lithium electrode in the form of electrochemical reactions. In essence these are chemical reactions as can be observed in various field of chemistry (governed by the chemical potential). In the specific case of electrochemical reactions, it involves transfer of electrical charge between the electrodes.[54] For the materials studied in this thesis, these reactions are limited to the exchange of Li^+ and e^-.

In a typical measurement, a potential difference exists between both electrodes. The metallic lithium present is strongly electronegative (0 V vs. Li^+/Li, by definition). If electrical current is allowed to flow in presence of an electrolyte to facilitate Li^+ transport, the metallic lithium (negative) electrode is oxidized, acting as an anode according to Equation 4.

$$Li \rightarrow Li^+ + e^- \quad \textbf{(4)}$$

On the other hand, the thin film (positive) electrode material with a higher reduction potential (e.g. 3.0 V vs. Li^+/Li), acting as a cathode, is reduced according to a typical reaction shown in equation 5. In this thesis, this reaction is referred to as lithiation, whereas delithiation describes the reversed process.

$$MO_x + Li^+ + e^- \rightarrow LiMO_x \quad \textbf{(5)}$$

To study the electrochemistry of these reactions, the flow of charge carriers is separated by using an electrolyte (c.f. section 1.1). Since only the flow of electrons can be controlled properly (with a galvanostat or potentiostat), this current is utilized to gain deeper insights in the electrochemical reactions occurring. Facilitating these reactions by building an electrochemical cell using a liquid electrolyte is explained in the following.

For the wet electrochemical measurements involving (de)lithiation, a custom made three-electrode setup was used, with a strong resemblance to the design presented by Donders et al.[55] A schematic representation is given in Figure 8.

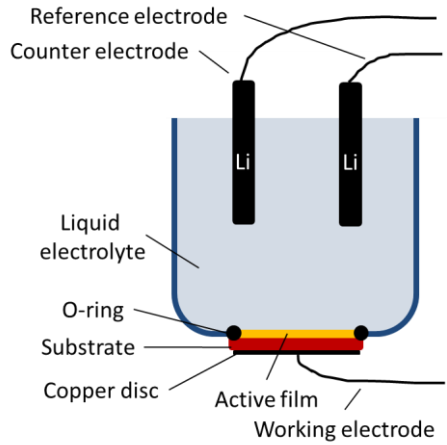

Figure 8: Schematic representation of the electrochemical cell used.

At the bottom of the setup, the *thin film electrode material* acts as the *working electrode* via connection to the potentiostat with a *copper disc* to ensure (electronic) conductivity to the silver paint at the bottom of the *substrate*. An *O-ring* ensures that *liquid electrolyte* remains inside the cell, wetting the *thin film electrode material* with a surface area of 0.96 cm^2. At the top of the cell, two similar lithium electrodes, acting as *counter electrode* and *reference electrode*, are inserted in the liquid electrolyte. Because the measure-

ment involves metallic lithium which tends to react with oxygen, nitrogen and water, all experiments were done inside an argon-filled glovebox.

The electrochemical reactions studied are strongly temperature dependent. Therefore, the measurements were done inside a custom-made temperature chamber (in cooperation with Eindhoven University of Technology), which was placed inside the glovebox. By pumping circulation liquid (Julabo Thermal H10) inside the temperature chamber with a 'refrigerated–heating circulator' (VWR 15R-30), a stable temperature regime could be established for the electrochemical measurements.

3.5.2 Cyclic voltammetry

Cyclic voltammetry relies on the setup shown in Figure 8. During cyclic voltammetry, a potential sweep with a fixed rate (i.e. scan rate, in $V \cdot s^{-1}$) is applied in a positive or negative direction between the working and counter electrode. A minimum and maximum potential, values which are defined on forehand, indicate the potential (voltage) boundaries of the experiment. It is called 'cyclic' voltammetry because the material is 'cycled' from high to low - and back to high potentials (or visa versa).

Depending on the composition of the various electrodes and electrolyte, electron transfer and diffusional processes are expressed in a measured current. Due to (a) reaction(s) occurring between the working electrode and the counter electrode, a current flowing between these two electrodes can be measured. The potential is measured between the working and reference electrode. This is shown schematically in Figure 9.

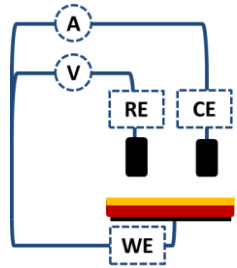

Figure 9: Relation between working electrode (WE), reference electrode (RE) and counter electrode (CE) and measured potential (V) and current (A).

Since redox reactions (e.g. lithiation) occur at specific, often known, potentials; the change of the potential difference triggers the start of a redox reaction between the working and counter electrodes. This is shown in the cyclic voltammogram (potential versus current plot), since this reaction involves exchange of electrons (i.e. a current). In a typical experiment, a potential is varied between to pre-defined values. While the potential increases, the reaction rate increases, causing a larger current. However, at a certain point the reaction rate may decrease again, due to – for instance – completion of the reaction. Because of the lower reaction rate, the current starts decreasing while the potential difference keeps increasing. This forms a peak in the cyclic voltammogram (CV), specifically relating to a certain reaction. Hence, analysis of the peaks in the CV peaks yields information about the electrochemical reactions occurring (charge transfer reactions), but also about transport-limited phenomena. This is where the so-called 'overpotential' is of importance, which is defined as the difference between the 'potential measured' and the 'potential under equilibrium conditions'. At low current densities, the overpotential arises from charge transfer limitations between electrolyte and electrode. At high currents, the overpotential is mainly caused by transport-limited phenomena or (low) reaction rates.[56]

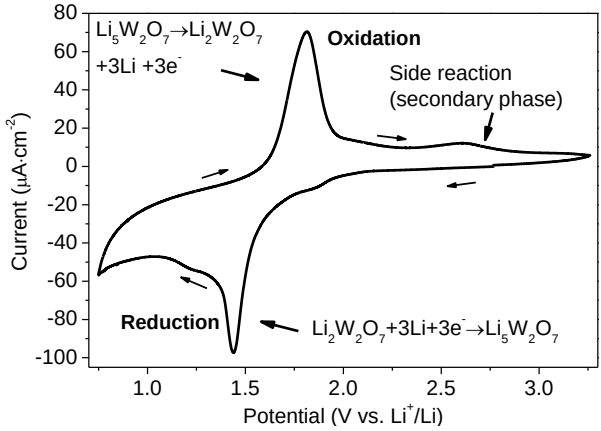

Figure 10: Example of a cyclic voltammogram, showing (de)lithiation of a $Li_2W_2O_7$ film at 1 $mV \cdot s^{-1}$ in 1.0 M $LiClO_4$ electrolyte.

An example of a CV is given in Figure 10, where a CV of $Li_2W_2O_7$ on Pt as working electrode is shown, cycled between indicated potentials against metallic lithium counter and reference electrodes in a non-aqueous electrolyte.

3.5.3 Galvanostatic cycling

A second method commonly used, is galvanostatic cycling. Instead of a potential applied with cycling voltammetry, for galvanostatic measurements the current is fixed and the voltage is measured. Galvanostatic cycling closely resembles actual operation of a battery.

Due to redox-reactions of the active material with the electrode, a current is allowed to flow and the voltage at which this occurs changes due to reaction completion or diffusional factors. The current inserted or extracted from the material is integrated over time, yielding the capacity of the material. The measured capacity of the battery material is combined with film thickness measurements (with SEM or ICP-AES), enabling the determination of the volumetric capacity or gravimetrical capacity of the film (based on

the theoretical density). This gives rise to a capacity versus voltage plot, often showing voltage plateaus for (de)lithiation reactions occurring. However, also for this method non-equilibrium conditions influence the shape of the graphs obtained. This includes resistance of the sample (IR drop) and charging of the double layer at the surface. However, it is a very suitable method to study materials, as it can distinguish charge insertion for different crystalline phases, since these occur at different potentials.[57,58]

The measured capacity depends on the current applied. Hence, reporting the applied current is crucial for the discussion of the results. Since the kinetics of (de)insertion depend on the (local) current density applied, the current is expressed in a C-rate to compare different sizes and geometries of a single electrochemical cell. The C-rate is defined as the reciprocal value of the time (in hours) it takes to charge or discharge the material. For instance, if a material is discharged at 2C, it implies that the measurement took half an hour. For new materials with unknown capacity, film porosity or crystallinity, the C-rate is only known after the experiment. Therefore, the work presented in this thesis utilizes various current densities, sometimes leading to seemingly 'arbitrary' C-rates.

Finally, the coulombic efficiency (η_c) is an important factor. This efficiency is defined as the ratio between the amount charge extracted and inserted with respect to electrochemical cell (Equation 6).

$$\eta_c = \frac{Q_{discharge}}{Q_{charge}} \times 100\% \qquad \textbf{(6)}$$

Especially for repeated galvanostatic cycling, the coulombic efficiency indicates if the desired electrochemical reaction occurs instead of competing side reactions. A low coulombic efficiency implies that only part of the charge inserted into the material is extracted again, which is unbeneficial from an application point of view.

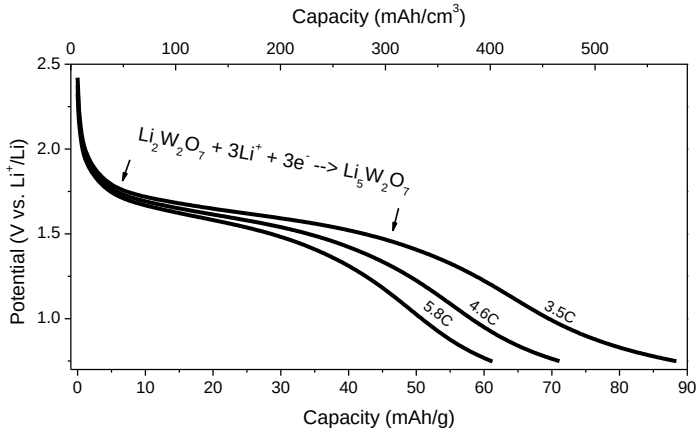

Figure 11: Example of lithiation curves of $Li_2W_2O_7$ films, measured during galvanostatic cycling in 1.0 M $LiClO_4$ electrolyte at various C-rates.

An example of a galvanostatic measurement is shown in Figure 11, showing lithiation of $Li_2W_2O_7$. The charge plateau at 1.7 V is related to the following delithiation reaction shown in Figure 10.

3.5.4 Impedance spectroscopy

Linear response theory is frequently used for several applications. It relies on causality, response and linearity. For example, this theory is used to describe interaction of light with matter. Impedance spectroscopy is closely related to these examples, but it considers potential and current as relevant signals. For an ideal resistor (R), the current wave signal (I) occurs perfectly simultaneous with the induced potential wave signal (U). In other words, potential and current are in phase; the imaginary part to describe the impedance wave function (Z) is equal to zero. For non-ideal resistors, I is not in phase with U, meaning that the imaginary part of Z is non-zero. In addition, the response is strongly wavelength / frequency (ω) dependent, implying that Z (imaginary part) depends on the frequency of the U wave.

This can be applied to batteries, or distinct battery materials as well, since they can be described as non-ideal resistors with a certain *Z*. Well-known factors that contribute to this non-ideal response are (i) charge transfer resistance (ideal resistor *R*), (ii) a double layer contribution (capacitor, *C*) and (iii) mass transport (Warburg impedance, *W*). For each of these contributions, mathematical expressions are formulated; and the combination of these equations yields an equivalent circuit that describes the *Z* function of a system. This can be used to simulate the impedance of materials as well; a well-known example is the Randles circuit (Figure 12). A Nyquist plot, frequently used for impedance spectroscopy, plots the real and imaginary part of *Z* on a x-y plot. A third variable, not directly visible on the plot axes, is the frequency (ω) of the applied wave function.[57,59,60]

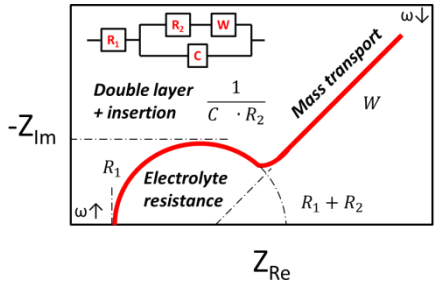

Figure 12: Simulated Nyquist plot of a Randles circuit.

At high ω, electrolyte resistance dominates, yielding a resistance without phase lag. While decreasing ω, a combination of resistor and capacitive effects become dominant because of resistance to insertion and formation of a double layer, respectively. This gives rise to an imaginary part of Z. At low ω, diffusion becomes dominant, expressed in the Warburg impedance contribution (*W*).[57,59]

In practice data interpretation can be hard, as noise or signal strength can complicate the interpretation. For solid electrolytes,

this involves surface roughness, the occurrence of grain boundaries and morphological issues such as pin-holes.

During this study an all-solid-state approach was used for impedance spectroscopy, implying that the current collectors were deposited directly on the samples (by evaporation) without the use of a liquid electrolyte. In this way, out-of-plane measurements could be done. This means that the z-direction of the solid-electrolyte is measured, sandwiched between a conductive substrate and a current collector. This method is preferred, since this measurement direction closely resembles the actual operation in case of a solid electrolyte. A different option would be in-plane-measurements. Here, the x-y direction of the solid-electrolyte is measured, and therefore does not require a conductive substrate. However, deposition of a current collector with an interdigitated structure (small separation with respect to the film thickness) is required. The two different measurements setups are shown in Figure 13.

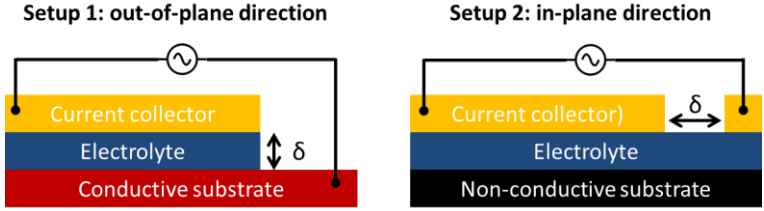

Figure 13: two different impedance setups for measurement of thin film solid electrolytes.

4. References

[1] M. K. Van Bael, A. Hardy, J. Mullens, in *Chem. Solut. Depos. Funct. Oxide Thin Film.* (Eds.: T. Schneller, M. Kosec, D. Payne), Springer, Viena, **2013**, pp. 93–140.

[2] R. Schwartz, T. Schneller, R. Waser, *Comptes Rendus Chim.* **2004**, *7*, 433.

[3] J. J. Cruywagen, L. Krüger, E. A. Rohwer, *J. Chem. Soc. Dalt. Trans.* **1991**, 1727.

[3] A. Hardy, J. D'Haen, M. K. Van Bael, J. Mullens, *J. Sol-Gel Sci. Technol.* **2007**, *44*, 65.

[4] M. K. Van Bael, D. Nelis, A. Hardy, D. Mondelaers, K. Van Werde, J. D'Haen, G. Vanhoyland, H. Van den Rul, J. Mullens, L. C. Van Poucke, F. Frederix, D. J. Wouters, *Integr. Ferroelectr.* **2002**, *45*, 113.
[5] T. Sugahara, Y. Hirose, S. Cong, H. Koga, J. Jiu, M. Nogi, S. Nagao, K. Suganuma, *J. Am. Ceram. Soc.* **2014**, *97*, 3238.
[6] R. Søndergaard, M. Hösel, D. Angmo, T. T. Larsen-Olsen, F. C. Krebs, *Mater. Today* **2012**, *15*, 36.
[7] R. W. Schwartz, T. Schneller, R. Waser, *Comptes Rendus Chim.* **2004**, *7*, 433.
[8] S. Darmawi, S. Burkhardt, T. Leichtweiss, D. a. Weber, S. Wenzel, J. Janek, M. T. Elm, P. J. Klar, *Phys. Chem. Chem. Phys.* **2015**, *17*, 15903.
[9] S.-K. Park, C.-Y. Seong, Y. Piao, *Electrochim. Acta* **2015**, *176*, 1182.
[10] K. Haas-Santo, M. Fichtner, K. Schubert, *Appl. Catal. A Gen.* **2001**, *220*, 79.
[11] K. Gilissen, J. Stryckers, P. Verstappen, J. Drijkoningen, G. H. L. Heintges, L. Lutsen, J. Manca, W. Maes, W. Deferme, *Org. Electron.* **2015**, *20*, 31.
[12] V. Penmatsa, T. Kim, M. Beidaghi, H. Kawarada, L. Gu, Z. Wang, C. Wang, *Nanoscale* **2012**, *4*, 3673.
[13] S. Gielis, A. Hardy, M. K. Van Bael, *Conformal Coating on Three-Dimenstional Substrates*, **2015**, EP 2 947 178 A1.
[14] M. M. Shaijumon, E. Perre, B. Daffos, P.-L. Taberna, J.-M. Tarascon, P. Simon, *Adv. Mater.* **2010**, *22*, 4978.
[15] L. Filipovic, S. Selberherr, G. C. Mutinati, E. Brunet, S. Steinhauer, A. Köck, J. Teva, J. Kraft, J. Siegert, F. Schrank, *Microelectron. Eng.* **2014**, *117*, 57.
[16] O. Salata, *Curr. Nanosci.* **2005**, *1*, 25.
[17] X. Li, C. Wang, *J. Mater. Chem. A* **2013**, *1*, 165.
[18] W. Y. Teoh, R. Amal, L. Mädler, *Nanoscale* **2010**, *2*, 1324.
[19] J. H. Bang, K. S. Suslick, *Adv. Mater.* **2010**, *22*, 1039.
[20] S. Jang, Y. Kim, D. Y. Kim, H. Kim, S. M. Jo, *ACS Appl. Mater. Inferfaces* **2012**, *4*, 3500.
[21] A. Kennedy, K. Viswanathan, K. Pradeev raj, *Phys. Lett. A* **2016**, *380*, 2842.
[22] a. Juma, I. Oja Acik, a. T. Oluwabi, a. Mere, V. Mikli, M. Danilson, M. Krunks, *Appl. Surf. Sci.* **2016**, *387*, 539.
[23] C. Özgür, *Solid State Ionics* **2010**, *181*, 1425.
[24] X.H. Ma, Q.-Y. Wan, X. Huang, C.-X. Ding, Y. Jin, Y.-B. Guan, C.-H. Chen, *Electrochim. Acta* **2014**, *121*, 15.

[25] J. Denayer, P. Aubry, G. Bister, G. Spronck, P. Colson, B. Vertruyen, V. Lardot, F. Cambier, C. Henrist, R. Cloots, *Sol. Energy Mater. Sol. Cells* **2014**, *130*, 623.
[26] B. Grbić, N. Radić, S. Stojadinović, R. Vasilić, Z. Dohčević-Mitrović, Z. Šaponjić, P. Stefanov, *Surf. Coatings Technol.* **2014**, *258*, 763.
[27] M. Regragui, M. Addou, A. Outzourhit, J. C. Bernede, E. El Idrissi, E. Benseddik, A. Kachouane, *Thin Solid Films* **2000**, *358*, 40.
[28] Z. He, Z. Wang, F. Wu, H. Guo, X. Li, X. Xiong, *J. Alloys Compd.* **2012**, *540*, 39.
[29] D. Yoshikawa, Y. Kadoma, J.-M. Kim, K. Ui, N. Kumagai, N. Kitamura, Y. Idemoto, *Electrochim. Acta* **2010**, *55*, 1872.
[30] C. H. Chen, E. M. Kelder, J. Schoonman, *J. Eur. Ceram. Soc.* **1998**, *18*, 1439.
[31] D. Perednis, Deposition by Spray Pyrolysis and the Application in Solid Oxide Fuel Cells, Swiss Federal Institute of Technology Zurich, **2003**.
[32] D. Perednis, L. J. Gauckler, *J. Electroceramics* **2005**, *14*, 103.
[33] J. Yang, Q. Liao, X. Zhou, X. Liu, J. Tang, *RSC Adv.* **2013**, *3*, 16449.
[34] K. Zhang, J. Li, Q. Li, J. Fang, Z. Zhang, Y. Lai, Y. Tian, *J. Solid State Electrochem.* **2013**, *17*, 3169.
[35] H. P. Deshmukh, P. S. Shinde, P. S. Patil, *Mater. Sci. Eng. B* **2006**, *130*, 220.
[36] B. Ebin, S. Gürmen, G. Lindbergh, *Ceram. Int.* **2014**, *40*, 1019.
[37] E. Benamar, M. Rami, C. Messaoudi, D. Sayah, a. Ennaoui, *Sol. Energy Mater. Sol. Cells* **1999**, *56*, 125.
[38] R. R. Prabhakar, S. S. Pramana, K. R. G. Karthik, C. H. Sow, K. B. Jinesh, *J. Mater. Chem.* **2012**, *22*, 13965.
[39] M. H. Kim, Y. J. Hong, Y. C. Kang, *RSC Adv.* **2013**, *3*, 13110.
[40] U. P. Muecke, G. L. Messing, L. J. Gauckler, *Thin Solid Films* **2009**, *517*, 1515.
[41] J. V. Alemán, a. V. Chadwick, J. He, M. Hess, K. Horie, R. G. Jones, P. Kratochvíl, I. Meisel, I. Mita, G. Moad, S. Penczek, R. F. T. Stepto, *Pure Appl. Chem.* **2007**, *79*, 1801.
[42] H. L. Berger, D. F. Mowbray, R. A. Copemand, R. J. Russel, *Ultrasonic Atomizing Nozzle and Method*, **2010**, US 7,712,680 B2.
[43] H. Xia, M. Shats, H. Punzmann, *EPL (Europhysics Lett.* **2010**, *91*, 14002.

[44] M. Prokic, "Ultrasonic Atomization Systems," can be found under http://www.activeultrasonic.com/applications/ultrasonic-atomization/, **n.d.**
[45] G. Vázquez, E. Alvarez, J. M. Navaza, *J. Chem. Eng. data* **1995**, *40*, 611.
[46] Q. Ye, B. Shen, O. Tiedje, T. Bauernhansl, J. Domnick, *At. Sprays* **2015**, *25*, 643.
[47] C. Fu, P. E. Sojka, Y. R. Sivathanu, in *Proc. 12th Annu. Conf. Liq. At. Spray Syst.*, Indianapolis, **1999**, pp. 271–276.
[48] M. Majumder, C. S. Rendall, J. A. Eukel, J. Y. L. Wang, N. Behabtu, C. L. Pint, T. Liu, A. W. Orbaek, F. Mirri, J. Nam, A. R. Barron, R. H. Hauge, H. K. Schmidt, M. Pasquali, *J. Phys. Chem. B* **2012**, *116*, 6536.
[49] M. Ortel, V. Wagner, *J. Cryst. Growth* **2013**, *363*, 185.
[50] C.K. Huang, V. P. Carey, *Int. J. Heat Mass Transf.* **2007**, *50*, 269.
[51] L. Baggetto, J. F. M. Oudenhoven, T. Van Dongen, J. H. Klootwijk, M. Mulder, R. A. H. Niessen, M. De Croon, P. H. L. Notten, *J. Power Sources* **2009**, *189*, 402.
[52] A. R. West, in *Basic Solid State Chem.*, Wiley, Sussex, **2012**, pp. 167–210.
[53] A. R. West, in *Basic Solid State Chem.*, Wiley, Sussex, **2012**, pp. 125–165.
[54] C. H. Hamann, A. Hamnett, W. Vielstich in *Electrochemistry*, Wiley-VCH, Weinheim, **2007** (second edition)**,** 77-98.
[55] M. E. Donders, W. M. Arnoldbik, H. C. M. Knoops, W. M. M. Kessels, P. H. L. Notten, *J. Electrochem. Soc.* **2013**, *160*, A3066.
[56] C. H. Hamann, A. Hamnett, W. Vielstich in *Electrochemistry*, Wiley-VCH, Weinheim, **2007** (second edition)**,** 185-207.
[57] D. Linden, T.B. Reddy in *Handbook of batteries*, McGraw-Hill, New-York, **2002** (third edition), 1.1-2.29.
[58] C. H. Hamann, A. Hamnett, W. Vielstich in *Electrochemistry*, Wiley-VCH, Weinheim, **2007** (second edition)**,** 258-278.
[59] H.T. Hintzen, M. Donders, lecture notes Electrochemistry, 2011
[60] C. H. Hamann, A. Hamnett, W. Vielstich in *Electrochemistry*, Wiley-VCH, Weinheim, **2007** (second edition)**,** 279-287.

Chapter 3

Overview of inorganic solid electrolytes for 3D thin film Li-ion batteries

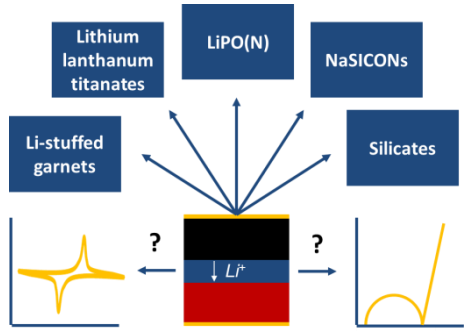

Abstract

An overview of various inorganic solid-state lithium-ion (Li-ion) conducting solid-state electrolytes is given in this chapter. The Li-ion conductivity, electrochemical stability and (thin) film synthesis results achieved are the main focus of this overview.

First of all, the NASICON class of materials is discussed, followed by lithium lanthanum titanates. Both classes exhibit superior Li-ion conductivity, but suffer from limited electrochemical stability and high thermal budget requirements. Strategies aimed at yielding amorphous lithium lanthanum titanates films proved useful, although the electrochemical stability remains an issue. Li-stuffed garnets are discussed as a possible alternative, showing a promising balance between Li-ion conductivity and high electrochemical stability. However, synthesis of Li-stuffed garnets appears to be a major challenge. The leading material within the field, LiPON, is also discussed. Recent developments yielding 3D deposition of this material by ALD are promising in view of 3D all-solid-state Li-ion batteries. Without N-doping, Li_3PO_4 proves to be an interesting material as well, although the conductivity is limited to 10^{-7} $S \cdot cm^{-1}$. Finally, some results on Li-ion conducting silicates are shown. Although conductivity of these materials is limited ($9.0 \cdot 10^{-8}$ $S \cdot cm^{-1}$), the move towards ultrathin films puts the silicates on par with LiPON.

This overview shows that progress is certainly booked, albeit in small steps, regarding solid electrolytes (especially) for 3D thin film all-solid-state Li-ion batteries.

1. Introduction

Solid electrolytes represent the core of the all-solid-state battery. The scientific progress in this field is therefore crucial for the development of these battery systems. Research on solid-state electrolytes dates back to the 1960's, where inorganic materials such as LiI, Li_3N, $LiBH_4$ were studied at first.[1,2] However, these materials suffered from various issues, including temperature instabilities, limited electrochemical stability and low Li-ion conductivity at room temperature.[1] In view of these short-comings, the focus shifted towards other materials such as polymers and sulfide based electrolytes. The former enables many advantages of polymer technology such as ease of processing, but it introduces many drawbacks similar to liquid electrolytes. These include limited battery lifetime (SEI formation) and safety hazards due to the use of organic liquids.[2,3] To date, sulfide materials (referred to as thio-LiSICONs or super ionic conductors) achieve very promising Li-ion conductivities (up to 10^{-2} $S \cdot cm^{-1}$), which in some cases surpass liquid electrolyte conductivities.[4] In addition, very high electrochemical stability from 0 to 10 V vs Li^+/Li has been shown.[5] However, application of these sulfides remains an issue due to persistent issues with hygroscopicity, leading to the formation of H_2S gas. Solutions to this problem seem to start emerging only recently.[5]

While facing all these (electro)chemical stability issues, oxide- and phosphate-based solid-state electrolytes are interesting because of their higher stability at elevated temperature and relative low reactivity under ambient conditions compared to other (in)organic solid electrolytes.[1,6] Therefore, a review is presented here, where the emphasis lies on oxide- and phosphate-based solid electrolyte. However, the synthesis of these materials is challenging in some cases, especially for thin films. Therefore the progress made in recent years is discussed here, including their deposition method(s) and application within the field of 3D all-solid-state Li-ion batteries.

To guide the reader, a graph summarizing the conductivity and electrochemical window of the material classes discussed is given in Figure 1 before going in to details.

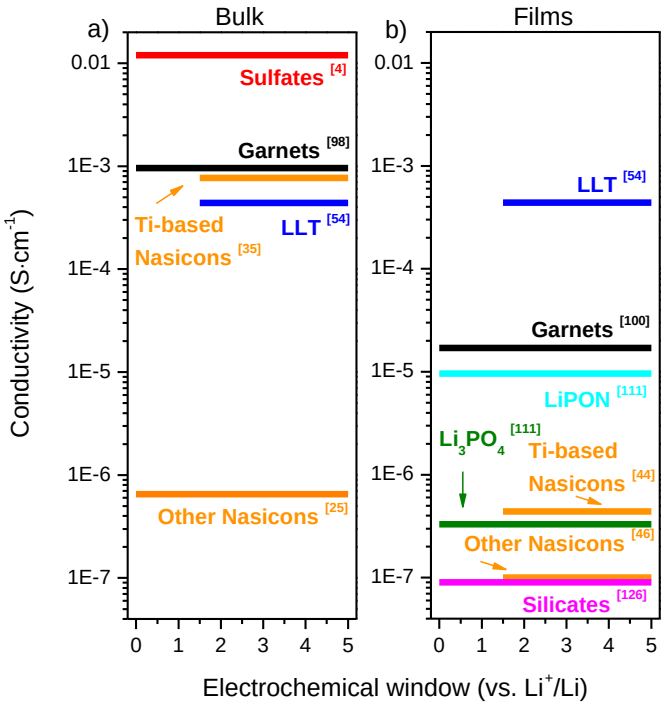

Figure 1: Summary of the best conductivity versus electrochemical stability of various a) bulk and b) film solid electrolytes discussed in this chapter.

2. NASICONs

As the name suggests, the Sodium(Na) Super(S) Ionic(I) Conductor(CON) (referred to as 'NASICON') class of materials was initially discovered for its sodium-ion conductivity in the form of $Na_{1+x}Zr_2P_{3-x}Si_xO_{12}$ ($0 < x < 3$).[7,8] The NASICON structure consists of MO_6 octhahedra which corner-share oxygen atoms with PO_4 tethrahedra leading to a network of interstitial sites that are respon-

sible for conduction of small cations such as sodium.[8] Despite the name, the NASICON phosphates appeared to be suitable for conduction of Li-ions as well.[7,9] Several years later, Aono et al. studied Li-ion conductivity of these materials by substituting metal ions in the $Na_{1+x}Zr_2P_{3-x}Si_xO_{12}$ structure; Na for Li, Zr for Al, Ti and / or Sc, yielding $Li_{1.3}M_{0.3}Ti_{1.7}(PO_4)_3$ (M = Al, Sc).[10] Due to this high conductivity (up to $7 \cdot 10^{-4}$ $S \cdot cm^{-1}$), a large number of studies focused on titanium containing lithium phosphates (LTP).[11]

Although good conductivity was established for LTP, the presence of Ti^{4+} limits the electrochemical stability window of the electrolyte.[2,12] Ti^{4+} reduction to occurs around 1.6 V for titanium based NASICON materials.[13] Besides Ti^{4+} reduction, it was found that for LATP ($Li_{1.3}Al_{0.3}Ti_{1.7}(PO_4)_3$) Li insertion is observed around 2,4 V.[13–16] However, in practice the low *electronic* conductivity of LTP hinders lithium insertion in the material.[14,16] The highest *bulk* Li-ion conductivity (i.e. inside the grains) reported for NASICON materials to date is $5 \cdot 10^{-3}$ $S \cdot cm^{-1}$ at room temperature.[17] It is important to note that the *total* Li-ion conductivity of a polycrystalline material depends on both the *bulk* conductivity and *grain boundary* conductivity. As is the case with most crystalline inorganic electrolytes, the total Li-ion conductivity is lowered due blocking effects at the grain boundaries due to issues regarding particle-to-particle transport. These grain boundaries form one of the major drawbacks of NASICONs.[2,18–20] Besides the influence of grain boundaries, Aono et al. indicated that the porosity of the (powder) pellet - which is strongly related to the stoichiometry of the material - has a major influence on the total Li-ion conductivity.[10]

Since all these NASICON materials are multi-metal-phosphates, the first synthesis method used to prepare this material was (conventional) solid-state synthesis,[10,17,21–26] but a wet-chemical (often referred to as 'sol-gel') approach has been used several times as well for materials with a wide range of compositions.[15,19,20,27–38] An overview is given in table 1. In first instance, the performance of the materials does not differ significantly while comparing wet-chemical and solid-state synthesis. However, it does indicate that wet-chemical synthesis requires lower synthesis temperatures to

achieve comparable conductivity values, which is the main motivation to use this synthesis method. However, the lower synthesis temperature used to prepare a particular phase leads to differences in crystallization as well, affecting the functional properties directly related to the crystallinity and size of the grains, making a direct comparison between wet-chemical and solid-state synthesis rather tricky.

Table 1: Various NASICON material compositions, their synthesis method and total Li-ion conductivity.

Composition	**Synthesis**	T_{syn} (°C)	σ_{Li} (S·cm^{-1})	**Ref.**
$Li_{0.2}Zr_2Nd_{0.267}(PO_4)_3$	Wet-chem.	900	$3.4\cdot10^{-7}$	[19]
$Li_{1.2}Al_{1.1}Ta_{0.9}(PO_4)_3$	Solid-state	800	$6.5\cdot10^{-7}$	[25]
$Li_{1.3}Al_{0.3}Ti_{1.7}(PO_4)_3$	Wet-chem.	1000	$1.5\cdot10^{-5}$	[28]
$Li_{1.3}Al_{0.3}Ti_{1.7}(PO_4)_3$	Wet-chem.	1000	$3.0\cdot10^{-4}$	[30]
$Li_{1.3}Al_{0.3}Ti_{1.7}(PO_4)_3$	Wet-chem.	900	$3.5\cdot10^{-4}$	[15]
$Li_{1.3}Al_{0.3}Ti_{1.7}(PO_4)_3$	Solid-state	1000	$1.0\cdot10^{-4}$	[28]
$Li_{1.4}Al_{0.15}Ti_{1.6}Fe_{0.25}(PO_4)_3$	Wet-chem.	1040	$7.7\cdot10^{-4}$	[35]
$Li_{1.4}Al_{0.4}Ti_{1.6}(PO_4)_3$	Wet-chem.	950	$6.1\cdot10^{-4}$	[32]
$Li_{1.5}Al_{0.5}Ge_{1.5}(PO_4)_3$	Wet-chem.	850	$1.4\cdot10^{-4}$	[31]
$Li_{1.5}Al_{0.5}Ge_{1.5}(PO_4)_3$	Wet-chem.	850	$2.8\cdot10^{-4}$	[28]
$Li_{1.5}Al_{0.5}Ge_{1.5}(PO_4)_3$	Wet-chem.	1000	$4.5\cdot10^{-4}$	[20]
$Li_{1.5}Al_{0.5}Ge_{1.5}(PO_4)_3$	Solid-state	1350	$4.0\cdot10^{-4}$	[33]
$Li_{1.7}Al_{0.7}Ti_{1.3}(PO_4)_3$	Solid-State	1000	$8.8\cdot10^{-6}$	[26]
$LiAlTa(PO_4)_3$	Solid-state	800	$6.5\cdot10^{-7}$	[25]
$LiTi_2(PO_4)_3$	Solid-State	1000	$1.6\cdot10^{-6}$	[26]

Some efforts have been made to transfer the good (total) Li-ion conductivity (10^{-4} S·cm^{-1}) for NASICON powders to 'films', although thicknesses range from 1 to 6 µm.[39–43] Despite good total conductivities and a proof of principle regarding positive electrode combinations with $LiCoPO_4$ and $LiCo_{1/3}Mn_{1/3}Ni_{1/3}O_2$,[40,41] the large thickness of the electrolyte induces a large voltage drop and hinders (practical) device integration. Regarding the 'thin film' approach (i.e. thickness <500 nm), only a few reports were found for the NASICON structure using either chemical solution deposition (CSD) or sputtering (c.f. Table 2).[44,45] These crystalline films are seriously hindered by a large grain-boundary resistance, leading to a low total Li-ion conductivity. Perhaps this is the reason why very

few studies could be found regarding thin films. It is therefore no surprise that 3D depositions have not yet been attempted for this material.

Table 2: NASICON films, their synthesis method and film characteristics..

Composition	**Sub.**	**Syn.**	$\mathbf{T_{syn}}$(°C)	**d** (nm)	$\boldsymbol{\sigma_{Li}}$ (S·cm^{-1})	**Ref.**
$LiTi_2(PO_4)_3$	SiO_2	CSD	800	300	$4.4\cdot10^{-7}$	[44]
$Li_{1.5}Al_{0.5}Ti_{1.5}(PO_4)_3$	Al_2O_3	CSD	650	200	$*2.9\cdot10^{-2}$	[45]
$LiZr_2(PO_4)_3$	Si	Sput.	800	320	$1.0\cdot10^{-7}$	[46]

***at 300°C**

3. Lithium lanthanum titanates

First reported as a highly Li-ion conductive material (10^{-3} S·cm^{-1}) back in 1993 by Inaguma et al., lithium lanthanum titanate ($Li_{3x}La_{2/3-x}TiO_3$, LLT) exhibits the highest Li-ion conductivity for oxide-based solid electrolytes.[47] However, Garnet-based electrolytes approach this value (c.f. next section), as well as some reports of very good performing NASICONs previously discussed.[35] LLT exhibits a perovskite ABO_3 structure where Li^+ and La^{3+} occupy part of the A-sites, and Ti^{4+} fully occupies the B-sites.[48] Therefore, this class of materials is often referred to as 'Li-ion conducting A-site deficient perovskites'.[2,6] The Li-ion conductivity of crystalline LLT is greatly influenced by the size of the A-site cation (La^{3+}), the Li^+ concentration and vacancy concentration. This reflects the fact that Li^+ moves via A-site vacancies, where the plane formed by four oxygen atoms forms the bottleneck for higher Li-ion conductivity.[48,49] In view of varying the Li^+ and vacancy concentrations, various compositions were synthesized. The resulting conclusion is that the crystalline $Li_{3x}La_{2/3-x}TiO_3$ structure is stable only over a composition range of $0.04 \leq x \leq 0.16$ with a maximum conductivity ($1\cdot10^{-3}$ S·cm^{-1}) at x=0.11.[48] Besides several compositions, various crystal structures were reported for this material depending on the synthesis temperature; namely cubic, tetragonal, hexagonal and orthorhombic.[48,49] For the tetragonal phase, the maximum bulk ionic conductivity was determined to be $1.1\cdot10^{-3}$ S·cm^{-1} for x = 0.11.[6,47]

With respect to the electrochemical stability, many studies indicate that the possibility of a Ti^{4+} to Ti^{3+} reduction seriously hinders the practical use of LLT electrolyte. As is the case with the Ti-based NASICONs, after this reduction the electrolyte loses its electronic insulating function.[2,48,50,51] A few studies investigated the potential of LLT as an *electrode* material. These studies indicate that Ti^{4+} reduction (accompanied with Li^+ intercalation) takes place at, or slightly below 1.5 V with respect to Li^+/Li.[52–54] This reduction seriously hinders the choice of negative electrode materials, e.g. metallic lithium, graphite or silicon-based negative electrodes are not feasible because this would lead to a short circuit of the battery. As a promising negative electrode material, the question remains if LLT is compatible with LTO. Although this material has a lithiation mechanism based on the Ti^{4+} reduction as well, some studies claim that both materials are compatible,[55] probably because the intercalation voltage of LTO is 1.55 V, slightly higher (0.05V) than the LLT reduction (1.45 to 1.50 V). However, this leaves little room to overcome several aspects that increase the over-potential, such as a low Li-ion conductivity due to the presence of secondary phases, compositional deviations and / or interfacial issues. The stability of LLT at high potential does not form any problems known from an integration point of view, since stability was shown up to 4.3 V.[54,56] Galvanostatic measurements of LLT with $LiMn_2O_4$ and $LiCoO_2$ were shown in the form of a composite electrode materials,[56–58] but these examples cannot be regarded as a half-cells because the (porous) electrolyte was mixed with the positive electrode material to improve the Li-ion conductivity.

Although many studies report the bulk Li-ion conductivity,[47,59–62] the total Li-ion conductivity is more relevant from an application point of view. Therefore, an overview of this property is listed in Table 3.

Table 3: Various lithium lanthanum titanate reports with similar composition, their synthesis method and total Li-ion conductivity. Amorphous phases are indicated with (a).

Composition	**Synthesis**	T_{anneal} (°C)	σ_{Li} ($S \cdot cm^{-1}$)	**Ref.**
$Li_{0.35}La_{0.5}TiO_3$	Solid-state	1350	$2 \cdot 10^{-5}$	[47]
$Li_{0.35}La_{0.5}TiO_3$	Solid-state	1150	$3.9 \cdot 10^{-4}$	[54]
$Li_{0.35}La_{0.5}TiO_3$ (a)	Wet-chem.	600	$1.0 \cdot 10^{-5}$	[55]
$Li_{0.35}La_{0.5}TiO_3$	Solid-state	1200	$1.0 \cdot 10^{-7}$	[59]
$Li_{0.35}La_{0.5}TiO_3$	Wet-chem.	1350	$1.6 \cdot 10^{-4}$	[61]
$Li_{0.35}La_{0.5}TiO_3$	Wet-chem.	1250	$2.0 \cdot 10^{-5}$	[61]
$Li_{0.35}La_{0.5}TiO_3$	Wet-chem.	700	2.710^{-6}	[63]

The bulk conductivities of LLT are the highest known for oxide based electrolytes, and it is only recently been surpassed by sulfur-based electrolytes such as $Li_{10}GeP_2S_{12}$.[64] However, as was the case for the NASICON class, LLT suffers from significant grain boundary resistance, leading to a lower *total* Li-ion conductivity.[2] Addition of different oxide material (e.g. Al_2O_3), forming a composite material, seems to lower the grain boundary resistance without hindering bulk conductivity of the 'composite LLT'.[62] A totally different approach to reduce grain boundary issues is also reported: amorphous LLT.[55,65] Although no high ´bulk´ conductivities are possible anymore, a good amorphous phase is arguably a better choice than a crystalline counterpart, as the amorphous phase exhibits a higher total Li-ion conductivity.[65]

Regarding the synthesis approach for bulk electrolyte materials, the difference between wet-chemical and solid-state synthesis seems to be absent for LLT. This is probably due to the very high (1350°C) synthesis temperatures required, even in case of wet chemical synthesis, to obtain the highly conductive crystalline phase, where enhanced molecular mixing and / or decomposition of residual organics does not form a (dis)advantage anymore.

Due to the high bulk Li-ion conductivity of LLT achieved for powders, which is only an order of magnitude lower than liquid electrolytes, several studies have been done for LLT films as well (Table 4). Phase formation was confirmed on (monocrystalline) $NdGaO_3$

and $SrTiO_3$, leading to epitaxial LLT films.[66] But also more 'common' substrates such as Si,[67] Pt coated Si and glass were used for the synthesis of polycrystalline LLT.[67–69] This indicates that phase formation of perovskite LLT is possible on a wide variety of substrate materials, which makes it more interesting to implement in a thin-film battery.

Table 4: Lithium lanthanum titatate films with various compositions, their synthesis details, thickness and total Li-ion conductivity.

Composition	**Sub.**	**Syn.**	T_{syn}(°C)	**d** (nm)	σ_{Li} (S·cm^{-1})	**Ref.**
$Li_{0.35}La_{0.5}TiO_3$ (a)	Steel	e-B.	100	$1.5\cdot10^3$	$1.8\cdot10^{-7}$	[58]
$Li_{0.35}La_{0.5}TiO_3$	NGO	PLD	900	40	$3.5\cdot10^{-5}$	[66]
$Li_{0.5}La_{0.5}TiO_3$	Glass	CSD	700	$0.8\cdot10^3$	$*1\cdot10^{-8}$	[69]
$Li_{0.1}La_{0.63}TiO_3$ (a)	Glass	PLD	RT	460	$4.4\cdot10^{-4}$	[70]
$Li_{0.75}La_{0.35}TiO_3$ (a)	Si	Sput.	RT	$2.6\cdot10^3$	$9.4\cdot10^{-7}$	[71]
$Li_{0.35}La_{0.5}TiO_3$	STO	CSD	1200	410	$4.4\cdot10^{-5}$	[72]
$LiLaTiO_3$ (a)	Sap.	CSD	350	$1.0\cdot10^3$	$4.5\cdot10^{-6}$	[73]

***at 120°C**

While considering the crystalline materials performance, it can be noted that the films seem to perform at least one order of magnitude worse in terms of total Li-ion conductivity (Table 4). This may be the reason why amorphous LLT is often studied for films as well.[65,67,71,73] Amorphous LLT films yield three main advantages over crystalline counterparts: (i) lower synthesis temperatures, (ii) higher total conductivity and (iii) no crystallization issues induced by the substrate.

For device integration, few examples of LLT coated electrodes are available. For instance, Li et al. prepared a $LiCoO_2$/LLT/LiPON/Li half-cells, where 43% of the expected $LiCoO_2$ capacity could be measured.[58] This indicates that integration of LLT is not evident, probably due its limited electrochemical stability. 3D depositions of LLT have not been presented as such. ALD deposited LLT should give some perspective, but no functional properties were reported for these (planar) films. [67] Kokal et al. were able to pattern LLT films for 3D Li-ion batteries via CSD, with film thicknesses up to 500 nm. Unfortunately no functional properties were shown for these patterned films.[63]

4. Lithium-stuffed garnets

The garnet structure contains a wide variety of chemical compositions. The chemical formula can be described as $A_3B_2(XO_4)_3$ (with A = Ca, Mg, Y, La; B = Al, Fe, Ga, Ge, Mn, Ni or V; X = Si, Ge, Al).[3] Recently, Thangadurai et al. discovered lithium containing garnets as a promising electrolyte material,[51] which are conveniently referred to as 'lithium-stuffed garnets'.[74] Initially $Li_5La_3Ta_2O_{12}$ and $Li_5La_3Nb_2O_{12}$ were studied,[51] in a later stage the composition was altered by doping with (primarily) rare-earth and transition metals on the B and X sites. This yielded a wide range of lithium containing garnets with high Li-ion conductivity (10^{-4} $S{\cdot}cm^{-1}$).[74–79] In general the conductivity mechanism for all lithium-stuffed garnets is related to LiO_4 tetrahedra and (distorted) LiO_6 octahedra, where the latter are responsible for the high Li-ion conductivity. More details about Li-ion conductivity mechanisms of distinct garnet materials and their compositions can be found in excellent, recent reviews.[3,80]

The main advantage of the garnet materials often stated is their high electrochemical stability,[50,75,77,81–90] especially compared to other oxide electrolytes such as NASICONS (especially Ti^{4+}-based) and lithium lanthanum titanates. A DFT study showed that - besides the metals involved - the crystal structure is of great importance to the electrochemical stability of a solid electrolyte.[91] The corner sharing octahedra of the perovskite structured materials lead to an increased covalent bonding character of the octahedrally coordinated metal, which makes it prone to react with metallic lithium. Since garnet structured materials consist of isolated polyhedra, the coordinated metals have a less covalent character, leading to a higher electrochemical stability towards metallic lithium (i.e. 0 V vs. Li^+/Li).[91]

Experimentally, $Li_5La_3Ta_2O_{12}$ and $Li_{6.4}La_3Zr_{1.4}Ta_{0.6}O_{12}$ are both proven to be stable against metallic lithium,[87,92] which is of great importance for device integration.

Table 5: Various Li-stuffed garnets, their synthesis methods and Li-ion conductivity.

Composition	Synthesis	T_{anneal} (°C)	σ_{Li} ($S \cdot cm^{-1}$)	Ref.
$Li_7La_3Zr_2O_{12}$	Solid-state / PLS	1000	$1.0 \cdot 10^{-4}$	[50]
$Li_7La_3Zr_2O_{12}$	Wet-chem.	1100	$3{,}5 \cdot 10^{-6}$	[88]
$Li_7La_3Zr_2O_{12}$	Wet-chem.	900	$3.7 \cdot 10^{-7}$	[95]
$Li_7La_3Zr_2O_{12}$	Wet-chem.	1230	$1.7 \cdot 10^{-4}$	[95]
$Li_7La_3Zr_2O_{12}$	Wet-chem.	900	$3.1 \cdot 10^{-7}$	[89]
$Li_8La_3Zr_2O_{12.5}$:Al	Wet-chem.	1180	$1.3 \cdot 10^{-4}$	[85]
$Li_6BaLa_2Ta_2O_{12}$	Wet-chem.	800	$1.7 \cdot 10^{-5}$	[96]
$Li_7La_3Zr_2O_{12}$	Wet-chem.	750	$2.9 \cdot 10^{-6}$	[97]
$Li_7La_3Zr_2O_{12}$:Al	Wet-chem.	1200	$2.4 \cdot 10^{-4}$	[94]
$Li_7La_3Zr_2O_{12}$	Solid-state	1230	$2.4 \cdot 10^{-4}$	[77]
$Li_7La_3Zr_2O_{12}$:Al	Solid-state	1230	$3.5 \cdot 10^{-6}$	[82]
$Li_7La_3Zr_2O_{12}$	Solid-state	1230	$1.4 \cdot 10^{-4}$	[87]
$Li_{6.7}La_3Zr_{1.7}Ta_{0.3}O_{12}$	Solid-state	900	$9.6 \cdot 10^{-4}$	[98]

Besides the electrochemical stability, the second advantage of Li-stuffed garnets to other crystalline solid electrolytes is related to the grain boundary conductivity. Whereas perovskite (and NASICON) solid electrolytes exhibit very high bulk conductivities, the total ionic conductivity is reduced because of low grain boundary conductivity (c.f. previous sections). The advantage of garnets is that the difference between bulk and grain boundary conductivity is relatively small.[51,79] The nature of this phenomenon is assigned to the 3D conductive pathway mechanism of lithium-stuffed garnets.[51] Hence, for garnet $Li_6BaLa_2Nb_2O_{12}$ a higher total ionic conductivity was reported in a direct comparison with perovskite LLT, even though the bulk conductivity of the garnet was lower (c.f. Table 3 and 5).[79]

Since $Li_7La_3Zr_2O_{12}$ (LLZO) was shown to have a relatively high Li-ion conductivity of 10^{-4} $S \cdot cm^{-1}$, most studies done on garnets are based on LLZO as shown in Table 5. Although high temperatures (approx. 1200°C) are required to form the highly conductive cubic phase,[50,85,89] recent studies indicate that doping with aluminium stabilizes the cubic phase of LLZO, leading to slightly lower sintering temperature requirements.[74,82,90,93,94] Table 5 shows that for garnets, the synthesis temperature has a profound influence on the magnitude of the Li ion conductivity. This is directly related to the

crystal phase obtained. Although pulsed laser annealing (PLS) seems to have a clear advantage, differences between synthesis methods with respect to Li-ion conductivity are minor, especially while taking into account the influence of annealing temperature and resulting (cubic) crystal phase.

Since lithium-stuffed garnets exhibit a high total Li-ion conductivity (10^{-4} S·cm^{-1}), combined with high electrochemical stability, garnet films are very interesting from an application point of view. Despite these positive features, the synthesis of *thin* film Li-stuffed garnets is rarely shown (Table 6).

Table 6: Various Li-stuffed garnet films with various composition, their synthesis, thickness and Li-ion conductivity.

Composition	**Sub.**	**Syn.**	**T_{syn}**(°C)	**d** (nm)	**σ_{Li}** (S·cm^{-1})	**Ref.**
$Li_7La_3Zr_2O_{12}$	GGG	PLD	1000	30	$1.0\cdot10^{-5}$	[83]
$Li_7La_3Zr_2O_{12}$:Al	MgO	CSD	900	$1.0\cdot10^{3}$	$2.4\cdot10^{-6}$	[99]
$Li_6BaLa_2Ta_2O_{12}$	MgO	PLD	550	$2.0\cdot10^{3}$	$1.7\cdot10^{-5}$	[100]
$Li_7La_3Zr_2O_{12}$	STO	Sput.	800	$1.0\cdot10^{3}$	$1.78\cdot10^{-6}$	[101]
$Li_7La_3Zr_2O_{12}$ (a)	STO	Sput.	RT	$1.0\cdot10^{3}$	$3.35\cdot10^{-7}$	[101]
$Li_7La_3Zr_2O_{12}$ (a)	Steel	Sput.	RT	560	$4\cdot10^{-7}$	[102]
$Li_7La_3Zr_2O_{12}$	Steel	CSD	800	50	$3.4\cdot10^{-8}$	[103]

Note that almost all these studies make use of lattice matching with the substrate material (a_{garnet} = 1/n $a_{substrate}$,, where *n* is an integer) to obtain crystalline garnet films.[83,99,100] This suggests that crystallization of garnet films is challenging. Bitzer et al. were able to prepare cubic $Li_7La_3Zr_2O_{12}$ on steel substrates by optimizing their synthesis procedure; apparently a large amount of lithium excess is required to form this phase. However, secondary phases were formed and the film showed a low Li-ion conductivity in the order of 10^{-8} S·cm^{-1}.[103] A thick crystalline garnet film (2 µm) was also achieved on a conductive (non-lattice-matched) substrate by Lobe et al. However, this led to the formation of a 200 nm hybrid interface layer between the electrolyte and the substrate, explaining the low Li-ion conductivity of $2\cdot10^{-9}$ S·cm^{-1}.[104]

A comparison between Li-ion conductivities of powders (Table 5) and films (Table 6) indicates that garnet (thin) films exhibit lower conductivities (10^{-5} S·cm^{-1} for films compared to 10^{-4} S·cm^{-1} for bulk materials). It has been suggested that the microstructure, lithium deficiency and lower synthesis temperature are the main reasons for the lower conductivity.[100] Although the crystallization of lithium-stuffed garnet films is clearly challenging, the result can be very rewarding as a highly conductive and stable electrolyte could in principle be obtained. Creative solutions are sought to circumvent crystallization issues. For instance, Ahn et al. deposited pre-annealed LLZO powders by means of aerosol deposition method. Unfortunately, the functional properties ($1.0 \cdot 10^{-8}$ S·cm^{-1}) were somewhat disappointing due to the lack of a sintering of the 20 µm thick films.[105] Kalita et al. showed a different approach with the deposition of amorphous $Li_7La_3Zr_2O_{12}$ films on steel substrates, where no lattice matching is required. However, the conductivity of amorphous $Li_7La_3Zr_2O_{12}$ is two orders of magnitude lower than their crystalline counterparts (10^{-6} S·cm^{-1}).[101,102]

Given the transfer of lithium-stuffed garnets to thin films is challenging, it is no surprise that no reports have been made for 3D depositions of this material.

5. Lithium phosphates

Besides the oxide- and phosphate-based bulk and thin film solid electrolytes listed, the leading material within the field of thin-film Li-ion batteries remains to be discussed: nitrogen doped lithium phosphate (LiPON). Dating back to the beginning of the 1990s, Bates et al. applied LiPON as a solid electrolyte for all-solid-state Li-ion batteries.[106] With moderate Li-ion conductivity values varying from 10^{-6} to 10^{-8} S·cm^{-1},[107–111] this amorphous material does not seem to be appealing in comparison to other materials. However, the electrochemical stability of LiPO(N) makes it compatible with lithium and Si negative electrodes .[108,112] In addition, the amorphous character leads to low synthesis temperature requirements and good morphologies. The combination of these features makes LiPON a very interesting solid electrolyte, remaining a

benchmarking material for over 20 years. Device integration is developed to such a high level that commercial products are available using LiPON as the solid electrolyte in combination with $LiCoO_2$ and metallic lithium.[113]

Recently, development of LiPON seems to have made the next step, as ALD LiPON films have been deposited on non-planar 3D structured substrates by Nisula et al.,[107] paving the road for 3D all-solid-state Li-ion batteries.

Nitrogen doping is often thought to be crucial to achieve high conductivity (10^{-6} $S \cdot cm^{-1}$), but a selection of recent results from literature indicates that not all LiPON films achieve the same conductivity (Table 7). Hence, the precise mechanism responsible for enhanced conductivity remains a debate in literature.[107,111,114] The N-doping step also marks one of the drawbacks of LiPON, since nitrogen doping of LiPO(N) has only been achieved thus far by vacuum based methods. Hence, no reports of successful LiPON deposited with wet-chemical methods have been made. Instead of nitrogen, boron doping is opted as one of the routes to achieve higher conductivity for lithium phosphates.[115,116] For films, good results were achieved with $1.9 \cdot 10^{-6}$ $S \cdot cm^{-1}$, equalling LiPON performance.[116]

Non-doped lithium phosphate (Li_3PO_4) also yields Li-ion conductive, electrochemically stable films.[117–120] The conductivity of Li_3PO_4 is slightly lower on average as could be expected, though a good Li_3PO_4 film is reported to surpass LiPON in terms of conductivity under comparable circumstances (Table 7). Regarding 3D depositions and device integration, Xie et al. were able to coat 3D structured surfaces with this material while showing activity of the electrolyte on (amorphous) Si negative electrodes, although aspect ratio was limited to 1.[120]

Table 7: Various (N-doped) lithium phosphate films with various compositions, their synthesis details, thickness and Li-ion conductivity.

Composition	**Sub.**	**Syn.**	$\mathbf{T_{syn}}$(°C)	**d** (nm)	$\boldsymbol{\sigma_{Li}}$ (S·cm^{-1})	**Ref.**
LiPON	N.A.	CVD	575	$0.9\cdot10^{3}$	$3.0\cdot10^{-7}$	[121]
LiPON	Glass	Sput.	300	$2.7\cdot10^{3}$	$1.7\cdot10^{-6}$	[109]
LiPON	Si	Sput.	RT	12	$1.5\cdot10^{-7}$	[108]
LiPON	Si	ALD	250	40	$1.5\cdot10^{-7}$	[122]
LiPON	Glass	ALD	330	115	$6.6\cdot10^{-7}$	[107]
LiPON	Pt	Sput.	500	350	$9.6\cdot10^{-6}$	[111]
LiPON	TiN	Sput.	RT	240	$2.5\cdot10^{-7}$	[110]
$Li_{3.59}PO_{4.64}B_{0.24}$	Glass	Sput.	RT	$1.5\cdot10^{3}$	$1.9\cdot10^{-6}$	[116]
Li_3PO_4	Pt	PLD	RT	$1.5\cdot10^{3}$	$3.3\cdot10^{-7}$	[117]
Li_3PO_4	Pt	CVD	300	200	$3.9\cdot10^{-8}$	[120]

6. Other thin film electrolytes

Finally, a few recent reports have been made on thin film electrolytes that do not fit in either of the material classes discussed (Table 8). Reports were made on spinel structured lithium magnesium aluminate solid electrolytes with various compositions (e.g. $Li_{0.25}Mg_{0.5}Al_{2.25}O_4$).[123,124] However, a thorough study of this material indicated that conductivity was too low for practical application as an electrolyte.[124] Elaborate studies were done on thin film lithium silicates. Compared to the other materials discussed, this class of materials exhibits the lowest Li-ion conductivity for thin film materials. The conductivity mechanism is not elaborated upon, which is the case for most amorphous electrolytes. The electrochemical stability of these systems is unknown up to now. Based on a comparison with other solid electrolytes, this is expected to depend primarily on the occurrence of (transition) metal-ions in the amorphous silicate material.

Table 8: Various lithium silicate films with various compositions, their synthesis details and properties.

Composition	**Sub.**	**Syn.**	$\mathbf{T_{syn}}$(°C)	**d** (nm)	$\boldsymbol{\sigma_{Li}}$ (S·cm^{-1})	**Ref.**
$Li_{0.6}AlSi_{0.4}O_x$	ITO	ALD	290	6	$9.0\cdot10^{-8}$	[125]
$Li_{0.69}V_{0.17}Si_{14}O_x$	Si	PLD	RT	$2.5\cdot10^{3}$	$3.0\cdot10^{-8}$	[126]

Since Li-ion conductivity of these materials is rather low, extremely thin films (at least for solid electrolyte standards) have been deposited for a vanadium doped lithium silicate by ALD, while ensuring the electronic insulating function of the electrolyte.[127] As a result, these thin film silicates' (10 nm) performance is comparable to an average LiPON film with 100 nm thickness (Table 7). In addition, high aspect ratio wires were coated,[127] indicating that this approach has also some potential for 3D all-solid-state Li-ion batteries. However, the fact that vanadium was included in this material makes its electrochemical stability somewhat uncertain, as this metal-ion shows a double reduction between 3 and 4 volt (vs. Li^+/Li) in a phosphate lattice.[128]

7. Summary

After several decades of research on inorganic solid electrolyte materials for Li-ion batteries, one can conclude that progress proceeds slowly in general, accelerated by new findings once in a while. For powders, NASICONs and lithium lanthanum titanates formed a major step forward in terms of conductivity, but no solutions were found for the limited electrochemical stability of these materials. By replacing titanium for other metals, a collapse of the high Li-ion mobility occurred. Lithium stuffed garnets appeared to be the answer. To date, they are the most stable, highly conductive solution for a bulk approach, with conductivity values approaching the best Li-ion conducting solid electrolytes available for Li-ion batteries (Figure 1).

However, for films, all these crystalline materials are highly problematic because of temperature requirements. In addition, few studies report the in-plane Li-conductivity that disregards morphological issues. Both high temperature requirements and morphological issues are dubbed to be major bottlenecks for these three classes of materials. Especially so, since all approaches attempting this achievement yielded poor conductivity results due to formation of secondary phases or reactivity with the substrate.

As Figure 1 shows, the highest conductivity is achieved by lithium lanthanum titanates (10^{-4} S·cm^{-1}). However, the major difference is the amorphous character of the lithium lanthanum titanate films, which perform better as compared to crystalline counterparts. Several studies speculate that this is due to the advantage that no grain boundaries are formed. In addition, amorphous lithium lanthanum titanates require significantly lower synthesis temperatures and are less susceptible to substrate influence, aiding device integration. Nevertheless, the limited electrochemical window remains a persistent problem, preventing further application of this material. Currently, amorphous lithium-stuffed garnet films (10^{-7} S·cm^{-1}) do not exhibit the same range of conductivity. Progress is still possible, as very few studies are done on this particular topic.

Therefore, LiPON (10^{-6} S·cm^{-1}) remains the material of choice for most studies, although Li_3PO_4 (10^{-7} S·cm^{-1}) performs only one order of magnitude lower in terms of conductivity. Although both materials are not particularly interesting because of their moderate conductivity; their low thermal budget requirements and electrochemical stability are highly beneficial.

As for 3D thin film all-solid-state batteries, deposition of solid electrolytes has a long way to go since only very few successful depositions were reported. Especially the 3D deposition of NASICON, lithium lanthanum titanates and lithium-stuffed garnets remain a large gap within this field. In fact, until recently no examples of successful 3D depositions of solid electrolytes were available at all. Fortunately, considerable progress has been made the last two years with the deposition of LiPON (ALD) and Li_3PO_4 (CVD). If thicknesses of these films could be reduced, further performance increase would be possible, as was shown with the ALD deposition of 10 nm vanadium doped lithium silicates. Although all these approaches require costly vacuum methods, to date it seems the most promising approach to realize the (inorganic) core of the 3D all-solid-state battery.

8. References

[1] Y. Ren, K. Chen, R. Chen, T. Liu, Y. Zhang, C.-W. Nan, *J. Am. Ceram. Soc.* **2015**, *98*, 3603.

[2] P. Knauth, *Solid State Ionics* **2009**, *180*, 911.

[3] V. Thangadurai, S. Narayanan, D. Pinzaru, *Chem. Soc. Rev.* **2014**, *43*, 4714.

[4] A. Hayashi, K. Noi, A. Sakuda, M. Tatsumisago, *Nat. Commun.* **2012**, *3*, 856.

[5] T. Othomo, A. Hayashi, M. Tatsumisago, K. Kawamoto, *Electrochemistry* **2013**, *81*, 428.

[6] H. Kawai, J. Kuwano, *J. Electrochem. Soc.* **1994**, *141*, 78.

[7] H. Y. Hong, *Mater. Res. Bull.* **1976**, *11*, 173.

[8] J. B. Goodenough, H. Y. Hong, J. A. Kafalas, **1976**, *I*, 203.

[9] B. E. Taylor, A. D. English, T. Berzlns, **1977**, *12*.

[10] H. Aono, E. Sugimoto, Y. Sadaoka, N. Imanaka, G. Adachi, *Solid State Ionics* **1991**, *47*, 257.

[11] N. Anantharamulu, K. Koteswara Rao, G. Rambabu, B. Vijaya Kumar, V. Radha, M. Vithal, *J. Mater. Sci.* **2011**, *46*, 2821.

[12] J. F. Ihlefeld, P. G. Clem, B. L. Doyle, P. G. Kotula, K. R. Fenton, C. a. Apblett, *Adv. Mater.* **2011**, *23*, 5663.

[13] C. Delmas, A. Nadiri, J. L. Soubeyroux, *Solid State Ionics* **1988**, *28-30*, 419.

[14] P. Birke, F. Salam, S. Doring, W. Weppner, **1999**, *118*, 149.

[15] Z. Xiao, S. Chen, M. Guo, *Trans. Nonferrous Met. Soc. China* **2011**, *21*, 2454.

[16] K. Hoshina, K. Dokko, K. Kanamura, *J. Electrochem. Soc.* **2005**, *152*, A2138.

[17] K. Arbi, J. M. Rojo, J. Sanz, *J. Eur. Ceram. Soc.* **2007**, *27*, 4215.

[18] J. W. Fergus, *J. Power Sources* **2010**, *195*, 4554.

[19] M. Barré, M.-P. Crosnier-Lopez, F. Le Berre, O. Bohnké, E. Suard, J.-L. Fourquet, *Dalt. Trans.* **2008**, *2*, 3061.

[20] M. Kotobuki, M. Koishi, *Ceram. Int.* **2013**, *39*, 4645.

[21] A. S. Best, M. Forsyth, D. R. Macfarlane, **2000**, *137*, 339.

[22] S. S. Ionics, N. P. Company, P. T. Conduction, S. Phosphates, C. Appliquge, U. Paris-sud, T. Li, *Solid state ionics* **1983**, *9 - 10*, 851.

[23] E. Kobayashi, L. S. Plashnitsa, T. Doi, S. Okada, J. Yamaki, *Electrochem. commun.* **2010**, *12*, 894.

[24] K. Takada, M. Tansho, I. Yanase, T. Inada, A. Kajiyama, M. Kouguchi, S. Kondo, M. Watanabe, *Solid State Ionics* **2001**, *139*, 241.
[25] V. Thangadurai, A. K. Shukla, J. Gopalakrishnan, *J. Mater. Chem.* **1999**, *9*, 739.
[26] K. Arbi, S. Mandal, J. M. Rojo, J. Sanz, *Chem. Mater.* **2002**, *14*, 1091.
[27] W. Belam, *J. Alloys Compd.* **2013**, *551*, 267.
[28] M. Cretin, P. Fabry, *J. Eur. Ceram. Soc.* **1999**, *19*, 2931.
[29] B. E. Francisco, C. R. Stoldt, J.-C. M'Peko, *Chem. Mater.* **2014**, *26*, 4741.
[30] G. B. Kunshina, O. G. Gromov, E. P. Lokshin, V. T. Kalinnikov, *Russ. J. Inorg. Chem.* **2014**, *59*, 424.
[31] M. Kotobuki, K. Hoshina, Y. Isshiki, K. Kanamura, *Phosphorus Res. Bull.* **2010**, *24*, 61.
[32] X. Xu, Z. Wen, J. Wu, X. Yang, *Solid State Ionics* **2007**, *178*, 29.
[33] X. Xu, Z. Wen, X. Wu, X. Yang, Z. Gu, *J. Am. Ceram. Soc.* **2007**, *2806*, 2802.
[34] L. Zhang, P. Chen, Z. Hu, C. Chen, *Chinese J. Chem. Phys.* **2012**, *25*, 703.
[35] P. Zhang, M. Matsui, Y. Takeda, O. Yamamoto, N. Imanishi, *Solid State Ionics* **2014**, *263*, 27.
[36] P. Kichambare, T. Howell, S. Rodrigues, *Energy Technol.* **2014**, *2*, 391.
[37] K. Takahashi, J. Ohmura, A. Im, Dno, D. Lee, T. Zhang, T. Imanishi, A. Hirano, M. B. Phillipps, Y. Takeda, O. Yamamoto, *J. Electrochem. Soc.* **2012**, *159*, A342.
[38] M. Zhang, K. Takahashi, N. Imanishi, Y. Takeda, O. Yamamoto, B. Chi, J. Pu, J. Li, *J. Electrochem. Soc.* **2012**, *159*, A1114.
[39] D. Popovici, H. Nagai, S. Fujishima, J. Akedo, *J. Am. Ceram. Soc.* **2011**, *94*, 3847.
[40] J. Xie, N. Imanishi, T. Zhang, a. Hirano, Y. Takeda, O. Yamamoto, *J. Power Sources* **2010**, *195*, 5780.
[41] J. Xie, N. Imanishi, T. Zhang, a. Hirano, Y. Takeda, O. Yamamoto, *J. Power Sources* **2009**, *192*, 689.
[42] R. Inada, K. Ishida, M. Tojo, T. Okada, T. Tojo, Y. Sakurai, *Ceram. Int.* **2015**, *41*, 11136.
[43] Q. Ling, Z. Yu, H. Xu, G. Zhu, X. Zhang, Y. Zhao, A. Yu, *Mater. Lett.* **2016**, *169*, 42.
[44] K. Takada, K. Fujimoto, T. Inada, A. Kajiyama, M. Kouguchi, S. Kondo, M. Watanabe, *Appl. Surf. Sci.* **2002**, *189*, 300.

[45] S. Takase, C. Kubo, R. Aono, Y. Shimizu, *J. Sol-Gel Sci. Technol.* **2016**, *79*, 564.
[46] H.S. Kim, K. S. Choi, E. J. Kim, K. Kang, J. H. Kim, J. Kim, C. S. Yoon, *J. Electrochem. Soc.* **2015**, *162*, A2080.
[47] Y. Inaguma, C. Liquan, M. Itoh, T. Nakamura, T. Uchida, H. Ikuta, M. Wakihara, *Solid State Commun.* **1993**, *86*, 689.
[48] S. Stramare, V. Thangadurai, W. Weppner, *Chem. Mater.* **2003**, *15*, 3974.
[49] O. Bohnke, *Solid State Ionics* **2008**, *179*, 9.
[50] S. Teng, J. Tan, A. Tiwari, *Curr. Opin. Solid State Mater. Sci.* **2014**, *18*, 29.
[51] M. Nb, V. Thangadurai, H. Kaack, W. J. F. Weppner, *J. Am. Ceram. Soc.* **2003**, *86*, 437.
[52] Y. J. Shan, L. Chen, Y. Inaguma, M. Itoh, T. Nakamura, *J. Power Sources* **1995**, *54*, 397.
[53] C. Hua, X. Fang, Z. Wang, L. Chen, *Electrochem. commun.* **2013**, *32*, 5.
[54] O. Bohnke, C. Bohnke, J. L. Fourquet, *Solid State Ionics* **1996**, *91*, 21.
[55] K. Kanamura, N. Akutagawa, K. Dokko, *J. Power Sources* **2005**, *146*, 86.
[56] M. Hara, H. Nakano, K. Dokko, S. Okuda, A. Kaeriyama, K. Kanamura, *J. Power Sources* **2009**, *189*, 485.
[57] Z. Zheng, Y. Wang, *J. Electrochem. Soc.* **2012**, *159*, A1278.
[58] C.-L. Li, B. Zhang, Z.-W. Fu, *Thin Solid Films* **2006**, *515*, 1886.
[59] C. H. Chen, K. Amine, *Solid State Ionics* **2001**, *144*, 51.
[60] D. T. Swamy, K. E. Babu, V. Veeraiah, **2013**, *36*, 1115.
[61] H. Geng, J. Lan, A. Mei, Y. Lin, C. W. Nan, *Electrochim. Acta* **2011**, *56*, 3406.
[62] H. Zhang, X. Liu, Y. Qi, V. Liu, *J. Alloys Compd.* **2013**, *577*, 57.
[63] I. Kokal, O. F. Göbel, E. J. van den Ham, J. E. ten Elshof, P. H. . Notten, H. T. Hintzen, *Ceram. Int.* **2015**, *41*, 13147.
[64] N. Kamaya, K. Homma, Y. Yamakawa, M. Hirayama, R. Kanno, M. Yonemura, T. Kamiyama, Y. Kato, S. Hama, K. Kawamoto, A. Mitsui, *Nat. Mater.* **2011**, *10*, 682.
[65] S. Furusawa, H. Tabuchi, T. Sugiyama, S. Tao, J. Irvine, *Solid State Ionics* **2005**, *176*, 553.
[66] T. Ohnishi, K. Takada, *Solid State Ionics* **2012**, *228*, 80.
[67] T. Aaltonen, M. Alnes, O. Nilsen, L. Costelle, H. Fjellvåg, *J. Mater. Chem.* **2010**, *20*, 2877.

[68] T. N. H. Le, M. Roffat, Q. N. Pham, S. Kodjikian, O. Bohnke, C. Bohnke, *J. Sol-Gel Sci. Technol.* **2008**, *46*, 137.
[69] K. Kitaoka, H. Kozuka, T. Hashimoto, T. Yoko, *J. Mater. Sci.* **1997**, *32*, 2063.
[70] S. Furusawa, H. Tabuchi, T. Sugiyama, S. Tao, J. Irvine, *Solid State Ionics* **2005**, *176*, 553.
[71] R. Chen, W. Liang, H. Zhang, F. Wu, L. Li, *Chinese Sci. Bull.* **2012**, *57*, 4199.
[72] T. Teranishi, Y. Ishii, H. Hayashi, A. Kishimoto, *Solid State Ionics* **2016**, *284*, 1.
[73] Z. Zheng, H. Fang, F. Yang, Z.K. Liu, Y.Wang, *J. Electrochem. Soc.* **2014**, *161*, 536.
[74] D. Pinzaru, V. Thangadurai, *J. Electrochem. Soc.* **2014**, *161*, A2060.
[75] G. T. Hitz, E. D. Wachsman, V. Thangadurai, *J. Electrochem. Soc.* **2013**, *160*, A1248.
[76] S. Narayanan, V. Thangadurai, *J. Power Sources* **2011**, *196*, 8085.
[77] R. Murugan, V. Thangadurai, W. Weppner, *Angew. Chem. Int. Ed. Engl.* **2007**, *46*, 7778.
[78] R. Murugan, V. Thangadurai, W. Weppner, *Ionics (Kiel).* **2007**, *13*, 195.
[79] V. Thangadurai, W. Weppner, *J. Am. Ceram. Soc.* **2005**, *88*, 411.
[80] W. G. Zeier, *Dalton Trans.* **2014**, *43*, 16133.
[81] S. Ohta, J. Seki, Y. Yagi, Y. Kihira, T. Tani, T. Asaoka, *J. Power Sources* **2014**, *265*, 40.
[82] H. Buschmann, S. Berendts, B. Mogwitz, J. Janek, *J. Power Sources* **2012**, *206*, 236.
[83] S. Kim, M. Hirayama, S. Taminato, R. Kanno, *Dalton Trans.* **2013**, *42*, 13112.
[84] T. Kasuga, K. Kanamura, **2013**.
[85] Y. Shimonishi, A. Toda, T. Zhang, A. Hirano, N. Imanishi, O. Yamamoto, Y. Takeda, *Solid State Ionics* **2011**, *183*, 48.
[86] G. Larraz, a. Orera, M. L. Sanjuán, *J. Mater. Chem. A* **2013**, *1*, 11419.
[87] Y. Li, J.-T. Han, C.-A. Wang, H. Xie, J. B. Goodenough, *J. Mater. Chem.* **2012**, *22*, 15357.
[88] M. Kotobuki, M. Koishi, *Ceram. Int.* **2014**, *40*, 5043.
[89] I. Kokal, M. Somer, P. H. L. Notten, H. T. Hintzen, *Solid State Ionics* **2011**, *185*, 42.
[90] N. Rosenkiewitz, J. Schuhmacher, M. Bockmeyer, J. Deubener, *J. Power Sources* **2015**, *278*, 104.

[91] M. Nakayama, M. Kotobuki, H. Munakata, M. Nogami, K. Kanamura, *Phys. Chem. Chem. Phys.* **2012**, *14*, 10008.
[92] M. Kotobuki, K. Kanamura, *Ceram. Int.* **2013**, *39*, 6481.
[93] C. A. Geiger, E. Alekseev, B. Lazic, M. Fisch, T. Armbruster, R. Langner, M. Fechtelkord, N. Kim, T. Pettke, W. Weppner, *Inorg. Chem.* **2011**, *50*, 1089.
[94] Y. Jin, P. J. McGinn, *Electrochim. Acta* **2013**, *89*, 407.
[95] J. Tan, A. Tiwari, in *Mater. Res. Soc. Symp. Proc.*, **2012**, p. 1440.
[96] I. Kokal, K. V. Ramanujachary, P. H. L. Notten, H. T. Hintzen, *Mater. Res. Bull.* **2012**, *47*, 1932.
[97] H. Xie, Y. Li, J. B. Goodenough, *Mater. Res. Bull.* **2012**, *47*, 1229.
[98] Y. Wang, W. Lai, *Electrochem. Solid-State Lett.* **2012**, *15*, A68.
[99] K. Tadanaga, H. Egawa, A. Hayashi, M. Tatsumisago, J. Mosa, M. Aparicio, A. Duran, *J. Power Sources* **2015**, *273*, 844.
[100] J. Reinacher, S. Berendts, J. Janek, *Solid State Ionics* **2014**, *258*, 1.
[101] J. Tan, a. Tiwari, *ECS Solid State Lett.* **2012**, *1*, Q57.
[102] D. J. Kalita, S. H. Lee, K. S. Lee, D. H. Ko, Y. S. Yoon, *Solid State Ionics* **2012**, *229*, 14.
[103] M. Bitzer, T. Van Gestel, S. Uhlenbruck, *Thin Solid Films* **2016**, *615*, 128.
[104] S. Lobe, C. Dellen, M. Finsterbusch, H.-G. Gehrke, D. Sebold, C.-L. Tsai, S. Uhlenbruck, O. Guillon, *J. Power Sources* **2016**, *307*, 684.
[105] C.-W. Ahn, J.-J. Choi, J. Ryu, B.-D. Hahn, J.-W. Kim, W.-H. Yoon, J.-H. Choi, D.-S. Park, *J. Electrochem. Soc.* **2014**, *162*, A60.
[106] J. B. Bates, N. J. Dudney, G. R. Gruzalski, R. A. Zuhr, A. Choudhury, *J. Power Sources* **1993**, *44*, 103.
[107] M. Nisula, Y. Shindo, H. Koga, M. Karppinen, *Chem. Mater.* **2015**, *27*, 6987.
[108] S. Nowak, F. Berkemeier, G. Schmitz, *J. Power Sources* **2015**, *275*, 144.
[109] D. Li, Z. Ma, J. Xu, Y. Li, K. Xie, *Mater. Lett.* **2014**, *134*, 237.
[110] B. Put, P. M. Vereecken, J. Meersschaut, A. Sepúlveda, A. Stesmans, *ACS Appl. Mater. Interfaces* **2016**, *8*, 7060.

[111] P. D. Mani, S. Saraf, V. Singh, M. Real-Robert, A. Vijayakumar, S. J. Duranceau, S. Seal, K. R. Coffey, *Solid State Ionics* **2016**, *287*, 48.
[112] L. Baggetto, J. F. M. Oudenhoven, T. Van Dongen, J. H. Klootwijk, M. Mulder, R. A. H. Niessen, M. De Croon, P. H. L. Notten, *J. Power Sources* **2009**, *189*, 402.
[113] STMicroelectronics, *EnFilm Rechargeable Solid State Thin Film Battery (EFL700A39) Datatsheet*, **2014**.
[114] F. Muñoz, *J. Power Sources* **2012**, *198*, 432.
[115] B. K. Money, K. Hariharan, *Solid State Ionics* **2008**, *179*, 1273.
[116] B. Fleutot, B. Pecquenard, H. Martinez, a. Levasseur, *Solid State Ionics* **2013**, *249-250*, 49.
[117] N. Kuwata, N. Iwagami, Y. Matsuda, Y. Tanji, J. Kawamura, Institute, *ECS Trans.* **2009**, *16*, 53.
[118] J. Hamalainen, J. Holopainen, F. Munnik, T. Hatanpaa, M. Heikkila, M. Ritala, M. Leskela, *J. Electrochem. Soc.* **2012**, *159*, A259.
[119] S. Yubuchi, Y. Ito, T. Matsuyama, A. Hayashi, M. Tatsumisago, *Solid State Ionics* **2016**, *285*, 79.
[120] J. Xie, J. F. M. Oudenhoven, P.-P. R. M. L. Harks, D. Li, P. H. L. Notten, *J. Electrochem. Soc.* **2014**, *162*, A249.
[121] H. T. Kim, T. Mun, C. Park, S. W. Jin, H. Y. Park, *J. Power Sources* **2013**, *244*, 641.
[122] A. C. Kozen, A. J. Pearse, C.-F. Lin, M. Noked, G. W. Rubloff, *Chem. Mater.* **2015**, *27*, 5324.
[123] S. Gielis, Chemical Solution Deposition of Oxides for Energy Storage Applications: A Breaktrough in Coating High Aspect Ratio 3D Structures, Hasselt University, **2015**.
[124] B. Put, P. M. Vereecken, M. J. Mees, F. Rosciano, I. P. Radu, A. Stesmans, *Phys. Chem. Chem. Phys.* **2015**, *17*, 29045.
[125] Y.-C. Perng, J. Cho, S. Y. Sun, D. Membreno, N. Cirigliano, B. Dunn, J. P. Chang, *J. Mater. Chem. A* **2014**, *2*, 9566.
[126] J. Kawamura, *Solid State Ionics* **2004**, *175*, 273.
[127] Y.-C. Perng, J. Cho, S. Y. Sun, D. Membreno, N. Cirigliano, B. Dunn, J. P. Chang, *J. Mater. Chem. A* **2014**, *2*, 9566.
[128] L. Zhang, G. Liang, G. Peng, F. Zou, Y. Huang, M. C. Croft, A. Ignatov, *J. Phys. Chem. C* **2012**, *116*, 12401.

Part II - Chapter 4

LLT films as solid electrolyte for all-solid-state Li-ion batteries

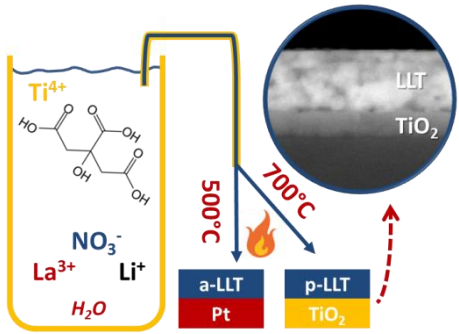

A major part of this chapter has been published:

E.J. van den Ham, N. Peys, C. De Dobbelaere, J. D'Haen, F. Mattelaer, C. Detavernier, P.H.L. Notten, A. Hardy and M.K. Van Bael – "*Amorphous and perovskite* $Li_{3x}La_{(2/3)-x}TiO_3$ *(thin) films via chemical solution deposition: solid electrolytes for all-solid-state Li-ion batteries*" – Journal of Sol-Gel Science and Technology 73 (2015), 536-543

Abstract

In this chapter, the synthesis of amorphous and crystalline perovskite LLT thin films is shown by means of aqueous chemical solution. Li-ion conductivity measurements of the pin-hole free, amorphous LLT thin films (90 nm thick) indicate a conductivity in the order of 10^{-8} $S \cdot cm^{-1}$ with out-of-plane measurements. GATR-FTIR measurements shows that all organic fragments have been decomposed at 500°C. In addition, in-situ (heating) X-ray diffraction analysis shows that phase pure crystalline perovskite LLT is formed on top of the rutile TiO_2 anode at 700°C. Furthermore, thickness control is possible by varying the precursor solution concentration and the number of deposition cycles. The current study presents a promising synthesis route to develop thin film all-solid-state Li-ion batteries based on multi-metal oxide materials using aqueous precursor chemistry.

1. Introduction

In Chapter 3 various thin film solid electrolyte materials were discussed with a broad Li-ion conductivity. Based on its high Li-ion conductivity, perovskite lithium lanthanum titanate (LLT) is a promising solid electrolyte to be implemented in all-solid-state Li-ion batteries.[1,2] In addition to the high conductivity of the perovskite phase (10^{-3} S·cm^{-1}), the bulk material retains a high conductivity in the amorphous state (10^{-5} S·cm^{-1}).[3,4] The main disadvantage of this electrolyte is its incompatibility with metallic lithium as a negative electrolyte due to reduction of Ti^{4+} around 1.5 V.[2,5] However, other negative electrode materials with higher (de)lithiation voltages have been combined with LLT. More specifically, LLT was synthesized in combination with LTO using macro porous morphologies to maximize the electrolyte-anode interface.[3]

Several synthesis routes such as solid state synthesis and sol-gel synthesis yielding bulk LLT are known (c.f. Chapter 3).[1,6] In addition, several attempts have been made to combine negative and positive electrodes with LLT, such as creating LLT coated $LiCoO_2$ particles as well as preparing 3D ordered macro porous LLT to create an electrolyte network with high Li-ion conductivity surrounded by a LTO matrix.[3,7] However, only a limited number of studies focus on thin film synthesis of this material: PLD was applied several times to yield epitaxial LLT layers (approximately 40 nm thick) on STO and NGO substrates,[8] amorphous LLT films of approximately 500 nm were grown on quartz glass substrates and both amorphous and crystalline LLT were deposited on Pt substrates with 400 nm thickness.[4,9] In addition, lanthanum deficient amorphous LLT ($Li_{0.32}La_{0.30}TiO_3$) was deposited on Si by ALD, but crystallization yielded relatively rough morphologies combined with slow growth rates between 0,30 and 0.50 Å·cycle^{-1}.[10] A first attempt at preparing crystalline perovskite LLT films (x=0.167) on indium tin oxide using chemical solution deposition was carried out by Kitaoka et al.[11] Using three different organic precursors solutions based on metal alkoxides or acetates dissolved in 2-methoxyethanol, films with thicknesses ranging from 200 nm to 1

µm were obtained by dip coating in combination with a post-deposition anneal of 700 to 1300°C.[11]

In the this chapter, amorphous and crystalline perovskite LLT thin films were prepared on various substrates by CSD using an aqueous precursor solution containing Li^+, La^{3+} and Ti^{4+}.

2. Experimental

2.1 Precursor synthesis

Aqueous precursor solutions were prepared for Li^+, La^{3+} and Ti^{4+}. Lithium nitrate ($LiNO_3$, Sigma Aldrich, ≥98.5%) and lanthanum nitrate hexahydrate ($La(NO_3)_3 \cdot 6H_2O$, Sigma Aldrich, ≥99%) were both dissolved in water by stirring at room temperature, yielding concentrations of 1.5 $mol \cdot L^{-1}$ and 1.0 $mol \cdot L^{-1}$ respectively. Titanium isopropoxide ($Ti[OCH(CH_3)_2]_4$, Sigma Aldrich, ≥97%) was added to water to form titanium hydroxide, followed by addition of citric acid mono hydrate (Sigma Aldrich, ≥99%), hydrogen peroxide (H_2O_2, Acros Organics, 35%) and ammonia (NH_3, Merck, 32%) to yield a citrate-peroxo-Ti^{4+} solution with a 0.9 $mol \cdot L^{-1}$. A detailed description of the citrate-peroxo-Ti^{4+} precursor was reported earlier by Hardy et al.[12]

The concentrations of the mono-ion solutions was determined by ICP-AES (Optima 3300, PerkinElmer) before mixing them together in stoichiometric amounts at room temperature (Figure 1). The final multi-metal ion precursor solution was prepared in a high (0.95 M) and low (0.38 M) total metal ion concentration with a Li^+:La^{3+}:Ti^{4+} molar ratio of 0.35:0.55:1.00.

2.2 Film deposition

The aqueous multi-metal ion precursor solution was spin-coated (3000 rpm, 30 s, 1000 $rpm \cdot s^{-1}$) onto small pieces (3 x 3 cm) of different substrates: Pt, TiO_2/Si (Si substrate with 90 nm TiO_2),[13] and TiO_2/Pt (a stack of TiO_2/Pt with 90 nm TiO_2).[13] See Chapter 2, section 3.3 for more details.

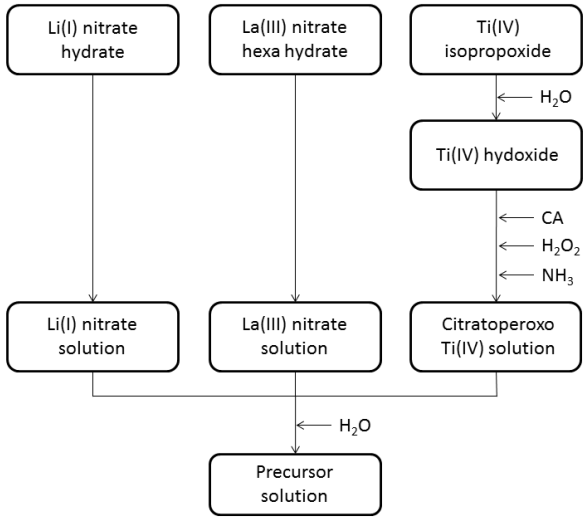

Figure 1: Synthesis scheme of the aqueous precursor solution.

All these substrates were cleaned by an UV/O_3 treatment at 60°C (40 min., Novascan PSD Pro Series). Heat treatments were carried out in ambient air after spin coating of the aqueous precursor at 250°C (2 min.), 375°C (2 min.) and 500°C (2 min.). The sequence of spin coating and heat treatment was repeated multiple times to obtain films with the desired thickness. The final film was annealed by either a heat treatment at 500°C (1 to 4 hours) in static air on a hot plate or at 700°C (1 to 4 hours) under a dynamic air flow (0.1 $L \cdot min^{-1}$) in a tube furnace.

2.3 Powder characterization

The thermal decomposition profile of the yellow precursor powder, obtained by drying the precursor solution at 60°C, was investigated by TGA/DSC (TA instruments SDT Q600). 6 mg of the powder was heated ramped at $10°C \cdot min^{-1}$ up to 1200°C using dry air (0.1 $L \cdot min^{-1}$) in an alumina crucible. The crystallization process of the

aqueous precursor powder was studied by HT-XRD (Bruker D8 with an Anton Paar HTK1200 high temperature chamber with a Kapton® window) from 250 - 900°C (10°C·min^{-1}), in steps of 50°C with a counting time of 52.8 s per step. The yellow precursor powder was underwent a pre-anneal (250°C in a drying oven overnight) to remove most of the organics before starting the HT-XRD experiment.

2.4 Film characterization

As-deposited and sequentially heated (250, 375, 500 and 700°C) layers were characterized by GATR-FTIR (Bruker Vertex 70 combined with Harrick 65° single reflection Ge-ATR) from 4000 to 600 cm^{-1} with 32 scans per sample with a torque of 24 kPa. Crystallization of amorphous LLT thin films was studied by isXRD (Bruker D8 Discover with experimental heating chamber)[14] in cooperation with the CoCoon Group of Ghent University, Belgium. A linear detector was used, recording a diffraction pattern with a 2θ range of 30 to 50° every 5 seconds within a temperature range of 25 to 900°C (with a heating rate of 1°C·min^{-1}). The morphology of annealed LLT films was investigated by means of SEM (FEI Quanta 200F). Finally, the Li-ion conductivity of LLT thin films was studied by means of impedance spectroscopy. Hereto, Au electrodes (300 nm thick, 6 mm^2 area) were evaporated (Vactec thermal evaporator, 3·10^{-7} mbar) on top of post-annealed LLT thin films with Pt or TiO_2/Pt as the underlying substrate. The Li-ion conductivity perpendicular to the film direction is of importance for the power density of the final battery, therefore the electric field was applied in this direction. The impedance was measured using an Autolab PGSTAT302N with frequencies ranging from 1MHz – 10 mHz, at open circuit voltage with an alternating voltage of 3 mV. The results were fitted with equivalent circuit models with resistor (R) and capacitor (C) elements using Nova software (Version 1.9.16, Metrohm Autolab B.V.). CV was measured with an Autolab PGSTAT128N, using a three electrode setup[15] (see Chapter 2). The LLT/Pt samples were used as the working electrode via a copper disc connected to the back of the substrate. Silver paint (Benelux scientific) was used to ensure good conductivity between the

copper disc and the substrate. The top of the substrate was accessible to the liquid electrolyte (1.0 M $LiClO_4$ dissolved in polycarbonate, Soulbrain MA) and a Kapton® O-ring was used for sealing. Metallic lithium (99,9% Sigma Aldrich) served as the counter and reference electrodes.

3. Results and discussion

3.1 Powders – decomposition and crystallization

Figure 2 shows the results of the TGA analysis. The thermal decomposition of the dried (60°C, overnight) aqueous precursor gel shows a weight loss between room temperature and 150°C, which is most likely the evaporation of residual water. Above 150°C, a major weight loss is observed while the heat flow indicates that this is accompanied with small endothermic step at 220°C followed by a sequence of exothermic events at 270 and 535°C, respectively.

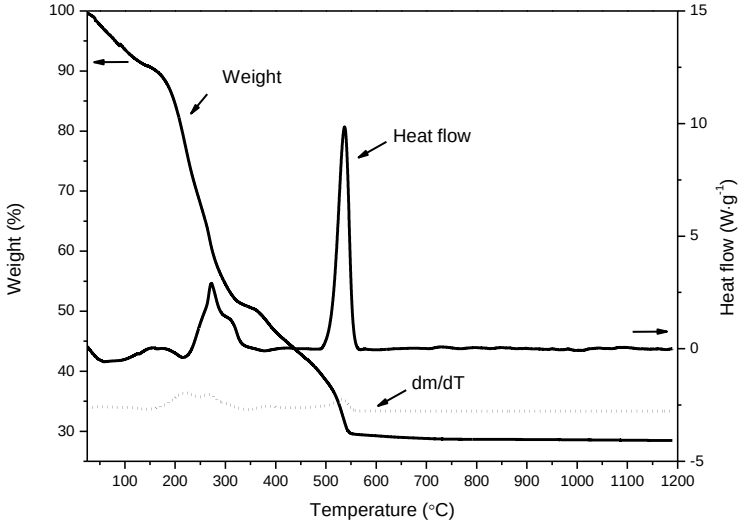

Figure 2: TGA-DSC graph of dried (60°C overnight) LLT precursor gel (10°C·min^{-1}, with dry air flow of 0.1 L·min^{-1}).

This sequence is related to the decomposition of organics and nitrates. Above 600°C, no significant weight loss is observed, indicating that the precursor has completely decomposed, and most probably only oxide phase(s) remain.

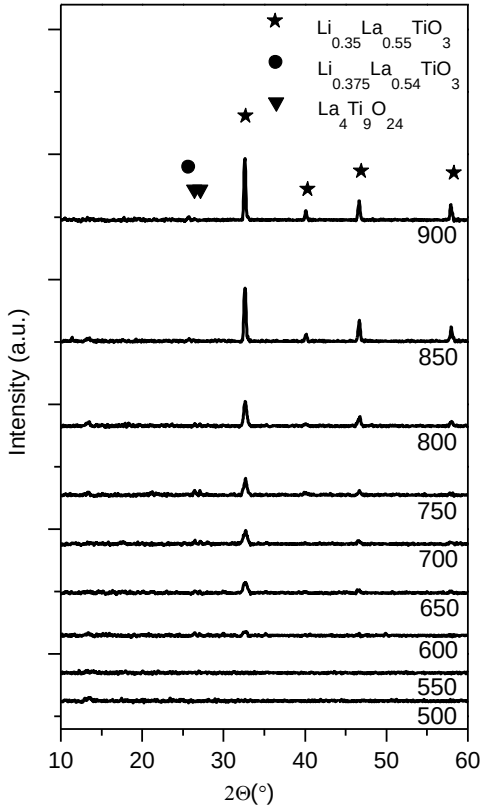

Figure 3: HT-XRD patterns a of dried and pre-calcined (250°C) precursor powder measured at several temperatures (in °C) with a heating rate of 10°C·min^{-1} in dry air (0.1 L·min^{-1}).

To study the crystallization of the LLT precursor powders, HT-XRD was used; heating the powder to high temperatures while recording an X-ray diffractogram (c.f. Chapter 2). The HT-XRD analysis

(Figure 3) indicates that the onset of perovskite LLT crystallization (JCPDS 46-0465) occurs at 600°C. From 600 to 850°C small peaks are present around 26,4 and 27,2° 2θ, indicating the presence of $La_4Ti_9O_{24}$ (JCPDS 036-0137) as a secondary phase.

These small peaks disappear at 900°C, but at this temperature a small single peak at 25,7° 2θ can be observed, implying that $La_4Ti_9O_{24}$ is transformed into $Li_{0.375}La_{0.54}TiO_3$ (JCPDS 47-0668) at higher temperatures, possibly by reacting with a lithium containing amorphous phase.

3.2 Films – Decomposition and crystallization

After showing the suitability of the water based precursor system to obtain LLT powders, the deposited and decomposition of the precursor was studied to obtain thin films. Due to differences in the surface to volume ratio between powders and thin films, leading to different heat transport and gas diffusion phenomena, their decomposition process may differ.[16] Therefore, the decomposition process was indirectly studied on the thin films, by identification of the organic residuals using GATR-FTIR.

A single layer deposited onto the TiO_2/Si substrate was measured; as-deposited and directly after different heat treatments (Figure 4). The TiO_2/Si substrate shows a strong band at 750 cm^{-1}, arising from TiO_2 lattice vibrations.[17,18] Si-O-Si longitude and transverse modes are also observed at 1250 and 1050 cm^{-1}, respectively.[19] For the as-deposited aqueous precursor, several bands could be observed: the (broad) band at 3500 to 2750 cm^{-1} is associated with C−H stretching vibrations, O-H stretching vibrations of (unbound) water and NH_4^+ anti-symmetric stretching vibrations broadened by hydrogen bond formation.[20,21] At 1600 and 1400 cm^{-1} strong bands are observed, associated with COO^- asymmetric and symmetric stretching vibrations of the citrate ligands.[20] In addition, the 1400 cm^{-1} band overlaps with the asymmetric stretching vibration of NO_3^-.[22] The (weak) band at 1250 cm^{-1} is assigned to C-OH stretching of a carboxylic acid, related to citric acid.[20]

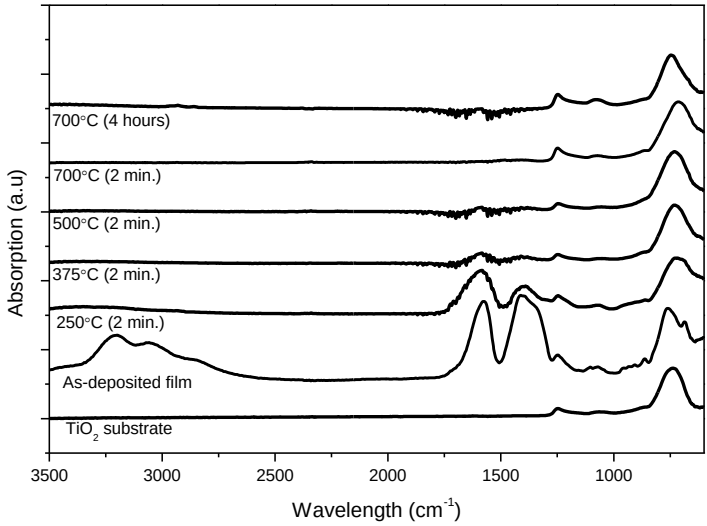

Figure 4: GATR-FTIR of the blank TiO_2/Si substrate (bottom), the as-deposited aqueous precursor and different heat treated LLT layers on TiO_2/Si. The spectra were recorded directly after spin coating (as-deposited) or after consecutive heating steps for 2 minutes at 250°C, 250°C+375°C or 250°C+375°C+500°C under static air. Samples annealed at 700°C (for 2 minutes or for 4 hours) were placed in a pre-heated tube furnace in dry air after completing all consecutive heating steps.

Finally, the (weak) bands at 850 to 800 cm^{-1} and 770 to 715 cm^{-1} are both related NO_3^-, respectively out-of-plane and in-plane bending vibrations.[21,22] At 250°C the broad band from 3500 to 2750 cm^{-1} is strongly reduced, associated with the removal of water and NH_4^+. Furthermore, a large reduction of the 1400 cm^{-1} band combined with absence of the weak bands at 850-800 cm^{-1} and 770-715 cm-1 suggest that NO_3^- has been removed from the sample. At 375°C, the 1600 and 1400 cm^{-1} band have strongly been reduced, indicating that most of the organic materials have been decomposed. At 500°C and above only bands related to substrate

can clearly be observed. Furthermore, above 375°C no bands are observed between 1550-1300 cm^{-1}, indicating that no (oxy)carbonates are formed.[17,21,23] In literature no FTIR results could be found regarding (perovskite) LLT. However, bands of closely related titanates are only visible at lower wavenumbers than recorded in this study.[20,24] In-situ XRD was therefore employed to study the crystallization of the films obtained with little organic residuals prepared at 500°C.

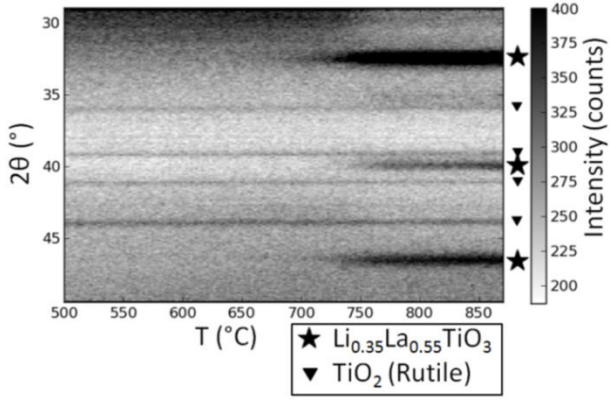

Figure 5: XRD intensity of a 240 nm thick LLT film on TiO_2/Si prepared with the aqueous precursor, pre-annealed at 500° for 1 hour in static air, as a function of temperature during non-isothermal heating with a heating rate of 6°C·min^{-1} in static air.

The crystallization process of LLT thin films, deposited on TiO_2/Si and pre-annealed at 500°C, was examined by in situ X-ray diffractometry as a function of temperature during its non-isothermal heating with constant heating rate (Figure 5) and as function of time during isothermal heating at 700°C (Figure 6). Before the heating starts, diffractions are only visible at 2θ = 36, 39, 41 and 44°; all these correspond to the rutile phase (JCPDS 021-1276) of the TiO_2 anode underneath the amorphous LLT film.

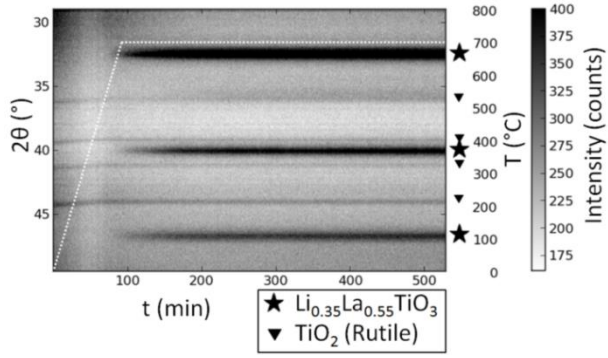

Figure 6: XRD intensity of a 240 nm thick LLT film on TiO_2/Si, prepared with the aqueous precursor (0.95 M), pre-annealed at 500° for 1 hour in static air, heated isothermally at 700°C with in static air (after a short period of non-isothermal heating to reach 700°C with 10°C·min^{-1}). The temperature profile is plotted (dashed line) as a function of time.

While heating the amorphous LLT films, the onset of perovskite LLT (x=0.117, JCPDS 046-0465) crystallization can be observed at 725°C, identified by the 33, 40 and 47° 2θ angle diffractions. Isothermal heating at 700°C leads to perovskite LLT phase formation as well (Figure 6), but prolonged heating at this temperature is required to fully crystallize the film. Based on these XRD measurements, there is no reason to assume that the LLT reacts with TiO_2, though other techniques are required to study this more thoroughly (e.g. XPS with Ar^+ milling). Note that XRD is capable to detect reactions of LLT with other underlying materials if they form crystalline phases. This is shown in Chapter 10, where LLT reacts with WO_3.

3.3 Films – Morphology and thickness

The top view SEM micrographs show crystalline perovskite LLT films on TiO_2/Si (Figure 7a and 7b), which were annealed comparable to the isothermal heating during the in-situ XRD study (Figure 6).

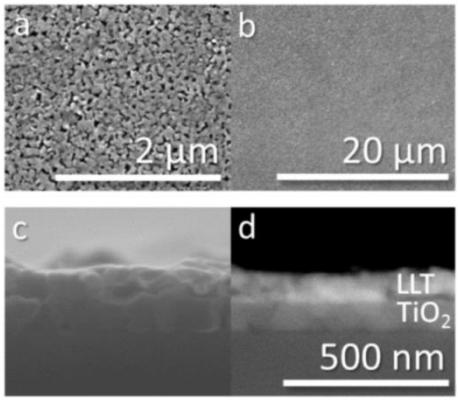

Figure 7: Top view SE micrographs at different magnifications (a & b) and cross sections SE micrograph (c) and BSE micrograph (d) and of 4 layers of LLT prepared with the aqueous precursor (0.38 M), deposited on TiO_2/Si annealed at 700°C for 1 hour in dry air.

The films exhibit a homogeneous morphology with macroporosity (i.e. pores > 50 nm). It is speculated (based on properties of the amorphous layers, see further in Figure 9) that this is introduced during the crystallization of the films. Using the Z-contrast in the BSE cross section micrograph (Figure 7d) the LLT layer (brighter, 90 nm thick) can clearly be distinguished from the rutile TiO_2 anode layer (darker, 90 nm thick) underneath. The thickness of the LLT layer on TiO_2 increases linearly with the number of deposition cycles for high and low precursor solution concentrations (Figure 8). This linear increase indicates beneficial conditions are realized for the spin-coat deposition; the heat treatments prevent dissolution of the deposited film during a following deposition step. This feature is of great importance to obtain high quality films with desired thickness and stoichiometry.

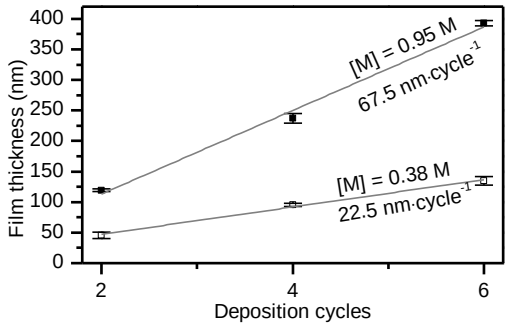

Figure 8: LLT film thickness as function of deposition cycles and precursor concentration deposited on TiO_2/Si, determined by SEM cross sections. After deposition the LLT films were annealed for 1 hour at 700°C in dry air. High (0.95M; black squares) and low total metal-ion concentrations (0.38 M; white squares) were measured with the standard deviation shown for each sample.

3.4 Films – Li-ion conductivity

Thus far, XRD and GATR-FTIR results have, respectively, confirmed the formation of perovskite phase LLT on TiO_2/Si and the presence of negligible organic contents in the films. To study functional properties of these films with impedance spectroscopy, an electronically conductive substrate is required; for this study Pt and TiO_2/Pt coated substrates are used. Initially the crystalline films prepared at 700°C (4 hours) and 1000°C (30 minutes) were measured (Figure 9). However, even with films as thick as 250 nm, with intermediate anneals at 700°C after each deposited layer to increase the density of the films (Figure 9c), the crystalline LLT films contained pin-holes. Although these pin-holes were not always visible with SEM analysis, the impedance spectroscopy showed induction behaviour (not shown), implying an electronically conductive pathway is present. This means a short is made over the electrolyte layer, implying that the gold top electrode touches the platinum bottom electrode. This is most clearly visible in Figure 9b.

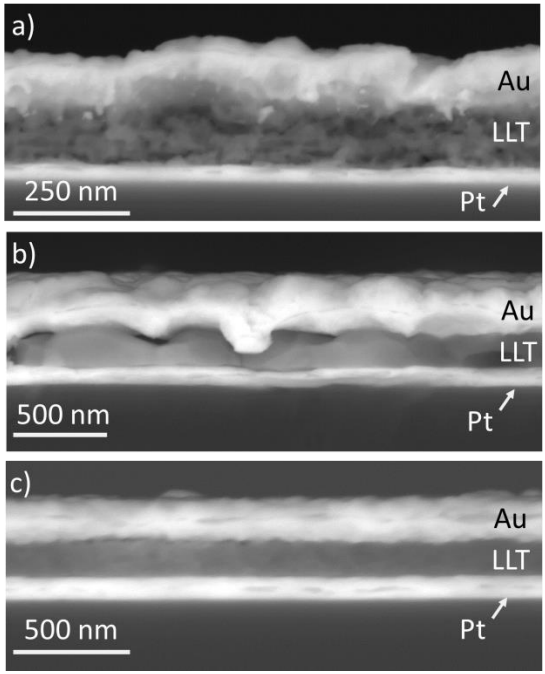

Figure 9: Cross section SEM BSE of crystalline LLT films prepared with 600 °C (2 min.) after each deposited layer, followed by final anneal at 700°C (4 hours) or (b) 1000°C (30 min.). (c) Anneal at 700°C (30 min.) after each deposited layer. All anneal were done in air.

A second issue encountered was instability of the Pt substrate at or above 700°C (Figure 10), leading to deformation or local delamination after an anneal at 700°C. In is unclear if this also contributed had a negative influence on morphology of the crystalline films.

To ensure stability of the current collector and limit the macroporosity of the films, the maximum annealing temperature was set at 500°C, yielding smooth amorphous LLT thin films (Figure 11).

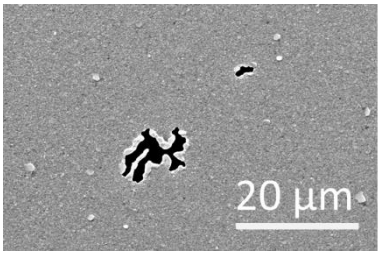

Figure 10: SEM SE top view of Pt substrate annealed at 700°C (4 hours in air).

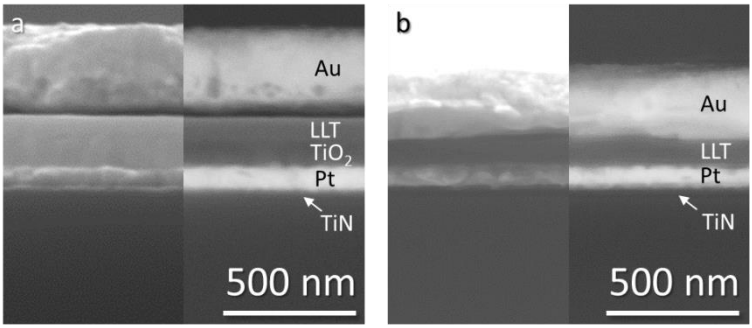

Figure 11: Cross section SEM SE and BSE micrographs of 4 layers (0.38 M) of amorphous LLT (90 nm) deposited on (a) TiO_2/Pt and (b) Pt, annealed at 500°C for 4 hours in static air. Afterwards, the Au electrode was evaporated on top.

The out-of-plane impedance results for amorphous LLT films prepared at 500°C are shown in Figure 12. First of all, it means that the morphology of the amorphous films is much better than the crystalline counterparts, since no induction was measured with impedance spectroscopy. Instead, one semicircle is observed for LLT on Pt, and two semicircles in case of the half-cell configuration (LLT on TiO_2/Pt). Based on this comparison, it is assumed that the high frequency range semi-circle is related to the amorphous LLT layer, whereas the small low-frequency range semi-circle is related to TiO_2 layer. The latter can either arise from (i) Li^+ ions that have

diffused from the LLT layer into TiO_2 during annealing (4 hours at 500°C) (ii) it can be related to the charge transfer resistance at the LLT-TiO_2 interface or (iii) a dielectric response of the TiO_2.

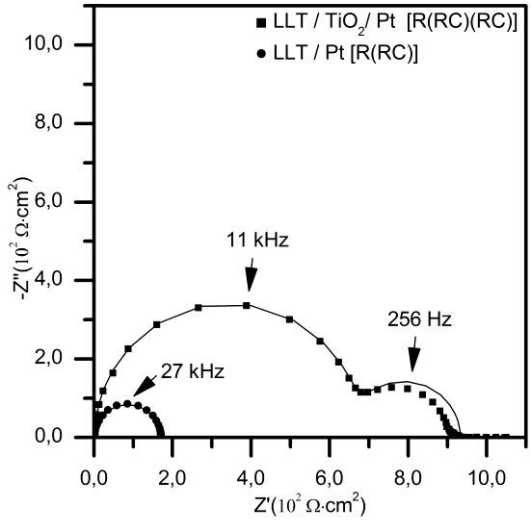

Figure 12: Nyquist plot of 90 nm thick LLT films annealed for 4 hours at 500°C, with 300 nm Au electrodes evaporated on top (6 mm^2). Two semi-circles are observed for LLT on TiO_2 (Pt) (squares) as shown in Figure 9, whereas one semi-circle was observed for LLT on Pt (circles) as shown in Figure 10. Results of the fitted equivalent circuit models are also shown (lines) with resistor (R) and capacitor (C) elements.

Notably, no spike is observed at lower frequencies. This spike was expected for ideal systems due to polarization of Li^+ ions at a (metal) interface that is inaccessible for Li^+.(c.f. Chapter 2). However, the platinum or gold electrodes used do not seem to fulfil this criterion, due to possible porosity or poor Li^+ blocking properties. Based on fitting with an equivalent circuit, the Li-ion conductivities of amorphous LLT thin films, with thicknesses under 100 nm, on Pt and TiO_2/Pt were found to be in the order of 10^{-8} $S \cdot cm^{-1}$. The con-

ductivities obtained with the current approach are considerably lower compared to the conductivity of bulk amorphous LLT prepared at 600°C (10^{-5} S·cm^{-1}, measured at room temperature).[3] Although a previous study on LLT thin films (with a thickness under 100 nm) prepared at higher temperatures nearly accomplished this value, the reported Li-ion conductivity was measured in in-plane direction,[8] whereas the current study regards the out-of-plane Li-ion conductivity of the thin film, which is of higher relevance for the final battery.

Finally, the electrochemical stability of the LLT films is studied by cycling the sample versus metallic lithium in a non-aqueous electrolyte (Figure 13 and 14). Although the morphology did not allow out-of-plane measurements after annealing at 700°C, the electrochemical stability could be determined (Figure 13) by using a liquid electrolyte. For high potentials up to 4.5 V (vs. Li^+/Li), the solid electrolyte shows no Li-reactivity. Higher voltages were not investigated because of the strong solvent oxidation of the liquid electrolyte used (PC) above 4.5 V.[25]

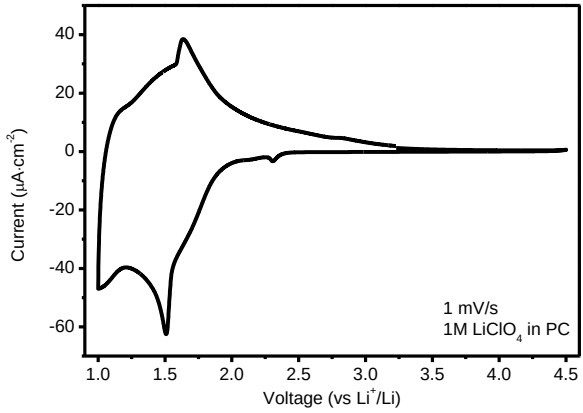

Figure 13: Cyclic voltammetry of crystalline LLT deposited on Pt, annealed at 700°C for 4 hours in dry air.

However, while approaching 1.7 V (vs. Li^+/Li), a strong reduction appears in the solid electrolyte film, leading to a sharp reduction peak at 1.5 V, related to Ti^{4+} reduction.[9,12] The large negative current observed just little above 1 V can be the onset of a second intercalation reaction of LLT at 0.66 V.[26,27] The oxidation peak is assigned to Ti^{3+} oxidation. Hence, crystalline LLT films exhibit little stability in the low voltage range (below 1.7 V). The combination of LLT with LTO and TiO_2 negative electrodes seems unlikely for films, in contrast to the conclusions of Kanamura for LLT and LTO powders et al.[3]

The electrochemical stability of the amorphous LLT (500°C anneal) was also probed (Figure 14). Some similarity is observed with its crystalline counterpart (700°C anneal) although reduction peak(s) are shifted to slightly higher potentials. The shape of this peak is not as sharp as the Ti reduction observed for the crystalline counterpart. In addition, the oxidation peak can hardly be observed. In addition, the current range is significantly lower, which reflects the lower Li-ion conductivity of the amorphous structure. The absence of an oxidation peak is ascribe to a lack of electronic conductivity by Chen et al., since addition of conductive binder materials to LLT powders does lead to oxidation (delithiation).[27]

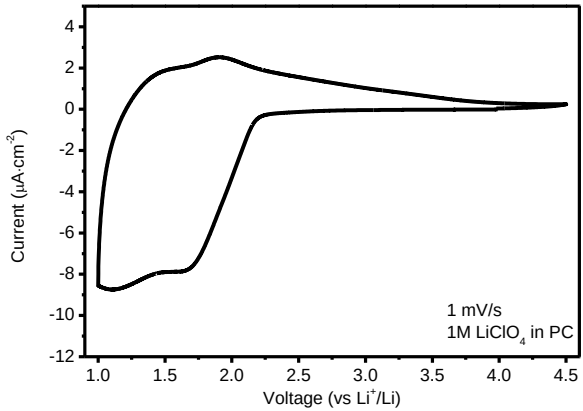

Figure 14: CV of amorphous LLT deposited on Pt, annealed at 500°C for 4 hours in static air.

In colaboration with Sven Gielis (UHasselt), the combination of LTO [28] and amorphous LLT did not yield (de)lithiation with 1.5 V (vs. Li^+/Li) as the lowest potential (not shown). Either the LTO became inactive during the LLT synthesis (directly on top) or the overpotial as a result of the electrolyte resistivity shifted LTO lithiation to much lower values than expected (1.55 V vs. Li^+/Li).[28-30] As will be shown in Chapter 10, other (non-Ti based) electrode materials such as WO_3 appear to be a better choice because of the higher (de)lithiation potential.

4. Conclusion

The results of the current study have shown that amorphous and crystalline perovskite LLT (thin) films could be established using an aqueous precursor system, at respectively 500 and 700°C. The thickness of the films can easily be tuned by varying the number of deposition cycles and the concentration of the aqueous precursor, which is of importance to tailor the ideal electrolyte thickness in a battery device. In addition, the uniform depositions on the rutile TiO_2 anode and Pt current collector indicate that the current approach has potential to be applied to other electrode materials as well. However, the limited electrochemical below 1.7 V seems to hinder combination with functional TiO_2 or LTO negative electrodes. Other materials combination are therefore required (Chapter 10). Various approached to obtain dense crystalline films (prepared at 700°C or higher) could not prevent the occurrence of pin-holes. This is an unfortunate result, since the Li-ion conductivity is reported to be significantly higher (2 orders of magnitude) than amorphous LLT.[3,4] The morphology of amorphous LLT was shown to be significantly better; an electronic short circuit could be prevented across the films. The final value obtained for the Li-ion conductivity of the amorphous thin films in this study (10^{-8} $S \cdot cm^{-1}$) still has to be improved in view the application of LLT as a solid electrolyte. Nevertheless, it is a promising result compared to other studies on LLT thin films, considering the more realistic, out-of-plane measurement method used. Combination with other electrode materials

5. References

[1] Y. Inaguma, C. Liquan, M. Itoh, T. Nakamura, T. Uchida, H. Ikuta, M. Wakihara, *Solid State Commun.* **1993**, *86*, 689.

[2] S. Stramare, V. Thangadurai, W. Weppner, *Chem. Mater.* **2003**, *15*, 3974.

[3] K. Kanamura, N. Akutagawa, K. Dokko, *J. Power Sources* **2005**, *146*, 86.

[4] S. Furusawa, H. Tabuchi, T. Sugiyama, S. Tao, J. Irvine, *Solid State Ionics* **2005**, *176*, 553.

[5] Y. J. Shan, L. Chen, Y. Inaguma, M. Itoh, T. Nakamura, *J. Power Sources* **1995**, *54*, 397.

[6] H. Geng, J. Lan, A. Mei, Y. Lin, C. W. Nan, *Electrochim. Acta* **2011**, *56*, 3406.

[7] S. Noh, J. Kim, M. Eom, D. Shin, *Ceram. Int.* **2013**, *39*, 8453.

[8] T. Ohnishi, K. Takada, *Solid State Ionics* **2012**, *228*, 80.

[9] J.-K. Ahn, S.-G. Yoon, *Electrochim. Acta* **2004**, *50*, 371.

[10] T. Aaltonen, M. Alnes, O. Nilsen, L. Costelle, H. Fjellvåg, *J. Mater. Chem.* **2010**, *20*, 2877.

[11] K. Kitaoka, H. Kozuka, T. Hashimoto, T. Yoko, *J. Mater. Sci.* **1997**, *32*, 2063.

[12] a. Hardy, J. D'Haen, M. K. Van Bael, J. Mullens, *J. Sol-Gel Sci. Technol.* **2007**, *44*, 65.

[13] I. Truijen, M. K. Van Bael, H. Van Den Rul, J. D'Haen, J. Mullens, *J. Sol-Gel Sci. Technol.* **2006**, *41*, 43.

[14] W. Knaepen, C. Detavernier, R. L. Van Meirhaeghe, J. Jordan Sweet, C. Lavoie, *Thin Solid Films* **2008**, *516*, 4946.

[15] M. E. Donders, W. M. Arnoldbik, H. C. M. Knoops, W. M. M. Kessels, P. H. L. Notten, *J. Electrochem. Soc.* **2013**, *160*, A3066.

[16] D. Sanchez-Rodriguez, J. Farja, P. Roura, S. Richart, N. Mestres, X. Obradors, T. Puig, *J. Phys. Chem. C* **2013**, *117*, 20133.

[17] P. A. Connor, K. D. Dobson, A. J. McQuillan, *Langmuir* **1999**, *15*, 2402.

[18] V. C. Farmer, *The Infrared Spectra of Minerals*, Mineralogical Society, London, **1974**.

[19] D. Rouchin, N. Rochat, F. Gustavo, A. Chabli, O. Renault, P. Besson, *Surf. interface Anal.* **2202**, *34*, 445.

[20] A. Hardy, D. Nelis, G. Vanhoyland, M. K. Van Bael, H. Van den Rul, J. Mullens, L. C. Van Poucke, J. D'Haen, L. Goux, D. J. Wouters, *Mater. Chem. Phys.* **2005**, *92*, 431.

[21] R. A. Nyquist, C. L. Putzig, M. A. Leugers, *Handbook of Infrared and Raman Spectra of Inorganic Compounds and Organic Salts*, Academic Press, Massachusetts, **1997**.
[22] Q. Zhang, Y. Zhang, C. Cai, Y. Guo, J. P. Reid, *J. Phys. Chem. A* **2014**, *118*, 2728.
[23] S. Irusta, L. M. Carnaglia, E. A. Lombardo, *Mater. Chem. Phys.* **2004**, *86*, 440.
[24] R. Salzer, J. Dressler, M. K. Gergs, D. Michel, H. Schlemmbach, W. Windsch, P. Reich, *J. Mol. Struct.* **1990**, *219*, 177.
[25] D. Aurbach, M. Daroux, P. Faguy, E. Yeager, J. Electrocanal. Chem. 1991, 297, 225.
[26] O. Bohnke, C. Bohnke, J. L. Fourquet, *Solid State Ionics* **1996**, *91*, 21.
[27] C. H. Chen, K. Amine, *Solid State Ionics* **2001**, *144*, 51.
[28] S. Gielis, Chemical Solution Deposition of Oxides for Energy Storage Applications: A Breaktrough in Coating High Aspect Ratio 3D Structures, Hasselt University, **2015**.
[29] D. Yoshikawa, Y. Kadoma, J.M. Kim, K. Ui, N. Kumagai, N. Kitamura, Y. Idemoto, *Electrchimica Acta* **2010**, *55*, 1872.
[30] S.Y. Tsai, K.Z. Fung, C.T. Ni, *ECS Transactions*, **2015**, *68*, 37.

Part II - Chapter 5

3D structured lithium lanthanum titanate as solid electrolyte for 3D all-solid-state Li-ion batteries

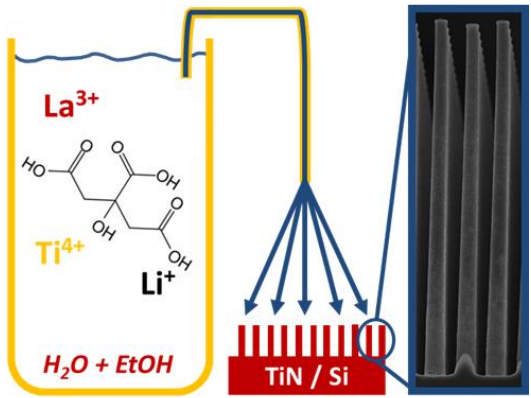

A large part of this chapter has been published:

E.J. van den Ham*, S. Gielis*, M.K. Van Bael and A. Hardy – "*Ultrasonic spray deposition of metal oxide films on high aspect ratio microstructures for 3D all-solid-state Li-ion batteries*" – ACS Energy Letters 1 (2016), 1148-1188

*equal contribution

Abstract

In this chapter the 3D deposition of LLT is studied via two different routes. A citrate-nitrate precursor (Chapter 3) and an all-citrate precursor were deposited on 3D architectures by ultrasonic spray deposition. Precursor concentration, deposition temperature and spray height proved to be of importance for successful 3D deposition with ultrasonic spray deposition. Finally, 3D structures with an aspect ratio of 10 were coated with a wet-chemical approach, yielding a breakthrough for 3D deposition of 3D thin film solid electrolyte materials.

1. Introduction

As a follow-up of Chapter 4, where the synthesis and planar deposition of LLT is discussed, the 3D deposition of this material is studied by means of ultrasonic spray deposition. The flexibility of chemical solution deposition is fully utilized during deposition of inorganic solid-state electrolytes, since many of these materials are composed of several different metal ions (c.f. Chapter 3). Very few 3D thin film depositions of inorganic solid electrolyte materials are reported, and no reports were found about non-vacuum based methods. Therefore, successful 3D deposition of solid-state electrolytes by CSD would lead to major advantages not only for upscaling purposes, but primarily in achieving complex multi-metal-ion based materials in 3D.

As proposed by Gielis et al., (all-) citrate chemistry is of interest for deposition of oxide coatings on non-planar surfaces with high aspect ratio's.[1] Hence, besides the citrate-nitrate precursor discussed in Chapter 4, an all-citrate precursor is studied in this chapter for deposition LLT on 3D structures.

2. Experimental

2.1 Precursor synthesis

A citrate-based Li^+ precursor was prepared by dissolution of lithium citrate (99%, Sigma Aldrich) in water, while stirring at room temperature.

The citrate-based La^{3+} precursor was prepared similarly to the Hardy et al.[2] First, La_2O_3 (99,9%, Sigma Aldrich) and citric acid mono-hydrate (99,9%, Sigma Adrich) powders were mixed by grinding with a mortar, after which a minimal amount of water was added to disperse the powders in a round bottom flask. After stirring for 24 hours at 120°C under reflux conditions, the pH of the slurry was increased to 12 by addition of ammonia (32%, Merck). After stirring for an additional 24 hours at 110°C under reflux conditions a light yellow, transparent precursor solution was yielded

with pH 8. For the Ti-precursor, the same citrate-peroxo-Ti^{4+} precursor was used as described in Chapter 4.

Before combining the Li-, La- ant Ti-precursors, their exact concentration was determined by ICP-AES (Optima 3000, PerkinElmer). Finally, an all-citrate Li-La-Ti-precursor was prepared. The ratio of Li:La:Ti was 0.35:0.55:1; the same as the citrate-nitrate precursor (c.f. Chapter 4). The synthesis of the all-citrate precursor is summarized in Figure 1.

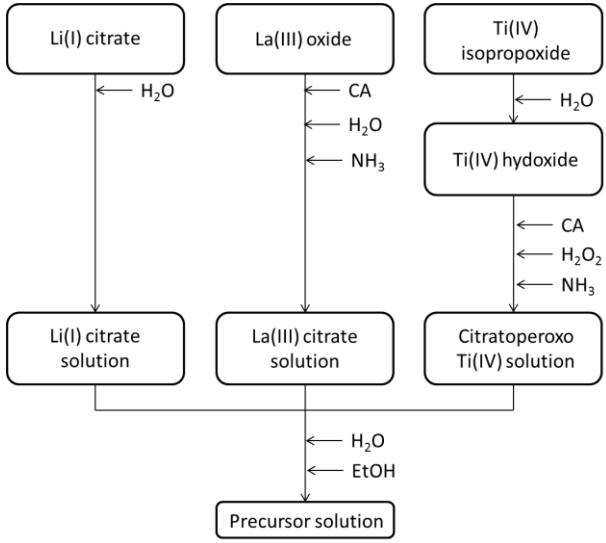

Figure 1: Synthesis scheme of the all-citrate Li-La-Ti-precursor.

Besides the all-citrate Li-La-Ti-precursor, the same citrate-nitrate described in Chapter 4 was used. Wettability of the precursors was increased by addition of ethanol in a 10:9 H_2O:EtOH ratio with a total metal-ion concentration of 0.01 M, according to Gielis et al.[1]

2.2 Film deposition

Two different types of substrates were used for this study: (i) Pt (ii) 3D TiN (2x5) (iii) 3D TiN (2x10), see Chapter 2 Section 3 for details. All these substrates were cleaned by a UV/O_3 treatment at 60°C (40 min., Novascan PSD Pro Series) prior to deposition. Heat treatments were carried out for the as-deposited films at various temperatures.

Ultrasonic spray deposition (USD, Exacta Coat, Sono-Tek cooperation) was done using the Accumist nozzle (Sono-Tek cooperation). The deposition temperature was varied to influence the 3D deposition. The citrate-nitrate Li-La-Ti-precursor was deposited in two distinct sets of spray deposition parameters:

(i) Large nozzle distance; implying a spray nozzle to substrate distance of 6.9 cm with a flowrate varying between 0.5 and 1.0 ml·min^{-1}.
(ii) Small nozzle distance; implying a nozzle-to-substrate substrate distance of 2.6 cm with a flowrate varying between 0.2 ml·min^{-1}; according to Gielis et al.[1]

In both cases the N_2 carrier gas pressure was set at 1.5 psi, the spray nozzle moved with a speed of 100 mm·s^{-1}. For the all-citrate Li-La-Ti-precursor, only the 'small nozzle distance' parameters were used.

2.3 Powder characterization

The thermal decomposition profile of the dried all-citrate Li-La-Ti-precursor was obtained similar to the description in Chapter 4. To investigate the possible influence of ethanol on decomposition, a fully aqueous gel and 10:9 (volume ratio) water to ethanol based gel were measured.

2.4 Film characterization

The morphology of annealed LLT films was investigated by means of SEM (FEI Quanta 200F and Nova 200). The crystallinity of the

films was investigated by XRD by means of a Bruker D8 apparatus, equipped with a line-scan detector (Lynx eye), using a step size of 0.040° and a counting time of 3 seconds per step at room temperature.

3. Results and discussion

3.1 All-citrate precursor: decomposition

The decomposition of the all-citrate precursor is shown in Figure 2. The first small weight loss up to 150°C is assigned to evaporation of water due to drying of the gel. Next, the profile shows several weight loss steps due to the presence of several citrate based Li-, La- and Ti-precursors (Figure 3) and ammonium citrate.[3] Hence, features of ammonium citrate are visible in the decomposition profile shown in Figure 2. The presence of ammonium citrate can most clearly be observed by the endothermic features at 200°C, decarboxylation reactions of the ammonium citrate.[3] The melting around 150°C shows no distinct endothermic peak,[3] perhaps it is masked by water evaporation at a relatively high temperature of 180°C. Because of the high CA to metal ratio used for the La- and Ti-precursor synthesis (3:1 CA:M), significant amounts of ammonium citrate are present in these solutions, explaining the large weight loss at 200°C. In addition, part of the citrate-peroxo-Ti^{4+} appears to decompose at the same temperature, yielding an additional weight loss at this temperature. For the Li-precursor, no substantial weight loss is found within this region because these precursors contain only minor amounts of ammonium citrate, related to the initial 3:1 Li:CA ratio.

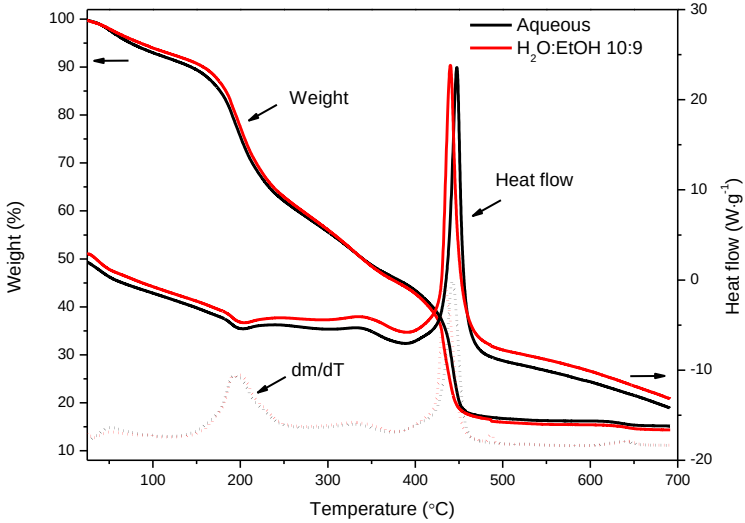

Figure 2: TGA-DSC graph of dried (60°C overnight) all-citrate LLT precursor gel, showing the relative weight, relative weight derivative and heat flow as a function of temperature (10°C·min^{-1}, with dry air flow of 0.1 L·min^{-1}).

At higher temperatures of 360 and 440°C, the Li-La-Ti-precursor shows events with a strong weight loss, which can both be related to decomposition of Li- and La-precursor products. The large weight loss at temperatures close to 450°C is assigned to a decomposition reaction primarily involving the La- and Ti-precursor, followed by a minor loss at 545°C caused by the Li-precursor derivative (c.f. Figure 3). Finally, the last decomposition step at 650°C is probably caused by products of the Li-precursor decomposition since the La- and Ti-precursor decompositions show no weight loss in this region. Since lithium carbonate only starts decomposing above 650°C,[4] the weight loss at high temperatures is explained. Complete decomposition of the Li-La-Ti-precursor is therefore achieved at 700°C. The TGA analysis indicates that besides the temperature required for crystallization, at least 700°C is

required to fully decompose the carbonate formed with this precursor.

Figure 2 (red curves) shows that the addition of ethanol has no influence on the decomposition of the all-citrate precursor. This also implies that the ethanol does not react with any of the complexes present (e.g. esterification at higher temperatures), and all the ethanol evaporated during the drying step at 60 °C prior to the TGA analysis.

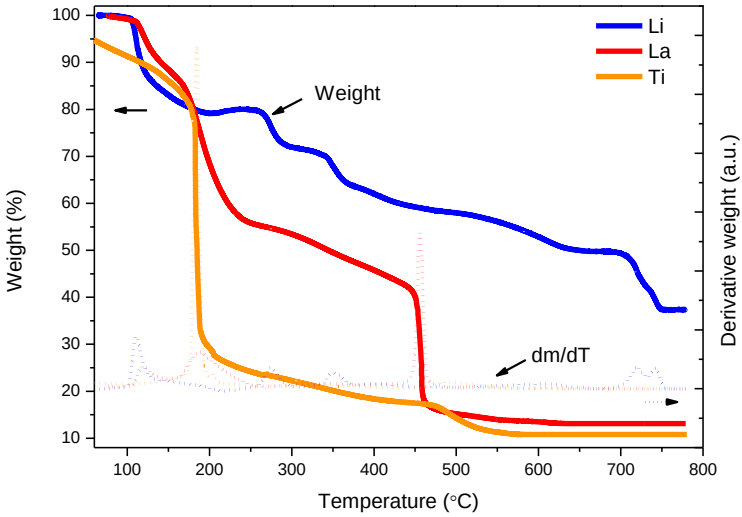

Figure 3: TGA analysis of dried (60°C overnight) citrate based Li-, La- and Ti-precursor gels, showing the relative weight, and relative weight derivative as a function of temperature (10°C·min^{-1}, with dry air flow of 0.1 L·min^{-1}).

3.2 All-citrate precursor: 3D deposition

Since the main objective of this study is to investigate 3D deposition of LLT, film formation based on this precursor was not studied extensively on planar substrates. Instead, depositions were done in line with the approach of Gielis et al.,[1,5] including the same spray

nozzle to substrate distance, yielded interesting results. Figure 4 and 5 show that the all-citrate Li-La-Ti-precursor can indeed be deposited on 3D TiN (2x5, see Chapter 2 for details).

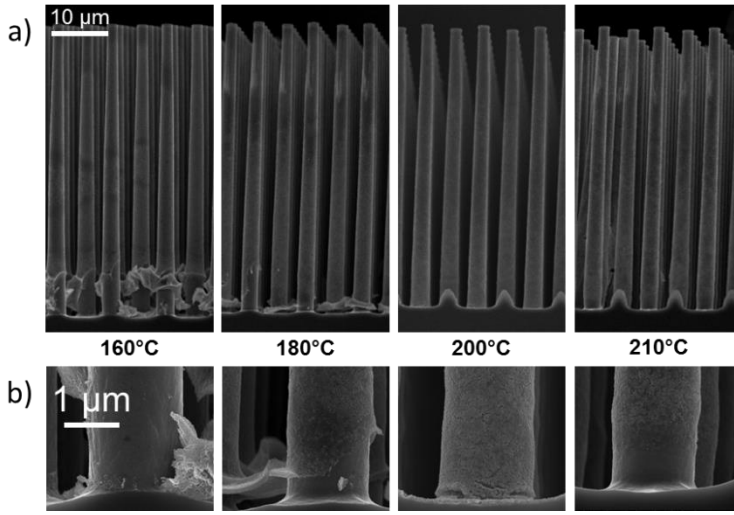

Figure 4: Morphology as function of deposition temperature; 3D TiN (2x5) coated with the all-citrate Li-La-Ti precursor (10 mM) for 50 cycles. Deposition temperature was set at indicated temperatures with a flowrate of 0.2 ml·min^{-1} with a nozzle height of 2.6 cm. The samples were annealed 4 hours at 700°C in oxygen. The whole micro-cylinders (a) as well as the bottom sections (b) are shown.

The quality of the deposited coatings was strongly influenced by precursor concentration.[5] Lower precursor concentrations lead to smaller droplets hitting the heated substrate,[6] since significantly smaller amounts of non-evaporating material are available per droplet (c.f. Chapter 2). These smaller droplets are quickly immobilized at the surface and prevent accumulation of the precursor gel down the micro-cylinders. Hence, a low precursor concentration of 10 mM was used to achieve the coatings shown in Figure 4 and

5. The temperature at which the atomized precursor droplets hit the substrate proved to be the most important parameter to obtain a complete coating of the micro-cylinder. It is thought that, due to lack of gel immobilization at low deposition temperature (<180°C), the precursor gel flows down the vertical structure,[7] yielding largely uncoated micro-cylinders (Figure 4).

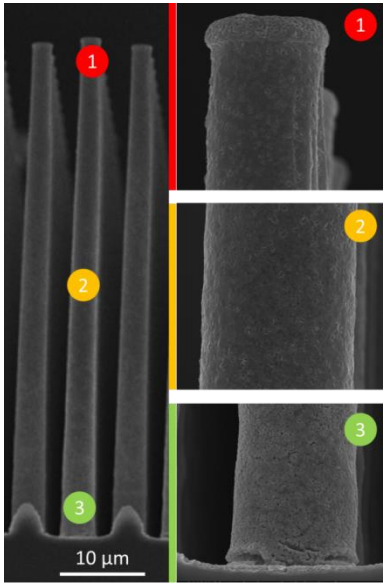

Figure 5: Morphology obtained with a deposition temperature of 200°C; 3D TiN (2x5) coated with the all-citrate Li-La-Ti precursor (10 mM) for 50 cycles. Flowrate was set at 0.2 ml·min^{-1} with a nozzle height of 2.6 cm. The sample was annealed 4 hours at 700°C in oxygen.

Therefore, the deposition temperature was increased to 210°C. At this temperature the bottommost 2 µm of the 50 µm micro-cylinders remained uncoated (Figure 4b). Recalling that both gravity (small droplets) and Leidenfrost effects (too low temperature) can be excluded (Chapter 2) in this particular case, the phenomena acting during the deposition are probably (i) high gel immobiliza-

tion and (ii) strong thermophoretic forces at the bottom of the micro-cylinders.[6,8] Therefore no droplets are able to reach this part of the substrate at high deposition temperatures. Finally, the optimum deposition temperature to coat the high aspect ratio micro-cylinders for the all-citrate LLT precursor was determined to be 200°C (Figure 5).

The diffractogram (Figure 6) of the LLT coated micro-cylinders shows that the LLT phase is present on the pillars. However, a lot of other peaks arise that require clarification.

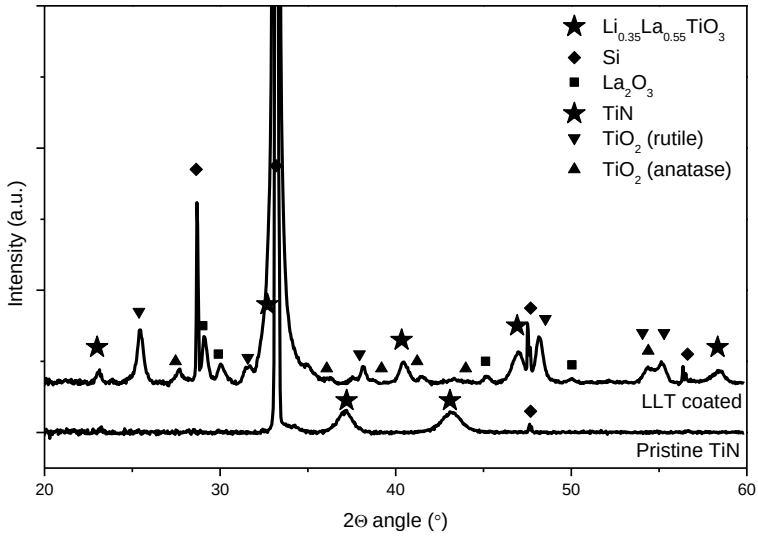

Figure 6: X-ray diffractograms of pristine TiN / Si micro-cylinders as well as a Li-La-Ti-precursor coated sample (50 passes, 10 mM), submitted to a post-deposition anneal of 700°C for 4 hours in oxygen.

First of all, La_2O_3 is identified as secondary phase, implying that not all of the coating is crystallized in the perovskite LLT phase. The occurrence of TiO_2 may suggest this is a secondary phase as well, but the appearance of TiO_2 (anatase and rutile) can also be caused by the oxidation of the TiN current collector.[9] This clarifies

why the peaks belonging to the TiN phase disappear upon prolonged heating (annealed for 4 hours at 700°C in oxygen). However, phase segregation of LLT during the long anneal, forming TiO_2 and La_2O_3, may also be the cause of the TiO_2 present. Hence, it is unclear if phase pure LLT existed before segregation, or that secondary phases have been present all the time.

For mono-crystalline Si substrates, normally a single peak at 32° is (often) observed. Here several additional peaks related to Si are present. This is explained by broken micro-cylinders present on the sample, leading to additional orientations of Si, rendering a more polycrystalline pattern.

The oxidation of the TiN current collector is an unfortunate result, due to the long anneal applied to yield highly crystalline LLT films (c.f. Chapter 4). Because of the oxidation, the functional properties of the coating cannot be measured (e.g. cyclic voltammetry or impedance spectroscopy). More importantly, this high temperature anneal is expected to be a bottleneck for device integration, since positive electrodes, negative electrode and current collecting materials will not be able to withstand these high thermal budgets.[10] Apart from this issue, there are concerns with respect to the morphology of the crystalline coatings. As was shown in Chapter 4, crystalline films LLT are difficult to prepare in a pin-hole free manner. Continuous films are however of major importance for the function of the electrolyte to prevent short-circuits.

3.3 Citrate-nitrate precursor: 3D depositions

Initially the citrate-nitrate precursor (Chapter 4) was used for 3D depositions. After tuning the deposition temperature and precursor flowrate, the best results obtained for 3D TiN (2x10) are shown in Figure 7. At the bottom section of the micro-cylinders, a coating can clearly be observed, mainly due to the heavy lanthanum which shows up in the BSE micrograph. Up to the first 20 µm the coatings seems to be present. However, while inspecting figure 7b, there does not seem to be sufficient deposition below the first 10 µm measured from top of the micro-cylinders. Tuning deposition tem-

perature, precursor concentration and number of passes did not seem to alter this issue (not shown).

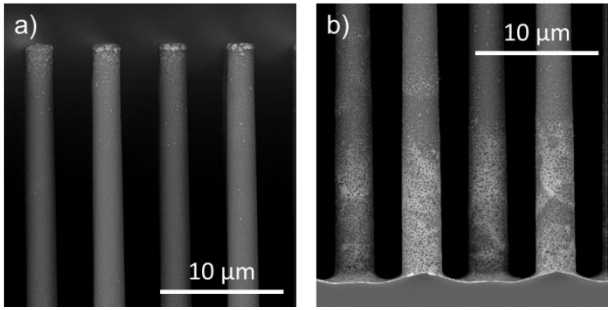

Figure 7: 3D TiN (2x10) coated with the citrate-nitrate Li-La-Ti precursor (10 mM) for 30 cycles. Deposition temperature was set at 200°C with a flowrate of 0.5 ml·min^{-1} with a nozzle height of 6.9 cm. The sample was annealed 4 hours at 700°C in oxygen.

In a later stage, the same deposition parameters used for successful deposition of the all-citrate precursor, were applied on the citrate-nitrate precursor. This led to successful deposition of LLT films on 3D TiN (2x10) (Figure 8), coating the middle section of the micro-cylinders as well. However, it must be noted that slightly different substrates were used with an inter-cylinder distance of 10 µm. Although this does not yield completely comparable results, it does show that the citrate-nitrate precursor has potential for 3D depositions on high aspect ratio structures. Therefore, the deposition of the citrate-nitrate precursor will be studied in more detail in combination with other materials in Chapter 10. Especially so, since this precursor decomposed at slightly lower temperatures (Chapter 4, Figure 2) as compared to the all-citrate precursor (Figure 2). This allows preparation of amorphous LLT films (Chapter 4), which lead to serious advantages in terms of morphology and thermal budget requirements.

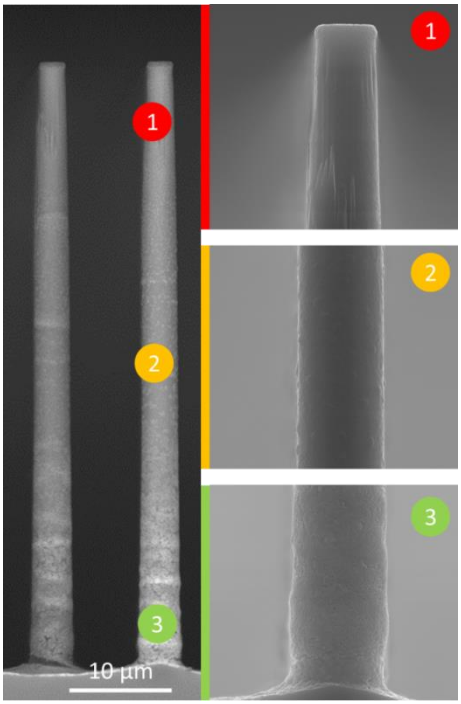

Figure 8: 3D TiN (2x10) coated with the citrate-nitrate Li-La-Ti precursor (10 mM) for 50 cycles. Deposition temperature was set at 200°C with a flowrate of 0.2 ml·min^{-1} with a nozzle height of 2.6 cm. The sample was annealed 4 hours at 700°C in oxygen.

4. Conclusion

An optimized all-citrate precursor and fine-tuned ultrasonic spray deposition yielded a complete metal-oxide coating on micro-cylinders with an aspect ratio of 10 and an inter-distance of 5 µm (3D TiN (2x5)). Although deposition of mono-metal oxide negative electrode materials was shown before using a citrate-based precursor in combination with ethanol,[1] the results of this multi-metal oxide electrolyte material prove how versatile this approach can be. Although future improvements are required with respect to

temperature requirements and morphology of the solid electrolyte, the 3D deposition of LLT on such high aspect ratio's is a unique achievement. Since the aqueous metal-citrate precursor solutions have been developed for a very broad range of metal-ions, this multi-metal ion all-citrate precursor approach can have a large impact in different fields of application as well (c.f. Chapters 9 and 11).

However, this chapter also showed that the citrate-nitrate route has potential with respect to 3D deposition as well. These results underline the intertwined set of parameters used during ultrasonic spray deposition, since the nozzle-to-substrate-distance and/or flowrate seem to have a large influence as well. A further study on the deposition of this particular precursor would be interesting, because of lower temperature requirements and morphology of the resulting (amorphous) material. This could lead to significant advantages in view of device integration (c.f. Chapter 10).

5. References

[1] S. Gielis, A. Hardy, M. K. Van Bael, *Conformal Coating on Three-Dimenstional Substrates*, **2015**, EP 2 947 178 A1.

[2] A. Hardy, D. Nelis, G. Vanhoyland, M. K. Van Bael, H. Van den Rul, J. Mullens, L. C. Van Poucke, J. D'Haen, L. Goux, D. J. Wouters, *Mater. Chem. Phys.* **2005**, *92*, 431.

[3] M. Rajendran, M. Subba Rao, *J. Solid State Chem.* **1994**, *113*, 239.

[4] V. Berbenni, A. Marini, *J. Anal. Appl. Pyrolysis* **2002**, *64*, 43.

[5] S. Gielis, Chemical Solution Deposition of Oxides for Energy Storage Applications: A Breaktrough in Coating High Aspect Ratio 3D Structures, Hasselt University, **2015**.

[6] D. Perednis, L. J. Gauckler, *J. Electroceramics* **2005**, *14*, 103.

[7] M. K. Van Bael, A. Hardy, J. Mullens, in *Chem. Solut. Depos. Funct. Oxide Thin Film.* (Ed.: D. Schneller, T., Waser, R., Kosec, M., Payne), Springer-Verlag Wien, **2013**, pp. 93–140.

[8] L. Filipovic, S. Selberherr, G. C. Mutinati, E. Brunet, S. Steinhauer, A. Köck, J. Teva, J. Kraft, J. Siegert, F. Schrank, *Microelectron. Eng.* **2014**, *117*, 57.

[9] N. C. Saha, H. G. Tompkins, *J. Appl. Phys.* **1992**, *72*, 3072.
[10] M.S. Wittingham, *Chem. Rev.* **2004**, *104,* 4271

Part II - Chapter 6

Wet-chemical synthesis of garnet lithium lanthanum zirconate films as solid electrolyte for Li-ion batteries

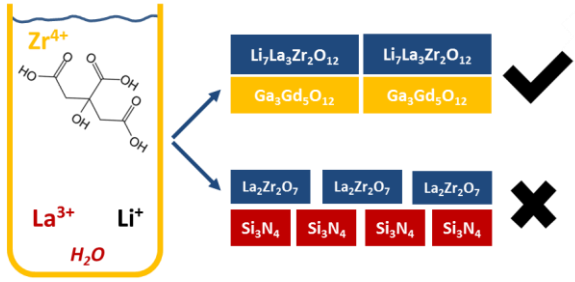

Valerie Nijs, Dr. Ken Elen, Dr. Nikolina Pavlovic and Felix Mattelaer are acknowledged for their contributions to this work.

Abstract

An aqueous all-citrate precursor for the synthesis of garnet $Li_7La_3Zr_2O_{12}$ (LLZO) has been developed in view of application in an all-solid-state Li-ion battery. Whereas garnet phase formation was established for powders, films deposited on Si_3N_4 substrates via chemical solution deposition only yielded the undesired $La_2Zr_2O_7$ phase. It appeared that the latter phase was formed before complete decomposition of the precursor, probably in the form of lithium carbonate. Epitaxial stabilization was required to overcome the crystallization issues, yielding epitaxial LLZO on monocrystalline GGG substrates for the (100) and (111) orientation. Finally, the versatility of the USD approach was shown with preliminary results for 3D structured coatings achieved by the all-citrate Li-La-Zr-precursor.

1. Introduction

In Chapter 3 an overview of the solid electrolytes was given. Based on the comparison of all inorganic solid electrolyte candidates' properties, a successful deposition of garnet electrolytes on film would lead to large benefits (Chapter 3). For instance, garnet films would be able to replace LiPON, providing the same electrochemical stability with higher Li-ion conductivity. Hence, the rate performance of the battery would be improved.

Initially garnet $Li_5La_3Ta_2O_{12}$ (LLTO) was studied in view of its lower crystallization temperature (650°C) as compared to $Li_7La_3Zr_2O_{12}$ (700°C).[1,2] Though phase formation for powders was shown, several experiments with aqueous and non-aqueous precursor systems did not yield crystalline LLTO films. Especially the deposition with an alkoxide (tantalum ethoxide) / nitrate (lanthanum nitrate) / acetate (lithium acetate) with ethanol as solvent seemed promising, but despite the good morphologies obtained via spin-coating, only separate tantalate and lanthanate phases were obtained. Various heating programs and substrates (Si_3N_4, Pt, Si) did not alter this fact and the desired LLTO garnet phase was not obtained (not shown). After these unfortunate findings the focus shifted towards to the synthesis of $Li_7La_3Zr_2O_{12}$ (LLZO). Similar to LLTO, the large electrochemically stability of LLZO allows direct combination with metallic lithium. However, the high total Li-ion conductivity achieved for powders makes LLZO (10^{-4} $S{\cdot}cm^{-1}$) even more appealing than LLTO (10^{-5} $S{\cdot}cm^{-1}$).[3,4] The negative results on LLTO film depositions and indications from literature review (Chapter 3) lead to the conclusion that synthesis of garnet films is rather complicated. Nevertheless, this study investigates the feasibility of aqueous chemical solution deposition for LLZO. Based on recent findings by Gielis et al.[5] and 3D deposition of LLT shown Chapter 5, the use of citrate chemistry yields large opportunities with respect to 3D depositions. Therefore, synthesis of LLZO films (via all-citrate-precursor) is the main objective of this study.

2. Experimental

2.1 Synthesis of the all-citrate Li-La-Zn-precursor

Mono-metal aqueous citrate solutions were prepared for Li^+, La^{3+}, and Zr^{4+}. The Li- and La-precursor were prepared as described in Chapter 5. The Zr^{4+} citrate precursor was prepared according to Van Werde et al.[6] Zr-propoxide was precipitated in water, forming Zr-hydroxide. After filtration, citric acid (CA, Sigma Aldrich, ≥99%) and hydrogen peroxide (H_2O_2, 35% Acros Organics) were added to the residue in a round bottom flask with a 5:6:100 Zr:CA:H_2O_2 ratio. After stirring under reflux conditions at 120°C for 2 hours, the pH was adjusted to 7.5 with ammonia (NH_3, Merck, 32%).

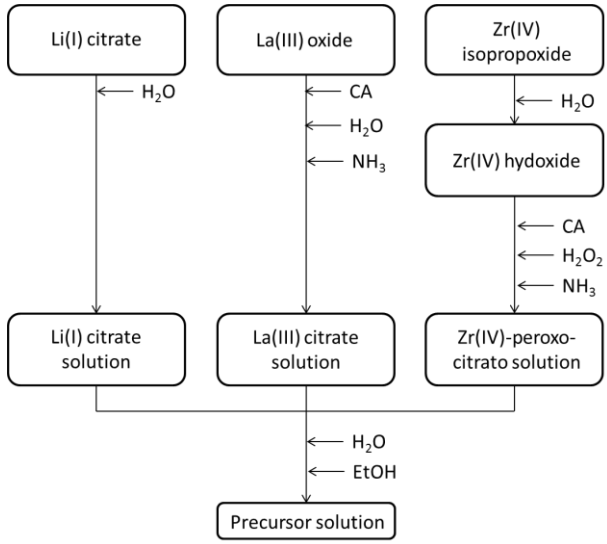

Figure 1: Synthesis scheme of the Li-La-Zr-precursor.

All the mono-metal ion precursor solutions were filtered using a membrane filter (Nalgene, 0.2 µm) to remove particles, such as dust, impurities and undissolved fractions. Subsequently, their exact concentration was determined by ICP-AES (Optima 3000,

PerkinElmer). Mixing of the mono-metal aqueous citrate solutions was based on the desired stoichiometry of LLZO with 10% Li excess to compensate for Li-loss (i.e. a 7.7:3:2 ratio for Li-citrate, La-citrate and Zr-citrate). A summary of the synthesis is shown in Figure 1. For 3D depositions, ethanol (absolute, VWR) was added to yield a 9:10 ethanol to water volume ratio, with a total metal ion concentration of 10 mM.

2.2 Synthesis of the citrate-nitrate Li-La-Zn-precursor

For comparison, a citrate-nitrate precursor was prepared for the synthesis of powder LLZO from a gel.

The Li- and La-nitrate solution synthesis is described in Chapter 4. In addition, Zirconium oxynitrate ($ZrO(NO_3)_2 \cdot xH_2O$, 99%, Sigma Aldrich) was dissolved in water at room temperature, yielding a Zr-nitrate solution. Next, a CA solution was prepared (3 M). The separate Li-, La- and Zr-nitrate solutions in a 7.7:3:2 ratio, were combined together with CA in a 3:2 CA to metal ratio. Finally, the pH was raised to 8 by addition of NH_3.

Ethanol addition, to enhance wettability for spray-deposition similar to the all-citrate precursor (9:10 ethanol to water ratio) led to precipitation. Based on a series of ethanol and aqueous nitrate based Li-La-Zr-precursor from 0 to 50 vol.% in ethanol contents steps of 10%, the highest ethanol fraction preventing precipitation was found to be 40 vol.%. Hence, 40 vol.% ethanol was used for spray deposition of this precursor, with a total metal ion concentration of 10 mM.

2.3 Precursor depositions

Three substrates were used for this study: (i) Si_3N_4, (ii) GGG in 100 and 111 orientations and (iii) 3D Si (2x5), c.f. Chapter 2 section 3. Si_3N_4 substrates were used to prevent silicate formation, which is common for rare-earth metals [7,8]. In addition, the Si_3N_4 structure prevents lithium diffusion [9] into the Si wafer under-

neath. All substrates were cleaned with UV/O_3 (30 minutes, 60°C) prior to deposition.

For planar depositions of the all-citrate Li-La-Zr-precursor, spin-coating and ultrasonic spray depositions were used. Spin-coating was done at 6000 rpm for 30 seconds with 1000 rpm·s^{-1} acceleration, with a total metal ion concentration of 0.254 M. After deposition, the substrate was heated heating of 200, 300 and 600°C for 2 minutes consecutively. Metal tweezers tips were heated at the same temperature as the hot plate before removing the treated substrate from the hot plate, since the GGG substrates appeared to be very sensitive to sudden temperature changes. This process was repeated 5 to 10 times. USD was used for deposition as well (similar to Chapter 5). The deposition temperature was set to 200°C. The precursor with a total metal concentration of 10 mM was dispensed at 0.2 ml·min^{-1} and the N_2 carrier gas pressure was set at 1.5 psi. The spray nozzle was located 2.6 cm above the substrate and moved with a speed of 100 mm·s^{-1}. The spray cycle was repeated 5 times with a waiting time of 5 seconds. After deposition, the consecutive heating similar to the one used for spin-coating was applied. This process was repeated 2 times (10 spray cycles in total).

After deposition, the films were annealed in two different ways; for low heating rates the samples were heated in a tube furnace for 4 hours at 800°C in oxygen (0.5 ml·min^{-1}) with a heating rate of 10°C·min^{-1}. For high heating rates a rapid thermal processing unit was used (Annealsys, AS-one). The Si_3N_4 were heated to 800°C in oxygen (1 ml·min^{-1}) for 30 minutes with heating rates of 50 and 100°C·s^{-1}.

2.3 Characterization

The thermal decomposition profile of the dried Li-La-Zr-precursors and separate Li-, La- and Zr-precursor gels, obtained by drying the precursor solution at 60°C, were investigated by TGA (TA instruments Q500). 2 mg of the gel was heated at 10°C·min^{-1} using dry air (0.1 L·min^{-1}) in a platinum crucible.

As-deposited and sequentially heated (200, 300, 600 and 800°C) films were characterized by GATR-FTIR similar to the description in Chapter 4. In addition, FTIR measurements with the same apparatus and settings as the GATR-FTIR measurements were done on the combined and separate dried precursor gels dispersed (1 wt.%) in KBr pellets.

Phase formation of annealed LLZO powders was investigated by XRD, using a Siemens D-5000 diffractometer with a step size of 0.040° and a counting time of 3 seconds per step at room temperature. Crystallization of the LLZO films deposited on Si_3N_4 and GGG substrates was investigated by XRD (similar to Chapter 4). Crystallization of non-annealed LLZO films on Si_3N_4 coated substrates, was studied by isXRD[10] (similar to Chapter 4). The morphology of annealed LLZO films was investigated with SEM (FEI Quanta 200F).

3. Results and discussion

3.1 Gel and powder analysis

With FTIR, ligand coordination was analysed in view of the decomposition behaviour discussed in a later stage (Figure 2). In view of the decomposition analysis of the gel deposition on substrates, a deeper understanding of the citrate complexes present is vital.

The citrate Li-, La-, and Zr-precursors and the combined all-citrate Li-La-Zr-precursor were studied. The difference between the asymmetric and symmetric stretching frequency of carboxyl groups of the complexed metal ions indicates the nature of the citrate chelation.[11]

In addition to the asymmetric stretch at 1415 cm^{-1}, the Li-precursor shows a broad symmetric stretch (1580 cm^{-1}) with a shoulder at 1685 cm^{-1}. Combined with the fact that the Li to citrate molar ratio amounts to 3:1, it seems that the precursor consists of a mixture of bidentate (Δ <160 cm^{-1}) and unidentate (Δ >200 cm^{-1}) Li-carboxyl interactions. For the Zr-precursor, a more pronounced unidentate character is found, since Δ >200 cm^{-1}. The La-precursor exhibits a bridging La-carboxyl interaction, as difference

between symmetric and asymmetric stretching exhibits approximately 180 cm^{-1}. However, this precursor shows a shoulder around 1720 cm^{-1}, implying that non-complexed citrate is also present in the precursor in the form of ammonium citrate or citric acid, caused by the excess of CA used to dissolve the La_2O_3. Finally, the all-citrate Li-La-Zr-precursor primarily shows blended interactions. As was the case with the La-precursor, non-complexed citrate is present here as well (i.e. ammonium citrate).

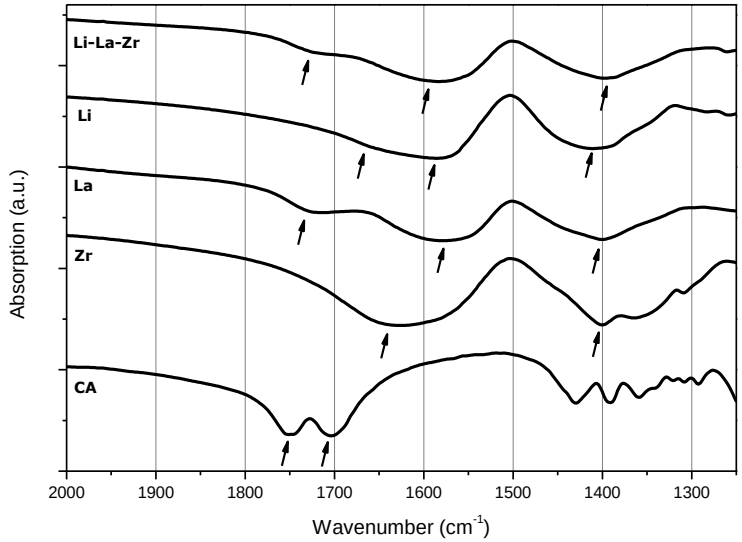

Figure 2: FTIR spectra of aqueous Li-, La-, and Zr-precursor, as well as the combined Li-La-Zr precursor and CA. The gels were prepared by overnight drying the liquid precursor at 60°C and dispersing the dried precursor in a KBr pellet.

3.2 Precursor decomposition and phase formation

The thermal decomposition of the dried precursor powder is shown in Figure 3. During this discussion, it is assumed decomposition reactions of the separate metals occur separately because the precursor is fully citrate-based. By contrast, the decomposition of the citrate-nitrate Li-La-Ti-precursor presented in Chapter 4 clearly indicates the coupled effect for the mixed citrate-nitrate precursor.

Hence, the analysis of the Li, La and Zr-precursors yields insights in the decomposition behaviour of the aqueous Li-La-Zr-precursor.

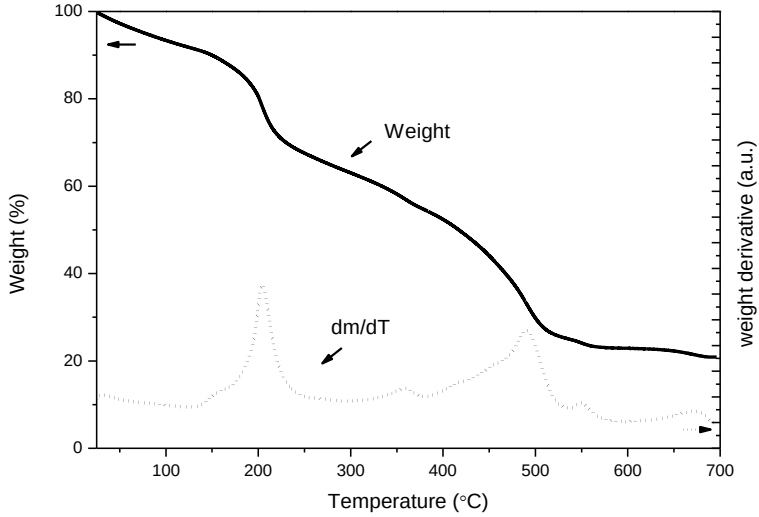

Figure 3: TGA-analysis of the Li-La-Zr-precursor dried at 60°C, recorded at 10°C·min^{-1} in dry air (0.1 ml·min^{-1}).

The first small weight loss up to 150°C is assigned to loss of water upon further drying of the gel. Hereafter, the profile shows several separate weight loss steps due to the presence of several different ammonium citrate and metal citrates (Li-, La- and Zr, Figure 4).[12] The FTIR analysis of dried gels (Figure 2) indicated that an excess of CA is present in the Li-La-Zr-precursor, which is converted to ammonium citrate. Events related to ammonium citrate decomposition can therefore be distinguished in profile shown in Figure 3. The derivative maxima at 150 and 200°C are ascribed to melting and decarboxylation reactions of the ammonium citrate, respectively.[12] Since the Li- and Zr-precursors hardly contain ammonium citrate, related to the initial 3:1 Li:CA and 5:6 Zr:CA ratios, no strong decomposition is found at low temperatures. The decomposition of the Li-La-Zr-precursor starts at higher temperatures,

showing strong weight losses at 360 and 430°C, both related to decomposition of Li- and Zr-precursor products.

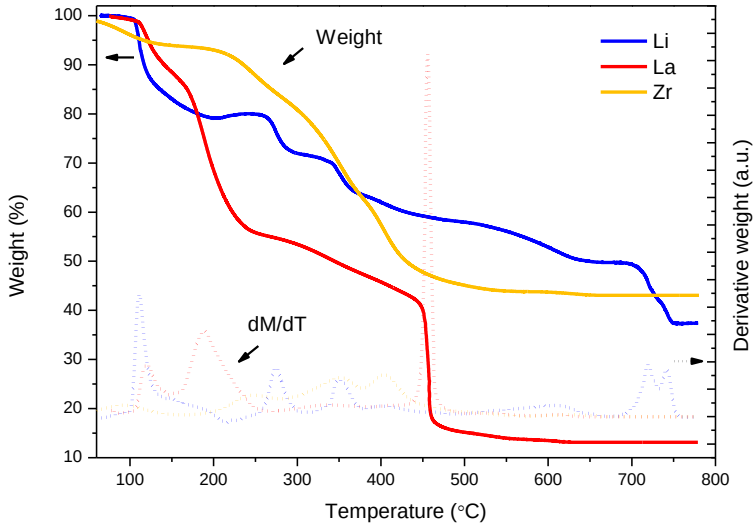

Figure 4: TGA-analysis of the separate citrate-based Li-, La- and Zr-precursors dried at 60°C, recorded at 10°C·min^{-1} in dry air (0.1 ml·min^{-1}).

The La-precursor mainly contributes to the weight loss around 500°C, whereas the minor loss at 545°C is related to the decomposition of products related to the Li-precursor. Similar to the decomposition to the all-citrate LLT precursor in Chapter 5, the last decomposition step (680°C) is clearly caused by decomposition of Li-precursor products as well since the La- and Zr-precursor show no weight loss in this temperature range. This probably involves the decomposition of lithium carbonate (Li_2CO_3), known to decompose only above 650°C.[13] Therefore, the TGA analysis indicates that at least 700°C is required to fully decompose the Li-La-Zr-precursor, besides the fact that the same temperature range is required for crystallization of the desired LLZO phase.[2]

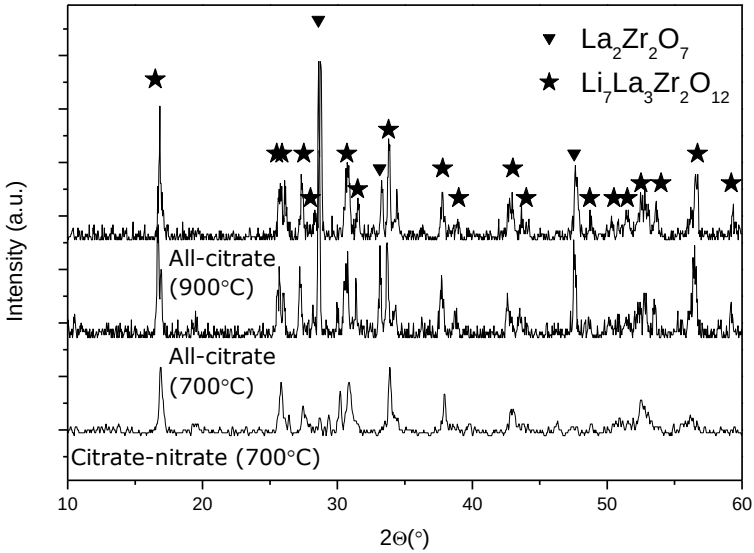

Figure 5: X-ray diffractograms of the all-citrate and citrate-nitrate aqueous Li-La-Zr-precursor gels, annealed at indicated temperatures for 4 hours in oxygen. Pyrochlore $La_2Zr_2O_7$ (JCPDS 01-073-0444) and cubic $Li_7La_3Zr_2O_{12}$[2] phases are indicated.

An important question is how the decomposition and crystallization are related, since lithium may be available for oxide formation at higher temperatures than lanthanum and zirconium, and M-O-M bonds can only be formed upon complete removal of M-O-C bonds present in the Li_2CO_3. To analyse if the crystallization occurs only after decomposition of the Li_2CO_3 phase, XRD was done on the dried precursor gels (Figure 5). This shows that an anneal at 700°C for 4 hours in oxygen yields the desired garnet phase. However, a secondary phase was identified; the pyrochlore $La_2Zr_2O_7$. As completion of the decomposition of Li_2CO_3 or solid-state reactions with the La- and Zr-oxide phases may require a higher thermal budget, the annealing temperature was increased. However, a treatment at 900°C – well above the decomposition temperature of Li_2CO_3 - still yields the same secondary phases. In comparison with synthesis of LLZO powders shown in Figure 5, as well as reports in literature,[2]

phase formation should be possible approximatly 200°C lower. This suggests that further increasing the temperature would not yield the LLZO garnet phase.

Similar to the all-citrate precursor, the citrate-nitrate precursor yields the desired LLZO phase for powders. A close analysis of the XRD pattern (Figure 5, bottom) reveals that hardly any $La_2Zr_2O_7$, if any, is present in this sample. Based on the occurrence of stable high temperature carbonate formation observed for the all-citrate precursor, it is thought that the citrate-nitrate interaction may suppress the formation of these phases. However, initial TGA analysis (not shown) does not exclude Li_2CO_3 formation in the citrate-nitrate precursor, indicating a more fundamental study of this precursor systems is required. However, this goes beyond the scope of this chapter.

3.3 Decomposition and crystallization of films

Based on the XRD on powders, the citrate-nitrate precursor may seem to be the better choice because the formation of the $La_2Zr_2O_7$ phase seems to be suppressed. However, spin-coated films on Si_3N_4 yielded very rough morphologies, possibly due to a violent citrate-nitrate decomposition reactions and / or poor wettability of the substrates. In addition, no phase formation was achieved on Si_3N_4 films (not shown). Due to these issues, the latter precursor was studied more thoroughly in the following.

Since the TGA analysis (Figure 3) indicated that stable high temperature phases are formed, GATR-FTIR measurements as function of heating temperature were done to track all-citrate Li-La-Zr-precursor film decomposition. This should yield information whether (bonded) organic residuals are still present on the film (Figure 6). The decomposition of the metal citrate complexes is followed by tracking the decrease of the symmetric and asymmetric vibration signals of the carboxyl-groups, as seen before in Figure 2. Although the signal is weak due to poor contact (rough surface of partly decomposed, spray-deposited films), a clear trend can be seen. The chelating citrates are clearly removed between 300 and 600°C. A small absorption can still be observed at 600°C, which

corresponds to the Li_2CO_3 formation as discussed during the TGA analysis. Recall that the complexation of this complex was partly defined as bidentate, yielding a smaller difference (Δ) between the symmetric and asymmetric stretch of the carboxyl groups. The shift of the asymmetric vibration at 600°C (i.e. Δ decreases compared to the 300°C case) further supports the hypothesis that only one of the metals is chelated by carbonate groups: Li_2CO_3.

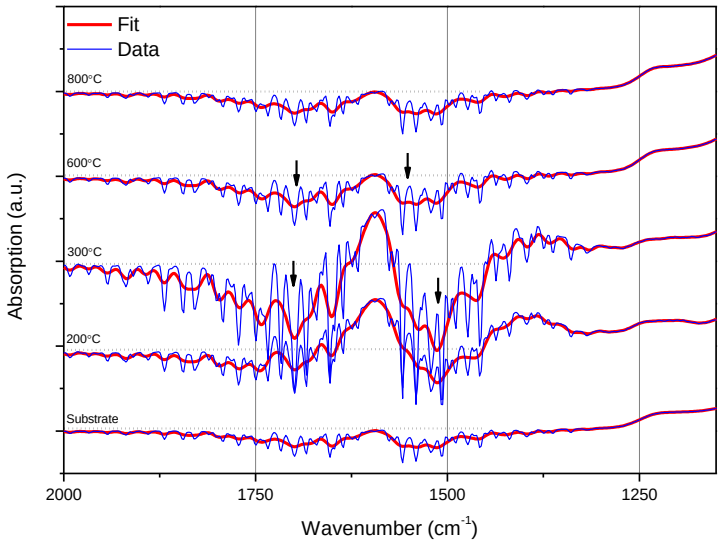

Figure 6: GATR-FTIR spectra of uncoated and Li-La-Zr-coated substrates with various indicated annealing temperatures. The fit was made based on the noisy data as a guide to the eye. The precursor was deposited on Si_3N_4 coated Si substrates with ultrasonic spray deposition of 10 cycles at 200°C.

At 800°C complete decomposition of the precursor is established since this spectrum equals the background levels between the wavenumbers measured.

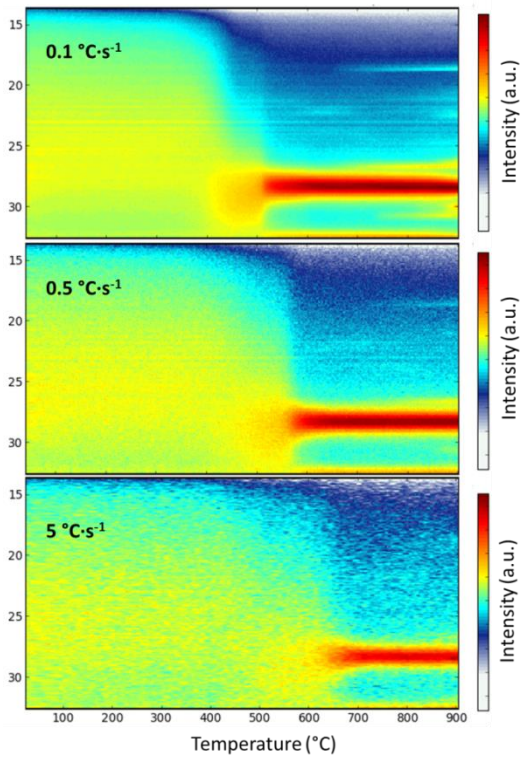

Figure 7: isXRD results showing Li-La-Zr-precursor films deposited with ultrasonic spray deposition at 200°C, heated at different heating rates (indicated). The measurements were done in static air.

Figure 7 shows the results regarding isXRD with a relatively low heating rate of 0.1°C·s^{-1}. As can been seen, no garnet phase was obtained. Instead, only the pyrochlore phase of $La_2Zr_2O_7$ was obtained as indicated by the 28° peak. As Figure 5 and several literature references indicate,[2,3,14–19] this phase is often encountered as an undesirable secondary phase during LLZO synthesis.

While comparing the XRD data with the GATR-FTIR as discussed previously, it seems no coincidence that a lithium-free phase

($La_2Zr_2O_7$) occurs before complete decomposition of Li_2CO_3. Assuming that the carbonate needs to decompose before lithium can crystallize in a (garnet) oxide crystal, it is thought that the garnet phase cannot be formed on films at 600°C because of the presence of Li_2CO_3. Since decomposition of Li_2CO_3 at 500°C is highly unlikely based on the TGA analysis of gels (Figure 3), it seems that La and Zr - which appear to be decomposed at lower temperatures - start oxide formation ($La_2Zr_2O_7$) before Li_2CO_3 starts to become reactive. For LLZO powders, this was confirmed before by Kokal et al.[2] Therefore, if Li_2CO_3 is involved, the garnet phase can only be formed upon a solid state reaction between (decomposing) Li_2CO_3 and $La_2Zr_2O_7$.

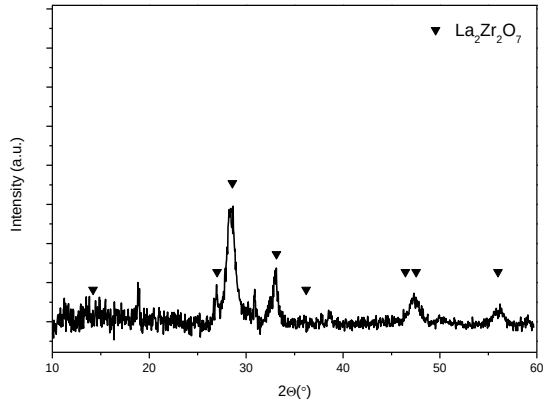

Figure 8: XRD pattern the all-citrate Li-La-Zr-precursor deposited on Si_3N_4 coated Si by ultrasonic spray deposition, annealed at 800°C for 4 hours in oxygen. The pyrochlore $La_2Zr_2O_7$ (JCPDS 01-073-0444) phase is indicated.

For powders this seems to occur after prolonged heating at 700°C, but on films this does not occur (Figure 7 and 8).

To investigate kinetic effects on crystallization of the films deposited, annealing was done at higher heating rates as well. At high heating rates, where kinetic factors may reduce the temperature

difference at which the $La_2Zr_2O_7$ crystallization and Li_2CO_3 decomposition occur; the garnet LLZO phase may be obtained. Note that this is based on the assumption that decomposition of Li_2CO_3 is kinetically favoured over $La_2Zr_2O_7$ crystallization. While shifting from 0.1 to 5°C/s, the temperature at which the $La_2Zr_2O_7$ phase formation starts indeed shifts to higher values (Figure 7). However, even very high heating rates (up to 100°C·s^{-1} with RTP) yielded the undesired $La_2Zr_2O_7$ phase (not shown). Thus, higher heating rates increase the temperature at which onset of $La_2Zr_2O_7$ crystallization is observed, but it does not prevent this phase to be formed. Even for extreme high heating rates, no garnet phase is obtained. This means Li_2CO_3 decomposition shifts as well, or that the temperature shift of $La_2Zr_2O_7$ crystallization is not large enough at 100°C·s^{-1}.

In literature, a number of other suggestions are found for the occurrence of the $La_2Zr_2O_7$ phase; (i) lithium deficiency caused by lithium loss during annealing [2,14] and (ii) the presence of air during annealing.[15]

(i) Lithium deficiency can be caused by several factors, such as Li_2O evaporation starting from 750°C.[20] It must be noted that the annealing temperatures chosen in this study (below 1000°C) yield very low evaporation rates.[20] In addition, similar to several studies reporting Li-stuffed garnets, [15,21–28] a small excess of lithium was used (10%) to compensate for this effect. However, lithium can also be lost due to reactions with the substrate. To prevent this from occurring, Si_3N_4 coated substrates were used due to the lithium barrier properties of this material.[29–31]

(ii) Unfortunately, the presence of air could not be circumvented because of the need for an oxidative environment to decompose the organic residues. Since garnet powders could be formed at 700°C (Figure 5), the air anneal does not seem to be the only cause of the $La_2Zr_2O_7$ formation.

Although no literature references were found explicitly discussing the influence of substrates on garnet phase crystallization, it ap-

pears that all successful thin film depositions of crystalline lithium-stuffed garnets are based on lattice matching (c.f. Chapter 3).[14,28,32,33] This suggests that this may be an important factor of influence specifically for thin-film garnets.

The concept of epitaxial stabilization is based on thermodynamic factors leading to growth of (meta)stable phases. Due to lattice matching of the desired phase with the substrate underneath, the free energy difference between the materials involved is reduced.[34] Therefore, a similar approach was used during this study (Figure 9). In contrast to the results shown on Si_3N_4, the use of GGG substrates yields the desired garnet phase of LLZO. Besides the huge substrate peaks, sharp peaks of the (004) and (008) LLZO phase could be observed on the (100) GGG substrate orientation, as well as the (444) LLZO peak on the (111) GGG substrate orientation. This indicates that the LLZO phase is present in epitaxial form, since only a few orientations can be observed, depending on substrate lattice orientation. Because alignment issues, isXRD was not possible for these substrates, but it is assumed that initially the same processes occur with respect phase formation on Si_3N_4. On GGG, probably the $La_2Zr_2O_7$ phase is formed initially as well. As soon as the Li_2CO_3 is decomposed it starts reacting with $La_2Zr_2O_7$. Because of epitaxial stabilization, the garnet $Li_7La_3Zr_2O_{12}$ phase is favoured over the $La_2Zr_2O_7$ phase (at least in comparison with the Si_3N_4 substrate case). Therefore, the garnet phase is formed on GGG substrates, but not on the Si_3N_4 films that lack epitaxial stabilization.

Notably, epitaxial LLZO on GGG was initially achieved by spin-coating (not shown). Since the layer thickness of these films was unmeasurable and achieving high thicknesses was not feasible because of the low precursor concentration, ultrasonic spray depositions were applied as well. The films obtained were rough with thickness variations, but LLZO shows good coverage on the GGG substrate. Because of charging effects, no larger magnification could be achieved during SEM measurements of these samples, leading to rough estimations of the film thickness between 30 and 70 nm.

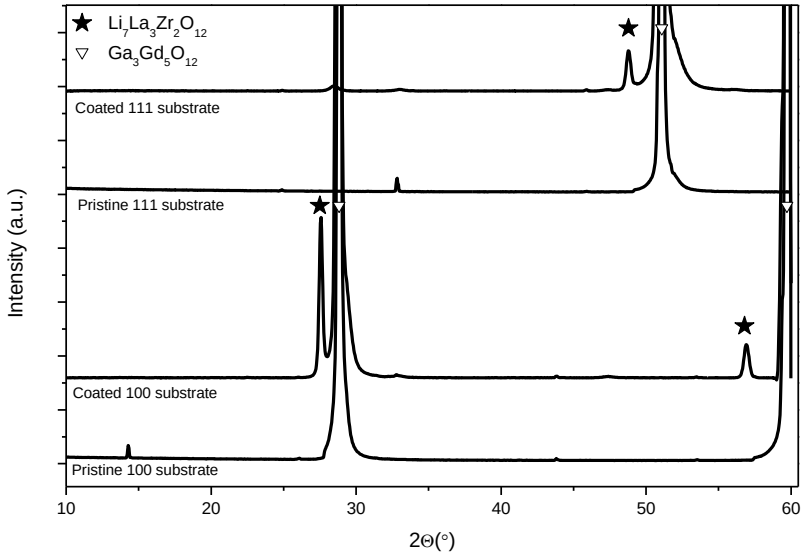

Figure 9: X-ray diffractograms of the all-citrate Li-La-Zr-precursor deposited on single crystalline GGG substrates with 100 and 111 orientation, annealed at 800°C for 4 hours in oxygen. Garnet GGG (JCPDS 1-71-701) and garnet LLZO[2] phases are indicated.

3.4 Functional properties

Now that the right crystal phase was achieved for deposited films, attempts were made to measure the Li-ion conductivity. In contrast to the measurements done on LLT films (Chapter 4), these measurements needed to be done in-plane because of the lack of a bottom current collector (c.f. Chapter 2). Unfortunately, only capacitive effects were measured. This indicates that either the material does not show (sufficient) conductivity, the surface was too rough or that the wrong length scale (1 mm) for the distance between Au electrodes were used. Follow-up measurements are required to further clarify this, possibly using a top current collector with interdigitated structures exhibiting much smaller length scales (instead 1 mm^2 squares used for this study) to exclude the latter effect.

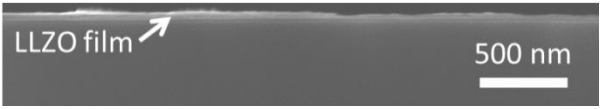

Figure 10: SEM (BSE) micrograph of LLZO film (30 to 60 nm thick) on a monocrystalline GGG substrate in the 111 orientation, as a results of 10 spray deposition cycles with the all-citrate Li-La-Zr-precursor (10 mM), with a deposition temperature of 200°C. The sample was submitted to a post-deposition anneal at 800°C for 4 hour in oxygen.

3.5 Li-La-Zr-precursor 3D deposition

Despite lack of a demonstration of the functional properties, and the fact that monocrystalline 3D GGG substrates were not available, 3D depositions were attempted for the all-citrate Li-La-Zr-precursor (Figure 11). The Si micro-cylinders were used only to study the morphology of the deposited films. Needless to say, Li-loss, (La) silicate formation and lack of epitaxial stabilisation imply that the LLZO phase was not expected to be formed on these substrates. Therefore, no attempts were made to optimize this process. However, preliminary results show a coating on the Si micro-cylinders, but the bottom part is not coated sufficiently.

Based on other results presented in this thesis (c.f. Chapters 5, 9 and 11), one could carefully suggest that further optimization of this process would enable 3D coatings on these structures with the all-citrate Li-La-Zr-precursor. From a practical point of view this would be of little significance if the boundary conditions of epitaxial stabilization are not met.

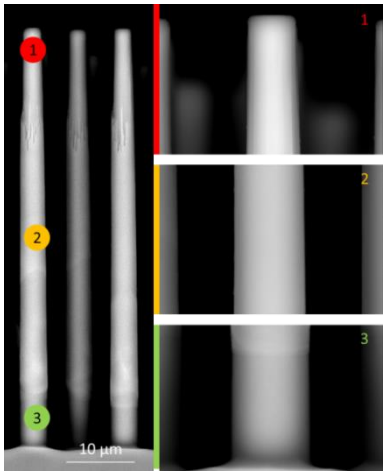

Figure 11: SEM micrograph of LLZO film on 3D Si (2x5), as a results of 50 spray deposition cycles with the all-citrate Li-La-Zr-precursor mixed with ethanol (10:9 ratio, 10 mM), with a deposition temperature of 200°C. The sample was submitted to a post-deposition anneal at 600°C for 1 hour in static air. Artefacts on top of the micro-cylinders are a result of the fabrication process.

4. Conclusion

The current study indicates that crystalline $Li_7La_3Zr_2O_{12}$ has a long way to go if it ever will be implemented as a solid electrolyte for thin-film 3D Li-ion batteries. First of all the required annealing temperature to decompose the all-citrate-precursor is rather high due to the formation of lithium carbonate. This seriously hinders integration. LLZO phase formation was not established on films without epitaxial stabilization. It is stressed though, that the effect is not related to the deposition approach of this study. Various vacuum deposited LLZO films also required epitaxial stabilization to form the garnet phase.[14,28,32,33] In the end, epitaxial stabilization did enable the synthesis of garnet $Li_7La_3Zr_2O_{12}$ films, but the practical significance is questioned. At best, an easily crystallisable buffer layer with the right lattice parameters has to be formed on

top of a positive or negative electrode material to enable successful crystallization of LLZO on top of an electrode, e.g magnesium oxide.[33] Hence, the current approach is not suitable for synthesis of 3D thin film all-solid-state Li-ion batteries. Deposition of pre-crystallized LLZO powders,[35] or simply ignoring crystallization issues and form a hybrid amorphous-crystalline ($La_2Zr_2O_7$) solid electrolyte,[36] seem to be more promising solutions. The latter approach may be of interest in combination with the aqueous precursor discussed in this chapter.

5. References

[1] I. Kokal, E. J. van den Ham, a. C. a. Delsing, P. H. L. Notten, H. T. Hintzen, *Ceram. Int.* **2015**, *41*, 737.

[2] I. Kokal, K. V. Ramanujachary, P. H. L. Notten, H. T. Hintzen, *Mater. Res. Bull.* **2012**, *47*, 1932.

[3] R. Murugan, V. Thangadurai, W. Weppner, *Angew. Chem. Int. Ed. Engl.* **2007**, *46*, 7778.

[4] M. Nb, V. Thangadurai, H. Kaack, W. J. F. Weppner, *J. Am. Ceram. Soc.* **2003**, *86*, 437.

[5] S. Gielis, A. Hardy, M. K. Van Bael, *Conformal Coating on Three-Dimenstional Substrates*, **2015**, EP 2 947 178 A1.

[6] K. Van Werde, G. Vanhoyland, D. Mondelaers, H. Den Rul, M. K. Van Bael, J. Mullens, L. C. Van Poucke, *J. Mater. Sci.* **2006**, *42*, 624.

[7] S. Gielis, M. Ivanov, N. Peys, E. J. van den Ham, N. Pavlovic, J. Banys, A. Hardy, M. K. Van Bael, *J. Eur. Ceram. Soc.* **2016**, *http://dx.*, DOI 10.1016/j.jeurceramsoc.2016.08.042.

[8] D. Dewulf, N. Peys, S. Van Elshocht, G. Rampelberg, C. Detavernier, S. De Gendt, a. Hardy, M. K. Van Bael, *Microelectron. Eng.* **2011**, *88*, 1338.

[9] R. N. Singh, *J. a* **1975**, *59*, 112.

[10] W. Knaepen, C. Detavernier, R. L. Van Meirhaeghe, J. Jordan Sweet, C. Lavoie, *Thin Solid Films* **2008**, *516*, 4946.

[11] K. Nakamoto, *Infrared & Raman Spectroscopy of Inorganic and Coordination Compounds, Part B.: Applications in Coordination, Organometallic and Bioinorganic Chemistry*, Wiley, New York, **1997**.

[12] M. Rajendran, M. Subba Rao, *J. Solid State Chem.* **1994**, *113*, 239.

[13] V. Berbenni, A. Marini, *J. Anal. Appl. Pyrolysis* **2002**, *64*, 43.
[14] K. Tadanaga, H. Egawa, A. Hayashi, M. Tatsumisago, J. Mosa, M. Aparicio, A. Duran, *J. Power Sources* **2015**, *273*, 844.
[15] G. Larraz, a. Orera, M. L. Sanjuán, *J. Mater. Chem. A* **2013**, *1*, 11419.
[16] X. Tong, V. Thangadurai, E. D. Wachsman, **2015**, DOI 10.1021/acs.inorgchem.5b00184.
[17] V. Thangadurai, S. Narayanan, D. Pinzaru, *Chem. Soc. Rev.* **2014**, *43*, 4714.
[18] K. H. Kim, Y. Iriyama, K. Yamamoto, S. Kumazaki, T. Asaka, K. Tanabe, C. a. J. Fisher, T. Hirayama, R. Murugan, Z. Ogumi, *J. Power Sources* **2011**, *196*, 764.
[19] J. Sakamoto, E. Rangasamy, H. Kim, Y. Kim, J. Wolfenstine, *Nanotechnology* **2013**, *24*, 424005.
[20] T. Chartier, L. Lostec, C. Gault, C. Chatillon, *J. Sol-Gel Sci. Technol.* **2002**, *23*, 27.
[21] G. T. Hitz, E. D. Wachsman, V. Thangadurai, *J. Electrochem. Soc.* **2013**, *160*, A1248.
[22] A. Gupta, R. Murugan, M. P. Paranthaman, Z. Bi, C. a. Bridges, M. Nakanishi, A. P. Sokolov, K. S. Han, E. W. Hagaman, H. Xie, C. B. Mullins, J. B. Goodenough, *J. Power Sources* **2012**, *209*, 184.
[23] J. S. Park, L. Cheng, V. Zorba, A. Mehta, J. Cabana, G. Chen, M. M. Doeff, T. J. Richardson, J. H. Park, J.-W. Son, W.-S. Hong, *Thin Solid Films* **2015**, *576*, 55.
[24] F. Gam, C. Galven, A. Bulou, **2014**, 10.
[25] S. Lobe, C. Dellen, M. Finsterbusch, H.-G. Gehrke, D. Sebold, C.-L. Tsai, S. Uhlenbruck, O. Guillon, *J. Power Sources* **2016**, *307*, 684.
[26] V. Thangadurai, W. Weppner, *J. Am. Ceram. Soc.* **2005**, *88*, 411.
[27] H. Xie, J. A. Alonso, Y. Li, M. T. Fern, J. B. Goodenough, **2011**, 3587.
[28] J. Tan, a. Tiwari, *ECS Solid State Lett.* **2012**, *1*, Q57.
[29] J. Ubrig, S. Martin, S. Cros, J.-E. Bouree, *J. Phys. Conf. Ser.* **2008**, *100*, 082030.
[30] R. Sousa, J. F. Ribeiro, J. A. Sousa, R. T. Montenegro, L. M. Goncalves, J. H. Correia, *Proc. MME 2013* **2013**, *1*, 2.
[31] E. M. F. Vieira, J. F. Ribeiro, R. Sousa, M. M. Silva, L. Dupont, L. M. Gonçalves, *J. Electron. Mater.* **2015**, *45*, 910.
[32] S. Kim, M. Hirayama, S. Taminato, R. Kanno, *Dalton Trans.* **2013**, *42*, 13112.

[33] J. Reinacher, S. Berendts, J. Janek, *Solid State Ionics* **2014**, *258*, 1.
[34] O. Y. Gorbenko, S. V. Samoilenkov, I. E. Graboy, a. R. Kaul, *Chem. Mater.* **2002**, *14*, 4026.
[35] C.-W. Ahn, J.-J. Choi, J. Ryu, B.-D. Hahn, J.-W. Kim, W.-H. Yoon, J.-H. Choi, D.-S. Park, *J. Electrochem. Soc.* **2014**, *162*, A60.
[36] R.-J. Chen, M. Huang, W.-Z. Huang, Y. Shen, Y.-H. Lin, C.-W. Nan, *J. Mater. Chem. A* **2014**, *2*, 13277.

Part III - Chapter 7

WO_3 films as a possible negative electrode for all-solid-state Li-ion batteries

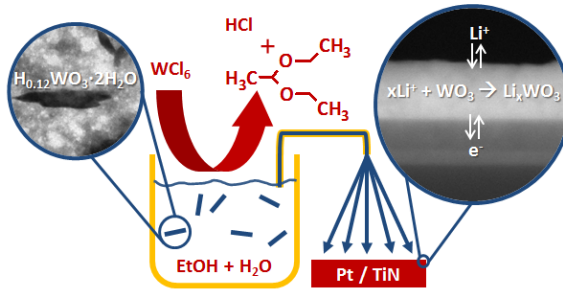

A large part of this chapter has been published:

E.J. van den Ham, K. Elen, I. Kokal, B. Yağci, N. Peys, G. Bonneux, F. Ulu, W. Marchal, M.K. Van Bael and A. Hardy - *"From liquid to thin film: colloidal suspensions for tungsten oxide as an electrode material for Li-ion batteries"* – RSC Advances 6 (2016) 51474-51756

Abstract

Using a colloidal suspension, tungsten oxide thin films (150 nm) have been prepared via USD using two different current collectors, namely TiN and Pt. First, the precursor chemistry was studied, revealing that the tungsten present is reduced due to the formation of chlorine gas. Due to a dehydrogenation 1,1-diethoxyethane and hydrogen chloride evolve from the precursor, reducing the amount of chloride in the precursor. The thin films were annealed at 400 and 500°C, yielding tetragonal tungsten oxide without the presence of chlorides. Electrochemical analysis indicated that the TiN current collector has a pronounced positive effect on cycling behaviour of the WO_3 thin film. A higher annealing temperature yields an improved performance, but annealing at temperatures as low as 400°C also yielded electrochemical active WO_3. The current study presents a versatile method to produce electrochemically active tungsten oxide thin films with a high volumetric capacity (640 $mAh \cdot cm^{-3}$) at relatively low temperature to be applied in thin film all-solid-state Li-ion batteries.

1. Introduction

As discussed in Chapter 1, the current generation of Li-ion batteries with liquid electrolytes suffers from several issues, including safety hazards and capacity fading.[1–3] One of the known approaches is the concept of thin film all-solid-state Li-ion batteries, limiting the thickness of both the electrolyte and electrodes to prevent high resistances.[2,4] In this way, the big advantages of solid electrolytes can be utilized, namely increased lifetime, improved safety and a broader operating temperature window.[1,2,5]

Various thin film electrode materials, such as LTO[6,7] LMO[6] and WO_3,[8] have been investigated. Traditionally, WO_3 is a material known for its catalytic capabilities.[9,10] Besides lithium,[8,11–13] other alkali ions can be inserted into its crystal structure.[13] This property makes WO_3 the basis of smart windows, based on its electrochromic properties.[13–19] Although various reports indicate the superiority of LTO as an oxide based negative electrode according to its higher energy density, the WO_3 outclasses the LTO according to its volumetric capacity (604 vs. 228 $mAh \cdot cm^{-3}$).[20–22] The volumetric capacity is more applicable for thin film all-solid-state Li-ion batteries since the total battery consists of scaffolding material, current collectors and electrolyte. In other words, the weight of active materials is a relatively small contribution to the total weight all-solid-state battery.

In addition, the relatively high (de)intercalation voltage between 1.5 - 3 V (vs. Li^+/Li)[8,11,13] proves to be very useful when combining WO_3 with a solid electrolyte. However, one of the main challenges of the thin film all-solid-state Li-ion batteries is the incorporation of a solid electrolyte.[22,23] Besides LiPON,[24,25] Li-ion conducting silicates and a few garnets;[26–30] thin film solid electrolytes have a limited electrochemical stability at low voltages (c.f. Chapter 3).[1,31] Thus the high voltage WO_3 negative electrode opens up a broader range of applicable solid electrolyte materials such as perovskite LLT[32–35] (c.f. Chapter 4) and LTP.[36,37] These considerations are summarized in Figure 1.

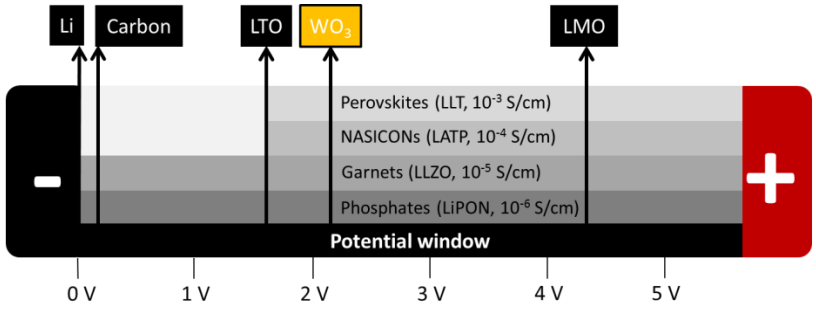

Figure 1: Schematic representation of the electrochemical window and (de)lithiation voltages of various electrode and solid electrolyte materials. The figure indicates that WO_3 is compatible with various solid electrolyte materials.

Finally, TiN is opted as an alternative for the rare and expensive Pt current collector since it combines good electronic conductivity with Li-ion blocking properties.[25,38] Unfortunately, TiN tends to oxidize under oxidative high temperature annealing conditions (Chapter 5).[39] Here, the potentially low annealing temperature needed for the realization of crystalline WO_3 (at 300°C)[15,40] prevents TiN oxidation and enables its use as a current collector.

In summary, WO_3 is a promising negative electrode worth studying in detail. The study presented in this Chapter employs wet-chemical synthesis routes [15,17,19,41] for reasons explained in Chapters 1 and 2, to study WO_3 as a potential negative electrode material for all-solid-state Li-ion batteries.

2. Experimental

2.1 Synthesis of the chlorine-based tungsten precursor

Tungsten Chloride (WCl_6, Sigma Aldrich, 99.9%) was dissolved in ethanol (ethanol absolute, VWR) by stirring for 20 minutes, yielding a transparent yellow liquid. Next, water was added until a 1:1

water to ethanol volumetric ratio was obtained similar to Regragui et al.,[15] resulting in a transparent dark blue liquid. The final tungsten concentration in the water/ethanol solution amounted 10 mM. The precursor synthesis is summarized in Figure 2.

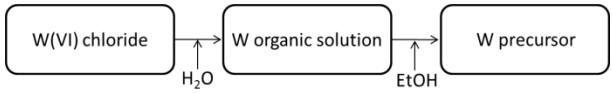

Figure 2: Synthesis scheme of the Cl-based W-precursor.

2.2 Deposition on substrates

TiN and Pt substrates were used in this study. Both substrate types were treated by UV/O_3 (60°C, 30 min., Novascan PSD Pro Series) prior to the deposition. The precursor solution was deposited onto the substrates via USD (Exacta Coat, Sono-Tek cooperation) using the Accumist nozzle (Sono-Tek cooperation). The deposition temperatures were set at 150, 200 and 250°C. The precursor was dispensed at 0.5 ml·min^{-1} and the N_2 carrier gas pressure was set at 1.5 psi. The spray nozzle was located 6.9 cm above the substrate and moved with a speed of 100 mm·s^{-1}. The spray cycle was repeated 10 times with a waiting time of 5 seconds between each deposition. Next, a sequential heat treatment, in static air, was carried out at 300°C (2 min.) and at 400 or 500°C (1 hour). Both WO_3/TiN and WO_3/Pt samples received the same thermal treatments and were all stored in an Ar-filled glovebox after the post-deposition anneal.

2.3 Characterization - Liquid phase

Ultraviolet–visible spectroscopy was performed on precursor solutions with 1 mm of tungsten by a Amersham Biosciences Ultrospec 100 pro tool. A Tyndall experiment was done with the tungsten precursor (1 mm) using a 35 mW diode laser (NanoBrook 90Plus). GCMS was performed on the headspace of the preheated (10 min, 70°C) precursor solution via a Thermo Scientific Trace 1310 GC using a DB5-MS capillary (length 30 m, diameter 0.25 mm and

filter size 0.25 µm); coupled with a Thermo Scientific ISQ LT MS, scanning between 33 and 350 u every 0.2 seconds.

2.4 Characterization - Powders

The thermal decomposition profile of the precursor powder, obtained by drying of the precursor solution at 60°C, was investigated by TGA-MS (TA instruments Q5000 with Pfeiffer quadrupool MS). 6 mg of the powder was heated in a Pt sample pan, ramped at 10°C·min-1 from room temperature to 500°C in dry air (25 $mL \cdot min^{-1}$) and a N_2 balance gas (10 $mL \cdot min^{-1}$).

The crystallization process of the precursor powder was similar to the HT-XRD experiment mentioned in chapter 4. TEM was done on a FEI Technai G2 Spirit Twin, operated at 120 kV. For this purpose, the precursor solution was sonicated for 2 minutes, small drops were casted onto a carbon coated copper grid (EMS, FCF-200-Cu) and dried under an infrared lamp for 20 minutes.

2.5 Characterizations – Films

The morphology of annealed tungsten oxide films was investigated via SEM (FEI Quanta 200F). The thickness of the films was determined via SEM cross sections, coupled with the density of WO_3 (7.15 $g \cdot cm^{-3}$) the total amount of deposited WO_3 could be determined. The composition of the film was probed by XPS via a Thermo Scientific K-Alpha spectrometer using an Aluminum anode (Al Kα = 1468.3 eV) at an electron take-off angle of 90° (between the sample surface and the axis of the analyser lens). The depth-profiling experiment was effected by bombarding 1.000 eV Ar^+ ions for 6 levels of 60 s etching rate. The spectra were recorded using an Avantage 5.9 data system. The binding energy scale was calibrated by assigning the C1s signal at 284.5 eV. CV and galvanostatic measurements were performed with an Autolab PGSTAT128N, using a three electrode setup with a custom made Teflon cell., c.f. Chapter 2.[42] The WO_3/TiN and WO_3/Pt samples were used as the working electrode via a copper disc connected to the back of the substrate. Silver paint (Benelux scientific) was used to ensure good conductivity between the copper disc and the substrate. The top of

the substrate was accessible to the liquid electrolyte (1.0 M $LiClO_4$ dissolved in polycarbonate, Soulbrain MA) and a Kapton® O-ring was used for sealing. Metallic lithium (99,9% Sigma Aldrich) served as the counter and reference electrodes. After 3 cycles of CV at 1 mV/s between 1.5 and 4.0 V, galvanostatic measurements were done between the same cut-off voltages with a constant current of 10 µA (1C). The test cell was operated at 20.0°C via a custom made temperature control chamber, inside an Ar-filled glovebox with water an oxygen concentrations < 1 ppm. The crystallinity of the films was investigated by XRD, similar to the XRD setup mentioned in Chapter 4. Ex-situ, post-cycling XRD analysis were performed after 100 cycles for both WO_3/TiN and WO_3/Pt samples. After removal from the electrochemical cell, the samples were rinsed with ethanol to remove the organic electrolyte and immediately measured by XRD under ambient conditions.

3. Results and discussion

3.1 Precursor analysis – the liquid phase

Dissolution of tungsten chloride (WCl_6) in ethanol leads to a transparent, yellow solution, although the yellow colour decays over time. After a few days a greenish precipitation was observed. Figure 3 (red curve) shows that a significant absorption band is present in the UV-A region. The onset of this band is situated on the edge of the visible spectrum, hence the solution exhibits a yellow colour. Based on the sample composition and location of the band, it is assigned to dissolved chlorine gas (Cl_2).[40,43–46] Figure 1 shows that the absorption of this band decreases as a function of time; after 90 minutes a colourless liquid is observed. This indicates that the majority of the Cl_2 has left the precursor during the first 90 minutes after synthesis. By adding water, a dark blue, transparent liquid is observed and the UV-Vis spectrum shows a significant absorption band between 600 and 780 nm (Figure 3). This suggests the reduction of W^{6+} and / or forming WO_x agglomerates.[47]

Besides light absorption, light scattering of the precursor was observed with a simple Tyndall experiment. This implies that particles

are present in the liquid. Figure 4 shows a TEM micrograph of these particles and indicated the presence of two types of particles: large rod-like particles with 100 – 150 nm length (Figure 4a) and small circular particles of 20 nm (Figure 4b).

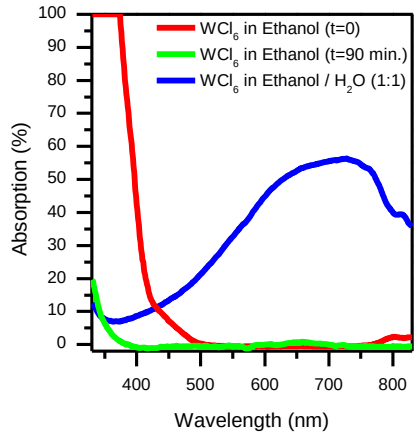

Figure 3: UV/VIS spectrum of 1 mM WCl_6 precursors in Ethanol and Ethanol / Water (1:1) solutions.

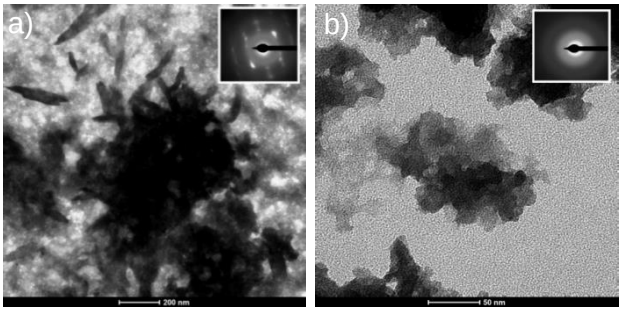

Figure 4: TEM micrograph of the tungsten precursor with deposited on a copper grid and dried before measuring. Rod-like, crystalline particles are observed (a) in an amorphous matrix with smaller particles (b). The inset shows electron diffraction (ED) of both types of particles.

Therefore, it is assumed that the blue coloration is caused by tungsten oxide agglomerates. This blue colour can directly be related to polaron transitions between W^{6+}/W^{5+} or W^{5+}/W^{4+},[48–50] or by a bipolaronic transaction based on W^{6+}/W^{4+}.[51] This supports the statement that W^{6+} is reduced in the solution. Note that the rod-like particles are crystalline, as indicated by the ED results (Figure 3a, inset).

Headspace GCMS measurements (Table 1) indicate that hydrochloric acid (HCl) evolves during the dissolution of the tungsten chloride by the presence of a large intensity peak at a retention time of 1 min. 18 s. The GC-MS results do not indicate the evolution of Cl_2 directly. However, 1,1-diethoxyethane (DEE) was observed at a retention time of 3 min. 40 s (Table 1). Assuming that (i) the Cl_2 instantaneously reacts with the ethanol matrix, forming acetaldehyde, and (ii) the acetaldehyde instantaneously reacts with the ethanol matrix forming DEE;[52,53] the occurrence of DEE is clarified. The hydrochloric acid, originating from the WCl_6 dissolution, fulfils the acidic condition known to catalyse the latter reaction at room temperature.[53,54]

Table 1: Summary of the Headspace GCMS results for WCl_6 dissolved in ethanol only, as well as the ethanol / water mixture.

Product	Retention time EtOH (trace H_2O)	Retention time EtOH:H_2O 1:1
HCl	1 min. 17 s	1 min. 18 s
DEE	3 min 40 s	3 min. 40 s

In summary, the following reaction mechanism is proposed:

(i) Chloro – alkoxide substitution shown in Equation 1:[40]

$$W^{6+}Cl_6 + x\ CH_3CH_2OH \rightleftharpoons W^{6+}Cl_{6-x}(CH_3CH_2O)_x + x\ HCl \quad \textbf{(1)}$$

with $(1 \leq x \leq 6)$

(ii) Cl_2 formation shown in Equation 2:[44]

$$2\,W^{6+}Cl_{6-x}(CH_3CH_2O)_x \rightleftharpoons 2\,W^{5+}Cl_{5-x}(CH_3CH_2O)_x + Cl_2 \quad \textbf{(2)}$$
with $(1 \leq x \leq 5)$

(iii) Dehydrogenation of ethanol shown in Equation 3:[44]

$$Cl_2 + CH_3CH_2OH \rightleftharpoons CH_3CHO + 2\,HCl \quad \textbf{(3)}$$

(iv) Reaction between acetaldehyde and ethanol to DEE shown in Equation 4:[53,54]

$$CH_3CHO + 2\,CH_3CH_2OH \rightleftharpoons CH_3CH(OCH_2CH_3)_2 + H_2O \quad \textbf{(4)}$$

3.2 Precursor analysis – towards oxide formation

The XRD of the dried precursor, without any further thermal treatment (Figure 5), already indicates the presence of the hydrogen tungsten oxide hydrate ($H_{0.12}WO_3{\cdot}2H_2O$, JCPDS 40-0693). The presence of this crystal phase supports the (partial) W^{6+} reduction hypothesis, explaining the blue colour of the colloid suspension and of the prepared precursor powder.

Since TEM-ED (Figure 4 and inset) indicates that only the rod-like particles are crystalline, this crystal phase is assigned to the rod-like particles. This crystalline phase can only be formed by (i) hydrolysis of ethoxy groups into hydroxy groups and (ii) by condensation of the formed hydroxy group with another hydroxy or ethoxy group into an oxygen bridge between two tungsten ions.[55,56]

Heating the dried precursor powder reveals a transition to monoclinic WO_3 (JCPDS 24-0747) already at 300°C in Figure 5. Though a shift of XRD peaks to lower 2θ values is expected based on thermal expansion (e.g. the (112) peak of the orthorhombic phase at 28.0°), a more pronounced shift is observed for the (222) and (400) peaks of the monoclinic phase, at 41.9 and 50.0° respectively. This indicates a phase transition from the monoclinic to orthorhombic WO_3 (JCPDS 1-71-0131). Although both phases are diffi-

cult to differentiate, this temperature-dependent phase transition was reported previously in detail.[57,58]

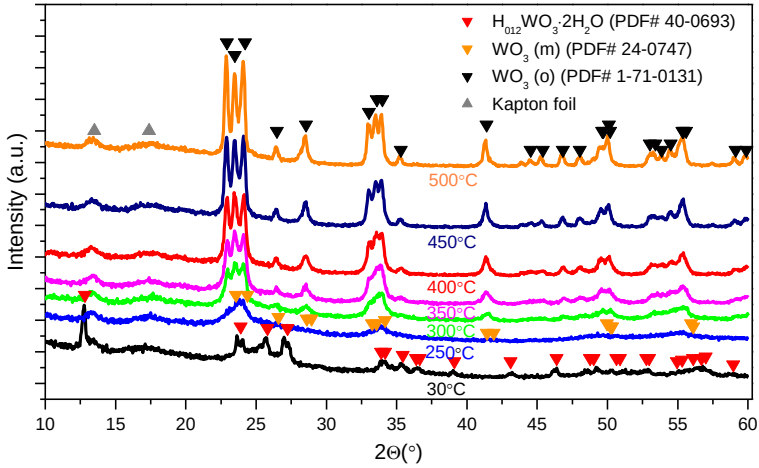

Figure 5: HT-XRD of dried precursor powder, at various temperatures (indicated) in static air.

To further study the changes occurring during heating, TGA-MS was carried out on the dried precursor (Figure 6). The MS only indicates the evolution of water: OH^+ (m/z = 17) and H_2O^+ (m/z = 18). This evolution is separated in two steps: around 65 and 225°C. Combined with the results gained from the HT-XRD (Figure 5), the first weight loss at 65°C is attributed to evaporation of residual (free) water. The second weight loss at 225°C is assigned to the release of crystal water. The last step only accounts for 6 wt. % of the total weight loss, revealing that the majority of the sample contains amorphous phases. A fully crystallized sample (i.e. $H_{0.12}WO_3 \cdot 2H_2O$) would lead to the removal of crystal water with a weight loss of approximately 13 wt.%.

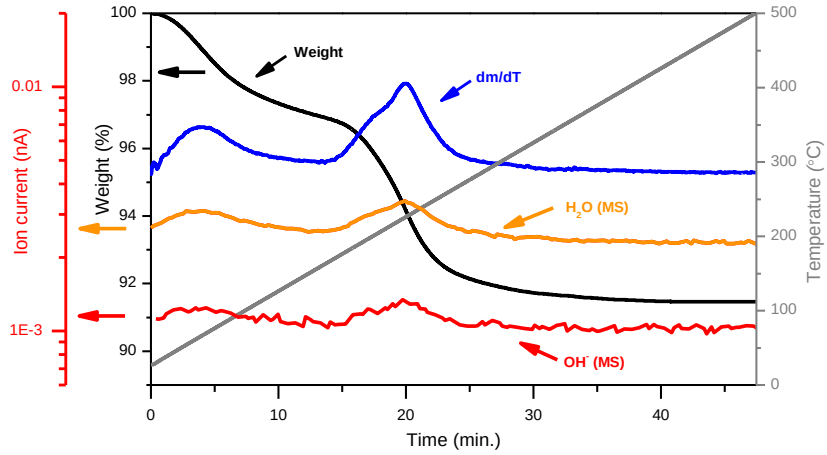

Figure 6: TGA-MS of dried tungsten precursor, during heating to 500°C at 10°C·min^{-1}. in dry air.

Since no evolution of chlorides or chlorine is found during the thermal treatment, the hypothesis that the chlorides leave the system during precursor synthesis is further confirmed. The total weight loss of 8 wt.% during the thermal treatment up to 500°C is a beneficial precursor property regarding film formation since less shrinkage and densification is to be expected leading to less cracks in the final film.[59]

In summary the following insights regarding the tungsten precursor chemistry are obtained:

(i) A part of the W^{6+} originating from the WCl_6 source is reduced to W^{5+} or W^{4+} via the evolution of HCl and DEE from the liquid phase;
(ii) Water causes hydrolysis and condensation reactions leading to a colloidal suspension containing crystalline particles;
(iii) The precursor powder only releases a very small amount of water (8 wt. %) during thermal treatment which will be beneficial for the film formation.

3.3 WO_3 films - Morphology

(Cross-sectional) SEM was used to visualize the films' morphology and thickness (Figure 7). Whereas the surface of the thin film deposited at 150°C is relatively smooth (Figure 7a and c), the surface looks rather rough while increasing the deposition temperature to 200°C (Figure 6b). After the deposition at 250°C, no material is present on the substrate (not shown). These observations are in agreement with the film formation mechanism proposed by Perednis et al.,[60] which was discussed in Chapter 2. As the deposition temperature increases, the size of precursor droplets decreases due to an increased solvent evaporation. In an extreme case (here 250°C), the droplets are converted to powders before hitting the substrate, resulting in the deposition of particles with a poor substrate adhesion.

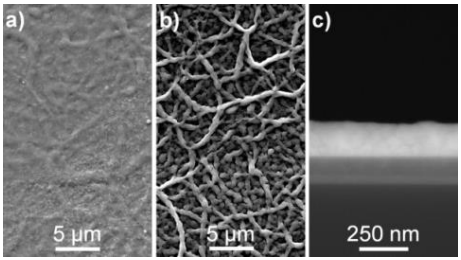

Figure 7: SEM micrographs of WO_3 coated TiN substrate. Top view micrographs are shown for (a) TiN at 150°C, (b) TiN at 200°C. A cross section using back-scattered imaging is shown in (c) for TiN at 150°C. All samples were annealed at 500°C in static air after deposition.

However, this film formation mechanism does not explain the difference in morphology as observed between the deposition temperatures of 150 and 200°C, respectively resulting in a smooth or rough surface. It is proposed that a lower deposition temperature (i.e. 150°C) leads to a lower solvent evaporation rate allowing for coalescence to occur for the particles present in the sprayed sus-

pension after hitting the substrate surface,[61] hence leading to a smooth surface. Here, 10 deposition cycles result in a film thickness of about 150 nm (Figure 7c). A higher deposition temperature (200°C) causes a fast solvent evaporating inhibiting particle coalescence and leading the root-like surface morphology.

3.4 WO_3 films - composition and phase formation

As discussed previously, the precursor study indicated that most of the chlorides are leaving the precursor in the liquid phase. This is confirmed by XPS measurements performed on thin films, which do not show any signs of chlorine (not shown). Regarding the oxidation state of tungsten, the XPS spectrum of W4f resulted in doublets of $4f_{7/2}$ at 37.6 eV and $4f_{5/2}$ at 35.2 eV (Figure 8). These energy positions correspond to the valence state of W^{6+}[15,62,63]. This implies that the oxidative anneal applied after deposition oxidizes the W^{5+} present in the precursor. No difference in film composition was found while changing the substrate from TiN to Pt (not shown). To probe more than just the top, surface etching was done. As was the case for the top surface, no chlorides were detected deeper inside of the layer.

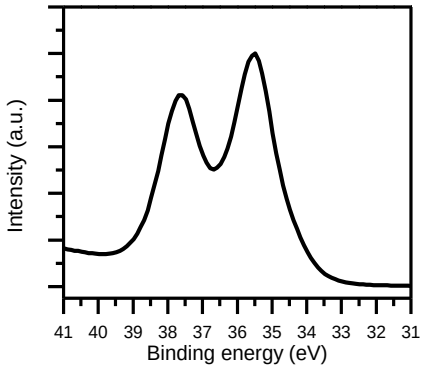

Figure 8: W4f XPS spectrum of WO_3 films annealed at 500°C for 1 hour (static air) on TiN.

However, due to the fact that Ar^+ was used for etching, no conclusions could be drawn regarding the oxidation state of the tungsten present. It is known that a high energy etching tool, Ar^+ etching reduces metal ions, especially in case of tungsten.[48,64]

Although the XPS measurements regarding tungsten were restricted to surface analysis, cyclic voltammetry (CV), probing a larger volume of the WO_3 films, also confirmed the presence of W^{6+} (Figure 9), as W^{6+} and W^{5+} can be discriminated based on their reduction potentials.[51,65] A first reduction peak at 2.67 V can be related to the reduction of W^{6+} to W^{5+} (indicated by 1 in Figure 9), the second reduction at 2.38 V corresponds to the consecutive W^{5+} to W^{4+} reduction (indicated by 2 in Figure 9).[51] In accordance with XPS, cyclic voltammetry confirms that W^{6+} is present in the films. The fact that the W^{5+} to W^{4+} reduction occurs does not mean W^{5+} is present in the pristine film as this reaction takes place after the W^{6+} to W^{5+} reduction, yielding an overall W^{6+} to W^{4+} reduction.

XRD measurements on the films deposited on the two different substrates both indicate the presence of tetragonal WO_3 phase (Figure 10, bottom), for which W^{6+} is required. The tetragonal phase was identified, especially because of the double peak in the 22-24° region. Three peaks would be observed in case of monoclinic or orthorhombic phases and only a single peak for the cubic phase of WO_3. In both cases the substrates peaks of TiN and Pt were identified. For Pt, this is expected since this metal is inert in the used annealing conditions. The presence of TiN is less obvious as TiN tends to oxidize to form TiO_2 while annealing in oxidative conditions.[39] Since at least part of the tungsten is reduced as-deposited, it may act as a protection to prevent (partial) oxidation of the TiN. However, CV of WO_3 on TiN (Figure 9, black) shows small reduction and oxidation peaks at 1.6 and 2.0 V, respectively. This suggest that a fraction of TiN is oxidized during annealing at 500°C, yielding TiO_2.[66] This leads to a possibly lower conductivity of the TiN current collector. Notably, both films have a different crystal structure than the powders annealed at the same temperature. The tetragonal phase normally exists at temperatures above 700°C or by insertion of alkali ions.[57,58,67,68] Since both are not the

case here, it is thought that the substrate favours the formation of the tetragonal phase at a lower annealing temperature (500°C) and remains stable at room temperature.

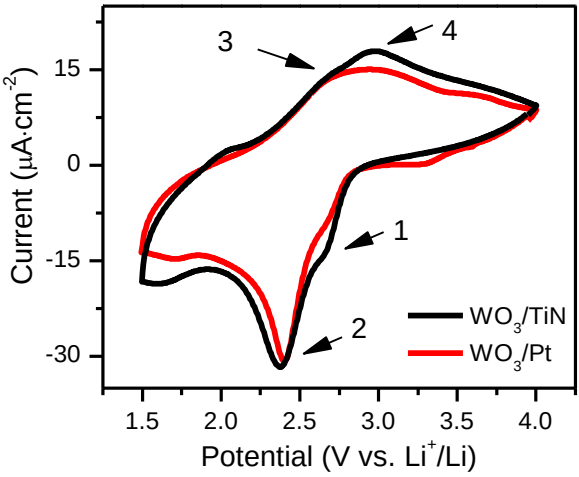

Figure 9: Cyclic voltammogram of 10 layers of WO_3 deposited on TiN (black) and Pt (red), measured at 1 $mV \cdot s^{-1}$ in 1 M $LiClO_4$ in PC. The films were submitted to a post deposition anneal of 1 hour at 500°C in static air. The numbers indicate the reduction and oxidation reactions occurring: (1) $W^{6+} \rightarrow W^{5+}$, (2) $W^{5+} \rightarrow W^{4+}$, (3) $W^{4+} \rightarrow W^{5+}$ and (4) $W^{5+} \rightarrow W^{6+}$.

3.5 WO_3 films - electrochemical analysis

The presence of W^{6+} was investigated with XPS and cyclic voltammetry as was discussed above. While inserting lithium into the crystal structure, the tungsten is reduced. This is shown in equation 5.

$$WO_3 + x \cdot Li + x \cdot e^- \rightleftharpoons Li_xWO_3 \qquad \textbf{(5)}$$

Table 2: Peak potentials measured by cyclic voltammetry of 10 layers of WO_3 deposited on TiN and Pt, measured at 1 $mV \cdot s^{-1}$ in 1 M $LiClO_4$ in PC. The films were submitted to a post deposition anneal of 1 hour at 500°C in static air.

Substrate	Reaction	Reduction potential (V)	Oxidation potential (V)
TiN	$W^{6+} + e^- \leftrightarrow W^{5+}$	2.67	2.97
Pt	$W^{6+} + e^- \leftrightarrow W^{5+}$	2.67	2.96
TiN	$W^{5+} + e^- \leftrightarrow W^{4+}$	2.38	2.68
Pt	$W^{5+} + e^- \leftrightarrow W^{4+}$	2.40	2.68

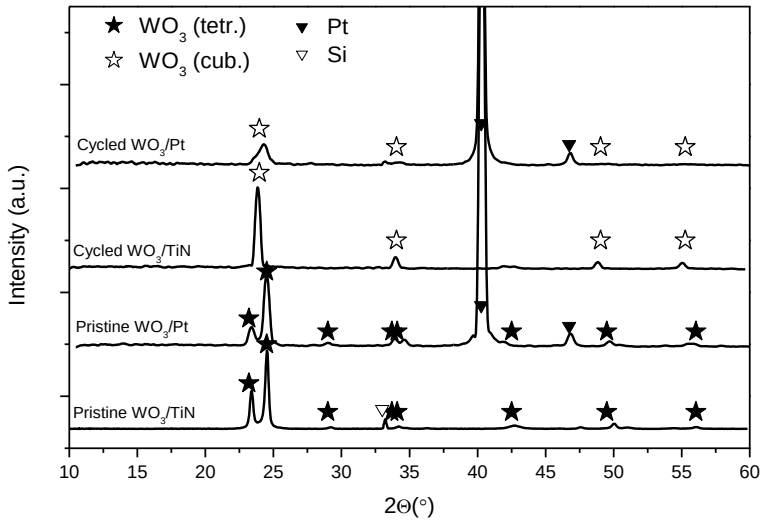

Figure 10: XRD of 10 layers of WO_3 deposited, deposited at 150°C. The films were submitted to a post deposition anneal of 1 hour at 500°C in static air. WO_3 pristine / after 100 cycles (at 1 C) on TiN and Pt. References indicated as followed: TiN (JCPDS 01-87-0632), Pt (JCPDS 01-87-0647), Si (JCPDS 01-72-1088), tetragonal WO_3 (JCPDS 01-85-807) and cubic WO_3 (JCPDS 20-1323).

The CV (Figure 9) shows that this reaction is not limited to W^{5+}, but W^{4+} is also present as was previously shown. In Figure 9, two oxidation peaks can be observed which are associated to the W^{4+} to W^{5+} and W^{5+} to W^{6+} (indicated by 3 and 4, respectively). The results are summarized in Table 2.

In case of TiN a slightly larger overpotential is measured compared to Pt. This is probably due to larger resistance of the substrate, as part of the TiN is oxidized during the annealing. Significant differences are found between the type of substrates while comparing the peaks of the W^{5+} oxidation peak, as indicated by 4 in Figure 9. Especially in the case of Pt the oxidation peaks have a relatively low intensity, indicating that part of the tungsten present is irreversibly reduced with Pt as a substrate.

Overall the (de)lithiation curves obtained by galvanostatic cycling of WO_3 on TiN and Pt look comparable (Figure 11), although some differences will be discussed in the next section. In general, for both substrates a first small voltage plateau is found at 2.7 V, which is assigned to the intercalation of Li^+ into the tetragonal phase.[67,68] A second, large plateau is found between 2.6 and 2.4 V, which is related to Li^+ insertion in the cubic phase. This phase is formed upon sufficient lithiation ($x>0.13$ for Li_xWO_3) of the tetragonal phase.[67,68] Finally, a considerable amount of charge is measured while maintaining a slight slope (i.e. without clearly defined voltage plateau); kinetic factors and / or amorphous phases appear to be present and responsible for intercalation at lower voltages, expressed in long slopes instead of charge plateaus.[16]

The capacity fading observed during 100 (de)lithiation cycles for both WO_3/TiN and WO_3/Pt seems to be related to the destruction or irreversible lithiation of the cubic phase, as the voltage plateau between 2.6 and 2.4V (lithiation) shortens significantly. This means that less crystalline phases are available for Li^+ insertion. In addition, the voltage slope before cut-off, previously assigned to kinetic factors or amorphous WO_3, is significantly longer in case of Pt. All these arguments suggest small differences for (crystalline) WO_3 lithiation exist between Pt compared to TiN substrates.

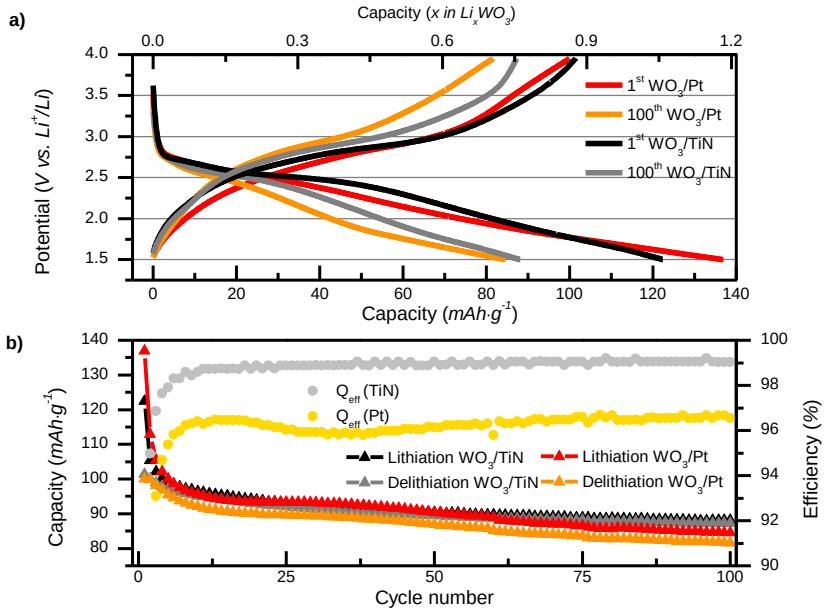

Figure 11: Galvanostatic measurements for 10 layers of WO_3 deposited on TiN and annealed at 500°C for 1 hour in static air, measured at 1C in 1.0 M $LiClO_4$ at 20°C. a) shows capacity / potential curves and b) shows capacity and coulombic efficiency versus cycle number.

(ex-situ) XRD done on cycled films (Figure 10, top) yields another clue what the main differences between the two substrates are. For WO_3 on TiN, a clear transition from tetragonal to cubic WO_3 can be observed upon cycling. However, in case of Pt a difference is noted. In the first place the crystallinity is significantly lower, as the peaks at 24 and 33.5° are much broader. In addition, the (100) peak at 24° is significantly shifted to the right as to compared to TiN as substrate; combined with a small peak at 34° this may imply that a mixture of cubic and predominantly tetragonal phase is present.

The poor performance of Pt as substrate is expressed as well in the galvanostatic measurements as a function of cycle number (Figure 11). Although the overall capacity of WO_3 on TiN and Pt seems comparable at first, in case of Pt the delithiation capacity drops to a significant lower level from the 5th cycle and onward. WO_3 on TiN leads to a steady coulombic efficiency of 99.2%, whereas Pt leads to much more variation with a maximum efficiency of 96.6%, although both samples were submitted to the same synthesis conditions and anneals. The capacity of the WO_3/TiN films surpasses the theoretical value of 0.75 Li^+ per WO_3 unit for the cubic phase,[68] although Figure 11 shows that after 100 cycles a more stable capacity value close to the theoretical maximum is reached. Very low coulombic efficiencies are registered the first cycles (starting from 82.8 and 73.1% for TiN and Pt, respectively), the capacity values surpassing theoretical values are therefore attributed to irreversible intercalation into amorphous phases as observed in the slope before cut-off noted previously. The capacity values reached are however equal to WO_3 in bulk (powder) form using a comparable voltage range,[20] indicating that at least in case of TiN as substrate sufficient crystallinity and phase stability is reached.

In view of device integration and oxidation of TiN into TiO_2, films annealed at temperatures were investigated by galvanostatic measurements. 300°C appeared to be too low to yield electrochemically active material (not shown). After 1 hour at 300°C not all the (crystal) water has left the system yet (Figure 6), which may be an indicator for inactivity. Another explanation may be that bleaching, i.e. oxidation to tungsten from either W^{4+} or W^{5+}, occurs so slowly that tungsten oxide phases are insufficiently formed. It was reported previously that bleaching by thermal annealing of tungsten oxide films occurs at much lower rates at 400°C as compared to 500°C in oxygen rich conditions.[48] Nevertheless, at 400°C electrochemically active films were obtained, although activity was significantly lower as compared to the 500°C case for both WO_3/TiN and WO_3/Pt samples (Figure 11 and 12). This matches with the bleaching behaviour at these temperatures.[48] However, after 100 cycles part of the Pt is visible macroscopically (Figure

13). This implies that due to cycling WO_3 on Pt, structural changes appear as was the case for the 500°C anneal (Figure 11).

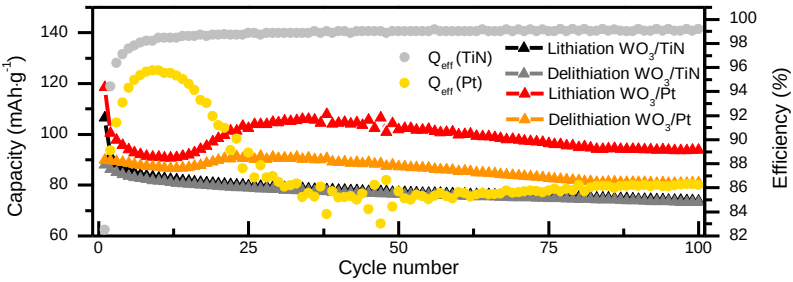

Figure 12: Galvanostatic measurements for 10 layers of WO_3 deposited on TiN and annealed at 400°C for 1 hour in static air, measured at 1C in 1.0 M $LiClO_4$ at 20°C.

However, in case of the 400°C anneal the effect seems to be more severe. On Pt as the substrate, the film adhesion appeared to be more stable after an anneal at 500°C as compared 400°C. Delamination of the 400°C films is shown in Figure 13, which was not observed for films treated at 500°C. In both 400 and 500°C cases (Figures 11 and 12) there is a drop in efficiency and capacity followed by a slight improvement between 20 and 40 cycles, it is therefore thought that the same physical process acts on the WO_3/Pt combination which is intensified at lower annealing temperatures. Adhesion of the WO_3 film to TiN is therefore regarded significantly better as compared to Pt. Nevertheless, the overall performance of WO_3/TiN at 400°C (coulombic efficiency 99.0%, capacity of 75 $mAh \cdot g^{-1}$, c.f. Figure 12) is lower than the same WO_3/TiN combination annealed at 500°C (Figure 11). These differences are ascribed to better crystallization induced by improved bleaching and / or increase of oxygen vacancies at higher annealing temperatures.[20,48]

Figure 13: WO_3 on Pt after galvanostatic measurements shown in Figure 12.

3.6 WO_3 films – 3D deposition

In Chapter 5 and 6 examples were given with the 3D deposition of solid electrolyte materials. Although the colloidal suspension used here to obtain WO_3 films strongly differs from an all-citrate and citrate-nitrate precursors used previously, 3D deposition of WO_3 was attempted. For this purpose, the tungsten precursor was deposited on 3D TiN (2x10). The results are shown in Figure 14. Although a thin coating of 100 nm is present at the bottom of the pillars (possibly including oxidized TiN), the deposition is rather as inhomogeneous. This result differs largely from the deposition of the molecular precursors reported in Chapter 5 and 6. Although the use of these molecular precursor requires optimization of the deposition temperature, a much higher homogeneity is obtained. Given the difference in precursor chemistry, it seems plausible that a particle based precursor system is less suitable for 3D depositions. Especially so since Chapter 9 shows that 3D deposition of WO_3 is much more successful with a (molecular) citrate precursor.

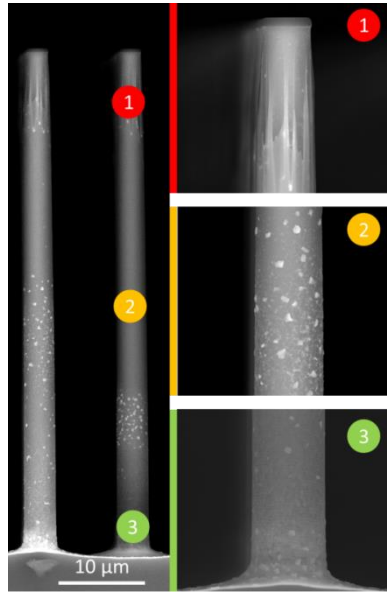

Figure 14: SEM micrographs of the tungsten precursor deposited (10 cycles, 150°C) on 3D TiN (2x10). The sample was annealed 1 hour at 500°C in static air after deposition.

4. Conclusion

The chemistry of tungsten chloride in an ethanol / water mixture was explored for the synthesis of tungsten oxide films starting from a tungsten chloride-based solution. Part of the tungsten present in the precursor was reduced while forming chlorine gas and DEE. The chlorine leaves the precursor as hydrogen chloride gas leading to a chlorine depleted precursor. In addition, via hydrolysis and condensation, particles were formed resulting in a colloidal suspension.

Via USD of the colloidal suspension, planar and 3D structured substrates were coated. Unfortunately, the 3D deposition yielded inhomogeneous coatings. For planar films, electrochemically active thin films were obtained with a capacity value of 90 $mAh \cdot g^{-1}$ or 640

$mAh \cdot cm^{-3}$, using a 500°C anneal. A clear difference in the performance was noted between the TiN and Pt substrate. The TiN allows a higher coulombic efficiency and a much more stable capacity evolution, especially in the case of an annealing temperature as low as 400°C. The relative low annealing temperature required for the formation of active tungsten oxide thin films is an important breakthrough allowing the use of TiN as low-cost alternative for the Pt current collector. In addition, this approach opens up new possibilities for the fabrication of all-solid-state Li-ion batteries as these WO_3 films, exhibiting a high volumetric capacity, can be combined with electrochemically instable solid electrolytes such as LLT (c.f. Chapter 10). Arguably, the significant loss of power density expected for an all-solid-state Li-ion battery – caused by the relatively high intercalation voltage the of the proposed WO_3 films – is compensated by the (i) compatibility with several (oxide-based) solid-state electrolytes, (ii) ease of processing and (iii) relative low temperature requirements. Since the proposed route is a low cost method in combination with inexpensive materials, USD of WO_3 colloidal suspensions is a promising method for upscaling purposes.

5. References

[1] P. Knauth, *Solid State Ionics* **2009**, *180*, 911.
[2] K. Takada, *Acta Mater.* **2013**, *61*, 759.
[3] V. Thangadurai, W. Weppner, *Ionics (Kiel).* **2006**, *12*, 81.
[4] J. B. Bates, N. J. Dudney, B. Neudecker, A. Ueda, C. D. Evans, *Solid State Ionics* **2000**, *135*, 33.
[5] V. Thangadurai, S. Narayanan, D. Pinzaru, *Chem. Soc. Rev.* **2014**, *43*, 4714.
[6] M. Roeder, A. B. Beleke, U. Guntow, J. Buensow, A. Guerfi, U. Posset, H. Lorrmann, K. Zaghib, G. Sextl, *J. Power Sources* **2016**, *301*, 35.
[7] S. Y. Tsai, K. Z. Fung, C. T. Ni, *ECS Trans.* **2015**, *68*, 37.
[8] W.J. Li, Z.-W. Fu, *Appl. Surf. Sci.* **2010**, *256*, 2447.
[9] D. G. Barton, S. L. Soled, E. Iglesia, *Top. Catal.* **1998**, *6*, 87.
[10] C. Di Valentin, F. Wang, G. Pacchioni, *Top. Catal.* **2013**, *56*, 1404.
[11] J. P. Perereira-Ramos, R. Baddour-Hadjean, N. Kumagai, K. Tanno, *Electrochim. Acta* **1993**, *38*, 431.

[12] K. Huang, Q. Zhang, *Nano Energy* **2012**, *1*, 172.
[13] A. Yu, N. Kumagai, Z. Liu, J. Y. Lee, *J. Solid State Electrochem.* **1998**, *2*, 394.
[14] G. a. Niklasson, C. G. Granqvist, *J. Mater. Chem.* **2007**, *17*, 127.
[15] M. Regragui, M. Addou, A. Outzourhit, J. C. Bernede, E. El Idrissi, E. Benseddik, A. Kachouane, *Thin Solid Films* **2000**, *358*, 40.
[16] J. Garciacanadas, *Solid State Ionics* **2004**, *175*, 521.
[17] K. Nishio, T. Sei, T. Tsuchiya, *J. Ceram. Soc. Japan* **1999**, *107*, 199.
[18] C. Guo, S. Yin, M. Yan, M. Kobayashi, M. Kakihana, T. Sato, *Inorg. Chem.* **2012**, *51*, 4763.
[19] J. Denayer, P. Aubry, G. Bister, G. Spronck, P. Colson, B. Vertruyen, V. Lardot, F. Cambier, C. Henrist, R. Cloots, *Sol. Energy Mater. Sol. Cells* **2014**, *130*, 623.
[20] W. Li, A. Sasaki, H. Oozu, K. Aoki, K. Kakushima, Y. Kataoka, A. Nishiyama, N. Sugii, H. Wakabayashi, K. Tsutsui, K. Natori, H. Iwai, *Microelectron. Reliab.* **2015**, *55*, 402.
[21] P. V Braun, J. Cho, J. H. Pikul, W. P. King, H. Zhang, *Curr. Opin. Solid State Mater. Sci.* **2012**, *16*, 186.
[22] J. F. M. Oudenhoven, L. Baggetto, P. H. L. Notten, *Adv. Energy Mater.* **2011**, *1*, 10.
[23] P. H. L. Notten, F. Roozeboom, R. A. H. Niessen, L. Baggetto, *Adv. Mater.* **2007**, *19*, 4564.
[24] J. B. Bates, N. J. Dudney, G. R. Gruzalski, R. A. Zuhr, A. Choudhury, *J. Power Sources* **1993**, *44*, 103.
[25] H. I. Schlesinger, H. C. Brown, A. E. Finholt, X. Y. J. B. Bates, G. E. Jellison, F. X. Hart, *J. Electrochem. Soc.* **1997**, *144*, 524.
[26] J. Kawamura, *Solid State Ionics* **2004**, *175*, 273.
[27] Y.-C. Perng, J. Cho, S. Y. Sun, D. Membreno, N. Cirigliano, B. Dunn, J. P. Chang, *J. Mater. Chem. A* **2014**, *2*, 9566.
[28] S. Kim, M. Hirayama, S. Taminato, R. Kanno, *Dalton Trans.* **2013**, *42*, 13112.
[29] J. Reinacher, S. Berendts, J. Janek, *Solid State Ionics* **2014**, *258*, 1.
[30] K. Tadanaga, H. Egawa, A. Hayashi, M. Tatsumisago, J. Mosa, M. Aparicio, A. Duran, *J. Power Sources* **2015**, *273*, 844.
[31] S. Stramare, V. Thangadurai, W. Weppner, *Chem. Mater.* **2003**, *15*, 3974.

[32] Y. J. Shan, L. Chen, Y. Inaguma, M. Itoh, T. Nakamura, *J. Power Sources* **1995**, *54*, 397.
[33] Y. Inaguma, C. Liquan, M. Itoh, T. Nakamura, T. Uchida, H. Ikuta, M. Wakihara, *Solid State Commun.* **1993**, *86*, 689.
[34] S. Furusawa, H. Tabuchi, T. Sugiyama, S. Tao, J. Irvine, *Solid State Ionics* **2005**, *176*, 553.
[35] K. Kitaoka, H. Kozuka, T. Hashimoto, T. Yoko, *J. Mater. Sci.* **1997**, *32*, 2063.
[36] C. Delmas, A. Nadiri, J. L. Soubeyroux, *Solid State Ionics* **1988**, *28-30*, 419.
[37] K. Takada, M. Tansho, I. Yanase, T. Inada, A. Kajiyama, M. Kouguchi, S. Kondo, M. Watanabe, *Solid State Ionics* **2001**, *139*, 241.
[38] L. Baggetto, J. F. M. Oudenhoven, T. Van Dongen, J. H. Klootwijk, M. Mulder, R. A. H. Niessen, M. De Croon, P. H. L. Notten, *J. Power Sources* **2009**, *189*, 402.
[39] N. C. Saha, H. G. Tompkins, *J. Appl. Phys.* **1992**, *72*, 3072.
[40] K. Nishio, T. Tsuchiya, *Sol. Energy Mater. Sol. Cells* **2001**, *68*, 279.
[41] L. Muresan, E. J. Popovici, A. R. Tomsa, E. Indrea, *J. Optoelectron. Adv. Mater.* **2008**, *10*, 2261.
[42] M. E. Donders, W. M. Arnoldbik, H. C. M. Knoops, W. M. M. Kessels, P. H. L. Notten, *J. Electrochem. Soc.* **2013**, *160*, A3066.
[43] D. B. Kokh, A. B. Alekseyev, R. J. Buenker, *J. Chem. Phys.* **2004**, *120*, 11549.
[44] O. J. Klejnot, *Inorg. Chem.* **1965**, *4*, 1668.
[45] K. Arbi, S. Mandal, J. M. Rojo, J. Sanz, *Chem. Mater.* **2002**, *14*, 1091.
[46] M. I. Bernal-Uruchurtu§, G. Kerenskaya, K. C. Janda, *Int. Rev. Phys. Chem.* **2009**, *28*, 223.
[47] S.-H. Wang, T.-C. Chou, C.-C. Liu, *Sensors Actuators B Chem.* **2003**, *94*, 343.
[48] G. Leftheriotis, S. Papaefthimiou, P. Yianoulis, a. Siokou, *Thin Solid Films* **2001**, *384*, 298.
[49] L. Berggren, J. C. Jonsson, G. a. Niklasson, *J. Appl. Phys.* **2007**, *102*, 083538.
[50] D. Dini, F. Decker, E. Masetti, *J. or Appl. Electrochem.* **1996**, *26*, 647.
[51] S. Darmawi, S. Burkhardt, T. Leichtweiss, D. a. Weber, S. Wenzel, J. Janek, M. T. Elm, P. J. Klar, *Phys. Chem. Chem. Phys.* **2015**, *17*, 15903.
[52] X. He, H. Liu, *Catal. Today* **2014**, *233*, 133.

[53] M. Kaufhold, M. El-Chahawi, *Process for Preparing Acetaldehyde Diethyl Acetal*, **1996**, 5527969.
[54] M. R. Capeletti, L. Balzano, G. de la Puente, M. Laborde, U. Sedran, *Appl. Catal. A Gen.* **2000**, *198*, L1.
[55] J. Livage, D. Ganguli, *Sol. Energy Mater. Sol. Cells* **2001**, *68*, 365.
[56] H. Ryu, K. Park, I. Kim, K. Hong, W. Lee, J. Park, **2003**, *42*, 727.
[57] T. Vogt, P. M. Woodward, B. A. Hunter, *J. Solid State Chem.* **1999**, *144*, 209.
[58] S. Pokhrel, J. Birkenstock, A. Dianat, J. Zimmermann, M. Schowalter, A. Rosenauer, L. C. Ciacchi, L. Mädler, *CrystEngComm* **2015**, *17*, 6985.
[59] R. Schwartz, T. Schneller, R. Waser, *Comptes Rendus Chim.* **2004**, *7*, 433.
[60] D. Perednis, L. J. Gauckler, *J. Electroceramics* **2005**, *14*, 103.
[61] M. Majumder, C. Rendall, M. Li, N. Behabtu, J. A. Eukel, R. H. Hauge, H. K. Schmidt, M. Pasquali, *Chem. Eng. Sci.* **2010**, *65*, 2000.
[62] A. Temmink, O. Anderson, K. Bange, *Thin Solid Films* **1990**, *192*, 211.
[63] G. Hollinger, T. M. Duc, *Phys. Rev. Lett.* **1976**, *37*, 1564.
[64] T. J. Driscoll, L. D. McCormick, W. C. Lederer, *Surf. Sci.* **1987**, *187*, 539.
[65] P. L. Hagedoorn, J. R. Freije, W. R. Hagen, *FEBS Lett.* **1999**, *462*, 66.
[66] Z. He, Z. Wang, F. Wu, H. Guo, X. Li, X. Xiong, *J. Alloys Compd.* **2012**, *540*, 39.
[67] Q. Zhong, J. R. Dahn, K. Colbow, *Phys. Rev. B* **1992**, *46*, 2554.
[68] K. H. Cheng, M. S. Whittingham, *Solid State Ionics Communications* **1980**, *1*, 151.

Part III - Chapter 8

Lithium doping of WO_3 films as negative electrode for Li-ion batteries

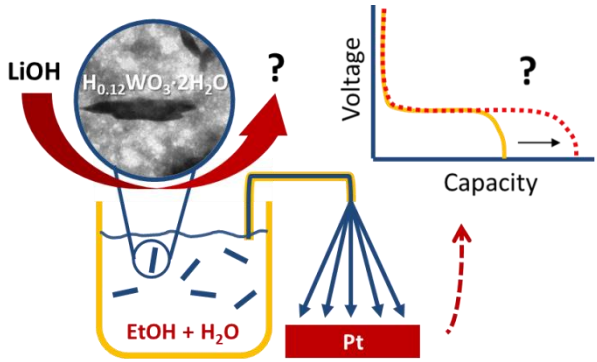

Dr. Ken Elen, Gilles Bonneux and Fulya Ulu are acknowledged for their contribution to this chapter.

Abstract

The possibility of lithium insertion into the crystalline tungsten oxide rods (shown in Chapter 7) is investigated in this chapter. Although XRD and especially TGA suggest that lithium doping of the rods did not occur at low temperatures, the resulting films yield large differences with lithium-free tungsten oxide films. The USD of $Li_2W_2O_7$ (LWO) films is shown here for 1:1 Li:W ratio in the precursor, including the electrochemical properties. Although the results of the nearly phase pure LWO films show a clear increase in capacity with well-defined voltage plateaus in comparison to the lithium-free case, the phase instability and contraction makes this material unsuitable for thin film Li-ion batteries. However, films with a lower lithium doping (Li:W = 1:2) did enable more cycling stability, as well as increased capacity in comparison with the lithium-free case.

1. Introduction

Based on the interesting properties of the WO_3 thin film electrode for Li-ion batteries (Chapter 7), namely a low crystallization temperature in combination with high volumetric capacity, further research can be done to tune and optimize this material. If the WO_3 can be doped with lithium before electrochemical (de)lithiation, irreversible lithium loss may be prevented, leading to higher overall capacity. Little research is done on the Li – W intercalation chemistry,[1] therefore new approaches are discussed in this study.

The results of the colloidal suspensions achieved previously (Chapter 7), suggest protons are present in crystalline WO_3 colloids, forming $H_{0.12}WO_3 \cdot 2H_2O$ at room temperature. The presence of protons as well as the dark blue coloration indicated that the tungsten is present in reduced form; possibly creating opportunities for lithium doping in the liquid phase. Here the question is raised if lithium can be inserted in the colloidal crystallites, to replace protons in the presence of reduced tungsten. Alternatively, it may results in lithiated tungsten oxide phase(s) at relatively low temperature (e.g. cubic $Li_{0.5}WO_3$). Since colloid formation occurs in the liquid phase of the ethanol-water precursor system, an adjusted synthesis route is investigated based on the addition of lithium hydroxide. This salt is able to dissolve in both water and ethanol phase, increasing the possibility of low temperature Li-doping.

2. Experimental

The synthesis approach closely resembles the route chosen in Chapter 7, but prior to tungsten chloride (WCl_6) dissolution in ethanol (10 mM), lithium hydroxide (LiOH, 98%, Merck) was dissolved in ethanol in amounts matching a 1:1 and 1:2 Li:W molar ratio (10 and 5 mM, respectively) upon stirring for 24 hours. Next, tungsten chloride and water where added as described in Chapter 7. The synthesis is summarized in Figure 1.

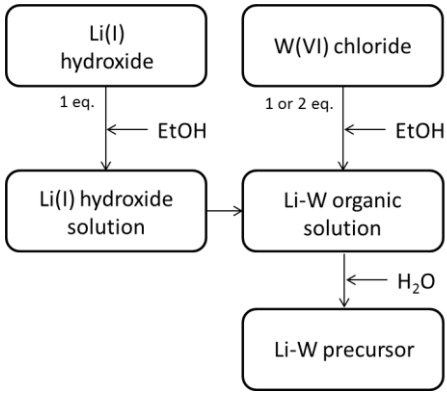

Figure 1: Synthesis scheme of the Li-W precursor.

Deposition was done as described in Chapter 7, with a deposition temperature of 150°C. Characterization by TEM, TGA, cyclic voltammetry (CV) and galvanostatic cycling were done as described in Chapter 7, although different cut-off voltages were chose (0.75 to 3.25 V vs. Li^+/Li) based on initial CV results.

3. Results and discussion

3.1 Low-temperature Li-doping of WO_3 rods

Figure 2 shows TEM analysis of the dried 1:1 Li-W precursor droplets. As can be observed, rod-like particles are observed here as well, similar to the lithium-free case (Chapter 7). The ED confirms the rods are crystalline, although the quality of these patterns is too low to extract a particular crystal system. To analyse the structure of these rods, XRD analysis of the dried precursor was done (Figure 3). Although the low intensity of the signals indicates poor crystallinity, a mixture of $H_{0.12}WO_3 \cdot 2H_2O$ and $WO_3 \cdot H_2O$ can be distinguished. Note that this slightly differs from the lithium-free case discussed in Chapter 7, where the latter phase was not encountered.

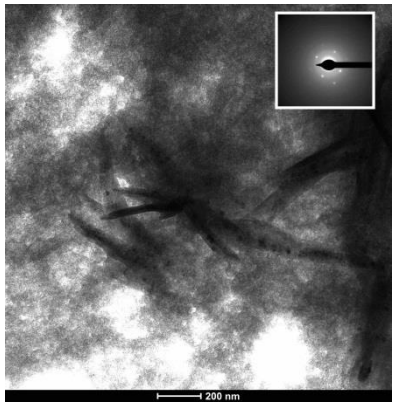

Figure 2: TEM micrograph of the Li-W precursor deposited on a copper grid and dried before measuring. Rod-like, crystalline particles are observed in a matrix of smaller amorphous particles (c.f. Chapter 7). The inset shows ED of the rod-like particles.

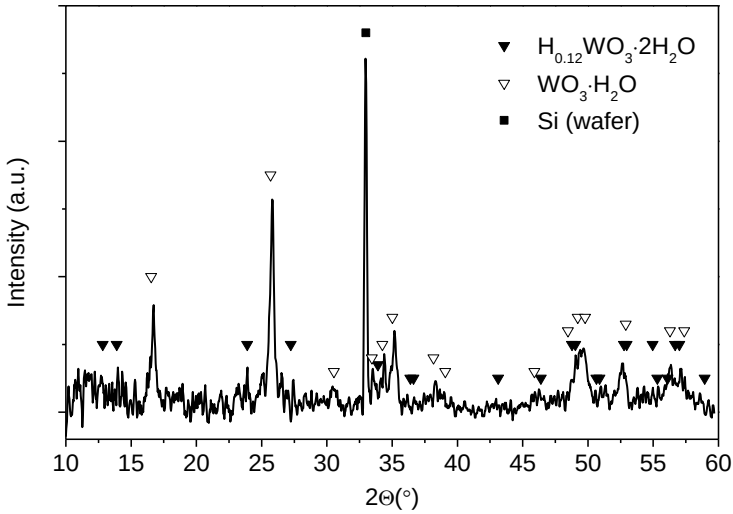

Figure 3: XRD pattern of dried Li-W precursor (1:1 ratio), without annealing.

Both phases suggest that no Li-doping occurred at all, since no Li-ions are present in the identified crystal structure. However, due to the large interstitial space of the WO_3 structure, both H^+ and Li^+ are readily inserted into the structure yielding small structural differences.[2] Therefore, it is difficult to discriminate if Li^+ and / or H^+ is present in the crystalline rods based on the XRD shown in Figure 3.

In search for clues whether lithium enters the crystalline WO_3 rods, TGA analysis was done (Figure 4). For all Li:W ratios (i.e. 1:0, 1:1, 1:2 and 0:1) a significant loss of solvents is observed up to approximately 120°C. The lithium-free case (Chapter 7) shows one weight loss event after this, attributed to the loss of crystal water. Upon addition of LiOH to the precursor system, in both the 1:2 and 1:1 Li:W ratio, the process of (crystal) water evolution does not occur, or at least not at the same temperature. It is noted that a higher weight loss is observed at lower temperatures ('normal' water evolution); therefore LiOH possibly inhibits formation of crystal water seen in the lithium-free case (Chapter 7). At higher temperatures, both LiOH containing samples show a small weight loss starting at 350°C, where the weight loss difference (1.6 and 3.4%) approximately doubles together with twice the amount of LiOH present in the precursor. To gain understanding of the underlying reaction mechanism in the Li-W precursor system, first the decomposition of (solely) LiOH is considered (Figure 4, cyan line). LiOH decomposition seems to occur in two distinct regimes; from 300 till 500°C with a gradual slope of the weight loss curve, followed by a steeper slope above 500°C. The first slope is assigned to LiOH decomposition, to form Li_2O and H_2O as shown in Equation 1.[3,4] The second, steeper slope, may be the combined decomposition and evaporation of LiOH; the latter reaction is shown in Equation 2.[4] The evaporation of Li_2O is reported to take place at higher temperatures (>750°C) and is therefore not considered here.[4]

$$2\,LiOH(s) \rightarrow Li_2O(s) + H_2O(g) \quad \textbf{(1)}$$

$$LiOH(s) \rightarrow LiOH(g) \quad \textbf{(2)}$$

Returning to the Li-W precursor system; Equation 1 may apply for the Li-W precursor as well, based on the small weight loss observed slightly above 300°C. Moreover, Equation 2 does not apply because no weight loss is recorded above 500°C. This may suggest a solid-state reaction occurring; LiOH is decomposed to form Li_2O, which readily reacts with (deprotonated / bleached) tungsten oxide phases present. This reaction is shown in Equation 3, where *x* indicates the Li/W ratio.

$$xLiOH(s) + WO_3(s) \rightarrow Li_xWO_{\left(3+\frac{1}{2}x\right)}(s) + \tfrac{1}{2}xH_2O\ (g) \qquad \textbf{(3)}$$

Based on a mass calculation of Equation 3, a weight loss of 1.75% for x=0.5 and 3.50% for x=1.0 is expected. These values resemble the experimental values in Figure 4 closely (1.6 and 3.4%, respectively).

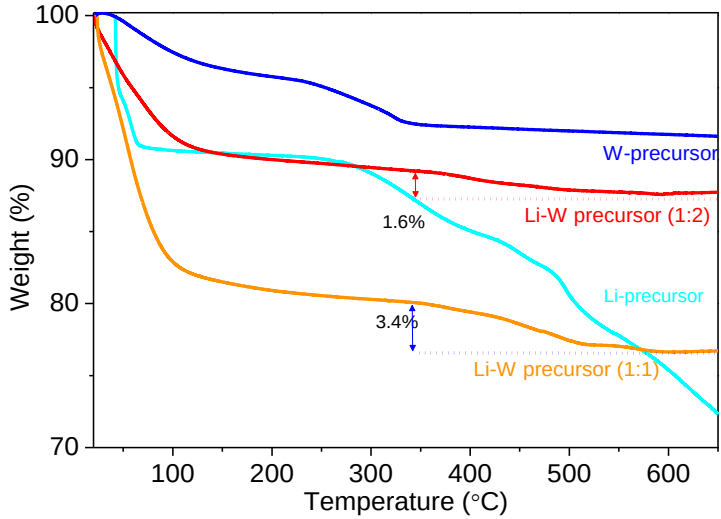

Figure 4: TGA of dried Li-,W-, Li-W-precursors, with the latter in a 1:1 and 1:2 ratio. The samples were heated at 10°C·min^{-1} in dry air. The dashed lines serve as a guide to the eye.

Thus, (i) the decomposition temperatures as well as (ii) the weight loss quantification point in the direction of the solid-state reaction (Equation 3) involving LiOH, Li_2O and WO_3. However, it is stressed that this is a hypothesis that requires more analysis before definite conclusions can be drawn.

Besides this hypothesis for the underlying reactions, the TGA analysis leads to the conclusion that, unfortunately, low temperature doping into the WO_3 lattice probably does not occur. In other words, it is highly unlikely that the rods shown Figure 2 contain lithium.

3.2 Morphology and phase formation of Li-W precursor films

Since the LiOH only starts reacting at temperatures above 300°C, other phases than lithiated WO_3 (e.g. $Li_{0.5}WO_3$) may start appearing at higher temperatures, such as $Li_2W_2O_7$.[1] For films, the presence of this phase was confirmed for 1:1 and 1:2 Li:W ratios (x=1.0 and x=0.5, Eq. 3) after an anneal at 500°C for 1 hour in static air (Figure 5). Note that W^{6+} is present in $Li_2W_2O_7$ (LWO) to maintain charge neutrality, matching with the hypothesis formulated in Equation 3.

With a 1:1 Li:W ratio, primarily LWO (JCPDS 70-869) was obtained, though traces of Li_2WO_4 (JCPDS 72-86) seems to be present as well. To the best of our knowledge, LWO films have not been reported before. For 1:2 Li:W ratio several additional peaks are observed. Next to LWO, a phase containing lower Li:W ratios is present: $Li_2W_5O_{16}$ (JCPDS 28-0600). These results are in good agreement with a (subsolidus) Li_2O-WO_3 phase diagram reported before, based on materials annealed at 700°C.[5] A small lithium excess with respect to the 1:1 ratio used, yields a mixture of LWO and Li_2WO_4; this may be the case because ICP-AES analysis was not applied before mixing the separate Li- and (organic) W-precursors. Another reason for stoichiometric deviations is the fact that molecular mixing does not apply for this precursor based on a colloidal suspension. According to the same diagram, a 1:2 Li:W ratio (as well as a small deviation from this value) leads to a mix-

ture of LWO and $Li_2W_5O_{16}$.[5] The oxidative conditions used to anneal the deposited films probably suppress $Li_{0.5}WO_3$ phase formation, because Li^+ insertion into the cubic WO_3 lattice requires slightly reduced tungsten.[6,7] Hence, simply adding LiOH to the reduced W-precursor, consisting of a colloidal suspension (Chapter 7), is no suitable method to obtain $Li_{0.5}WO_3$.

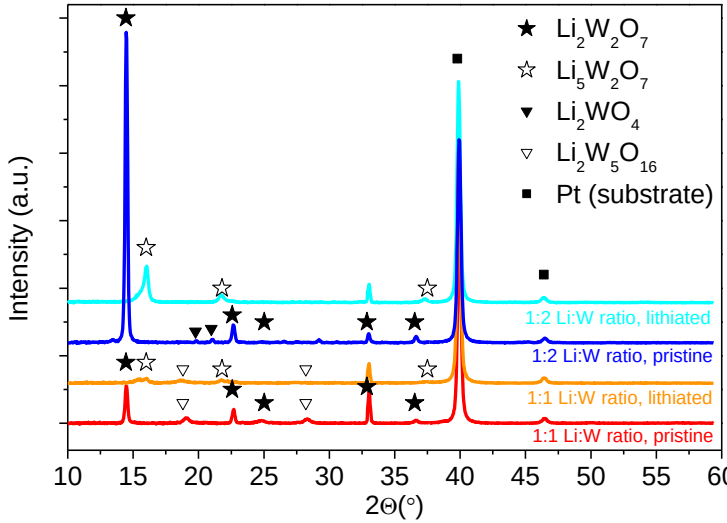

Figure 5: X-ray diffractogram of Li-W-precursor (1:1 and 1:2 ratio) deposited on Pt substrates by ultrasonic spray deposition, after annealing for 1 hour in static air.

The 1:1 Li:W precursor deposition with the mixed colloidal / molecular precursor yields smooth films by ultrasonic spray deposition. The morphology strongly resembles the lithium-free case discussed before (Chapter 7). The thickness obtained after 10 deposition cycles shows fluctuations (±20 nm), with an average thickness of 150 nm (Figure 6).

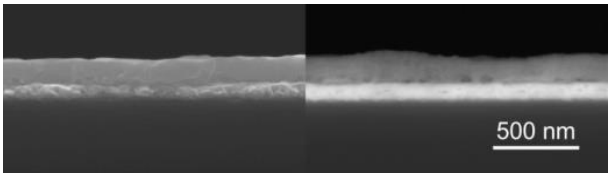

Figure 6: SEM micrograph of Li-W-precursor (1:1) deposited on Pt substrates by ultrasonic spray deposition (10 cycles, 150°C), after annealing for 1 hour in static air.

3.3 Electrochemical properties of Li-W precursor films

The LiOH doped samples, forming the LWO phase on films, behave significantly different than lithium-free WO_3, as was studied previously by Pralong et al on powders.[1] Electrochemically, three main differences are observed compared to lithium-free WO_3: (i) a shift to lower (de)intercalation voltages (ii) higher capacities and (iii) higher Li-ion conductivity.[1]. Figures 7 and 9 illustrate that the 1:1 Li:W ratio films, forming LWO (in presence of a secondary phase) indeed yield a completely different behaviour compared to the lithium-free WO_3 discussed in Chapter 7.

The CV for the 1:1 Li:W ratio film, shown in Figure 7, exhibits a sharp reduction peak during the first cycle at 1.4 V (vs. Li^+/Li). Comparing with the study on powders of Pralong et al., this reduction is assigned to the reduction of tungsten while lithiating the LWO phase to $Li_5W_2O_7$.[1] This matches with the XRD pattern after a single cycle of galvanostatic lithiation (Figure 5), which shows a strong decline of the 14° peak and rise of a 16° peak due to lithiation of the LWO phase.[1] Regarding delithiation reactions, de CV shows an oxidation peak at 1.7 V (Figure 7), which is assigned to delithiation of the $Li_5W_2O_7$ phase. However, for the third cycle a peak shift is observed, and the main reduction and oxidation peaks shift towards higher voltages along with the occurrence of an additional oxidation reaction at around 2.1 V. It is not completely clear why this occurs, but a comparison with the voltammogram of the 1:2 Li:W ratio film gives some indications (Figure 8).

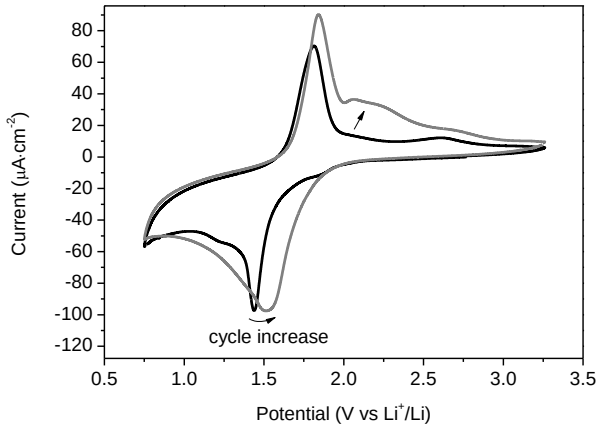

Figure 7: CV of 10 layers of Li:W 1:1 ratio precursor deposited on Pt substrates and anneaed at 500°C for 1 hour in static air. The figure shows the first and third cycle.

At first two small reduction peaks are observed for the 1:2 Li:W ratio film, but for the third cycle a clear difference is observed as well. Apart from intensity loss related to initial irreversible Li-loss, the 1.4 V peak nearly disappears and the reduction peak at 1.6 V only shows a small shift. In addition, two oxidation peaks are observed, at 1.8 and 2.1 V. Since the 1:2 Li:W ratio film shows a mixture of phases (including $Li_2W_5O_{16}$), the 1.6 V and 2.1 V peaks are assigned to other phases than LWO. Hence, it is assumed that the peak shift of the 1:1 Li:W ratio sample in Figure 7 is caused by phase instability during prolonged cycling, possibly leading to other (amorphous) phases.

Besides phase instability upon (de)lithiation, another issue encountered for LWO is related to contraction and expansion events during cycling. During lithiation to $Li_5W_5O_7$, a shrinkage of 6.5% is encountered.[1]

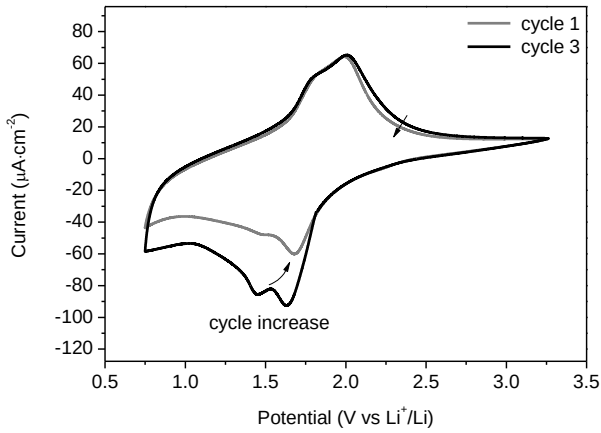

Figure 8: CV of 10 layers of Li:W 1:2 ratio precursor deposited on Pt substrates and annealed at 500°C for 1 hour in static air. The figure shows the first and third cycle.

The galvanostatic cycling reflects both phase instability and loss of active material due to contraction and expansion, since very poor capacity retention is observed for the 1:1 Li:W ratio samples (Figure 9). Comparison of these curves with the 1:2 Li:W ratio sample (Figure 10), reveals several differences. First of all, a slightly sloping plateau at 0.9 – 0.75 V can be observed for the low rate intercalation of the 1:1 ratio sample. Based on contraction and expansion during cycling, cracks are formed which expose the Pt substrate (Figure 11). Hence, the Pt substrate becomes directly accessible for the electrolyte, which leads to additional reactions in this voltage region. Underpotential deposition (UPD) of lithium as well as reduction of the polycarbonate (PC, present in the electrolyte) can occur on the Pt substrate.[8]

However, since no plateaus are observed in this voltage region for the delithiation curve, the highly irreversible character points in the direction of PC reduction only. In fact, without this irreversible reaction occurring, the lithiation capacity achieved (approximately

130 mAh·g^{-1}) approaches the theoretical capacity of 156 mAh·g^{-1} accompanied with the LWO to $Li_5W_2O_7$ transition.

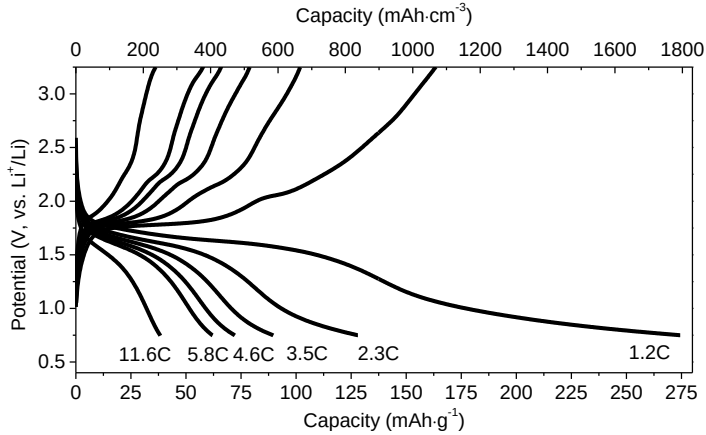

Figure 9: (de)Lithiation curves of 10 layers of Li:W 1:1 ratio precursor deposited on Pt substrates and annealed at 500°C for 1 hour in static air.

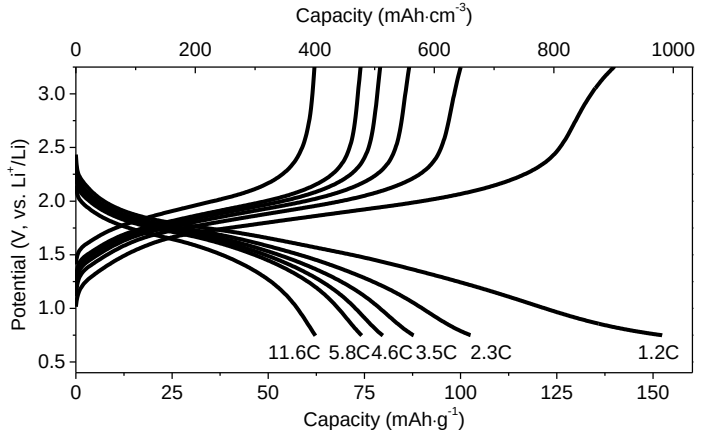

Figure 10: (de)lithiation curves of 10 layers of Li:W 1:2 ratio precursor deposited on Pt substrates and annealed at 500°C for 1 hour in static air.

Besides this, the 1:2 Li:W ratio films shows more of a sloping behaviour for its voltage plateau, possibly related to the presence of amorphous phases. This is underlined by the fact that little crystalline material is present for this sample after lithiation and the $Li_5w_2O_7$ phase can hardly be detected anymore (Figure 5).

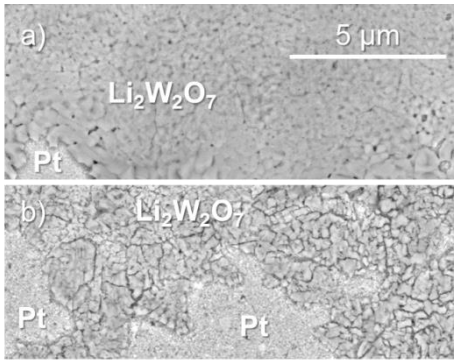

Figure 11: SEM micrograph (BSE) of (a) pristine and (b) cycled samples similar to Figure 9. Both samples were washed with ethanol prior to analysis.

Interestingly, at high current density the well-defined plateau of the 1:1 ratio sample diminishes, whereas the slightly sloped plateau of the 1:2 ratio is sustained to much greater order, especially during delithiation. Hence, the 1:2 ratio is more stable as compared to the 1:1 Li:W ratio films. Although a previous study claims that the stability of $Li_2W_2O_7$ is no major issue,[1] the results of the current study indicate that for thin film electrodes the lattice contraction of LWO upon lithiation is a large problem for practical applications. For films therefore, it seems more interesting to study mixed Li/W oxide phases in steads of the nearly phase pure LWO material.

4. Conclusion

While studying the Li/W precursor system, in an effort to further improve the results obtained by the WO_3 colloidal suspension, it can be concluded that the route chosen probably did not lead to

low temperature Li-doping of the WO_3 rods. The addition of LiOH still enables the formation of WO_3 rods, and a hypothesis was proposed for a solid reaction occurring between LiOH and WO_3 at temperatures from 300°C and up. This (primarily) results in $Li_2W_2O_7$ films, where the electrochemical properties can be steered by changing the Li:W ratio. With ratio of 1, nearly phase pure $Li_2W_2O_7$ films were obtained, which appeared to show strong electrochemical activity. However, the lattice contraction leads to cracking and a very low capacity retention, making the material unusable for thin film Li-ion batteries. On the bright side, the adjusted doping level (1:2 Li:W) forms stable secondary phases that partly stabilize the resulting hybrid material with improved (de)lithiation stability. However, from a practical point of view the performance of this hybrid material will probably fall behind undoped WO_3 upon prolonged cycling. Hence, other routes for improvement of WO_3 related materials should be considered.

5. References

[1] V. Pralong, G. Venkatesh, S. Malo, V. Caignaert, R. Baies, B. Raveau, **2014**, 8.

[2] Q. Zhong, Lithium and Hydrogen Intercalation into Electrochromic Materials : Tungsten Trioxides and Cesium Tungsten Oxides, **1992**.

[3] H. Kudio, *J. Nucl. Mater.* **1979**, *87*, 185.

[4] T. Chartier, L. Lostec, C. Gault, C. Chatillon, *J. Sol-Gel Sci. Technol.* **2002**, *23*, 27.

[5] P. Lv, D. Chen, W. Li, L. Xue, F. Huang, J. Liang, *J. Alloys Compd.* **2008**, *460*, 142.

[6] K. H. Cheng, M. S. Whittingham, *Solid State Ionics Commun.* **1980**, *1*, 151.

[7] S. Darmawi, S. Burkhardt, T. Leichtweiss, D. a. Weber, S. Wenzel, J. Janek, M. T. Elm, P. J. Klar, *Phys. Chem. Chem. Phys.* **2015**, *17*, 15903.

[8] D. Aurbach, M. Daroux, P. Faguy, E. Yeager, *J. Electroanal. Chem. Interfacial Electrochem.* **1991**, *297*, 225.

Part III - Chapter 9

3D structured WO_3 thin films as electrode for 3D Li-ion batteries

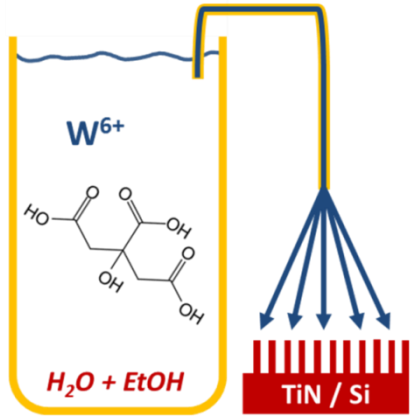

A large part of this chapter is submitted for publication:

E.J. van den Ham, G. Maino, G. Bonneux, W. Marchal, K. Elen, S. Gielis, F. Mattelaer, C. Detavernier, P.H.L. Notten, M.K. Van Bael and A. Hardy - *"3D all-solid-state Li-ion half-cells of lithium lanthanum titanate and tungsten oxide by ultrasonic spray deposition"*

Abstract

In this chapter a thorough study on the deposition of tungsten oxide on high aspect ratio microstructures is presented. Using ultrasonic spray deposition in combination with metal citrate chemistry, high quality WO_3 films were deposited on various high aspect ratio Si structures. These results were achieved by controlling the precursor chemistry, wetting properties, gel mobility and precursor decomposition. Finally, a proof of the potential of chemical solution deposition within the field of 3D thin-film all-solid-state batteries was achieved by coating of TiN / Si micro-cylinders with WO_3 using a minimized thermal budget to preserve the (oxidative) TiN current collector. This led to an near threefold electrode capacity enhancement per footprint area, due to the high surface to bulk ratio of the 3D WO_3 film.

1. Introduction

Tungsten oxide is an interesting negative electrode material for all-solid-state Li-ion batteries, as was pointed out in Chapter 7. Although it has a high (de)intercalation voltage just above 2 V (vs. Li^+/Li), it does enable combination with the less electrochemically stable solid electrolytes such as LLT. In addition, it has a high volumetric capacity that is vital for 3D Li-ion batteries. Finally, Chapter 7 showed stable cycling behaviour of WO_3 films, up to 100 cycles.

To further increase the capacity per footprint area, high quality 3D coatings are pursued. In Chapter 7, some progress was booked with the tungsten chloride based precursor, consisting of a colloidal suspension crystalline, rod-like tungsten oxide particles. For planar films good morphologies were obtained. However, initial results for 3D deposition of this colloidal precursor, using USD, yielded inhomogeneous coatings. As was shown in Chapter 5, using a citrate based precursor in combination with USD has a lot of potential for 3D deposition.[1] In this chapter, a citrate based tungsten precursor is developed, deposited and resulting films are studied; all in view of 3D thin film all-solid-state batteries.

2. Experimental

2.1 Synthesis of the citrate-based tungsten precursor

An aqueous tungsten citrate solution was prepared by adding tungstic acid (H_2WO_4, Sigma Aldrich, ≥99%) and citric acid hydrate (Sigma Aldrich, ≥99%) to a round bottom flask, dispersed with a small amount of water. This yellow suspension was stirred and heated at 120°C for two hours under reflux conditions. Subsequently, the pH was raised to pH > 12 with ammonia (NH_3, Merck, 32% in water), after which the solution was left to stir for 24 hours. After cooling, a transparent, slightly grey coloured, solution was obtained. Final pH = 8 with a concentration of 0.35 M, as was determined by ICP-AES (similar to Chapter 4). Before USD, the precursor was diluted and mixed with ethanol (10:9 water/ethanol volume ratio) to yield a 25 mM concentration.[1] Two different

tungstic acid to citric acid ratio were used, namely 1:4 and 2:3 (W:CA).

2.2 Deposition on substrates

Three different types of substrates were used for this study: (i) Pt (ii) Si trenches and (iii) 3D TiN (2x5); see Chapter 2 for details. All these substrates were cleaned by a UV/O_3 treatment at 60°C (40 min., Novascan PSD Pro Series) prior to deposition.

The precursors were deposited via USD (Exacta Coat, Sono-Tek cooperation) with a deposition temperature set at various temperatures. The liquid was dispensed at 0.2 ml·min^{-1} and the carrier gas pressure was set at 1.5 psi. The distance of the spray nozzle to the substrate was approx. 2.6 cm and moved with a speed of 100 mm·s^{-1}. The number of deposition cycles was varied. The deposited W-precursor was annealed at 600°C for 1 hour on the Pt planar substrate, 10 minutes at 500°C for 10 minutes on the other substrates.

2.3 Characterizations

TGA-DSC on powders was done as described in Chapter 5. The thermal decomposition profile of the W-precursor films was investigated by TGA-MS (TA instruments Q5000 with Pfeiffer quadrupool MS). The film was obtained by deposition of W-precursor deposition on thin borosilicate glass (VWR Micro Cover Glasses, thickness 0.08 mm) according to deposition conditions described in the paragraph. The coated glass was heated in a Pt sample crucible, ramped at 10°C·s^{-1} from room temperature to 500°C in static air.

Crystallization of the WO_3 films deposited on Pt was investigated by XRD, similar to the experiments in Chapter 4, including isXRD.[2] The morphology of annealed WO_3 films was investigated via SEM (FEI Quanta 200F). The thickness of the films was determined via SEM cross sections. In addition, the average film thickness of WO_3 films was determined by ICP-AES, after dissolving the deposited films in 32% ammonia in water solutions (overnight). Cyclic voltammetry and galvanostatic measurements were done in accord-

ance to the details mentioned in Chapter 7.[3] After 3 cycles of CV at 1 $mV \cdot s^{-1}$ between 1.75 and 3.5 V, galvanostatic measurements were done between the same cut-off voltages with various indicates (dis)charge currents. The test cell was operated at 20.0°C via a custom made temperature control chamber, inside an Ar-filled glovebox with water and oxygen concentrations < 1 ppm.

3. Results and discussion

3.1 Decomposition of the precursor gel

The decomposition of the W-precursor (1:4 W:CA molar ratio) is shown in Figure 1. After evaporation of residual water from the precursor gel due to incomplete drying, a first weight loss is observed at 140 and 180°C with endothermal features. This is followed by two minor exothermal decomposition steps at 365 and 485°C.

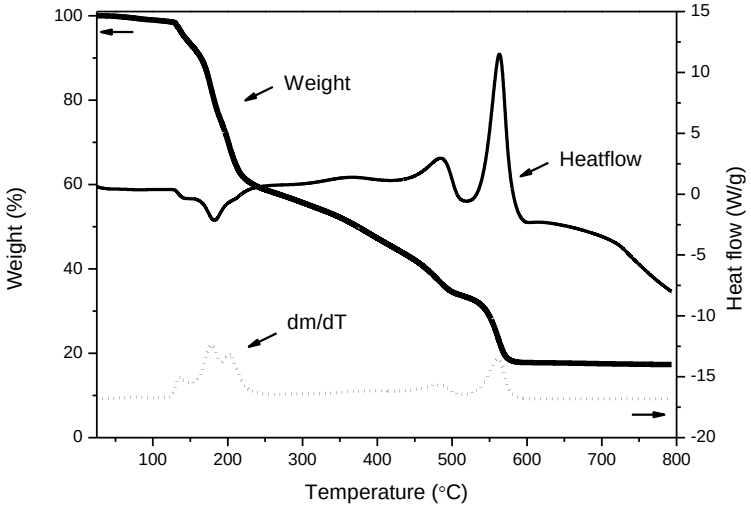

Figure 1: TGA-DSC analysis of the W-precursor gel (1:4 W:CA ratio) dried at 60°C, recorded at 10°C·min^{-1} in dry air (0.1 ml·min^{-1}).

Finally, a major weight loss is observed at 560°C during a strongly exothermic reaction. No significant weight loss is observed at higher temperatures, implying that the precursor is fully decomposed at 595°C. Since the tungsten precursor was prepared at pH 8, the solution consists of tungsten complexes with three oxo groups, one aqua group and a single citrate ligand coordinated to the tungsten, where the citrate co-exists in protonated and deprotonated form.[4]

The excess of citric acid required to completely dissolve the tungstic acid (4:1 citric acid to tungsten ratio) converted to ammonium citrate upon the addition of ammonia. Hence, features of ammonium citrate are visible in the decomposition profile shown in Figure 1.

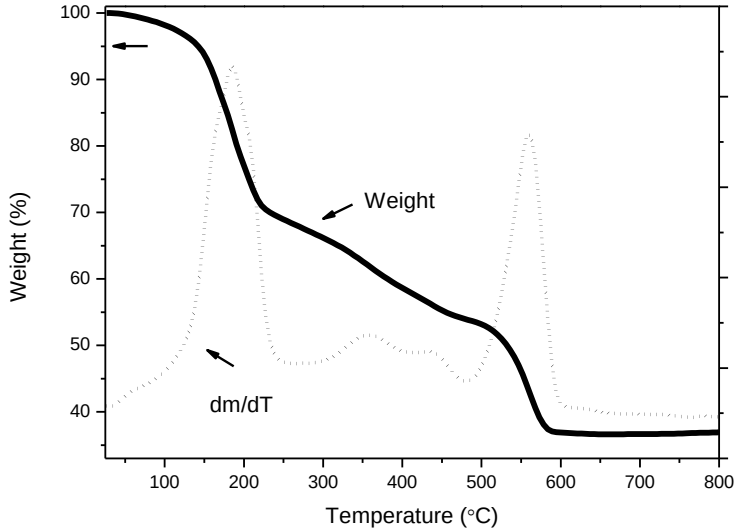

Figure 2: TGA-DTG analysis of the W-precursor powder (2:3 W:CA ratio) dried at 60°C, recorded at 10°C·min^{-1} in dry air (0.1 ml·min^{-1}).

The presence of ammonium citrate can most clearly be observed during the endothermic peaks at 140 and 185°C, ascribed to melt-

ing and decarboxylation reactions of the ammonium citrate, respectively.[5] The other features of the decomposition profile resemble decomposition of metal(per)oxo-citrato complexes studied before,[6–9] although the temperature at which these reactions occur are shifted for this tungsten based complex, due to specific tungsten-oxygen interactions.

For the 2:3 W:CA ratio precursor, the main features are the same, but differences can be noted (Figure 2). The first main loss shows one broad peak in the derivative curve, whereas the 1:4 ratio shows 3 more distinct peaks. In addition, the 480°C peak in the derivative curve present in the 1:4 ratio is almost absent in the 2:3 ratio case. Both differences are ascribed to a reduction of the relative amount of ammonium citrate present in the 2:3 precursor. Finally, less total weight loss occurs for 2:3 precursor, indicating at least 20% of the weight loss occurring in case of the 1:4 ratio precursor is due to decomposition of ammonium citrate.

3.2 Planar films: morphology and thickness

USD of the 4:1 precursor yielded smooth films (Figure 3), although strong deviation of film thickness was observed on different parts of the sample. To estimate the amount of material present on a certain area, ICP-AES analysis was done on films dissolved (1 to 2 cm^2) in ammonia. For 10 cycles of 25 mM deposition, an average film thickness of 280 nm was obtained (assuming 0% porosity and a density of 7.16 $g \cdot cm^{-3}$).

In contrast to the 1:4 W:CA ratio, the planar deposition of the 2:3 ratio precursor yielded films of very poor quality (not shown). Possibly, precipitation reactions occur during evaporation of the solvents (water and ethanol), which leads to poor film formation. This is suggested by the fact that no stable gelation behaviour was observed for this precursor, whereas the 4:1 CA:W ratio did yield typical citrate based homogeneous precursor gels (not shown).

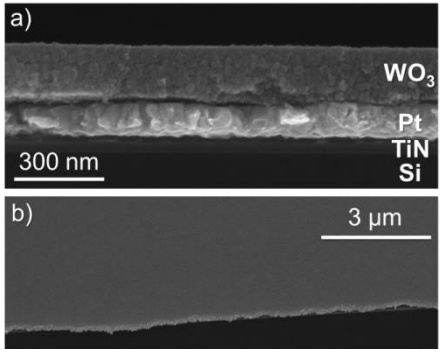

Figure 3: SEM micrograph showing secondary electron (SE) micrographs of a) cross sectional and b) tilted view of 10 cycles of W-precursor (25 mM, 1:4 ratio) deposition on a planar Pt substrate, annealed at 600°C for 1 hour in static air.

3.3 Planar films: electrochemical activity

Electrochemical activity of the WO_3 films as function of annealing temperature was checked by means of CV (Figure 5; 10 mV/s). At high annealing temperatures (500 and 600°C), the films appeared to be significantly more active compared to a 400°C anneal. Though crystalline WO_3 was found for all annealing temperatures measured (Figure 4), electrochemical activity seems to be less at lower temperatures, especially at 400°C. Clearly indicating why this occurs is a complicated matter, but the chlorine based precursor system shown in Chapter 7 may provide a few clues. With 400°C synthesis temperature, the citrate precursor is not fully decomposed. Hence, crystallinity at the same synthesis temperature may very well be lower compared to the Cl-based precursor shown in Chapter 7, which already consists of crystalline WO_3 at room temperature. This may the reason that the electrochemical activity of the WO_3 films prepared at 400°C is limited.

The CVs of the active WO_3 films show two main features while scanning at 10 $mV \cdot s^{-1}$; namely a broad reduction peak at 2.3 V and a less pronounced oxidation peak at 2.7 V.

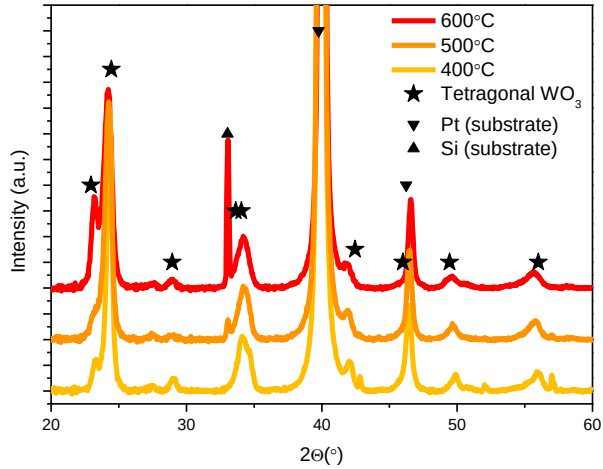

Figure 4: XRD pattern of 10 passes of W-precursor (25 mM, 1:4 ratio) deposition on a planar Pt substrate, annealed at various temperatures (indicated) for 1 hour in static air. Tetragonal WO_3 (JCPDS 01-85-807), Pt (JCPDS 01-87-0647) and Si (JCPDS 01-72-1088) phases are all indicated according to the stated reference.

The broad reduction peak of WO_3, annealed at 500 and 600°C (Figure 5), can be deconvoluted upon lowering the scan rate to 1 $mV \cdot s^{-1}$ (Figure 6). The reduction peak at 2.3 V in Figure 5 can be separated into two distinct reductions;[10] namely W^{6+} to W^{5+} at 2.708 V, which continues with a W^{5+} to W^{4+} reduction at 2.40 V. Although less intense, the oxidations reactions occur at 2.67 V for the W^{4+} to W^{5+} oxidation and 2.95 V for the W^{5+} to W^{6+} oxidation. This closely resembles values obtained for the Cl-based tungsten precursor in Chapter 7. In addition, a relatively large current can be observed below the main reduction voltage, i.e. below 2.0 V. The large currents at low voltages (i.e. during intercalation at 1.5 V, Figure 5) indicate either that degenerate energy levels of amorphous WO_3 phases are available for Li-intercalation,[11] or it may be due to kinetic factors.

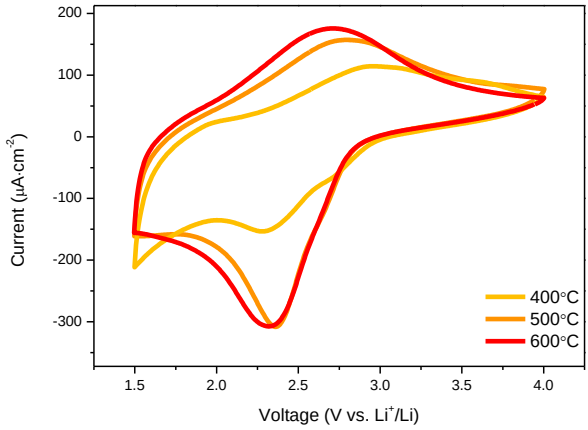

Figure 5: CVs of 10 passes of W-precursor (25 mM, 1:4 ratio) deposition on a planar Pt substrate, annealed at various temperatures (indicated) for 1 hour in static air. The samples were measured at 10 $mV \cdot s^{-1}$ in 1M $LiClO_4$ in PC.

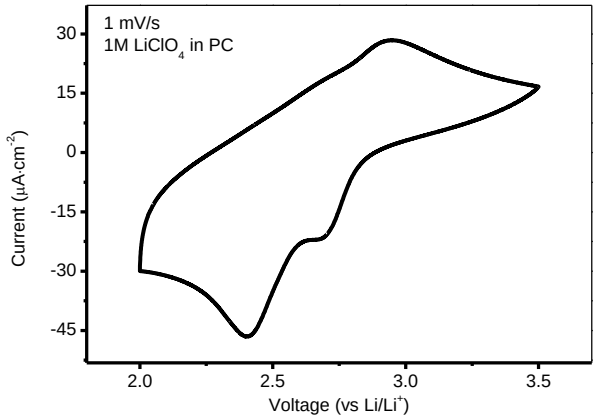

Figure 6: Cyclic voltammogram of 10 passes W-precursor (25 mM, 1:4 ratio) deposition on a planar Pt substrate, annealed at 600°C for 1 hour in static air The sample was measured at 1 $mV \cdot s^{-1}$ in 1.0 M $LiClO_4$ in PC.

Both can be explained as function of annealing temperature; the lower reduction potential at 1.5 V for the 400°C probably contains more amorphous phases and due to possible presence of organic precursor, the kinetics of this sample are poorer as well.

Galvanostatic (de)lithiation curves of the deposited WO_3, shown in Figure 7, exhibit typical behaviour observed for WO_3 (Chapter 7). At first, a short plateau at 2.7 V is observed, followed by a more extended plateau between 2.6 and 2.4 V. Both plateaus are associated with the intercalation of Li^+ in the tetragonal and cubic phase, respectively.[11,12] The cubic phase was not detected by XRD (Figure 4) on the pristine WO_3 films since the cubic phase is only formed upon sufficient lithiation of monoclinic and/or tetragonal WO_3.[11,12] As was expected based on the CV results (Figures 5 and 6), kinetic factors and / or amorphous phases appear to be present and responsible for intercalation at lower voltages, expressed in long slopes instead of charge plateaus.[13] However, since the capacity drops considerably at higher currents (Figure 7b), kinetic effects are more likely to be the cause of voltage slopes.

At a first glance, the lithiation capacity of 1405 $mAh \cdot cm^{-3}$ (197 $mAh \cdot g^{-1}$) for the films measured at low current densities of 1.2 $\mu A \cdot cm^{-2}$ / 0.07C (Figure 7a) appeared to be very high (232% of WO_3 theoretical capacity), especially compared to films measured with the 10 fold current density of 12 $\mu A \cdot cm^{-2}$ / 0.7C (Figure 7b) yielding 540 $mAh \cdot cm^{-3}$ (76 $mAh \cdot g^{-1}$, 89% of WO_3 theoretical capacity). However, a closer inspection of samples cycled at high and low current densities showed a striking macroscopic difference. As an electrochromic material, the lithiation of WO_3 is macroscopically visible on the film due to dark blue coloration of reduced tungsten.[10] After a single lithiation down to 2.0 V, with a high current density of 12 $\mu A \cdot cm^{-2}$ / 0.7C, a dark blue coloration of the sample measured was confined within the O-ring of the electrochemical cell (Figure 8a), as was expected. However, at a low current density of 1.2 $\mu A \cdot cm^{-2}$ / 0.07 C, the dark blue coloration was visible over all the substrate, including the area outside of the O-ring. XRD of selected areas (Figure 8b) indicated the same, since

the cubic WO_3 (implying lithiation occurred) was observed outside the O-ring area for low current densities.

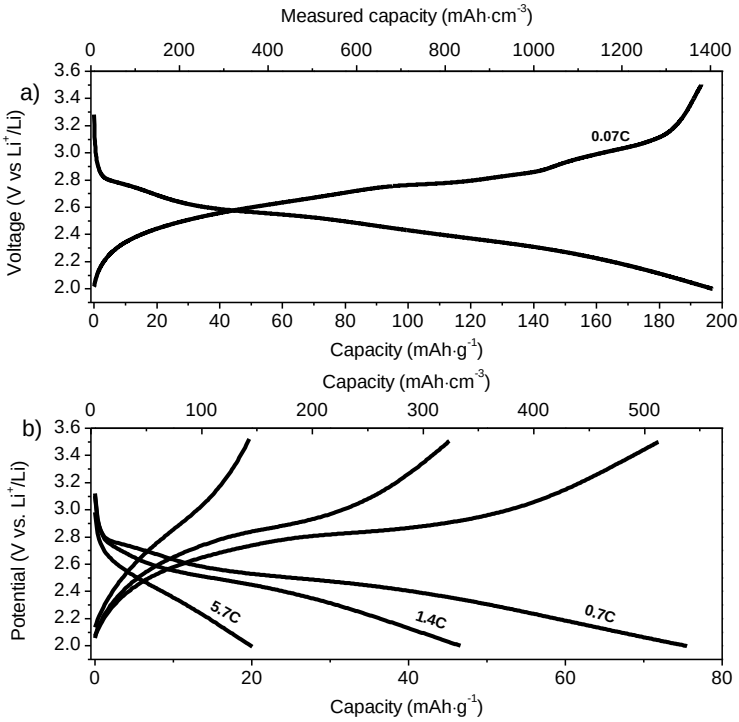

Figure 7: (de)lithiation curves of 10 cycles W-precursor deposition (25 mM, 1:4 ratio) on a planar Pt substrate, annealed at 600°C for 1 hour in static air. The samples were measured at various currents (indicated) in 1M $LiClO_4$ in PC.

Since electron transfer of the Pt to the WO_3 is possible all over the substrate, it is speculated that the relatively high Li-ion diffusion through the WO_3 film is responsible for this. With diffusion constants of lithium in (cubic) WO_3 in the order of 10^{-8} to 10^{-7} $cm^2 \cdot s^{-1}$,[14,15] a simple calculation (stochastic diffusion without convection) indicates that an average diffusion length in the mm range is feasible within the timescale of the experiment. However, unknown

effects caused by (long) exposure to the liquid electrolyte are not excluded, but more detailed analysis of this topic goes beyond the scope of this study. Besides coloration differences, XRD on isolated parts of the cycled films indicated that the area outside of the O-ring for high current densities consisted of tetragonal WO_3, whereas measurement of the same location on the film measured at low current density yielded a mixture of tetragonal and cubic WO_3 (Figure 8b). Note that the latter phase is associated with lithiated WO_3, this was shown before in Chapter 7.[11,12] Hence, the total capacity of the planar films measured at low current appear to yield unreliable capacity values due to this effect, and cycling at higher current density is required to yield more accurate capacity values.

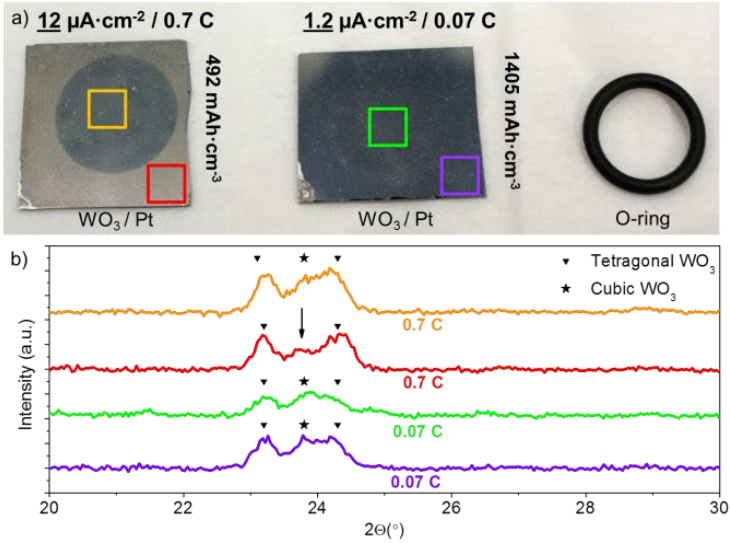

Figure 8: Comparison between WO_3 coated (10 cycles, 25 mM, 1:4 ratio) Pt samples after a single lithiation down to 2.0 V vs. Li^+/Li, at high and low current density. a) Photograph of the lithiated samples and O-ring used in the electrochemical cell, showing dark blue coloration of lithiated areas. The colored squares relate to b), XRD on isolated parts after cutting the samples.

3.4 Deposition of 3D films

3D depositions were studied in more detail as compared to previously shown in this thesis (Chapter 5 and 6). For this purpose, Si trenches were used which were approximately 30 µm deep and 30 µm wide, i.e. aspect ratio 1.[16,17] Upon deposition of the W-precursor at the optimized deposition temperature of 180°C, the heavy tungsten is clearly visible all over the trench using backscattered imaging (Figure 9), i.e. a fully covering WO_3 film is formed. The thickness is undoubtedly higher in the corners, which can be explained by a capillary pressure gradient, leading to enhanced flow towards the corners of the trench geometry.[18] However, the exact layer thickness quantification for the bottom corner is relatively difficult because of a possible reaction between the Si substrate and the tungsten oxide coating (forming e.g. tungsten silicates)[19] at the thickest part of the deposited layer. This is observed in a local difference in tungsten concentration as expressed in intensity difference of the backscattered micrograph.

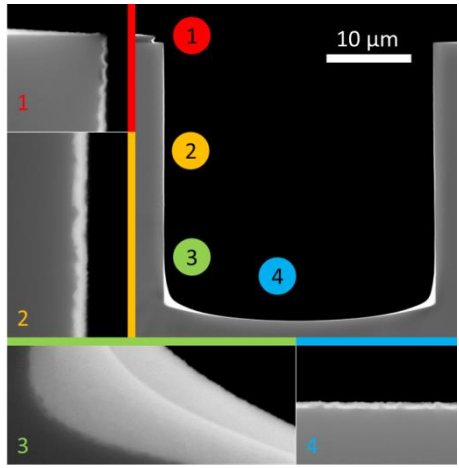

Figure 9: SEM micrograph of 10 cycles of 1:4 W-precursor deposition on Si trenches of 30 by 30 µm, annealed at 500°C for 10 minutes in static air. The numbers indicate enlarged micrograph locations.

Similar results were found for the deposition of W-precursor on a planar Si substrate (Figure 10), whereas this phenomenon did not occur in presence of a buffer layer such as Pt (Figure 3).

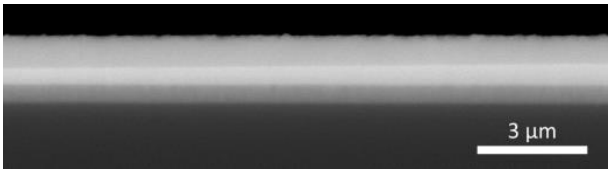

Figure 10: SEM micrograph showing backscattered (BSE) micrograph of 10 cycles of W-precursor (25 mM, 1:4 ratio) deposition on a planar Pt substrate, annealed at 500°C for 10 minutes in static air. The micrograph shows density differences, indicating reactivity of the deposited W-precursor with Si substrate during annealing.

Within the uncertainty explained above, the conformality is quantified to be at least 2%, i.e. the minimum layer thickness (top edge of the trench) divided by the maximum layer thickness (bottom corner). However, with increasing the aspect ratio of the trenches, i.e. decreasing the width of the trench, no conformal deposition was achieved (Figure 11). It is speculated that three main phenomena are causing the difference in conformality with respect to the high aspect ratio trenches: (i) available surface, (ii) thermophoretic forces and (iii) capillary forces and surface tension.

(i) The probability of a droplet reaching the bottom of the trenches scales with the area of the trench opening (top). As the width of the trench reduces, less material is able to reach and spread at the bottom of the trench.

(ii) Thermophoretic forces, i.e. a repelling force due to a large pressure gradient caused by a hot surface (Chapter 2),[20] is larger in case of small trenches. Carrier gas diffusion into a small trench is more difficult than in to a broad trench, leading to an increased thermophoretic force for smaller trench. Therefore, layer dep-

osition into deeper parts of the trenches is becoming more difficult.

(iii) A necking mechanism is observed, especially for the smallest trench. The surface tension of the gel leads to necking (contacting similar material) instead of wetting the dissimilar (Si) material down the trench.

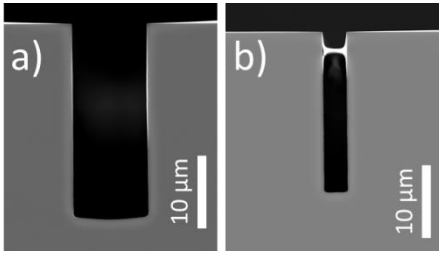

Figure 11: SEM micrograph of 10 cycles of W-precursor (25 mM, 1:4 ratio) deposition on a trench of a) 10 by 27 µm and b) 3.5 by 22.5 µm, annealed at 500°C for 10 minutes in static air.

3.5 Towards electrochemically active 3D films

The activity of the materials was demonstrated for planar substrates, in addition to full coverage of the non-planar trench structures with WO_3. However, the capacity gain due to the use of 3D architectures is yet to be shown using this approach.[21] In order to do so, a substrate with a high aspect ratio and a suitable current collector was required. For this study 3D TiN (2x5) was used, enabling a potential 8-fold capacity increase. Figure 12 shows that good coatings could be obtained by submitting these micro-cylinders to the W-precursor spray, with an aspect ratio of 10. Although only limited aspect ratios were achieved for the trenches – with a 'closed' structure – apparently higher aspect ratio 'open' micro-cylinder can indeed be coated with this approach (Figure 12).

It is speculated that the large openings (at the top) and beneficial capillary forces of these micro-cylinder structures attribute to this

difference. In addition, no material accumulates at the top of the cylinders, preventing the 'necking' that occurs in case of the trenches (Figure 11).

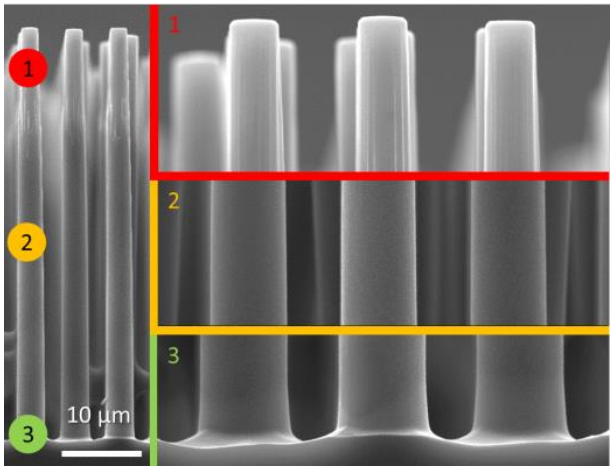

Figure 12: SEM micrograph of 10 cycles of W-precursor deposition (25 mM, 1:4 ratio) at 180°C on 3D TiN (2x5). The sample was annealed at 500°C for 10 minutes in static air.

Besides SEM micrographs (Figure 12), the charge discharge measurements also indicates the micro-cylinders are coated (c.f. Figure 15 and discussion). Although TiN (present on the micro-cylinders) is a good electronic conductor and is very interesting for this specific application because of its excellent (Li) barrier properties,[22] the TiN current collector is highly susceptible to oxidation at elevated temperatures in air, which leads to the formation of TiO_2 with a low electronic conductivity.[23] This therefore initially resulted in unmeasurable samples (not shown). Optimized annealing conditions were therefore sought, in order to achieve precursor decomposition, crystallization and electrochemical activity of the material (WO_3) on the one hand, and preserve the current collector (TiN) on the other. Isothermal heating at 500°C was applied to decompose the W-citrate, preserving the TiN current collector for a limited time. The non-isothermal TGA profile of the W-precursor

suggests that part the citrate complex is not fully decomposed at 500°C, even while applying an isotherm at this temperature (not shown). To make sure that heat transfer, volume and geometry differences concerning the decomposition analysis with isXRD and TGA were minimized, the TGA was measured on films instead of gels.[24] The result is a profile (Figure 13) showing continuous weight loss, but to a smaller extend than in case of gels (not shown), which is mostly attributed to higher heat transfer rates for film-based TGA. Using coupled MS, the weight loss could be assigned to CO_2 and OH^+; meaning that a continuous decomposition of organic groups occurs during the isothermal period at 500°C.

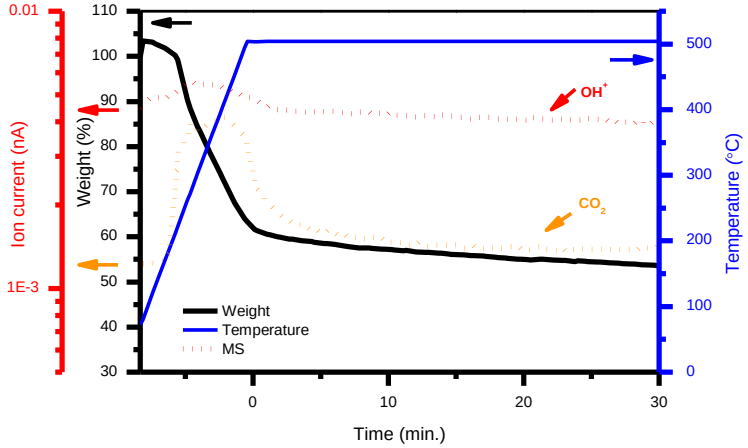

Figure 13: TGA-MS, showing isothermal analysis of a non-annealed 1:4 W-precursor film. The analysis was performed after USD of 20 cycles on a glass substrate at 180°C, using a heating rate of 10°C·min^{-1} in static air. OH^- and CO_2 gas evolution is assigned based on m/z values.

The slow combustion occurs together with a gradual increase of crystallinity, which was monitored in real-time using in-situ XRD (isXRD, Figure 14). Since W-O-W bonds are required for crystallization of WO_3, W-O-C bonds of the citrate complex should be di-

sattached or decomposed to form a crystalline W-O-W structure. The gradual but immediate crystallization was to be expected, since amorphous WO_3 is reported to crystalize at temperatures as low as 300°C.[25,26] This does however not fully exclude occurrence of residual organic groups after crystallization, because ammonium citrate (partly decomposed) residues or disattached citrate ligand groups can decompose after crystallization. The crystallization increases over time to form the tetragonal phase of WO_3.

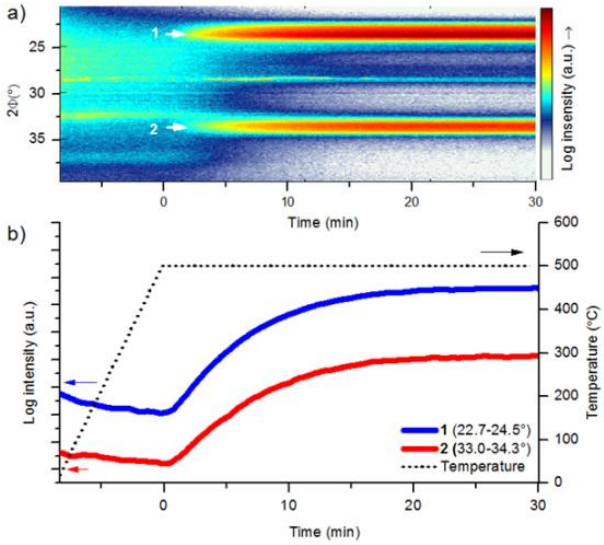

Figure 14: isXRD results showing (a) peak intensity as function of peak position and time, as well as (b) integrated peak intensities of specified diffraction peaks as function of temperature, and the applied temperature profile. Both graphs are based on the same sample; 1:4 W-citrate deposited using 10 cycles on 3D TiN (2x5) at a deposition temperature of 180°C. Integrated intensities of between 22.7°-24.5° (1) and 33.0°-34.3° (2) are shown.

A relatively large gain in intensity is found during the first 10 minutes of the isothermal anneal as approximately 75% of the

maximum intensity is reached within this time for the 23.5 and 33.5 peaks (Figure 14b). This matches with the H_2O and CO_2 evolution, which show a decreasing intensity over this period of time. Therefore, 10 minutes of isothermal heating was chosen as an optimum between film crystallization and preservation of the current collector (TiN) present on the micro-cylinders. Despite the presence of residual organic fragments and incomplete crystallization after only 10 minutes of isothermal heating at 500°C, active WO_3 present on the micro-cylinders could be cycled as shown in Figure 15a.

To study the effect of 3D deposition, the micro-cylinder sample was compared with a planar substrate exhibiting the same amount of material per footprint area (i.e. 2 deposition cycles for 2D, compared to 16 deposition cycles for 3D with an area enhancement factor of 8). In addition, the current applied to the 3D samples is 8 fold the current passed through the 2D samples (Figure 15a). The (de)lithiation curves look similar for 2D and 3D, although the capacity is significantly larger for the 3D sample. All curves in Figure 15a lack plateaus as observed on planar samples which were annealed longer at higher temperature. Instead, slopes are observed, especially during delithiation.

This is an indicator that primarily amorphous WO_3 is present in the samples, [13] despite indications of isXRD that part of the material is crystalline (Figure 14). Since these peaks are broad compared to a non-isothermal anneal at higher temperature (not shown), it can be concluded that the crystallites are rather small. It is speculated that these nanocrystals might lead to comparable, (quasi) amorphous (de)lithiation behaviour.

At 0.5C, the 2D sample is able to store a charge of 3.35 $\mu Ah \cdot cm^{-2}$ whereas the 3D sample stores 8.90 $\mu Ah \cdot cm^{-2}$ with a comparable current per equivalent coating area. This is a 2.6-fold capacity improvement which can be attributed to the benefit 3D geometries exhibit over 2D electrodes. This equals the capacity enhancement obtained for LTO deposited using CVD, on similar high aspect ratio substrates (TiN coated micro-cylinders).[17]

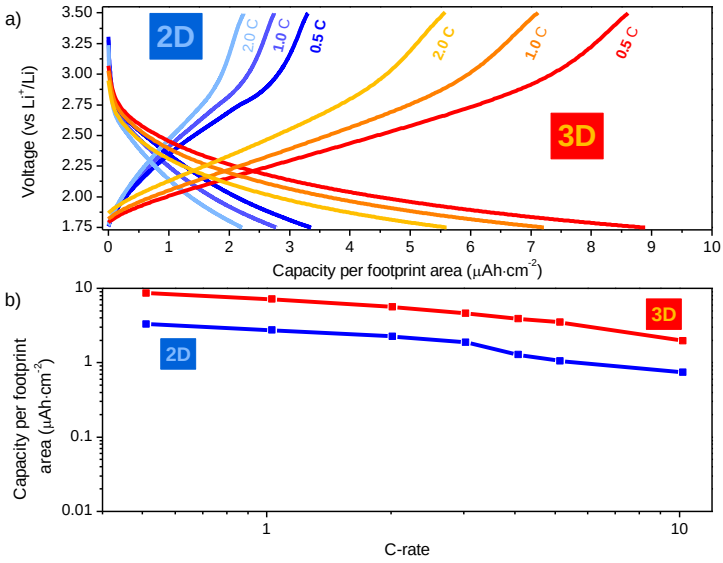

Figure 15: Galvanostatic cycling showing a) (de)lithiation curves and b) capacity / C-rate double log plot of (2D) TiN and 3D TiN (2x5) coated substrates, subjected to 1:4 W-precursor for 2 and 16 deposition cycles, respectively. The samples were annealed at 500°C for 10 minutes in static air and measured in 1.0 M $LiClO_4$ in PC at C-rates currents.

The de-lithiation kinetics of the 2D and 3D film are comparable between 0.5C to 10C (Figure 15b). The same slope of the lines in the double log plot indicates the same kinetic regime acts on both films,[27] where the 2.6 fold capacity enhancement is maintained at higher current densities. However, considering the total capacity enhancement, the 8-fold improvement which theoretically should be achievable, is not met at any measured current density. There are several reasons for not achieving the theoretical capacity increase:

(i) The deposition of W-citrate on the trench structures (Figure 9) illustrate that layer thickness cannot be con-

trolled perfectly, which leads to local differences in capacity of the layer and therefore lowering the capacity enhancement.

(ii) Although the coating is present on the micro-cylinders, certain defects can be observed. These defects could be prevented by lowering the amount of ammonium citrate in the W-precursor (3:2 citric acid to tungsten ratio), this came at the cost of incomplete coverage of the micro-cylinders (not shown).

(iii) The current collector remains an issue; upon cycling, the voltage drop at the start of the measurement is significantly larger for the 3D samples than for the 2D samples. This illustrates that higher resistance is presence in these 3D samples, which is primarily attributed to the partial oxidation of the TiN current collector (20 nm). Since the TiN current collector is much thicker for the 2D samples (80 nm), and the applied currents are much lower, this leads to lower IR-drop for planar films, compared to the 3D counterparts.

4. Conclusion

Planar and 3D deposition of WO_3 has been shown in this chapter. Although functionality of the planar films are comparable to other studies (Chapter 7), especially the fact that 3D measurements could be established by optimizing the annealing conditions is regarded as a major step forward. The combination of low crystallization temperature and high volumetric capacity are strong benefits of this electrode material that is often overlooked. The near threefold capacity enhancement of the 3D-structured WO_3 negative electrodes is an important indicator of the versatility of wet-chemical method in combination with ultrasonic spray deposition, but it also indicates that further improvement is possible and necessary. Obtaining a suitable current collector with a larger thermal budget is of high importance, as this is the limiting factor while probing the performance of 3D-structured electrode materials (c.f. Chapter 11). Nevertheless, these results open up new routes for low cost,

3D all-solid-state Li-ion batteries, including flexibility of (instable) solid electrolyte choice such as LLT.

5. References

[1] S. Gielis, A. Hardy, M. K. Van Bael, *Conformal Coating on Three-Dimenstional Substrates*, **2015**, EP 2 947 178 A1.

[2] W. Knaepen, C. Detavernier, R. L. Van Meirhaeghe, J. Jordan Sweet, C. Lavoie, *Thin Solid Films* **2008**, *516*, 4946.

[3] M. E. Donders, W. M. Arnoldbik, H. C. M. Knoops, W. M. M. Kessels, P. H. L. Notten, *J. Electrochem. Soc.* **2013**, *160*, A3066.

[4] J. J. Cruywagen, L. Krüger, E. A. Rohwer, *J. Chem. Soc. Dalt. Trans.* **1991**, 1727.

[5] M. Rajendran, M. Subba Rao, *J. Solid State Chem.* **1994**, *113*, 239.

[6] A. Stanulis, A. Hardy, C. De Dobbelaere, J. D'Haen, M. Van Bael, A. Kareiva, *J. Sol-Gel Sci. Technol.* **2012**, *62*, 57.

[7] N. Peys, Y. Ling, D. Dewulf, S. Gielis, C. De Dobbelaere, D. Cuypers, P. Adriaensens, S. Van Doorslaer, S. De Gendt, A. Hardy, M. K. Van Bael, *Dalton Trans.* **2013**, *42*, 959.

[8] A. Hardy, D. Mondelaers, M. K. Van Bael, J. Mullens, L. C. Van Poucke, G. Vanhoyland, J. D'Haen, *J. Eur. Ceram. Soc.* **2004**, *24*, 905.

[9] I. Truijen, M. K. Van Bael, H. Van Den Rul, J. D'Haen, J. Mullens, *J. Sol-Gel Sci. Technol.* **2006**, *41*, 43.

[10] S. Darmawi, S. Burkhardt, T. Leichtweiss, D. a. Weber, S. Wenzel, J. Janek, M. T. Elm, P. J. Klar, *Phys. Chem. Chem. Phys.* **2015**, *17*, 15903.

[11] K. H. Cheng, M. S. Whittingham, *Solid State Ionics Commun.* **1980**, *1*, 151.

[12] Q. Zhong, J. R. Dahn, K. Colbow, *Phys. Rev. B* **1992**, *46*, 2554.

[13] J. Garciacanadas, *Solid State Ionics* **2004**, *175*, 521.

[14] A. Yu, N. Kumagai, Z. Liu, J. Y. Lee, *J. Solid State Electrochem.* **1998**, *2*, 394.

[15] I. D. Raistrick, A. J. Mark, R. A. Huggins, *Solid State Ionics* **1981**, *5*, 351.

[16] J. Xie, J. F. M. Oudenhoven, P.-P. R. M. L. Harks, D. Li, P. H. L. Notten, *J. Electrochem. Soc.* **2014**, *162*, A249.

[17] J. Xie, P.-P. R. M. L. Harks, D. Li, L. H. J. Raijmakers, P. H. L. Notten, *Solid State Ionics* **2016**, *287*, 83.

[18] M. Dong, I. Chatzus, *J. Colloid Interface Sci.* **1995**, *172*, 278.
[19] J. ten Dam, D. Badloe, A. Ramanathan, K. Djanashvili, F. Kapteijn, U. Hanefeld, *Appl. Catal. A Gen.* **2013**, *468*, 150.
[20] D. Perednis, L. J. Gauckler, *J. Electroceramics* **2005**, *14*, 103.
[21] J. W. Long, B. Dunn, D. R. Rolison, H. S. White, *Chem. Rev.* **2004**, *104*, 4463.
[22] L. Baggetto, J. F. M. Oudenhoven, T. Van Dongen, J. H. Klootwijk, M. Mulder, R. A. H. Niessen, M. De Croon, P. H. L. Notten, *J. Power Sources* **2009**, *189*, 402.
[23] N. C. Saha, H. G. Tompkins, *J. Appl. Phys.* **1992**, *72*, 3072.
[24] W. Marchal, C. De Dobbelaere, J. Kesters, G. Bonneux, J. Vandenbergh, H. Damm, T. Junkers, W. Maes, J. D'Haen, M. K. Van Bael, A. Hardy, *RSC Adv.* **2015**, *5*, 91349.
[25] M. Regragui, M. Addou, A. Outzourhit, J. C. Bernede, E. El Idrissi, E. Benseddik, A. Kachouane, *Thin Solid Films* **2000**, *358*, 40.
[26] K. Nishio, T. Tsuchiya, *Sol. Energy Mater. Sol. Cells* **2001**, *68*, 279.
[27] T. Dobbelaere, F. Mattelaer, J. Dendooven, P. Vereecken, C. Detavernier, *Chem. Mater.* **2016**, *28*, 3435.

Part III - Chapter 10

3D all-solid-state Li-ion half-cells of LLT and WO_3 by ultrasonic spray deposition

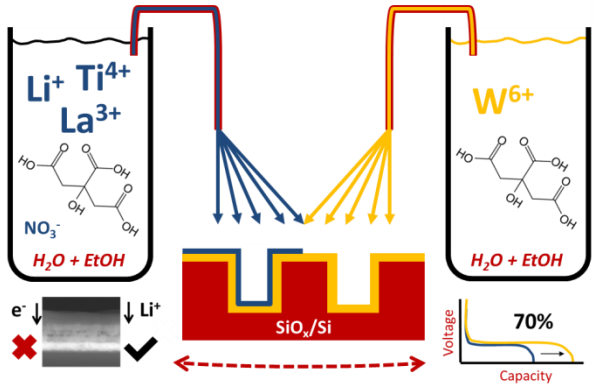

A large part of this chapter (together with Chapter 9) is submitted for publication:

E.J. van den Ham, G. Maino, G. Bonneux, W. Marchal, K. Elen, S. Gielis, F. Mattelaer, C. Detavernier, P.H.L. Notten, M.K. Van Bael and A. Hardy - *"3D all-solid-state Li-ion half-cells of lithium lantha-num titanate and tungsten oxide by ultrasonic spray deposition"*

Abstract

By USD of solution precursors, conformal deposition on non-planar surfaces of amorphous LLT solid electrolyte on top of tungsten WO_3 negative electrode has been studied, the results are presented in this chapter. First, the combination of both materials was studied in a planar configuration. Via ferrocenium reduction studies, the electron blocking properties of the LLT solid electrolyte were shown – vital for an all-solid-state device. In addition, cyclic voltammetry indicated activity of the LLT electrolyte as a Li-ion conductor in a half-cell configuration. Galvanostatic measurements indicate that up to 70% of the maximum pristine capacity could be reached for the half stacks. Finally, 3D depositions were done on various micro-sized Si template structures, showing fully covering LLT films on top of 3D WO_3 films. The results of this study mark the start of 3D material integration for 3D thin film all-solid-state Li-ion batteries via CSD.

1. Introduction

In a short summary, several building blocks of 3D thin film an all-solid-state Li-ion battery are shown to be in place. For the solid electrolyte, Chapter 4 and 5 showed LLT syntheses and characterization. Although 3D deposition was achieved (Chapter 5), the significance of these findings remains to be proven. Especially the morphology of the crystalline films remains a concern. Amorphous LLT was proposed in Chapter 4, improving the morphology at the cost of Li-ion conductivity. Unfortunately, synthesis of more stable, garnet based LLZO solid electrolyte left little room for device integration due to the need of epitaxial stabilization and high thermal budgets (Chapter 6). Therefore, the focus shifted towards alternative strategies.

In Chapter 7 a different approach was proposed, instead of choosing the solid electrolyte material to match the negative electrode, the approach was inversed. This led to the formation of active WO_3 films with good cyclability. Further improvement of this material was attempted in the form of lithium doping (Chapter 8), but due to the contraction during lithiation, this appeared to be a dead end for a thin film all-solid-state battery. In addition, the (de)intercalation voltage shifted to values outside the stability window of the LLT. Hence, planar and 3D deposition of tungsten oxide (WO_3) was shown (Chapter 9) as the start of a possible all-solid-state half-cell. In this chapter, the combination of LLT and WO_3 is studied in view of device integration.

2. Experimental

2.1 Synthesis of the tungsten oxide films

For 3D deposition purposes, the citrate precursor was selected for this study. The precursor synthesis for the W-precursor (25 mM, 1:4 M:CA ratio) was reported in Chapter 9, as well as the deposition conditions for USD.

2.2 Synthesis of the LLT / WO_3 stacks

In view of limiting the thermal budget, the citrate-nitrate precursor was used for this study. The Li-La-Ti-precursor synthesis was reported in chapter 4. Deposition was done as reported in Chapter 5, although WO_3-coated Pt substrates were used, annealed at 600°C (Chapter 9). Planar Pt and Si trench structures were used for this study, as described in chapter 9.

2.3 Characterization

SEM, XRD and electrochemical analyses were done in accordance to the description found in Chapter 9. To check the electronic conductivity of the films, a ferrocenium reduction experiment was done. Cyclic voltammetry of the annealed samples were measured at 10 $mV \cdot s^{-1}$ for 5 cycles in 0.1 M of ferrocene (Sigma Aldrich, ≥98%) in anhydrous acetonitrile (ATN; VWR, ≥99,9%), using $Ag/AgNO_3$ (0.01 M) in 0.1 M $Bu4NPF_6$ as reference electrode. Deposited films were used as working electrode. The ferrocene solution was bubbled in N_2 for 2 to 3 mins before the start of the experiment.

3. Results and discussion

3.1 Decomposition of the precursor gel

Figure 1a shows WO_3 similar to the ones showed in Chapter 9. The backscattering micrograph shows a clear difference between the Pt and WO_3. Upon deposition of the LLT electrolyte on top, a slightly darker layer of 120 nm can be found on top of the sandwiched WO_3 (Figure 1b). To ensure a dense morphology of the layer, a lower precursor concentration (10 mM) was chosen to lower the growth rate (6 $nm \cdot cycle^{-1}$). The LLT has a very smooth morphology, due to the fact that the material remained amorphous at 500°C. Further heating towards the crystalline perovskite phase was not attempted, since previous attempts regarding a spin-coated film led to crack formation (Chapter 4).

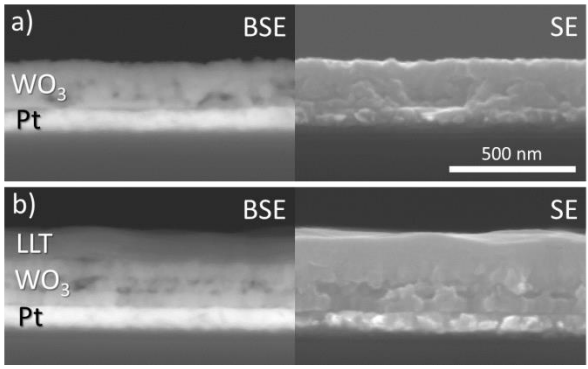

Figure 1: Cross-section SEM micrograph showing BSE and SE micrographs. a) 10 cycles of W-precursor (25 mM) deposition on a planar Pt substrate, annealed at 600°C and b) 20 cycles of Li-La-Ti-precursor (10 mM) deposition on WO_3/Pt substrate, annealed at 500°C. All anneals were carried out for 1 hour in static air.

3.2 Phase formation of LLT-coated WO_3 films

The XRD analysis (Figure 2) indicates that predominantly tetragonal WO_3 (prepared with 600°C annealing) remains present after the LLT coating (prepared with 500°C annealing). Since the LLT is amorphous after the 500°C anneal (Chapter 4), no additional peaks were expected for this material. However, a close analysis of the lower scattering angles revealed that minor amounts of LWO are present due to a solid-state reaction as a result of lithium diffusion from the LLT layer to the WO_3 underneath. LWO is known as a negative electrode material with high Li-ion mobility (Chapter 8). Although it has a larger storage capacity than crystalline WO_3, the intercalation voltage (1.55 V vs. Li^+/Li) is too low to be compatible with the LLT electrolyte, which suffers from a Ti^{4+} reduction at lower voltages.[1,2] Hence, for this study the LWO is regarded as an undesirable but unavoidable secondary phase for the LLT-WO_3 half-cell.

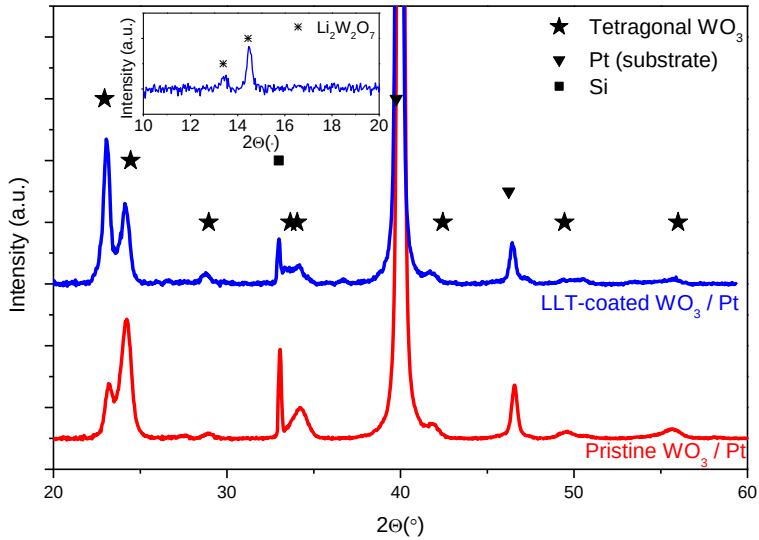

Figure 2: X-ray diffractogram of 10 deposition cycles of W-precursor deposition on a planar Pt substrate, annealed at 600°C for 1 hour in static air (red) and LLT-coated WO_3 (prepared under the same conditions) annealed at 500°C for 1 hour in static air (blue). Tetragonal WO_3 (JCPDS 1-85-807), Pt (JCPDS 1-87-647), Si (JCPDS 1-72-1088) and LWO (JCPDS 28-598) phases are all indicated according to the stated reference.

3.3 Electrochemical analysis of LLT-coated WO_3 films

First of all, electrochemical experiments were carried out to study the electron-blocking properties of the spray deposited electrolyte.[3] Figure 3 shows a cyclic voltammogram of pristine and LLT-coated samples in presence of ferrocene in a non-aqueous liquid electrolyte. Upon increasing the working electrode potential, ferrocene is oxidized to ferrocenium because of electron-transfer at the surface of the sample (Equation 1[3]).

$$Fe(C_5H_5)_2 \rightarrow [Fe(C_5H_5)_2]^+ + e^- \quad \textbf{(1)}$$

For pristine WO_3, this clearly occurs, as expressed in the oxidation and reduction peaks. The semi-conducting WO_3 film clearly leads to electron-transfer, facilitating a ferrocene oxidation and ferrocenium reduction. Comparing this with the LLT-coated WO_3, no reactivity of ferrocene can be observed for this sample. This implies that no surface is available for electron transfer although the ferrocene is fully exposed to the LLT surface. Hence, the lack of electron transfer indicates that the LLT electrolyte film is strongly electron insulating, which is crucial for application in an all-solid-state Li-ion battery.

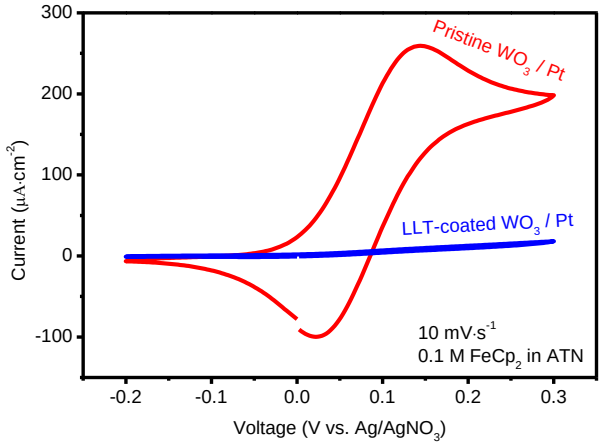

Figure 3: Cyclic voltammogram showing ferrocenium reduction for of 10 cycles W-precursor deposition on a planar Pt substrate, annealed at 600°C for 1 hour in static air (red) and LLT-coated WO_3 (prepared under the same conditions) annealed at 500°C for 1 hour in static air (blue). The samples were measured at 10 $mV \cdot s^{-1}$ in 0.1 M of ferrocene in anhydrous acetonitrile.

Besides the Li-ion conductivity of the materials is of crucial importance for the function of the electrolyte. From Chapter 4, a Li-ion conductivity of amorphous LLT could be derived in the order of 10^{-8} $S \cdot cm^{-1}$. In the current study USD was used instead of spin-coating for 3D deposition purposes, but the same nitrate-citrate precursor was used in both cases. Therefore, pristine and LLT coated WO_3 were (de)lithiated in order to confirm the Li-ion conductivity of the electrolyte. First of all, it must be noted that the electrochemical window is limited to values suitable for the LLT electrolyte, since Chapter 4 showed that strong reduction reactions occur below 1.7 V. To make sure no reduction of Ti^{4+} occurs, the lower limit is therefore fixed to 2.0 V vs. Li^+/Li. Comparing the cyclic voltammogram of the LLT-WO_3 stack to pristine WO_3 reveals that a current drop occurs (Figure 4). In addition, a larger overpotential (approximately 50 mV) is observed in case of the LLT-coated WO_3 sample. Although passivating effects of the electrolyte deposition and anneal are not excluded, possibly related to the formation of the LWO phase (Figure 2), both the drop in current and the increase in over-potential can be related to the resistance induced by the amorphous solid electrolyte layer on top of the WO_3. By calculating the ohmic drop from Figure 4, combined with the 120 nm thickness of the amorphous LLT (Figure 1), the Li-ion conductivity of the solid electrolyte amounted 10^{-9} $S \cdot cm^{-1}$ for the LLT/WO_3 stack. In comparison to Chapter 4, where amorphous LLT was deposited on Pt or TiO_2, the conductivity appears to be an order of magnitude lower for the deposition on WO_3. The reactivity with WO_3 (LWO formation, c.f. Figure 2) and different morphology of the USD deposited films are thought to be the cause of the lower Li-ion conductivity.

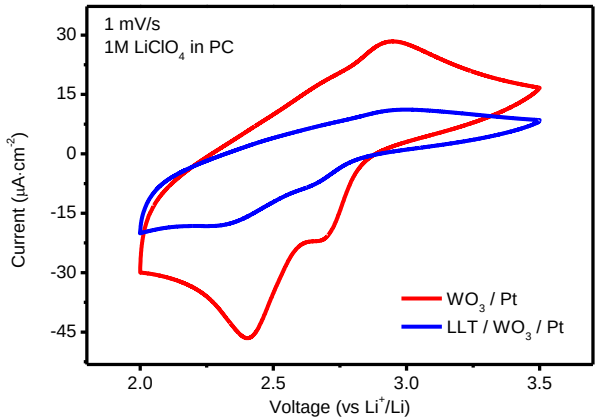

Figure 4: Cyclic voltammogram of a WO_3-coated planar Pt substrate, annealed at 600°C for 1 hour in static air (red) and LLT-coated WO_3 on a planar Pt substrate (prepared under the same conditions) annealed at 500°C for 1 hour in static air (blue). The samples were measured at 1 $mV \cdot s^{-1}$ in 1M $LiClO_4$ in PC.

Now the electronic insulation and Li-ion conductivity of the amorphous LLT film has been confirmed, the storage capacity of the LLT-WO_3 stacks is studied. At first, relatively high current densities were used (Figure 5) to make sure the confined volume approximation is valid (c.f. Chapter 9). However, this yields rather low capacities as compared to pristine WO_3 films. With the LLT coating, a current density of 12 $\mu A \cdot cm^{-2}$ / 0.7 C yields a capacity of approximately 150 $mAh \cdot cm^{-3}$, compared to 540 $mAh \cdot cm^{-3}$ for pristine WO_3 with the same current density.

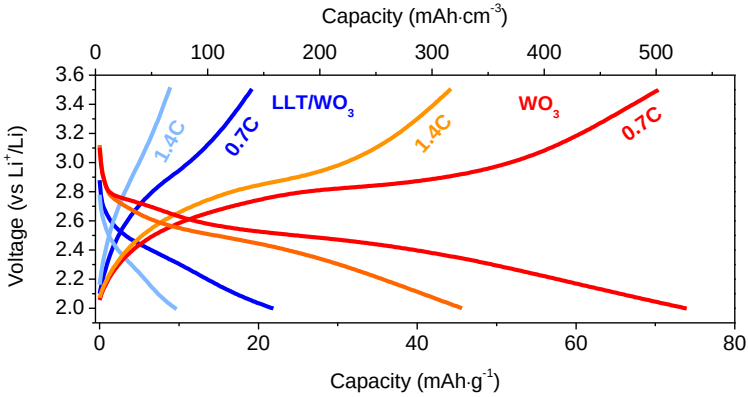

Figure 5: Galvanostatic measurements of 10 cycles W-precursor deposition on a planar Pt substrate, annealed at 600°C for 1 hour in static air (red) and LLT-coated WO_3 (prepared under the same conditions) annealed at 500°C for 1 hour in static air (blue). The samples were measured at various currents in 1.0 M $LiClO_4$ in PC.

At lower current densities a much higher capacity is reached by the LLT-coated WO_3 (Figure 6). However, since the confined volume approximation is not valid, normalized capacities are shown (i.e. pristine WO_3 lithiation = 1.0). The (de)lithiation curves of the LLT-coated WO_3 (Figure 6) exhibit similar features as the pristine WO_3 – including the charge plateaus of the WO_3 phases. The capacity reduction can partly be ascribed to the presence of the inactive LWO phase, as was shown by XRD (Figure 2). However, the other main factor limiting the capacity is related to a decreased rate performance induced by the LLT layer; over 65% of the pristine capacity is reached at 0.07C, but this drops to 31% at 0.7C. Thus, the smooth morphology and electronic blocking ensure crucial functions of the LLT electrolyte, but the amorphous character comes at a cost: reduced rate performance of the half-cell.

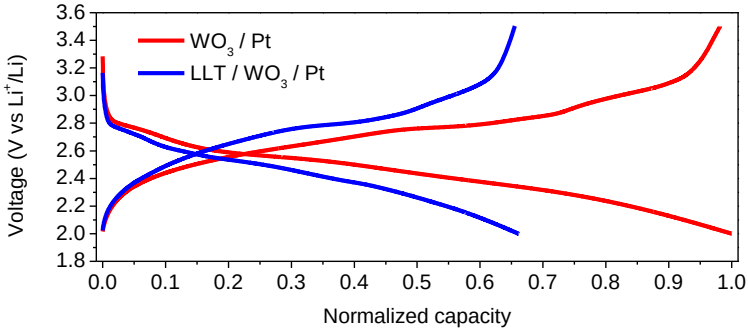

Figure 6: Galvanostatic measurements of 10 cycles W-precursor deposition on a planar Pt substrate, annealed at 600°C for 1 hour in static air (blue) and LLT-coated WO_3 (prepared under the same conditions) annealed at 500°C for 1 hour in static air (red). The samples were measured at 1.2 $\mu A \cdot cm^{-2}$ / 0.07C in 1.0 M $LiClO_4$ in PC, capacities are normalized for pristine WO_3.

3.4 LLT/WO_3 half cells on non-planar substrates

In accordance to the approach shown in Chapter 9, Si trench structures were coated with WO_3. Next, LLT was deposited on top. For comparison, the same results shown in Chapter 9 are shown again (Figure 7a). To allow successful stacking, only the trench with aspect ratio 1, coated with a fully covering WO_3 coating, was used for the LLT-precursor deposition. The result in Figure 7b shows that a conformal LLT solid electrolyte layer is deposited on top of the WO_3 layer. In addition, the quantified conformality (33%) of the LLT layer is much better than for the WO_3 deposition (at least 2%), since the difference in thickness at the edge and bottom are considerably smaller. Besides possible differences in the surface chemistry, the large difference is probably generated by the fact that the sharp edge present in the uncoated trench, is no longer present after coating with WO_3. Hence, the LLT layer covers a curved surface instead of a sharp corner, which is beneficial for the deposition homogeneity. Although there is room for optimization of layer

thicknesses, these results indicate that stacked fully covering coatings are possible using a wet-chemical approach.

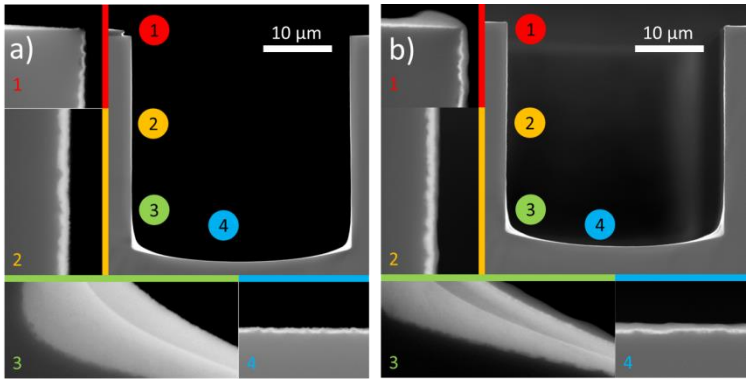

Figure 7: a) SEM BSE micrograph of 10 cycles of W-precursor deposition on a trench of 30 by 30 µm, annealed at 500°C for 10 minutes in static air and b) additional deposition of 10 layers of Li-La-Ti-precursor deposition at 200°C with an anneal at 500°C for 10 minutes. Numbers indicate enlarged micrograph locations.

3.5 Functional 3D half-cells

Based on the results shown for the trenches and micro-cylinders shown previously (Chapter 5), the next step would be to measure 3D all-solid-state half cells consisting of LLT / WO_3 / TiN / Si micro-cylinders. Although thicker films were observed on the bottom of the micro-cylinders (not shown), it was impossible to tell with certainty if the stack was present on the pillars due to a lack of contrast between the (thin) layers. The trench structure analysis proved to be a much more valuable approach (Figure 7). Besides the ambiguity about the presence of a LLT coating on the WO_3 coated micro-cylinders, the thermal budget used (10 + 10 minutes at 500°C for both WO_3 + LLT) appeared to be too large for the TiN current collector, or too short to yield active LLT, since no capacity could be measured (not shown).

4. Conclusion

With smooth morphologies and relatively mild thermal budgets, the combination of citrate and citrate-nitrate chemistry yields functional planar half-cells of LLT on top of WO_3. The traces of secondary LWO phase identified in the LLT/WO_3 half-cell is a mere indicator of the reactivity of combined oxide materials during stacking processes, and clarifies the slightly reduced half-cell capacity at low (dis)charge currents. Nevertheless, these results form the start to tackle problems related to the Achilles' heel of the all-solid-state 3D Li-ion battery research: 3D deposition of suitable solid electrolyte materials. In addition, the achievement of stacked oxide materials using USD – in 3D – is a major step forward in terms of possible new material architectures. Especially so, because both layers were deposited with an easy-to-upscale process which can possibly be applied to many other materials and devices as well.

5. References

[1] P. Knauth, *Solid State Ionics* **2009**, *180*, 911.
[2] S. Stramare, V. Thangadurai, W. Weppner, *Chem. Mater.* **2003**, *15*, 3974.
[3] Y.C. Perng, J. Cho, S. Y. Sun, D. Membreno, N. Cirigliano, B. Dunn, J. P. Chang, *J. Mater. Chem. A* **2014**, *2*, 9566.

Part IV - Chapter 11

3D indium tin oxide electrode by ultrasonic spray deposition for 3D current collection applications

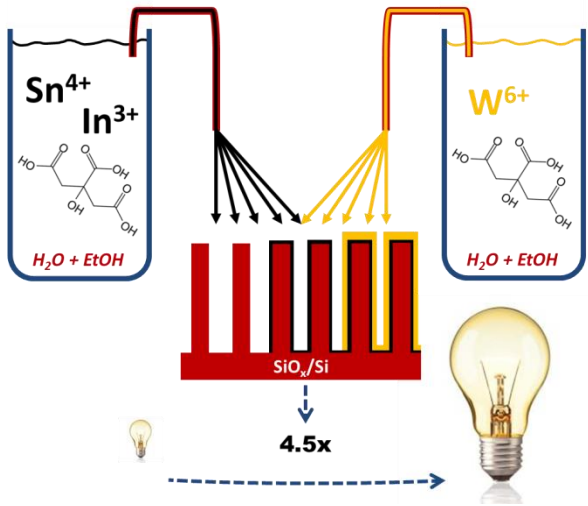

This chapter has been published:

E.J. van den Ham, K. Elen, G. Bonneux, G. Maino, P.H.L. Notten, M.K. Van Bael and A. Hardy - *"3D indium tin oxide electrodes by ultrasonic spray deposition for current collection applications"* – Journal of Power Sources 348 (2017), 130-137

Abstract

In this chapter, 3D structured ITO thin films are synthesized and characterized as a 3D current collector applications. Using metal citrate chemistry in combination with USD, a low cost wet-chemical method has been developed to achieve conformal ITO coatings on non-planar scaffolds. Although there is room for improvement with respect to the resistivity ($9.9 \cdot 10^{-3}$ Ω·cm, 220 nm thickness), high quality 3D structured coatings were shown to exhibit conductive properties based on ferrocene reactivity. In view of applications in Li-ion batteries, the electrochemical stability of the current collector was investigated, indicating that stability is guaranteed for voltages of 1.5 V and up (vs. Li^+/Li). In addition, subsequent 3D coating of the ITO with WO_3 as a negative electrode (battery) material confirmed the 3D ITO layer functions as a proper current collector. Using this approach, an over 4-fold capacity increase was booked for 3D structured WO_3 in comparison to planar samples, confirming the current collecting capabilities of the ITO layer. Therefore, the 3D ITO presented is considered as a highly interesting material, for 3D battery applications and beyond.

1. Introduction

In a world seeking a sustainable future, smart materials and structures are opted for energy harvesting, storage and consuming applications. 3D structure enhancements are often applied to enhance active material performance, mostly based on a kinetic advantage due to a better current distribution per (active) material volume. Examples of this technology can be found within the field of hydrogen technology,[1] 3D supercapacitors,[2] PV applications,[3] 3D lighting (LEDs)[4,5] and battery technology.[6,7] For 3D LED applications, which are based on the enlargement of active surface area for light generation, 3D structured transparent conductive oxides (TCO's) can contribute to highly efficient 3D LEDs.[4] Upon successful implementation of such a 3D electrode, further improvement of these devices would be possible as these systems currently lack a transparent, 3D structured current collector as top contact for the GaN pillar structures.[5] For 3D Li-ion batteries, 3D structured current collectors are essential for transportation of electrons to the active battery materials (c.f. Part III). Since all these applications involve the exchange of electrons; suitable current collector materials are required for 3D structured (energy) materials. Although several examples of 3D structured metals and doped semi-conductors are available,[8–10] conductive coatings resistant to high temperatures are rare.

Although the choice is limited, some suitable current collector materials are known for these energy applications, including but not limited to various metals, metal nitrides and transparent conductive oxides (TCOs). However, to date, few of these materials have been deposited on 3D structures or patterned substrates. Currently, the choice of these specific 3D structured electrodes is primarily limited to ALD grown TiN[11,12] and Pt.[13,14] More specifically, TiN is an excellent choice as a current collecting electrode for 3D Li-ion battery applications, since the material acts as a current collector and buffer layer to prevent lithium diffusion into the 3D structures support.[12] Although both TiN and Pt exhibit superior conductivity, the vacuum conditions of the costly deposition method may limit upscaling possibilities. Moreover, TiN tends to oxidize and form

badly conducting TiO_2 under oxidative annealing conditions.[15] Hence, emerging 3D structured technologies requiring elevated annealing temperatures are limited by the lack of choice of suitable 3D structured current collector materials (c.f. Chapter 10).[16]

For TCO´s, attempts have been made for 3D depositions as well. Using ALD, conformal coatings of AZO[17] and ITO[18] have been reported. However, as stated previously, ALD is a costly route. Via chemical bath deposition, ZnO was deposited in trenches, though the aspect ratio's achieved were below unity.[19] Within this study, the deposition and function of ITO as a current collector is investigated by using a wet-chemical route with a large upscaling potential. Being an oxide, concessions have to be made with respect to the resistivity, especially in comparison with metallic conductors. Needless to say, the crystallinity and occurrence of vacancies is influenced by annealing, hence the conductivity of ITO is susceptible to (high temperature) annealing conditions dictated by a second material in case stacking is attempted (in view of device integration, c.f. Chapter 10). However, oxidation issues (a major issue for the TiN previously mentioned in Chapter 9 and 10) cannot occur for ITO, since the ions involved are in the highest oxidation state (In^{3+} and Sn^{4+}). Similar to the approach shown in Chapter 5, 6, 9 and 10, here attempts have been made to coat 3D structured substrates with ITO based on an all-citrate precursor. In this study, the current collecting capabilities of ITO were studied in view of application in 3D Li-ion batteries.

2. Experimental

2.1 Synthesis of the Sn-In-precursor

An aqueous citrato peroxo Sn^{4+} solution was prepared according to the synthesis route developed by Stanulis et al.[20] Hydrogen peroxide (H_2O_2, Acros Organics, 35%) was added to tin oxalate (Sigma Aldrich, 98%) in a 12:1 molar ratio and heated to 80°C. Next, citric acid (Sigma Aldrich, ≥99%) was added in a 6:1 molar ratio with respect to Sn and heated to 80°C. Finally, the pH was raised to 7.0 with ammonia (NH_3, Merck, 32%) to obtain the aqueous Sn^{4+} precursor, with a colorless, transparent appearance. In^{3+} cit-

rate was prepared by mixing indium hydroxide ($In(OH)_3$, U.M. Electro-optic materials) and CA in a 1:4 molar ratio, followed by the addition of water. This mixture was heated under reflux conditions for 90 minutes at 120°C. After cooling, the pH was adjusted to 7.0 with ammonia, yielding a transparent colourless solution. For both Sn^{4+} and In^{3+} solutions, the excess of CA was required to prevent precipitations. The concentrations of both precursors were determined by ICP-AES (Chapter 4). Next, the aqueous Sn^{4+} and In^{3+}-solutions were mixed in a 1:9 molar ratio. Finally, ethanol was added to the aqueous precursor in a 9:10 volumetric ratio, as proposed by Gielis et al.[21] The total metal-ion concentration of the final mixed In-Sn-precursor amounted to 10 mM.

2.2 Film deposition

Four different types of substrates were used for this study: (i) Si, (ii) SiO_x, (iii) 3D Si (2x5), (iv) Si trenches (c.f. Chapter 2, Section 3). All the substrates were submitted to a modified piranha cleaning procedure: a consecutive sulphuric acid-peroxide and ammonia-peroxide (SPM/APM) treatment.[22] In case of consecutive deposition on top of the ITO coated substrates, cleaning with an UV/O_3 treatment was applied at 60°C (30 min., Novascan PSD Pro Series) prior to deposition.

The mixed In-Sn-precursor was deposited on various substrates via USD (Exacta Coat, Sono-Tek cooperation) with deposition temperatures ranging from 170°C to 230°C. The liquid was dispensed at 0.2 ml·min^{-1} and the N_2 carrier gas pressure was set at 1.5 psi. The distance of the spray nozzle to the substrate was approx. 2.6 cm and it moved with a speed of 100 mm·s^{-1}. The number of deposition cycles (i.e. the number of times the spray head passes a point on the substrate) was varied from 10 to 50 times with waiting times of 5 seconds between the deposition cycles. For planar samples, intermediate heat treatments were applied every 5 cycles. On 3D micro-cylinders and trench structures no intermediate annealing was applied. Heat treatments were done on hot plates (300°C and 600°C) for 2 minutes. The post deposition anneal was performed using a rapid thermal processing unit (Annealsys, AS-one) at 800°C in dry air (1 ml·min^{-1}) for 10 minutes, followed by 3

hours at 400°C in nitrogen (1 ml·min^{-1}). In both cases, the heating rate was 10°C·s^{-1}. This annealing procedure was adopted from Sugahara et al.[23] WO_3 was deposited consecutively on top of the ITO coated substrates, as reported earlier in Chapter 9.

2.3 Characterization

The thermal decomposition profile of the dried In-Sn-precursor gel, obtained by drying the precursor solution at 60°C, was investigated by TGA (TA instruments Q500). 2 mg of the gel was heated at 10°C·min^{-1} using dry air (0.1 L·min^{-1}) in a platinum crucible. The morphology of the annealed ITO films was investigated via SEM (FEI Quanta 200F). Profilometry was done with Bruker Dektak 150 Surface Profiler, with a 2 µm tip with a measurement length of 10 mm. The crystallization of the films was investigated by XRD, similar to Chapter 4. Van der Pauw measurements (Keithley 2400 SourceMeter) were done to determine the resistivity of the layers, in combination with a thickness estimation based on SEM cross sections. To check the electronic conductivity of the films, electron exchange by ferrocenium reduction was studied, similair to Chapter 10.[24] A reference measurement was made on a commercial ITO sample (coated boro-aluminosilicate glass, Sigma Aldrich). Cyclic voltammetry and galvanostatic measurements were done with an Autolab PGSTAT128N, using a three electrode setup (c.f. Chapter 2),[25] filled with 1.0 M $LiClO_4$ dissolved in polycarbonate (Soulbrain MA). During the galvanostatic measurements, the test cells were operated with various currents ranging from 1.5 to 237 µA between 1.75 and 3.5 V, at 20.0°C via a custom made temperature control chamber inside an Ar-filled glovebox.

3. Results and discussion

3.1 Decomposition of the Sn-In-precursor gel

The weight loss curve (Figure 1) of the mixed In-Si precursor gel decomposition shows similar features known from other citrato-metal decompositions.[20,26–28] First of all, loss of residual solvent, water and ethanol, occurs up to 100°C, followed by the onset of the first main decomposition peak (120-250°C). This results in a

gradual slope from 250°C till 475°C, where the onset of the final decomposition reaction starts. Finally, the reaction is completed at 510°C. The total weight loss after the final decomposition is 88%, due to decomposition of the citrato complexes. Besides the In^{3+} citrate complex, which is a polynuclear complex with a 1:1 In:CA ratio at pH 7,[29] and the citrato-peroxo–Sn^{4+} complex (1:2 Sn:CA ratio),[28] an excess of uncomplexed citric acid is present, forming ammonium citrate with the added ammonia. Van Werde et al. showed that oxidative decomposition of ammonium citrate results in strong NH_3 and CO_2 evolution between 150 and 280°C, as well as decomposition of nitrogen containing compounds between 300 and 650°C.[30] Since decomposition of ammonium citrate mostly coincides with the indium and tin complex decomposition, specific features related to ammonium citrate decomposition are hard to discriminate in the mixed metal citrate precursor.[31]

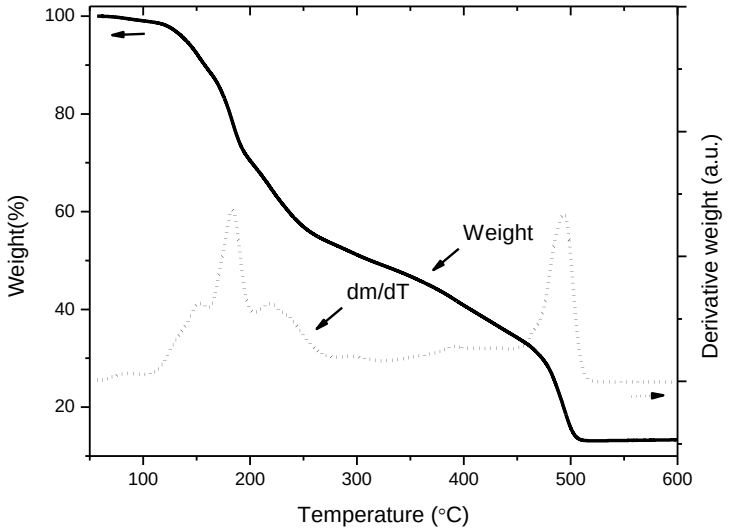

Figure 1: TGA of the In-Sn-precursor (10% Sn), with a heating rate of 10°C·min^{-1}in dry air.

Since 90% of the In-Sn-precursor is composed of the In-precursor, the decomposition profile of the In-Sn-precursor (Figure 1) shows great resemblance with the decomposition of the (separate) In-precursor (Figure 2). Small differences can however be observed between the In-Sn-precursor and In-precursor; this is clearly seen in the derivative curves (Figure 1 and 2a). These features are most clearly visible in the derivative curve shoulders at 130 and 470°C, as well as a (local) maximum at 220°C, representing decomposition reactions related to the citrato-peroxo-Sn^{4+} complex (Figure 2b). While approaching the final weight at 510°C, (partial) crystallization is expected to start slightly before or immediately at this temperature. The conversion of M-O-C bonds to M-O-M bonds (where M = Sn, In) readily leads to crystallization at these temperatures, as amorphous ITO is reported to crystallize at temperatures as low as 125°C.[32] However, to increase the conductivity, sufficiently high temperatures were chosen (up to 800°C), similar to other ITO films prepared by wet-chemical processing.[23,33]

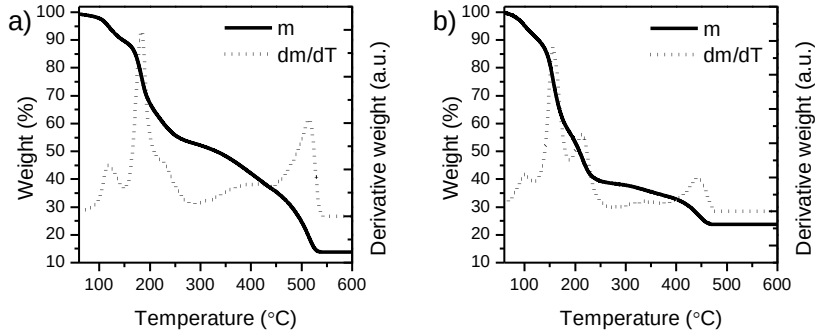

Figure 2: TGA's of (a) In-precursor and (b) Sn-precursor, both measured with a heating rate of 10°C·min^{-1} in dry air.

3.2 Film morphology and phase formation

The temperature of the substrate during spray-deposition, greatly influences the morphology of the films deposited on planar substrates (Figure 3). A lower deposition temperature leads to larger

droplets because less evaporation occurs before the droplets hit the substrate.[34] In addition, coalescence is more likely to occur at low temperatures since the droplets have more time to flow over the surface. [35] This results in large droplets on the substrate surface, leading to rough surfaces. At higher temperatures, smaller droplets are deposited due to solvent evaporation. In addition, droplet immobilization is accelerated and coalescence is less likely to occur (c.f. Chapter 2).

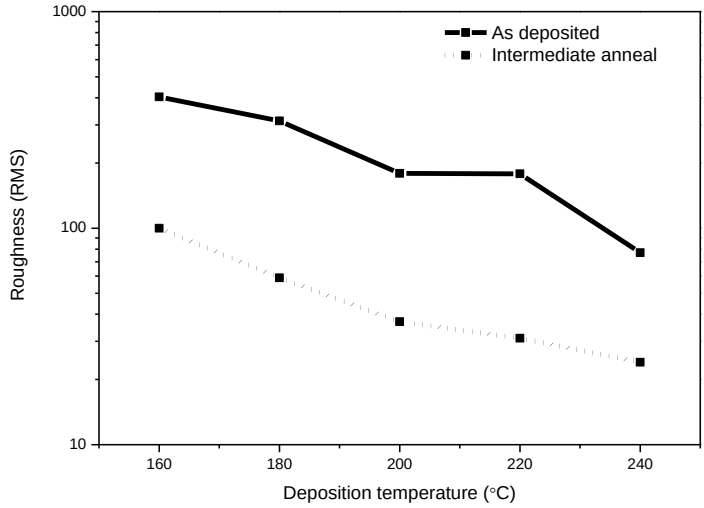

Figure 3: Profilometry results of In-Sn-precursor (10% Sn) showing as-deposited and intermediate anneal (2 min. at 300°C and 600°C) RMS roughness values as function of deposition temperature after 5 deposition cycles of In-Sn-precursor (10 mM) with ultrasonic spray deposition on Si native oxide substrates.

It is thought that the combination of smaller droplets and reduced coalescence is the reason that higher deposition temperature yields smoother films. As can be observed for all deposition temperatures measured (Figure 3), the intermediate annealing leads to a large roughness reduction. Roughness arising from the deposition is

reduced since height differences (i.e. roughness) are reduced as well, due to densification during the anneal. Hence, (rough) low temperature deposited films smoothen upon annealing, but they do not surpass (smooth) high temperature deposited films that also densify during annealing. This is the reason why the so-called 'intermediate annealing' was applied during the synthesis, i.e. every 5 deposition cycles the layers undergo a short high temperature anneal to decompose the precursor before the next deposition cycles.

An example of the obtained morphology is shown in Figure 4 (after high temperature annealing). Deposition of the In-Sn-precursor on silicon wafers with thermal oxide yielded a slightly rough, but continuous film after an anneal at 800 (10 minutes, dry air) and 400°C (3 hours, N_2). The growth rate was determined to be approximately 9 nm per deposition cycle, leading to a layer thickness between 220 and 230 nm for 25 deposition cycles (Figure 4).

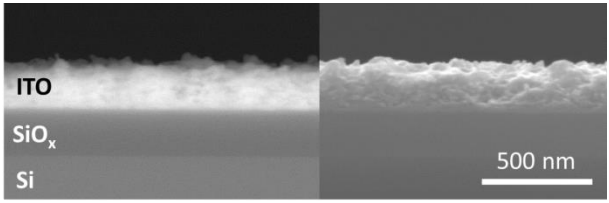

Figure 4: SEM micrograph (back-scattered and secondary) of ITO films (220 nm) on SiO_x, as a results of 25 spray deposition cycles at 220°C with intermediate annealing up to 600°C every 5 cycles. The sample was submitted to a post-deposition anneal at 800°C (5 minutes, dry air) followed by annealing under inert conditions (3 hours, 400°C in N_2).

Besides reduced roughness on the planar samples, the higher deposition temperatures are also favourable for the 3D deposition as observed in Figure 5. At low temperatures (<190°C) a poor coating is found on the silicon micro-cylinders. The material is primarily

deposited as a thick film on the bottom of the substrate, without coating the vertical areas. While assuming the deposited material consists of a slightly flowing gel at low deposition temperatures, the material flows downwards during the deposition process, yielding a layer that is primarily situated at the bottom of the micro-cylinders.[16] At higher deposition temperatures (>210°C), the deposition can be tuned to yield an ITO film which is covering the entire surface of the micro-cylinders. More specifically, 220°C was found to be the optimal deposition temperature (Figure 6).

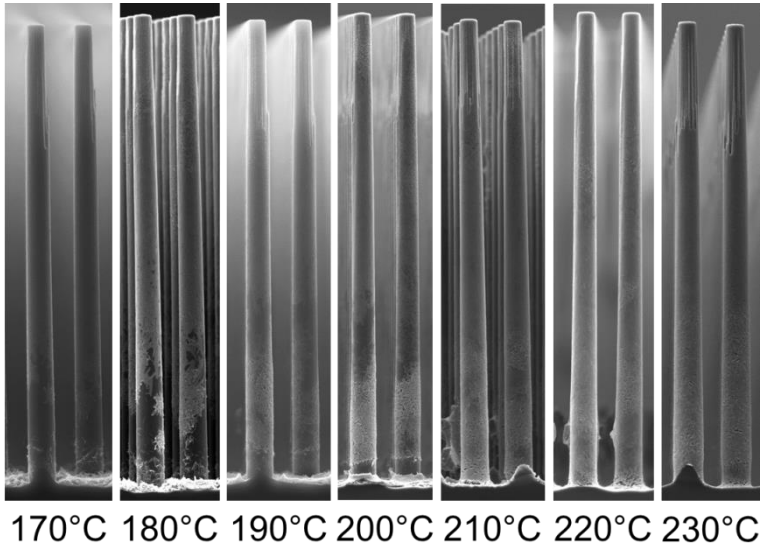

Figure 5: SEM micrographs of ITO films on 3D Si (2x5); as a results of 50 spray deposition cycles with 10 mM In-Sn-precursor, using the indicated deposition temperatures. The substrates were submitted to SPM/APM cleaning prior to deposition, and the ITO films were subjected to a post-deposition anneal at 600 for 1 hour in dry air (static). Artefacts on top of the micro-cylinders are a result of the fabrication process (not related to cleaning or ITO deposition).

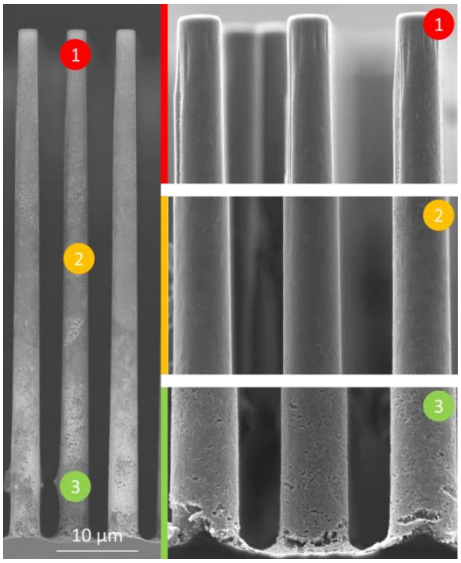

Figure 6: SEM micrograph of ITO film on 3D Si (2x5), as a results of 50 spray deposition cycles with 10 mM In-Sn-precursor, with a deposition temperature of 220°C. The sample was annealed at 600°C for 1 hour in static air after deposition. Artefacts on top of the micro-cylinders are a result of the fabrication process (not related to cleaning or ITO deposition).

It is thought that the higher temperature immobilizes the gel, preventing too much flow down the micro-cylinders, therefore leading to more evenly spread precursor all over the micro-cylinders (c.f. Chapter 9).

Besides the deposition temperature, which was shown to have a great influence on the coatings, the wettability of the precursor proved to be of importance. To achieve good wetting of the precursor, the surface chemistry is considered by optimizing the substrate surface and surface tension of the precursor. It was shown before that the addition of ethanol to the aqueous citrate solution is of importance because this lowers the surface tension of the

precursor, improving the wetting behaviour.[21] In addition, the substrate surface was tuned by improving the hydrophilicity using a modified piranha cleaning procedure: a SPM/APM treatment.[22]

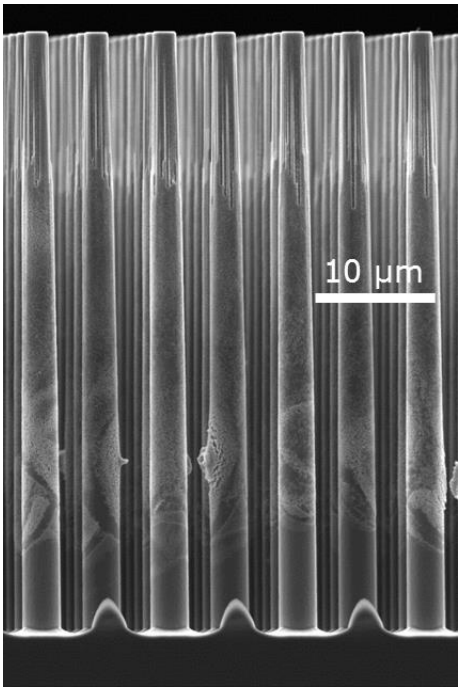

Figure 7: SEM micrograph of ITO films on 3D Si (2x5), as a results of 50 spray deposition cycles with 10 mM In-Sn-precursor at 200°C. The sample was cleaned with UV/O_3 prior to deposition, and annealed at 600°C for 1 hour in dry air (static) after deposition.

Without this additional cleaning, no complete coating of the entire micro-cylinders was achieved, especially with respect to the bottom part of the cylinders (c.f. Figure 7). Recalling Chapter 6, where 3D deposition of the Li-La-Zr-precursor was discussed briefly, the same phenomenon occurred on coating of 3D Si with LLZO. In contrast, LLT (Chapter 5) and WO_3 (Chapter 9) were successfully de-

posited with a citrate precursor on 3D TiN. Although a complete comparison does not apply because the materials differ, these results indicate that the surface chemistry of Si (as a result of an UV/O_3 clean) may be the reason why complete coating was not achieved without additional cleaning of 3D Si. For ITO, optimization of the surface chemistry with a SPM/APM clean, precursor wettability and deposition parameters together yields the desired result: high quality ITO layers on 3D structured scaffolds, down to the micron scale.

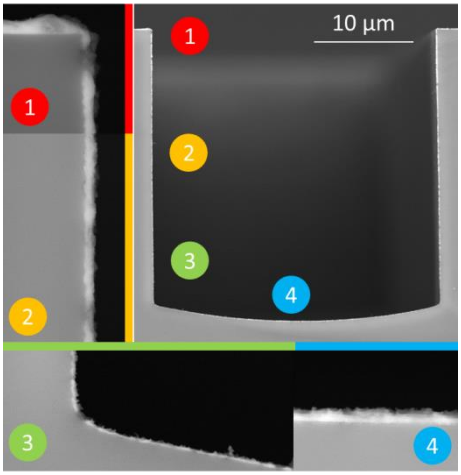

Figure 8: SEM micrograph of ITO films on Si trench structure 30 µm wide and 30 µm deep, as a results of 5+5 spray deposition cycles with 10 mM In-Sn-precursor, at a deposition temperature of 220°C. The samples were submitted to a post-deposition anneal at 600°C for 1 hour in dry air (static).

Whereas the use of micro-cylinders makes it difficult to check the conformality and layer thickness, deposition on micrometre sized trench structures enables an accurate determination of the conformality (Figure 8). At a deposition temperature of 220°C, thicknesses along the trench were found to vary from 160 nm at the top

of the trench, down to 55 nm in the corner of the trench. Therefore, the conformality of the deposition was determined to be 35%.

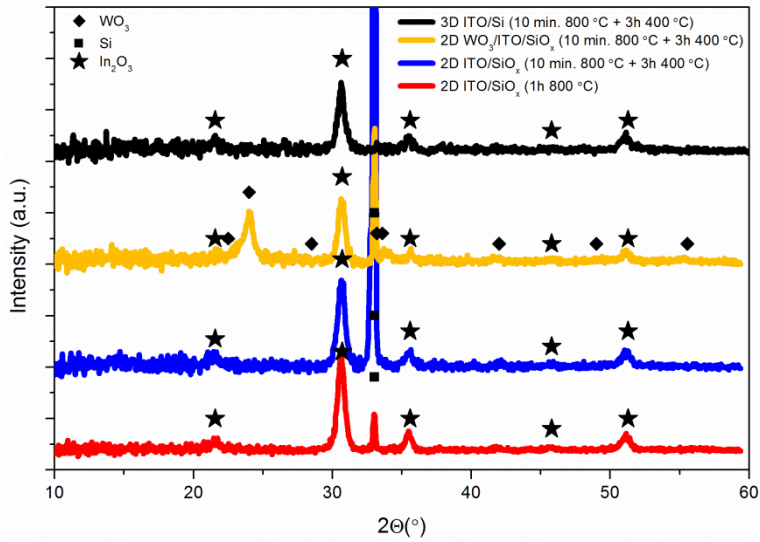

Figure 9: X-ray diffractograms of (3D) pristine and WO_3 coated ITO films (220 nm) on SiO_x, as a results of 25 spray deposition cycles at 220°C with intermediate annealing up to 600°C every 5 cycles. The samples were submitted to a post-deposition anneal at 800°C (10 minutes, dry air) followed by annealing under inert conditions (3 hours, 400°C in N_2). WO_3 coated samples (10 cycles of 25 mM W-precursor) were annealed at 600°C in static air for 1 hour. In_2O_3 cubic JCPDS (006-0416), Tetragonal WO_3 (JCPDS 01-85-807) and Si (JCPDS 01-72-1088) phases are all indicated.

Figure 9 shows the XRD results of the ITO films deposited on SiO_2. Except for the Si substrate peak, all peaks can be attributed to cubic indium oxide. Exact determination of successful Sn substitution is rather difficult on films by means of XRD, as several factors (other than Sn substitution) influence the expected increase of

lattice parameters.[36] On the other hand, no SnO_2 or related phase(s) could be detected, suggesting that doping was indeed successful.[33,37,38]

3.3 Electrical properties

For the planar samples, the resistivity values strongly depend on the applied annealing procedure, as can be observed in Table 1. With an anneal at 600°C in dry air, a very high resistivity is measured (not shown). A higher annealing temperature of 800°C under oxidative conditions significantly reduces the resistivity, which might be due to an increased crystallinity of the samples, as substitutional Sn ($[Sn^{\bullet}]$) does not contribute to conductivity in amorphous ITO.[32] Using inert annealing conditions at 800°C, after a short oxidative anneal to decompose the residual organics, significantly improved resistivity values are obtained. A final improvement was made while following findings of Sugahara et al.[23] While combining a short, oxidative high temperature anneal (10 minutes, 800°C, dry air) with a much longer, low temperature anneal under inert conditions (3 hours, 400°C, N_2), the best resistivity value measured amounted $9.9 \cdot 10^{-3}$ Ω·cm. No significant differences in crystallinity could be observed with XRD between samples annealed at 800°C for 1 hour or 10 minutes at 800°C combined with 3 hours at 400°C under inert conditions (Figure 7). Processing under inert conditions therefore suggests an increase in the oxygen vacancies ($V_O^{\bullet\bullet}$).[36] While comparing the conductivity results with other wet chemical synthesis routes, it must be noted that the resistivity is an order of magnitude higher than recent results obtained by spin-coating.[23] The reason that the resistivity of the films obtained by USD in the current study is still higher, is mainly sought in a higher surface roughness. For spin-coating, sub-nanometre values were reached,[23] whereas the roughness values obtained in this study are approximately two orders of magnitude higher (Figure 2).

Table 1: Resistivity values measured by the 'van der Pauw' method in combination with SEM to determine the layer thickness as function of various annealing conditions. The ITO films (220 nm) were deposited on SiO_x, as a result of 25 spray deposition cycles at 220°C with intermediate annealing up to 600°C every 5 cycles. The standard deviations of all samples were below $1 \cdot 10^{-4}$ Ω·cm.

Anneal	**Resistivity (Ω·cm)**
800°C 1h DA	$3.2 \cdot 10^{-2}$
800°C 1h Ar	$2.8 \cdot 10^{-2}$
800°C 5 min. DA + 3h N_2	$9.9 \cdot 10^{-3}$

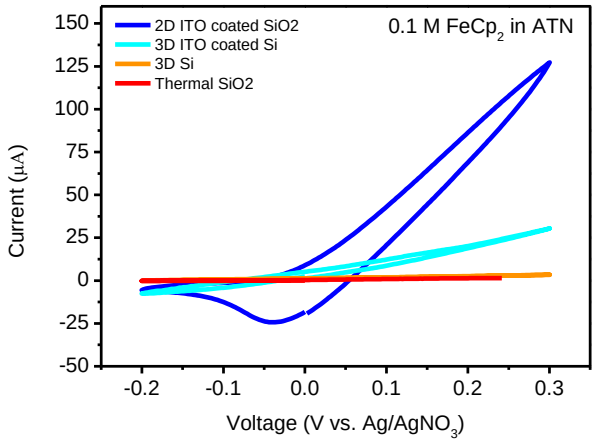

Figure 10: CV showing electron transfer of ferrocene/ferrocenium on planar samples (1 mV/s). The ITO films measured were deposited in accordance with samples shown in Figures 3 and 5. Both ITO coated samples were annealed 10 minutes at 800°C (dry air) and 3 hours at 400°C (nitrogen).

The current collecting-properties in 3D cannot be probed directly by the 'Van der Pauw' method, but qualitative assessment of the

ITO layer functionality was done by measuring ferrocenium reduction (Figure 10). Upon successful electron transfer, ferrocenium is reduced to ferrocene at the surface (c.f. Chapter 10).[24,39] For the planar samples – which did allow direct determination of the resistivity by 'Van der Pauw' method – a clear difference is observed in comparison with the (non-conductive) uncoated sample (SiO_x) and ITO coated sample in the CV (Figure 10). The uncoated sample hardly shows any response due to the non-conductive SiO_x at the interface, whereas the ITO coated sample shows a reduction of ferrocenium at the ITO surface at -0.04 V.

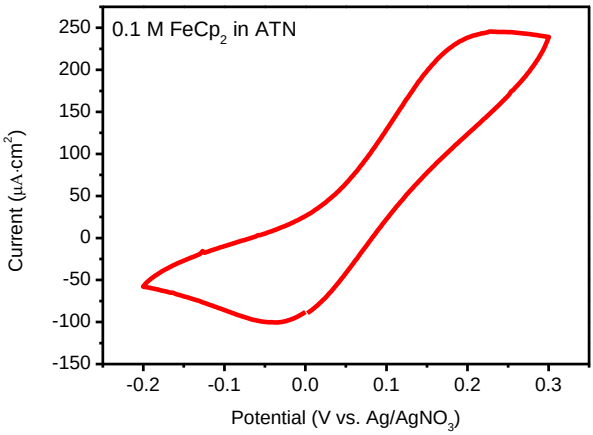

Figure 11: CV of a commercial ITO film (1 mV/s).

However, no clear oxidation peak is observed. A comparison of these results with a commercial ITO film reference measurement (Figure 11) explains the lack of an oxidation peak. The commercial ITO, with a lower resistivity, hardly shows an oxidation peak either, although a broad low intensity oxidation can be observed at 0.23 V (vs. $Ag/AgNO_3$). Hence, the higher resistivity of the spray-deposited ITO coating leads to a less intense oxidation peak, making it unmeasurable (Figure 10). The same experiment was done on ITO coated micro-cylinders, but no clear oxidation and reduction could be observed here either. The ITO coatings 3D Si micro-cylinders are significantly thinner (Figure 8). Hence, more resistivi-

ty leads to a lack of reduction and oxidation peaks for the 3D measurements in the cyclic voltammogram. However, these measurements do suggest a slight increase in surface activity with respect to electron transfer reactions for the 3D ITO coating compared to non-coated Si micro-cylinders.

3.4 Towards Li-ion battery applications

In general, any possible current collector within the field of (3D) Li-ion batteries requires low electrochemical reactivity with respect to Li^+. For example, TiN shows hardly any electrochemical activity, even at low voltages vs. Li^+/Li.[11] To judge if the ITO coatings are of interest within the field of Li-ion batteries, the electrochemical activity of these coatings was investigated. By means of cyclic voltammetry with metallic lithium as reference and counter electrodes in a non-aqueous electrolyte, the insertion and extraction into the deposited ITO was studied between 0 and 4 V (Figure 12). Clearly, the reactivity of the deposited layer strongly depends on the voltage range applied. Above 1.6 V (vs. Li^+/Li), no redox reactions take place, implying that the material is stable within this voltage range. At lower potentials, two reductions and one large oxidation can be observed (indicated with 1, 2 and 3 in Figure 12). The reductions (0.7 and 0 V) may be related to Sn^{4+} reduction and alloying of lithium with reduced Sn, respectively.[40,41] Although no clear indications of overlapping peaks are present, the 0.7 V reduction peak (1 in Figure 12) can also be associated with indium reduction below 1.0 V [42,43] as well as SEI formation.[40,41] The latter seems more plausible since irreversible reactions are clearly occurring (due to the lack of an oxidation peak).

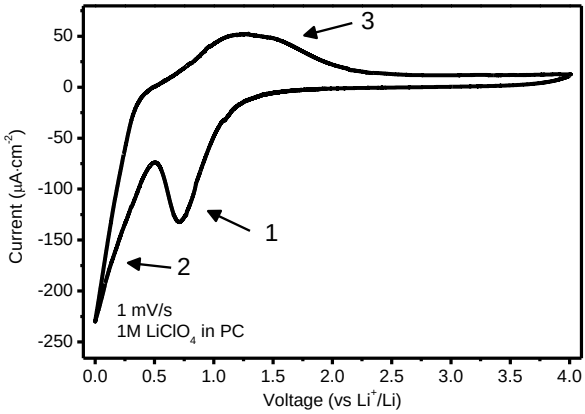

Figure 12: CV showing reactivity of ITO films with lithium (ions). The ITO films (220 nm) were deposited on SiO_x, as a results of 25 spray deposition with intermediate annealing up to 600°C every 5 cycles.

Finally, the reduction peak at 0 V and oxidation at 1.3 V (indicated by 2 and 3, Figure 12) can also be due to SiO_2 (de)lithiation,[44] although the negligible electronic conductivity of this material makes these reactions unlikely.

In view of applications as a current collector for Li-ion batteries, lithium reactivity with the ITO and / or substrate is undesired. Not all battery electrode materials are suitable for direct deposition on top of the ITO. The stability at high potentials makes the ITO suitable to be combined with positive electrode materials such as $LiCoO_2$.[25] On the negative electrode side, electrodes with (de)intercalation voltages below 1.5 V such as metallic lithium and lithiated graphite should be avoided, as these materials would instantly react with the ITO and lead to loss of charge. This means that combination with high voltage negative electrodes ('anodes') such as LTO,[45,46] TiO_2 and WO_3 should be possible.[40,47,48]

In this study, a proof-of-principle is shown using the latter material: WO_3. To study the influence on present crystalline phases, pristine ITO and WO_3-coated substrates were measured by XRD (Fig-

ure 9). Upon coating with WO_3, the peaks assigned to ITO remain present, indicating that at least part of the crystalline ITO coating is preserved. Furthermore, no secondary phases were observed; XRD gives no indications of ITO degradation or side reactions occurring during the annealing required to crystallize WO_3 (1 hour at 600°C). It is however possible that the long, relatively low temperature anneal (3 hours at 400°C in N_2), has an effect on the oxygen vacancies in ITO, and hence its conductivity. WO_3 peaks are clearly observed for the WO_3-coated ITO in Figure 9; the sample consists of tetragonal WO_3. The same result was obtained with WO_3 deposition on TiN and Pt, which was discussed in Chapter 7 and 9.

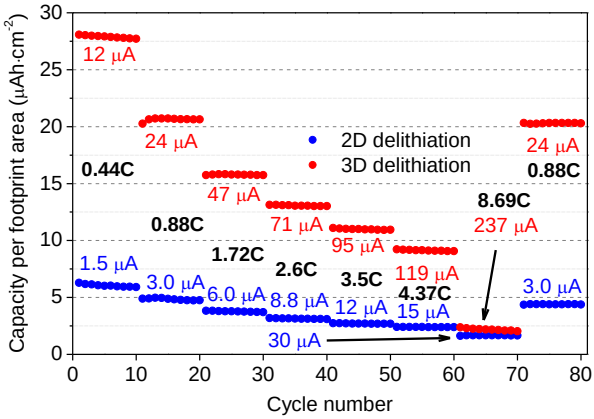

Figure 13: Delithiation results of planar (2D) and 3D WO_3 coated ITO on 3D Si (2x5). The planar and 3D samples were coated by 2 / 25 and 16 / 50 deposition cycles of W-precursor / In-Sn-precursor, annealed at 800°C (10 minutes) + 400°C (3 hours) in dry air + N_2. Cut-off voltages of 1.75 and 3.5 V (vs Li/Li^+) were chosen, with discharge currents per cm^2.

Although the 3D ITO coating suffers from resistivity limitations for the ferrocene electron transfer (Figure 10), Figure 13 is direct evidence for functionality of the 3D ITO coatings. The planar and 3D samples, yielding an 8-fold surface enhancement, were compared

via galvanostatic cycling (Figure 13). The same current per amount of deposited material is applied (i.e. 3D samples consist of 16 deposition cycles, measured with an 8-fold current of the planar samples consisting of 2 deposition cycles). With an 8-fold increase of the active material and electrode surface for current collection (due to the use of ITO coated Si micro-cylinders), an 8-fold capacity increase would be expected while applying the same current density (per cm^2 coating). In practice an over 4-fold capacity increase for 3D compared to planar samples (Figure 13) was achieved. Although this is not as high as theoretically possible, it does surpass previous results shown in Chapter 9 with TiN as a current collector. To make sure that this difference in capacity is not related to the ITO layer itself, galvanostatic measurements on pristine ITO were done, yielding a capacity of 53 $nAh \cdot cm^{-2}$ (with 1.5 $\mu A \cdot cm^2$ current density) within this voltage region. This implies that ITO has a negligible capacity during these measurements, and that the capacity probed indeed belongs to the active (WO_3) material.

The main reason why the 8-fold capacity improvement is not entirely reached is sought in the imperfect deposition of WO_3 leading to an uneven current distribution (Chapter 9). The over 4-fold capacity enhancement slowly drops to a 3.2-fold improvement while increasing the current to 119 µA per cm^2 footprint (15 µA per cm^2 coating, 4.4C), illustrating that the combined 3D stack is not perfect, but 3D enhanced capacity is achieved up to high currents (Figure 14). However, while further increasing to even larger currents of 237 µA per cm^2 footprint / 30 µA per cm^2 coating (i.e. 8.7C), the capacity of both planar and 3D samples drop significantly, implying that a kinetic drop-off is reached in terms of Li^+ diffusion and / or electronic conductivity of the active material (WO_3). Since the drop for the 3D sample is more severe, compared to the same experiment done with TiN as current collector (Chapter 9), it clearly indicates that spray-deposited ITO is more suitable for slightly lower current densities. This may be solved by depositing thicker 3D ITO films.

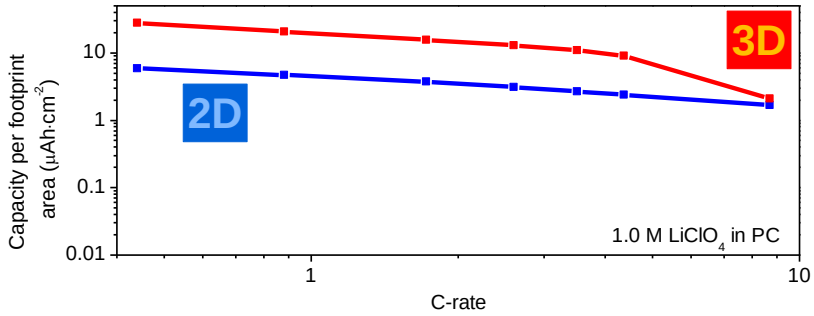

Figure 14: Capacity/C-rate Double-log plot of planar (2D) and 3D WO_3 coated ITO on 3D Si (2x5), similar to Figure 13.

4. Conclusion

The CSD route, using citrate based precursors in combination with USD, proves to be a very versatile route for the deposition of a 3D structured current collector material. Surface chemistry, precursor chemistry and deposition temperature proved to be of vital importance for successful 3D deposition. The study aiming at implementation in 3D all-solid-state Li-ion batteries, led to an over 4-fold capacity increase due to the use of 3D architectures. This illustrates the potential of this approach. Although the use of the ITO current collector already yields remarkable results for the field of 3D Li-ion batteries within the constraints dictated by the electrochemical stability of ITO, the main future challenge lies in roughness reduction to decrease the resistivity, thereby limiting the required film thickness and yielding more space for active (energy) materials. The outcome of this study is of interest to other applications as well, such as 3D LED or photovoltaic applications. However, for these applications new strategies to reach comparable results with lower annealing temperatures should be investigated, as the annealing temperature (800°C) remains a bottleneck for device integration with ITO as a top current collector. Nevertheless, this study underlines the potential the wet-chemical approach has in tackling the (smart materials) challenges of tomorrow.

5. References

[1] A. G. Tamirat, W.-N. Su, A. A. Dubale, C.-J. Pan, H.-M. Chen, D. W. Ayele, J.-F. Lee, B.-J. Hwang, *J. Power Sources* **2015**, *287*, 119.

[2] Z. Pan, Y. Qiu, J. Yang, F. Ye, Y. Xu, X. Zhang, M. Liu, Y. Zhang, *Nano Energy* **2016**, *26*, 610.

[3] R. Pietruszka, B. S. Witkowski, S. Gieraltowska, P. Caban, L. Wachnicki, E. Zielony, K. Gwozdz, P. Bieganski, E. Placzek-Popko, M. Godlewski, *Sol. Energy Mater. Sol. Cells* **2015**, *143*, 99.

[4] A. Waag, X. Wang, S. Fündling, J. Ledig, M. Erenburg, R. Neumann, M. Al Suleiman, S. Merzsch, J. Wei, S. Li, H. H. Wehmann, W. Bergbauer, M. Straßburg, A. Trampert, U. Jahn, H. Riechert, *Phys. Status Solidi* **2011**, *8*, 2296.

[5] B. O. Jung, S.-Y. Bae, S. Lee, S. Y. Kim, J. Y. Lee, Y. Honda, H. Amano, *Nanoscale Res. Lett.* **2016**, *11*, 215.

[6] J. W. Long, B. Dunn, D. R. Rolison, H. S. White, *Chem. Rev.* **2004**, *104*, 4463.

[7] J. F. M. Oudenhoven, L. Baggetto, P. H. L. Notten, *Adv. Energy Mater.* **2011**, *1*, 10.

[8] G. Oltean, M. Valvo, L. Nyholm, K. Edström, *Thin Solid Films* **2014**, *562*, 63.

[9] C.-P. Yang, Y.-X. Yin, S.-F. Zhang, N.-W. Li, Y.-G. Guo, *Nat. Commun.* **2015**, *6*, 8058.

[10] K.-S. Park, J.-G. Kang, Y.-J. Choi, S. Lee, D.-W. Kim, J.-G. Park, *Energy Environ. Sci.* **2011**, *4*, 1796.

[11] L. Baggetto, H. C. M. Knoops, R. a. H. Niessen, W. M. M. Kessels, P. H. L. Notten, *J. Mater. Chem.* **2010**, *20*, 3703.

[12] H. C. M. Knoops, L. Baggetto, E. Langereis, M. C. M. van de Sanden, J. H. Klootwijk, F. Roozeboom, R. a. H. Niessen, P. H. L. Notten, W. M. M. Kessels, *J. Electrochem. Soc.* **2008**, *155*, G287.

[13] J. Dendooven, R. K. Ramachandran, K. Devloo-Casier, G. Rampelberg, M. Filez, H. Poelman, G. B. Marin, E. Fonda, C. Detavernier, *J. Phys. Chem. C* **2013**, *117*, 20557.

[14] T. Dobbelaere, F. Mattelaer, J. Dendooven, P. Vereecken, C. Detavernier, *Chem. Mater.* **2016**, *28*, 3435.

[15] N. C. Saha, H. G. Tompkins, *J. Appl. Phys.* **1992**, *72*, 3072.

[16] E. J. van den Ham, S. Gielis, M. K. Van Bael, A. Hardy, *ACS Energy Lett.,* **2016**, *1*, 1184.

[17] B. H. Kong, M. K. Choi, H. K. Cho, J. H. Kim, S. Baek, J.-H. Lee, *Electrochem. Solid-State Lett.* **2010**, *13*, K12.

[18] J. W. Elam, D. a. Baker, A. B. F. Martinson, M. J. Pellin, J. T. Hupp, *J. Phys. Chem. C* **2008**, *112*, 1938.
[19] M. Kevin, G. H. Lee, G. W. Ho, *Energy Environ. Sci.* **2012**, *5*, 7196.
[20] A. Stanulis, A. Hardy, C. De Dobbelaere, J. D'Haen, M. Van Bael, A. Kareiva, *J. Sol-Gel Sci. Technol.* **2012**, *62*, 57.
[21] S. Gielis, A. Hardy, M. K. Van Bael, *Conformal Coating on Three-Dimenstional Substrates*, **2015**, EP 2 947 178 A1.
[22] M. K. Van Bael, D. Nelis, A. Hardy, D. Mondelaers, K. Van Werde, J. D'Haen, G. Vanhoyland, H. Van den Rul, J. Mullens, L. C. Van Poucke, F. Frederix, D. J. Wouters, *Integr. Ferroelectr.* **2002**, *45*, 113.
[23] T. Sugahara, Y. Hirose, S. Cong, H. Koga, J. Jiu, M. Nogi, S. Nagao, K. Suganuma, *J. Am. Ceram. Soc.* **2014**, *97*, 3238.
[24] Y.-C. Perng, J. Cho, S. Y. Sun, D. Membreno, N. Cirigliano, B. Dunn, J. P. Chang, *J. Mater. Chem. A* **2014**, *2*, 9566.
[25] M. E. Donders, W. M. Arnoldbik, H. C. M. Knoops, W. M. M. Kessels, P. H. L. Notten, *J. Electrochem. Soc.* **2013**, *160*, A3066.
[26] N. Peys, Y. Ling, D. Dewulf, S. Gielis, C. De Dobbelaere, D. Cuypers, P. Adriaensens, S. Van Doorslaer, S. De Gendt, A. Hardy, M. K. Van Bael, *Dalton Trans.* **2013**, *42*, 959.
[27] A. Hardy, D. Mondelaers, M. K. Van Bael, J. Mullens, L. C. Van Poucke, G. Vanhoyland, J. D'Haen, *J. Eur. Ceram. Soc.* **2004**, *24*, 905.
[28] I. Truijen, M. K. Van Bael, H. Van Den Rul, J. D'Haen, J. Mullens, *J. Sol-Gel Sci. Technol.* **2006**, *41*, 43.
[29] V. Y. Ivanova, V. V. Chevela, S. G. Bezryadin, *Russ. Chem. Bull.* **2016**, *64*, 1842.
[30] K. V. A. N. Werde, D. Mondelaers, G. Vanhoyland, D. Nelis, M. K. V. A. N. Bael, *J. Mater. Sci.* **2002**, *37*, 81.
[31] M. Rajendran, M. Subba Rao, *J. Solid State Chem.* **1994**, *113*, 239.
[32] D. C. Paine, T. Whitson, D. Janiac, R. Beresford, C. O. Yang, B. Lewis, *J. Appl. Phys.* **1999**, *85*, 8445.
[33] C. Legnani, S. a. M. Lima, H. H. S. Oliveira, W. G. Quirino, R. Machado, R. M. B. Santos, M. R. Davolos, C. a. Achete, M. Cremona, *Thin Solid Films* **2007**, *516*, 193.
[34] D. Perednis, L. J. Gauckler, *J. Electroceramics* **2005**, *14*, 103.
[35] M. Majumder, C. Rendall, M. Li, N. Behabtu, J. A. Eukel, R. H. Hauge, H. K. Schmidt, M. Pasquali, *Chem. Eng. Sci.* **2010**, *65*, 2000.

[36] H. Kim, C. M. Gilmore, a. Piqué, J. S. Horwitz, H. Mattoussi, H. Murata, Z. H. Kafafi, D. B. Chrisey, *J. Appl. Phys.* **1999**, *86*, 6451.
[37] E. Benamar, M. Rami, C. Messaoudi, D. Sayah, a. Ennaoui, *Sol. Energy Mater. Sol. Cells* **1999**, *56*, 125.
[38] M. . Alam, D. . Cameron, *Thin Solid Films* **2002**, *420-421*, 76.
[39] G. Zotti, G. Schiavon, S. Zecchin, A. Berlin, G. Pagani, *Langmuir* **1998**, *14*, 1728.
[40] D. Deng, M. G. Kim, J. Y. Lee, J. Cho, *Energy Environ. Sci.* **2009**, *2*, 818.
[41] D. Deng, J. Y. Lee, *Chem. Mater.* **2008**, *20*, 1841.
[42] Y. L. Lo, S. C. Chou, B. J. Hwang, J. A. Elec-, *J. Electrochem. Soc.* **1998**, *145*, 2225.
[43] J. Morales, L. Sanchez, *Solid State Ionics* **1999**, *126*, 219.
[44] N. Yan, F. Wang, H. Zhong, Y. Li, Y. Wang, L. Hu, Q. Chen, *Sci. Rep.* **2013**, *3*, 1568.
[45] M. Roeder, A. B. Beleke, U. Guntow, J. Buensow, A. Guerfi, U. Posset, H. Lorrmann, K. Zaghib, G. Sextl, *J. Power Sources* **2016**, *301*, 35.
[46] S. Y. Tsai, K. Z. Fung, C. T. Ni, *ECS Trans.* **2015**, *68*, 37.
[47] M.-J. Wang, C.-F. Li, W.-J. Lai, S.-K. Yen, *Thin Solid Films* **2012**, *520*, 6744.
[48] Q. Zhong, J. R. Dahn, K. Colbow, *Phys. Rev. B* **1992**, *46*, 2554.
[49] E. J. van den Ham, K. Elen, I. Kokal, M. B. Yagci, N. Peys, G. Bonneux, F. Ulu, W. Marchal, M. Van Bael, A. Hardy, *RSC Adv.* **2016**, *6*, 51747.

Chapter 12

Conclusions and outlook

1. Conclusions

The topic of this thesis was the deposition and characterization of functional thin film battery materials by means of wet-chemical routes, especially related to 3D depositions. At the end of this study, it can be concluded that versatility of this approach was shown for a lot of different parts of the all-solid-state battery, namely (i) the electrolyte, (ii) the electrodes and (iii) the current collector. Because the electrochemical window is often used for combining materials in the work presented in this thesis, a graph summarizing the studied materials with respect to their electrochemical stability (or activity) is shown in Figure 1.

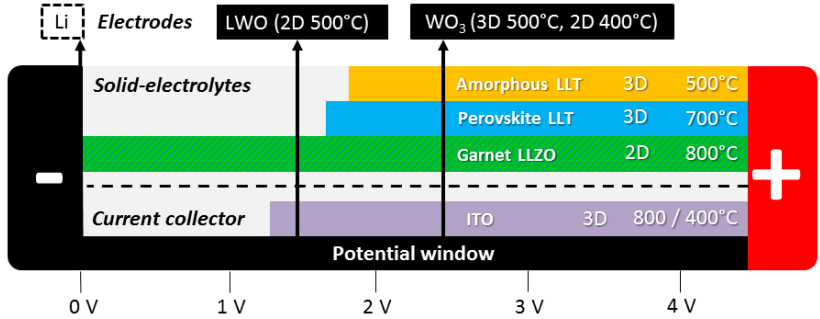

Figure 1: Schematic view of the electrochemical stability of the electrolytes and current collector studied. Furthermore, the studied electrodes are shown with respect to their main charge plateau. The Li electrode is shown for reference purposes. The electrochemical stability of LLZO could not be determined during this study, but the stability is based on literature. The proven 3D deposition or solely planar (2D) and minimal synthesis temperature are included as well.

For electrolytes, the deposition of garnet based LLZO appeared to be too big a challenge. First of all, the phase formation for this material appeared to be too demanding for device integration, since the phase could only be obtained via epitaxial stabilization.

Although no conclusive evidence could be presented, the formation of lithium carbonate does not seem to aid the crystallization process. Besides, even if epitaxial stabilization is applied, the annealing temperature (800°C) could not be lowered sufficiently, yielding temperatures that are highly challenging for electrodes and current collectors. Therefore, the future of (crystalline) Li-stuffed garnet electrolytes within the field of thin film Li-ion batteries is questioned.

As an alternative, deposition of LLT was investigated. Although the intrinsic issue of titanium reduction could not be circumvented, functional materials could be achieved. However, the highly conductive crystalline phase could not be formed within the tough morphological constraints, implying that pinholes could not be prevented for crystalline LLT. With a citrate-nitrate based precursor, amorphous LLT could however be established. Here, a major gain in morphology was established at the cost of conductivity (10^{-8} to 10^{-9} $S \cdot cm^{-1}$). Although the limited electrochemical stability and conductivity do not make this a state-of-the-art material, the fact that it can be deposited in 3D with a large degree of freedom with respect to synthesis conditions and underlying electrode material, make it an interesting candidate solid electrolyte. With a 3D deposition conformaility of over 30%, the wet-chemical deposition of this material is on par with deposition of several chemical vapour deposition processes.[1,2]

To integrate the LLT electrolyte, a suitable electrode material was selected with beneficial properties with respect to required synthesis conditions and electrochemical characteristics: WO_3 (c.f. Figure 1). The first approach, aimed at achieving WO_3 at relative low temperatures, involved unrevealing complex (redox) reactions occurring during the precursor synthesis, leading to the conclusion that crystalline WO_3 particles could be formed at very low temperatures. Spray deposition of these films led to electrochemical active films at relative low temperature (400°C). This is of great importance, since this synthesis temperature in combination with the slightly reduced tungsten precursor led to a protection of the oxidative TiN current collector. Hence, this approach yielded active

films on TiN (and Pt), which is a major step forward within the field of wet-chemical processing.

However, the particle based approach was unsuitable for 3D depositions. Therefore, a second approach was made to obtain 3D WO_3 films. A citrate-based molecular precursor was developed that did yield 3D deposition of WO_3 on various 3D architectures, at the cost of an increased thermal budget (required for the citrate decomposition reactions). The thermal budget dictated by the oxidative TiN posed a challenge yet again. In this thesis two possible solutions were explored. At first, a study was done regarding the decomposition and crystallization of the citrate-based tungsten precursor deposition. This led to a minimization of the annealing applied (10 minutes at 500°C), yielding active 3D structured WO_3 films. A second approach was done by replacing the oxidative TiN with 3D spray-coated ITO. For the latter approach, an all-citrate precursor was prepared and deposited successfully deposited on 3D architectures. By coating the 3D ITO films with WO_3, functionality of the WO_3 coatings was proved. In the best case, a 4.5 fold capacity increase per footprint area was established due to the use of 3D architectures, which surpasses all other results established before within the field of wet-chemical processing, as well as some examples of vacuum-based deposition.[1,3,4]

Integrating LLT and WO_3 proved to be a versatile combination, as active half-stacks were shown. Although secondary phases were found as a result of lithium diffusion from the top solid electrolyte to the negative electrode underneath, 70% of the pristine capacity was established with the all-spray-coated solid-state half-cell. In addition, a 3D half-cell was shown as well, showing the versatility of the wet-chemical processing in combination with spray-coating yet again.

In an effort to establish formation of cubic $Li_{0.5}WO_3$ negative electrodes by lithium doping on forehand (instead of electrochemical lithiation), LWO films were obtained. Though films of this negative electrode material with high volumetric capacity (over 1000 $mAh \cdot cm^{-3}$ was measured at 1.2C) were never reported before, the significance of the findings was overshadowed by the poor cyclabil-

ity of the films. Strong contraction and expansion effects deteriorated the LWO films. Although it was shown that these effects could be limited by lowering the lithium doping levels, the long term cyclability remained an issue. Therefore, this approach is clearly not of interest for thin film Li-ion batteries.

Besides progress established for the application of selected materials as well as deeper insights into new materials combinations and precursor chemistry, more general things can be learned from the work presented in this thesis:

(i) A colloidal suspension seems to be a poor choice to yield 3D coatings via spray-coating, since inhomogeneous depositions were established with this approach.

(ii) With the successful 3D deposition of LLT, WO_3 and ITO, the findings by Gielis et al. [5,6] appear to be applicable to a broad variety of materials and precursors. More importantly, it was shown that highly functional materials can be obtained with this approach. Although questions remain, this thesis yielded new insights in this process with respect to applicability. In addition, a critical assessment of the deposition on various substrates was made, as well as the functional properties of the deposited materials.

(iii) This work shows that 3D deposition by spray deposition is not exclusively possible with an all-citrate precursor.[5,6] With a rather common nitrate-citrate approach, 3D depositions were established as well. In some cases the citrate-nitrate route may be more suitable, since decomposition occurs more easily than for the all-citrate precursor. These findings open up new approaches for low-temperature routes such as combustion synthesis.[7]

(iv) Finally, this work underlines the significance of a system oriented approach. Conductivities and/or capacities can be optimized for a separate or isolated material, but most of the gained performance can be made undone upon integrating the material with other parts

to yield a full device. Diffusional issues, interfaces, disruption of the original lattice; numerous effects can come into play upon device integration. In this thesis just a few small examples were shown about how complex device integration can be, especially if large thermal budgets are required. Arguably, a combination of less perfect materials (in terms of crystallinity, stoichiometry, etc.) can be more versatile than high quality materials that are inflexible in view of integration.

Finally, this work showed that wet-chemical synthesis of thin film materials for 3D all-solid-state Li-ion batteries is not only possible, but the activity of the materials deposited was shown as well. Since all these results were achieved with cost-effective and highly up-scalable methods, it can be regarded as a major breakthrough within the field of wet-chemical processing and 3D thin film all-solid-state Li-ion batteries as well.

2. Outlook

Although the 3D deposition of LLT is great improvement for the field, the conductivity achieved for this amorphous material remains to be improved. Especially because 3D thin-film all-solid-state Li-ion batteries are designed to achieve high current densities, the loss in performance at high currents shown in this study is simply too large for many applications. Studying additional lithium doping, or exchanging the electrochemically instable titanium with other metals may yield interesting results in both conductivity and electrochemical stability of this amorphous material.

The main issue emerging several times in this work was the thermal budget of the current collector. Though a start was made with the ITO current collector, further improvements are required. For instance, a thorough study aimed at improving the electronic conductivity of this (3D) material could be done, yielding better performance at comparable current collector thicknesses.

Although current collectors, negative electrodes and solid electrolytes have been discussed, the positive electrode remains to be

deposited to yield a full 3D thin film all-solid-state battery. Future work is required here, especially regarding the deposition of high voltage positive electrodes such as lithium manganese nickel oxide (LMNO).[8] This material, with a (de)lithiation voltages as high as 4.7 V vs. Li^+/Li, would seriously improve the power density of the LLT/WO_3 stack studied in this work. Since no reactivity of the LLT is expected at high voltages, this regarded as a very promising route worth exploring.

Finally, questions remain regarding the deposition process used. Although new insights were gained here, a more fundamental study aimed at understanding all the different processes occurring during USD of 3D surfaces is expected to be very rewarding. This would not only aid the development of 3D Li-ion batteries, but various other smart (energy) materials as well.

3. References

[1] J. Xie, P.-P. R. M. L. Harks, D. Li, L. H. J. Raijmakers, P. H. L. Notten, *Solid State Ionics* **2016**, *287*, 83.

[2] J. Xie, J. F. M. Oudenhoven, P.-P. R. M. L. Harks, D. Li, P. H. L. Notten, *J. Electrochem. Soc.* **2014**, *162*, A249.

[3] M. M. Shaijumon, E. Perre, B. Daffos, P.-L. Taberna, J.-M. Tarascon, P. Simon, *Adv. Mater.* **2010**, *22*, 4978.

[4] J. Xie, J. F. M. Oudenhoven, D. Li, C. Chen, R.-A. Eichel, P. H. L. Notten, *J. Electrochem. Soc.* **2016**, *163*, A2385.

[5] S. Gielis, Chemical Solution Deposition of Oxides for Energy Storage Applications: A Breaktrough in Coating High Aspect Ratio 3D Structures, Hasselt University, **2015**.

[6] S. Gielis, A. Hardy, M. K. Van Bael, Conformal Coating on Three-Dimenstional Substrates, **2015**, EP 2 947 178 A1.

[7] M.-G. Kim, M. G. Kanatzidis, A. Facchetti, T. J. Marks, *Nat. Mater.* **2011**, *10*, 382.

[8] Z. Yang, J. Zhang, M. C. W. Kintner-Meyer, X. Lu, D. Choi, J. P. Lemmon, J. Liu, *Chem. Rev.* **2011**, *111*, 3577.

Scientific contributions

Published articles

van den Ham E.J.; Elen. K.; Bonneux, G.; Maino, G.; Notten, P.H.L.; Van Bael, M.K. & Hardy, A. (2017) *3D indium tin oxide electrode by ultrasonic spray deposition for current collection applications* – JOURNAL OF POWER SOURCES, 348, p. 130-137.

van den Ham, E.J.; Gielis, S.; Van Bael., M.K. and Hardy, A. (2016) *Ultrasonic spray deposition of metal oxide films on high aspect ratio microstructures for 3D all-solid-state Li-ion batteries* - ACS ENERGY LETTERS, 1, p.1184-1188.

van den Ham, E.J.; Elen, K.; Kokal, I.; Yağci, B.; Peys, N.; Bonneux, G.; Ulu, F.; Marchal, W.; Van Bael, M.K. & Hardy, A. (2016) *From liquid to thin film: colloidal suspensions for tungsten oxide as an electrode material for Li-ion batteries.* - RSC ADVANCES 6 (57), p. 51747-51756.

van den Ham, E.J.; Peys, N.; De Dobbelaere,C.; D'Haen, J.; Mattelaer, F.; Detavenier, C.; Notten, P. H. L.; Hardy, A. & Van Bael, M.K. (2015) *Amorphous and perovskite* $Li_{3x}La_{(2/3)-x}TiO_3$ *(thin) films via chemical solution deposition: solid electrolytes for all-solid-state Li-ion batteries.* - JOURNAL OF SOL-GEL SCIENCE AND TECHNOLOGY, 73 (3), p. 536-543.

Marchal, W.; Vandevenne, G.; D'Haen, J.; Calmont Andrade Ameida, A.; Antonio Durant Sola, M.; **van den Ham, E.J**.; Drijkoningen, J.; Elen, K., Deferme, W.; Van Bael, M.K. & Hardy, A. (2017) *Ultrasonically spray coated silver layers from designed precursor inks for flexible electronics* – NANOTECHNOLOGY, 28 (21), p. 215202

Gielis, S.; Ivanov, M.; Peys, N.; **van den Ham, E.J.**; Pavlovic, N.; Banys, J.; Hardy, A. & Van Bael, M.K. (2015) *Aqueous chemical solution deposition of ultra high-k* $LuFeO_3$ *thin films.* - JOURNAL OF THE EUROPEAN CERAMIC SOCIETY, 37 (2), p. 611-167

Submitted manuscripts

van den Ham E.J.; Maino, G.; Bonneux, G.; Marchal, W.; Elen, K.; Gielis, S.; Mattelaer, F.; Detavernier, C.; Notten, P.H.L.; Van Bael, M.K. & Hardy, A. (2017) *Wet-chemical Synthesis of 3D Stacked Thin Film Metal-oxides for All-solid-state Li-ion Batteries* - revision submitted.

Oral presentations

van den Ham, E.J; Van Bael, M.K.; Hardy, A.; Maino, G.; (2016) *Wet chemical synthesis of oxide nanomaterials for 3D thin film Li-ion battery applications* - E-MRS Fall meeting, Warsaw, 19-23/09/2016.

van den Ham, E.J.; Peys, N.; Kokal, I.; Yağci, B.; Elen, K.; Bonneux, G.; Marchal, W.; Hardy, A. & Van Bael, M. K. (2016) *From liquid precursor to film: WO_3 as promising high voltage anode for all-solid-state thin film Li-ion batteries.* - E-MRS spring meeting 2016, Lille, 02-06/05/2016

van den Ham, E.J.; Peys, N.; Elen, K.; Bonneux, G.; Marchal, W.; Hardy, A. & Van Bael, M.K. (2015) *WO_3 thin films by spray-coating as high voltage anode material for all-solid-state Li-ion batteries.* - E-MRS Fall meeting, Warsaw, 15-18/09/2015.

van den Ham, E.J.; Peys, N.; Elen, K.; Bonneux, G.; Marchal, W.; Hardy, A. & Van Bael, M.K. (2015) *Ultrasonic spray deposited WO_3 thin films as high voltage anodes for all-solid-state Li-ion batteries.* - 2015 BCerS Annual Meeting, Mons, Belgium, 26/10/2015.

Hardy, A.; Gielis, S.; Maino, G.; **van den Ham, E.J.** & Van Bael, M.K. (2016) *Towards a solution deposited 3D thin-film Li-ion battery.*- 40th International Conference and Expo on Advanced Ceramics and Composites, Florida, USA, 24-29/01/2016.

Van Bael, M. K.; Elen, K.; Gielis, S.; **van den Ham, E.J.**; Maino, G.; Peys, N. & Hardy, A. (2015) *Chemical solution deposition of oxides for energy applications.* - MCARE2015, Jeju - Korea, 24-27/02/2015.

Gielis, S.; Ivanov, M.; Peys, N.; **van den Ham, E.J.**; Pavlovic, N.; Robaeys, P.; Nesladek, M.; Banys, J.; Hardy, A. & Van Bael, M. K. (2015) *Aqueous chemical solution deposition of $LuFeO_3$ ultra high-k films.-* 39th International Conference and Exposition on Advanced Ceramics and Composites, Daytona Beach, Florida, USA, 25-30/01/2015.

Maino, G.; Gielis, S.; **van den Ham, E.J.**; Peys, N.; Vereecken, P.; Hardy, A. & Van Bael, M.K. (2015) *$LiMn_2O_4$ cathodes for 3D thin film all solid state Li-ion batteries: towards conformal deposition on high aspect ratio substrates.* - E-MRS, Warsaw, Poland, 15-16-17-18/09/2015.

Bonneux, G., Elen, K., **van den Ham, E.J.**, Marchal, W., D'Haen, J., Locquet, J.P., Hardy, A. & Van Bael, M.K. (2015) *Aqueous solution-based synthesis and deposition of crystalline In-Ga-Zn-Oxide films via spray-coating* - E-MRS, Warsaw, Poland, 15-19/09/2015.

Peys, N.; Gielis, S.; **van den Ham, E.J.**; Maino, G.; Hardy, A. & Van Bael, M.K. (2014) *Aqueous solution processing of Li-based oxides as candidate electrode or electrolyte in solid-state Li-ion batteries.-* Materials Science and Technology (MS&T), Pittsburgh, Pennsylvania, USA, 12-16/10/2014.

Poster presentations

van den Ham, E.J.; Bonneux, G.; Elen. K.; Maino, G.; Van Bael, M.K. & Hardy, A. (2017) *3D structured indium tin oxide electrodes via ultrasonic spray deposition on high-aspect ratios* – scheduled – 40th International Conference and Expo on Advanced Ceramics and Composites, Daytona beach, Florida, USA, 24-29/01/2017

van den Ham, E.J.; Gielis, S., Bonneux, G.; Marchal, W.; Mattelaer, F.; Detavernier, C.; Van Bael, M.K. & Hardy, A. (2016) *WO_3 deposition via ultrasonic spray deposition on high-aspect ratio TiN coated Si micro pillars for all-solid- state 3D Li-ion batteries* – 67th annual meeting of the international society of electrochemistry, The Hague, the Netherlands, 21-26/08/2016.

van den Ham, E.J.; Peys, N.; De Dobbelaere,C.; D'Haen, J.; Mattelaer, F.; Detavenier, C.; Notten, P. H. L.; Hardy, A. & Van Bael, M.K. (2014) *Amorphous and perovskite $Li_{3x}La_{(2/3)-x}TiO_3$ solid electrolyte for all-solid-state Li-ion batteries* - 2014 BCerS Annual Meeting, Ghent, Belgium, 23/10/2014.

Summary

With this thesis, the use of wet-chemical synthesis routes within the field of 3D thin film all-solid-state batteries was explored. This battery concept combines both high energy density and power density in the form of 3D architectures. Although the concept is simple, deposition of the materials involved is challenging. In this thesis, this topic is addressed with wet-chemical synthesis routes combined with spray-deposition, because of i) low cost, ii) scalability and iii) ease of multi-metal material deposition. Successful implementation of 3D thin film all-solid-state Li-ion battery concept would be very rewarding, since lifetime and safety of batteries would be improved tremendously.

Two materials classes were selected to be used as solid electrolyte within this study. First lithium lanthanum titanate ($Li_{0.35}La_{0.55}TiO_3$) was studied. By spin and spray-deposition of a nitrate-citrate precursor, high quality films were obtained with thicknesses between 90 to 120 nm. Although highly conductive tetragonal phase was obtained at higher annealing temperatures (700°C), morphological issues such as pin-holes could not be prevented. While preparing the material in amorphous form at 500°C, a conductivity of $3.8 \cdot 10^{-8}$ $S \cdot cm^{-1}$ was measured. However, the electrochemical stability was limited due to Ti^{4+} reduction at 1.5 V (vs. Li/Li^+). With spray-coating, two different synthesis routes yielded 3D coatings on various 3D architectures. With a conformality of over 30%, this proved to be a unique approach to obtain 3D structured thin film solid electrolytes. In an effort to resolve the issue of electrochemical stability of the solid electrolyte, the synthesis of Li-stuffed garnet lithium lanthanum zirconate ($Li_7La_3Zr_2O_{12}$) was studied. However, due to crystallization issues and demanding thermal budgets, this proved to be a less suitable material.

Tungsten oxide (WO_3) was prepared as a negative electrode to be combined with the less electrochemically stable lithium lanthanum titanate, in order to study functional half-cells. Two different routes were studied for WO_3 thin film synthesis. First, a colloidal suspension was prepared an studied, identifying the reaction mechanism

responsible for chloride removal from the tungsten-chloride based precursor. Spray-deposition of the crystalline, rod-shaped WO_3 particles yielded smooth WO_3 films of 150 nm thickness. Electrochemical activity of the films was achieved at 400°C and higher, with stable cycling performance shown for 100 cycles on (oxidative) TiN current collectors, with capacities over 600 $mAh \cdot cm^{-3}$. To establish higher capacities, lithium doping of WO_3 was studied, yielding the $Li_2W_2O_7$ phase. Contraction and expansion effects rendered this material unsuitable for thin-film Li-ion batteries. For 3D deposition of WO_3, a second (citrate) precursor was developed. Within thermal constraints, active WO_3 was achieved on 3D architectures. A 2.6 fold 3D capacity enhancement was booked with TiN as a current collector with current densities up to 10C. While using spray-deposited indium tin oxide (ITO) as a current collector, a 4.5 fold capacity increase was achieved at current densities of up to 4C.

Finally, the combination of an electrolyte with a 3D structured electrode was shown with a lithium lanthanum titanate – WO_3 stack. Although rate performance was reduced by the addition of the solid electrolyte, as well as a 30% capacity drop, a unique 3D half-stack was achieved completely by spray-deposition.

The research done in this study increases the knowledge on 3D depositions via spray-deposition. Various (gelating) precursors appeared to show similarities in deposition behaviour, whereas colloidal suspensions to be less suitable. In addition, combining materials to form all-solid-state half cells is a unique achievement, especially considering the low-cost and highly scalable methods used. Therefore, this this is considered a major step forward for wet-chemical synthesis of battery materials, as well as realization of a 3D thin-film all-solid-state Li-ion battery.

Samenvatting

Gezien de ontwikkelingen rondom energie en de transitie naar een meer duurzame toekomst, is de opslag van elektrische energie van cruciaal belang. Hiervoor zijn verschillende opties, maar met name lithium-ion batterijen zijn geschikt voor mobiele toepassingen vanwege de grote hoeveelheid energie die ze kunnen opslaan ten opzichte van hun gewicht.

Batterijen bestaan uit verschillende onderdelen van reactieve materialen. Onderlinge reacties vinden plaats door het uitwisselen van Li^+ ionen (positief geladen deeltjes) en elektronen (negatieve ladingen). Door deze reacties te controleren, kan men de energie die vrijkomt bij de reacties gebruiken om arbeid te verrichten, bijvoorbeeld om een auto te laten rijden. Echter, de huidige generatie Li-ion batterijen zijn niet veilig genoeg voor bepaalde toepassingen. Daarnaast is de levensduur beperkt vanwege het gebruik van vloeistoffen in de batterij.

Li-ion batterijen zouden qua veiligheid en levensduur sterk verbeteren door de gebruikte vloeistoffen te vervangen voor vaste stoffen; hierdoor zou een volledige vaste-stof batterij ontstaat. In praktijk blijken bepaalde keramische materialen geschikt als vervanging van eerder genoemde vloeistoffen; Li^+ ionen kunnen hier (met enige weerstand) doorheen bewegen. Vanwege transport limiteringen van Li^+ ionen in deze keramische stoffen is het echter beter om een 3D architectuur toe te passen, waardoor de effectieve capaciteit van de batterij verhoogd kan worden.

Met het volgende voorbeeld zou het voordeel van een 3D architectuur duidelijker moeten worden. Stel een groot huis voor in winterse omstandigheden dat slechts één haardvuur heeft; het duurt lang voordat alle kamers op temperatuur zijn, waardoor het haardvuur erg lang moet branden. Door het aanleggen van een centraal verwarmingssysteem (d.w.z. 3D structuur), kan de warmte zich veel sneller verspreiden door het hele huis, waardoor veel efficiënter gebruik gemaakt kan worden van dezelfde hoeveelheid warmte.

De lengteschaal waarbij 3D batterijen onderzocht worden is echter van een totaal andere orde dan het zojuist gegeven voorbeeld; om het systeem goed te laten functioneren zijn lengteschalen onder de micrometer nodig (ter vergelijking: een haar is gemiddeld 70 micrometer dik). Om het concept van 3D batterijen te laten slagen moeten de verschillende onderdelen van de batterij echter wel afgezet ('gemaakt') kunnen worden in de vorm van dunne laagjes (ook wel films genaamd). Hiervoor worden vaak dure methoden gebruikt die moeilijk op te schalen zijn. In dit proefschrift is echter gekozen voor een nat-chemische synthese benadering in combinatie met verneveling; dit proces is goedkoop en gemakkelijk op te schalen. Door verschillende nat-chemische synthese methoden te gebruiken - waarvan er veel gebaseerd waren op milieuvriendelijke chemicaliën - is in dit proefschrift een grote stap gemaakt om 3D Li-ion batterijen te realiseren:

(i) Er zijn materialen afgezet in 3D die voorheen alleen in 2D afgezet konden worden. Zo zijn bijvoorbeeld lithium lanthaan titanium oxide ($Li_{0.35}La_{0.55}TiO_3$) en wolfraam oxide (WO_3) afgezet op micro-cilinders van 50 micrometer lang en een straal van 1,5 micrometer.

(ii) Specifieke combinaties van 3D materialen zijn bestudeerd, die voorheen onmogelijk waren. De combinatie van indium tin oxide (In_2O_3:Sn) met wolfraam oxide is hierin uniek, omdat dit verdere ontwikkeling van 3D batterijen kan versnellen.

(iii) Nieuwe inzichten zijn verworven op het vlak van materiaal synthese en depositie. Voorheen leek het vooral mogelijk om via één bepaalde route (z.g.n. volledige citroenzuur route) materialen in 3D af te zetten, terwijl tijdens deze studie is aangetoond dat andere synthese routes ook mogelijk zijn. Dit is van belang voor 3D batterijen, maar ook voor andere energie toepassingen zoals de nieuwe generatie LEDs en zonnepanelen.

(iv) Dit proefschrift geeft meer inzicht in specifieke reactiemechanismen die voorkomen tijdens de synthese van diverse materialen (bijvoorbeeld de conversie van wolfraam chloride tot wolfraam oxide). Dit is niet direct

van belang voor batterijen, maar vergroot hiermee kennis van de chemie als wetenschap.

Samenvattend; vooral omdat niet alleen de synthese, maar vooral ook het functioneren van batterij materialen kon worden aangetoond in combinatie met een voordelige, milieu vriendelijke techniek die toepasbaar is op grote schaal, kan men de resultaten van dit proefschrift zien als een grote stap voorwaarts in de ontwikkeling 3D vaste-stof batterijen en andere 3D dunne film materialen.

Dankwoord (Acknowledgements)

Onderzoek doet men niet alleen. Een promotieonderzoek heeft vaak de reputatie een individuele aangelegenheid te zijn, maar er zijn veel mensen betrokken bij dit werk. In dit dankwoord zou ik graag mensen willen bedanken die me de laatste jaren hebben geholpen.

Als eerste wil ik graag mijn ouders en broers bedanken. Ma, je hebt je altijd compleet ingezet om mijn opleiding en dat van mijn broers (zelf) te regelen in Kenia; heel hartelijk dank daarvoor. Christiaan, als enige 'klasgenoot' was je jaren lang m'n 'partner in crime', en je hebt me veel geleerd over planning en zelfdiscipline; iets waar ik veel aan heb gehad! Pa, je hulp en steun tijdens de lastige transitie op school van Kenia naar Nederland was cruciaal, zonder jou was ik nooit zover gekomen. Tenslotte Henk-Jan, als 'bèta broer' was je altijd een voorbeeld voor me; tijdens het voordoen en uitleggen van experimenten met *kopersulfaat* wist je m'n interesse in de scheikunde al vroeg aan te wakkeren.

Ik wil ook graag de docenten en mentoren van de CSW Middelburg bedanken. De docenten van natuurkunde en scheikunde, met name meneer Van Dijk en meneer Leopold, wil ik hier graag bedanken voor hun lessen.

De mensen van Versatec Energy B.V., vooral Klaas-Otto Ykema, wil ik hier bedanken voor de mogelijkheden en vertrouwen in een (voor mij) lastige tijd. Tijdens mijn afstuderen bij Scheikundige Technologie aan de TU/e heb ik veel gehad aan de begeleiding van Prof. Hintzen. Nogmaals dank hiervoor Bert. Prof. Peter Notten (TU/e) wil ik op deze plaats ook bedanken; na het afstuderen kwamen we elkaar weer tegen in het SOS Lion project. Heel hartelijk dank voor uw hulp aan het begin van m'n periode in Hasselt, vooral voor het delen van kennis en apparatuur om een goede start te maken.

Dan wil ik ook de mensen van de Universiteit Hasselt bedanken. In de eerste plaats natuurlijk de collega's van de IPC groep. Dat zijn heel wat collega's door de jaren heen, maar ik wil er toch een paar

expliciet noemen. Vooral Wouter en Dries wil ik bedanken voor de samenwerking voor het TGA, FTIR, en andere werkzaamheden. Gilles ben ik enorm veel dank (en vrije avonden) verschuldigd vanwege al het SEM werk, maar ook voor SPM-APM/Koningswater experimenten. Ken, je hebt heel wat XRDs voor me gedaan, hartelijk dank hiervoor! Sven en Nick, hartelijk dank voor jullie hulp binnen het SOS Lion project. And of course Giulia; we started at UHasselt almost simultaneously. After a challenging start in the SOS Lion project, we were able to tackle a lot problems together. Thanks for all the time we spent discussing all kinds of scientific and other topics, along with a nice cup of coffee of course! Speaking of coffee; thanks for all the interesting discussions Fulya and Aleks! And off course for helping me with TEM and Raman analysis.

Hier wil ik ook andere UHasselt collega's bedanken, waaronder Jan D'Haen en Bart Ruttens voor de hulp met SEM en XRD tijdens mijn onderzoek. Johan Soogen en Johhny Baccus mag ik ook zeker niet vergeten, jullie hulp was absoluut onmisbaar! Uiteraard wil ik ook An en Marlies bedanken. Aan het begin was het misschien wat onwennig om met relatief directe 'Hollander' te werken, maar wat mij betreft kunnen we terugkijken op een zeer goede samenwerking de laatste jaren waarin ik veel heb kunnen leren op diverse vlakken. Dankzij jullie kon mijn wens om materiaalonderzoek te gaan doen in vervulling laten gaan. Ik wil ook graag de mensen van de andere onderzoeksinstituten bedanken die betrokken waren bij het SOS Lion project. Felix, je hebt me op diverse punten geholpen, nogmaals dank voor je hulp.

Tot slot wil ik ook Annemiek bedanken. Het had allemaal heel wat voeten in de aarde, zelfs verhuizen naar België, maar je hebt me altijd gesteund. Vooral toen het even minder ging tijdens de beruchte 2de jaars 'PhD dip' heb je me ontzettend veel geholpen. Ik zie er naar uit om samen met jou een nieuwe uitdaging aan te gaan, wat of waar dat ook zal zijn.